Atherosclerosis Biomechanical Simulation

Pedro Filipe de Oliveira Lopes

Supervisor: Professor Jorge Américo Oliveira Pinto Belinha, PhD

Co-Supervisor: Professor Renato Manuel Natal Jorge, PhD

Integrated Masters on Bioengineering - Biomedical Engineering

June, 2016

Faculty of Engineering of the University of Porto

Atherosclerosis Biomechanical Simulation

Pedro Filipe de Oliveira Lopes

Dissertation submitted to Faculty of Engineering of the University of Porto

to obtain the degree of **Master in Bioengineering**

June, 2016

Abstract

Cardiovascular Diseases (CVD) is a major cause of premature death in the world, being one of the usual causes of these diseases the build up of fatty deposits on the inner wall of arteries. This build up is part of a process called atherosclerosis where the subject experiences a thickening and increased rigidity of the arterial walls due to the deposition of fat, proteins and carbohydrates in conjunction with increased cell proliferation and immune responses. While this process has been already been studied extensively on a biological sense, there are very few studies that focus on the mechanical properties of the plaque or on mechanical simulations of this tissue.

This work proposes to use meshless methods to perform biomechanical simulations of the atherosclerotic plaque in two dimensional (2D) and three dimensional (3D) settings. This advanced numerical methods discretize the problem domain into a nodal cloud without any pre-established relations. In the meshless methods used for this work, these relations are afterwards defined with the use of the Voronoi diagrams and the respective shape functions with radial point interpolators. It has already been shown in the literature that these methods, when compared with the Finite Element Method (FEM), produce more accurate and smoother variable fields.

For this work the atherosclerotic plaque was simulated has being an elasto-plastic material with its mechanical properties based on literature. The work analyses four different 2D models, representing four different stages of the process, and two different 3D models, showing two different levels of stenosis. All these models were tested with 3 different sets of material properties for the plaque characteristic of different levels of calcification. The simulations where made considering symmetry conditions and by application of a static pressure in the artery's lumen. The results show that there is a relation between the plaque's thickness or the level of tissue calcification and the artery's stiffness. It can also be seen that at a physiological pressure level the atherosclerotic plaque does not experience any kind plastic deformation.

Keywords: Atherosclerotic Plaque, Meshless Methods, Elasto-Plastic

Resumo

As Doenças Cardiovasculares são uma das principais causas de morte prematura no mundo, sendo que uma das causas mais comuns destas doenças é a acumulação de gorduras nas paredes internas das artérias. Esta acumulação é parte de um processo chamado aterosclerose, no qual um sujeito experiencia um aumento da espessura e rigidez das paredes arteriais resultante da deposição de gordura, proteínas e hidratos de carbono, juntamente com um aumento da proliferação celular e da resposta imunitária. Apesar de este processo já se encontrar extensamente estudado de um ponto de vista biológico, existem poucos estudos focados nas propriedades mecânicas da placa ou em simulações biomecânicas deste tecido.

Assim, este trabalho pretende utilizar métodos sem malha para a realização de simulações biomecânicas da placa aterosclerótica em modelos a duas dimensões (2D) e a três dimensões (3D). Estes métodos numéricos permitem discretizar o domínio do problema numa nuvem de nós sem qualquer relação pré-estabelecida. Nos métodos sem malha utilizados neste trabalho, essas relações são posteriormente definidas com o uso de diagramas de Voronoi, sem as respetivas funções de forma definidas com interpoladores radiais. Já se encontra demonstrado na literatura que estes métodos, quando comparados com o Método de Elementos Finitos (FEM), permitem produzir campos de variáveis mais precisos e suaves.

Neste trabalho a placa aterosclerótica foi simulada como sendo um material elasto-plástico, com as suas propriedades mecânicas baseadas na literatura. Este trabalho analisa quatro modelos 2D diferentes, representando quatro estados diferentes deste processo, e dois modelos 3D diferentes, mostrando dois níveis diferentes de estenose. Todos os modelos foram testados com três conjuntos diferentes de propriedades mecânicas para a placa aterosclerótica característicos de diferentes níveis de calcificação. As simulações foram realizadas considerando condições de simetria e aplicando uma pressão estática no lúmen da artéria. Os resultados mostram que existe uma correlação entre a espessura ou o nível de calcificação da placa e a rigidez apresentada pela mesma. Para além disto também é possível concluir que a uma pressão fisiológica a placa aterosclerótica não apresenta qualquer deformação plástica.

Keywords: Placa Aterosclerótica, Métodos sem malha, Elasto-Plástico

Acknowledgments / Agradecimentos

Um sincero muito obrigado ao Prof. Jorge Belinha por todo o apoio e ajuda que deu durante a realização deste projecto. Não só refletido nas inúmeras vezes em que simplesmente aparecia sem aviso pelo seu gabinete para esclarecer uma dúvida ou mostrar um resultado, mas também na amizade, paciência e outras coisas, que por muito pequenas que possam parecer, me permitiram crescer como profissional e como pessoa.

Ao Marco Marques por todas as pequenas grandes ajudas que foi dando ao longo do trabalho e que sem as quais pequenos problemas teriam sido grandes dores de cabeça, um muito obrigado.

A todos os amigos destes 6 anos de faculdade, Duarte, Catarina, Ricardo, Tânia, Tiago, Miguel, Tito, Joana, Mariana, Abel, Filipa e demais. Obrigado por terem feito parte desta aventura e das histórias que levo daqui e que as histórias continuem durante as aventuras que vão seguir. E à Sofia, por ter sido o meu braço direito durante este ano, aturando os meus constantes desvaneios e por ser uma das melhores amigas que alguma vez podia ter tido, um muito, muito obrigado. Que nos continuemos a chatear com os desvaneios de cada um.

A todos os membros do NEB que tornaram este ano inesquecível para mim de tantas maneiras e por terem sido a equipa imparável que foram. Um obrigado por me darem o orgulho de ter trabalhado convosco.

À Patrícia por todo o apoio, motivação e carinho, por me ajudares a ter força mesmo quando podia ser díficil levantar os braços para voltar à luta. Obrigado por cada sorriso.

E por fim, aos meus pais, ao meu irmão e aos meus avós, por todo o apoio que me deram ao longo dos anos, pelos sermões que me fizeram crescer e pelos valores que me incutiram. Obrigado por me fazerem a pessoa que sou hoje.

Pedro Filipe de Oliveira Lopes

Institutional Acknowledgments

The author truly acknowledge the logistic conditions provided by Ministério da Educação e Ciência– Fundação para a Ciência e a Tecnologia (Portugal), under project funding UID/EMS/50022/2013 (funding provided by the inter-institutional projects from LAETA) and project NORTE-01-0145-FEDER-000022 - SciTech - Science and Technology for Competitive and Sustainable Industries, cofinanced by Programa Operacional Regional do Norte (NORTE2020), through Fundo Europeu de Desenvolvimento Regional (FEDER).

Additionally, the author truly acknowledge the work conditions provided by the department of Mechanical Engineering from FEUP and INEGI.

"The journey of a thousand miles begins with one step."

Lao Tzu

Contents

List of Figures

List of Tables

List of Abbreviations

2D	Bidimensional
3D	Tridimensional
ATR	Attenuated Total Reflectance
CVD	Cardiovascular Disease
DEM	Diffuse Element Method
EFGM	Element-Free Galerkin method
FEM	Finite Element Model
FPM	Finite Point Method
FSM	Finite Spheres Method
FTIR	Fourier Transform Infra-red Spectroscopy
MFEM	Meshless Finite Element Method
MLPG	Meshless Local Petrov-Galerkin method
NEM	Natural Element Method
NNFEM	Natural Neighbour Finite Element Method
NNRPIM	Natural Neighbours Radial Point Interpolation Method
PCI	Percutaneous Coronary Intervention
PIM	Point Interpolation Method
RBF	Radial Basis Function
RBFM	Radial Basis Function Method
RKPM	Reproduced Kernel Particle Method
RPIM	Radial Point Interpolation Method
SPH	Smoothed Particle Hydrodynamics Approach

Chapter 1

Introduction

Today we live in a world filled with technology. People spend their days looking at their smartphones, working in their computers and watching television. This more sedentary way of living, when compared to previous generations, combined with unhealthy diets and other lifestyle choices are all risk factors for Cardiovascular Diseases (CVDs) [1, 2].

CVD is the major cause of premature death in the world, with more than 17.5 million deaths worldwide in 2012 [1]. One of the most common causes for CVD is the build-up of fatty deposits over the inner walls of blood vessels [1], which is part of the process that its called atherosclerosis [3, 4]. This accomulation of fatty deposits, in conjunction with proteins, carbohydrates and increased cell proliferation, leads to (1) a recruitment of monocytes (imunologic response) and (2) the thickening of the artery's walls [3, 4]. This phenomena can lead to coronary heart disease, cerebrovascular disease or others, causing, in acute events, heart attacks or strokes due to blockages in the blood flow [1, 4].

Being the major cause of premature death worldwide, this is a problem that needs to be tackled. The first efforts to tackle CVD are prevention, primarily by changing habits or by using pharmaceuticals, as stated in European Guidelines [2]. In some severe cases, these might be insufficient and the subject may require surgical intervention in order to reduce the risks of trombosis [1]. One of these procedures is the Percutaneous Coronary Intervention (PCI), also known as angioplasty, consisting of the insertion of a balloon-tipped catheter that will be inflated on the affected location, thus expanding the vase. This approach is minimally invasive, and can also be combined with the use of a small metallic mesh (stent) that will remain on the vase, impeding it from closing back. Although simple and minimally invasive, this procedure is usually only used when patients are considered poor candidates for a bypass grafting [5]. This choice is made due to concerns about procedure risk and long time durability of PCI [5]. The main issue with long time durability is the potential restenosis of the vessel [6] and therefore the loss of vascularization.

A better understanding of the atherosclerotic plaque mechanics could help the development of the PCI technique reducing the restenosis rate. The Finite Element Method (FEM) has already been used to improve and support stent's design [7, 8, 9] but not many studies have been focused on the analysis of the atherosclerotic plaque itself [10]. Hence this thesis aims to create a reliable

biomechanical simulation of the atherosclerotic plaque with the use of the NNRPIM, which is a precise and flexible meshless numerical method [11].

1.1 Meshless Methods

Numerical methods, as the Finite Element Method (FEM) or Meshless methods, have been used on a large scale to solve problems coming from different study areas, such as astrophysics, mechanical engineering, fluid dynamics or even economy. In these fields there is the need to resolve partial differential equations that model these phenomena. Those equations are frequently so complex that solving them through analytical methods is percieved as either impossible or impracticable. The use of these computational methods opens the possibility to reach an approximation to that analytical solution [12].

1.1.1 Finite Element Method

Several computational methods exist nowadays, but among them the most popular is the Finite Element Method [13, 14]. Its applications range from analysis of effects of urban design [15] to biomechanical studies of the jaw [16].

This method allows for an approximation of the problem's solution by dividing its domain into discrete simpler parts, called elements. From the collection of all the elements a mesh is created which, aside of containing them, also finds the connectivity relations between each one [17]. After the problem has been discritized, the field function of the domain is interpolated within each element in terms of an assumed approximation function (shape function). The approximation function is used because the real solution of the element's field variable, represented by the aforementioned differential equations, is normally more complex. Finally, the global domain equation system is obtain by assembling of each element's local equation system [18].

But as new challenges arised other methods were needed to tackle more complex problems that FEM had difficulties solving. For example, a lack of precision is found when considering large deformations, complex geometries or fractures propagation. These shortcomings are caused by the own nature of FEM, by building a mesh that hinders the treatment of discontinuities which do not coincide with the original meshlines [19]. Meshless methods are supported by a formulation that eliminates the necessity of the mesh, constructing the approximation exclusively in terms of an arbitrary nodal set of nodes [19].

1.1.2 Meshless Methods

Considering the limitations of the FEM discretization, meshless methods appeared as an alternative approach. By creating their interpolation functions based on a distribution of scattered nodes instead of meshes [20] and using an influence-domain for each node rather than elements [21], the meshless methods surpassed at least part of FEM difficulties, such as mesh distortion and remeshing [20]. Besides this, the displacement and stress fields obtained from meshless methods are often

more close to an analytical solution than the ones created by low order element meshes (three and four nodes).

The history of meshless methods appears to start in 1980 with the Generalized Finite Differences [22], by the application of the Finite Difference method into a arbitrary irregular mesh. This work was followed by the Smoothed Particle Hydrodynamics Approach (SPH) in 1988 [23], which was applied to model boundless astrophysical phenomena, being afterwards extended to other fields, such as flow dinamics [24]. SPH was then refined into the Reproduced Kernel Particle Method (RKPM) by introducing a correction function into the used kernels the accuracy of the method increased [25].

Using a different method of approximations (the moving least squares approximations) a different set of methods were created. The first to appear was called the Diffuse Element Method (DEM) [26], which has later been modified and refined into the element-free Galerkin method (EFGM) [27]. This is a very consistent and stable method, applied to both solids and fluid mechanics.

Other methods also appeared along the years, as for example meshless local Petrov-Galerkin method (MLPG)[28], defined with local weak forms [20]; the method of the finite spheres (FSM) [29], viewed as a special case of the MLPG; the Finite Point Method (FPM) [30] and the Radial Basis Function Method (RBFM) [31, 32]. The latter method was distinct from the others as it used radial basis functions to approximate the variable fields. Besides, it was a 'truly' meshless method, has it did not require an integration mesh, and used the strong form formulation, in opposition to the previous which relied on the weak formulation form [21].

These methods had the particularity of using approximation functions instead of interpolation functions. This characteristic turned the definition of essential boundary conditions into an problem, given that the usage of these functions made the methods lack the delta Kronecker property [33].

In order to address this problem, there have been developed several meshless methods using interpolant functions in the last years. Some of these are the Point Interpolation Method (PIM) [34], the Point Assembly Method [35], the Meshless Finite Element Method (MFEM) [36], the Natural Neighbour Finite Element Method (NNFEM) [37, 38] or the Natural Element Method (NEM) [39, 40, 41].

Given the simplicity of the shape functions construction, when compared with the EFGM, and the ease of its derivatives calculations, the PIM method was considered an attractive method [33]. Additionally the use of interpolation functions allowed their shape functions to have the delta Kronecker property making essential boundary conditions easy to impose. In an effort to further improve this method, the polynomial basis function of the original formulation was replaced by Gaussian and multiquadratic radial basis functions, originating the Radial Point Interpolation Method (RPIM)[42, 43]. The RPIM has already been extended into three-dimensional analysis [44] and applied to several problems as buckling analysis [45] or simulations of piezo-electric structures [46].

In the last years one of the most discussed meshless method is the NEM. This method constructs its trial and test functions using natural neighbour interpolants [47], a multivariate data interpolation scheme initially used in data filling. When constructing the interpolation function, the method relies in mathematical concepts as the Voronoï diagrams [48] and the Delaunay tessellation [49].

The combination of the NEM and the RPIM allowed for the creation of an improved meshless method, the Natural Neighbour Radial Point Interpolation Method (NNRPIM) [21]. The NNRPIM contructs its interpolation functions with a similar process to the RPIM and uses the natural neighbour interpolant concept to define nodal connectivity and create a background integration mesh. Given this total dependency of the integration mesh to the nodal dependency, the NNRPIM is considered a 'truly' meshless method [21].

1.2 State of the Art - Mechanical Simulation applied to Arteries and Atherosclerosis

The study of the mechanical behaviour of blood vessels has already been done for several years, having some reports dating from the end of the 19th century [9]. Although this represents a large number of experimental studies made in *in-vivo* or in *ex-vivo* settings to understand the material properties of the tissue and its reactions to different forces, it also represents an extensive work done with the help of computational models [9]. An example of this work is the use of FEM by Han *et al.* to study the deformation of arteries, as for example twisting, kinking or tortuosity, due to ageing and hypertension [9, 50, 51, 52, 53, 54]. These models enable the prediction of mechanical parameters, as the angles of twisted arteries or critical loads as result of buckling. This kind of knowledge may lead to better treatment of hypertension and the effects of ageing [9]. The buckling effect on arteries is also a topic of study in other settings as for example in aneurysmal arteries [55]. In the work of Lee *et al.* [55], the objective was to assess the effect of aneurysms in arterial buckling instability and the effect of buckling on aneurysm wall stress. In this study the arteries are modelled as a homogeneous incompressible, orthotropic, non linear material using the Fung strain energy function [56] and uses a commercial software to perform a FEM analysis using linear hexahedral elements.

Studies as the aforementioned show that the knowledge of blood vessel mechanics is getting further and further, which can lead to improvements on healthcare, even more when creating patient-specific realistic models. There have been some attempts, by incorporating the patient specific 3D residual forces into FEM arterial models [57]. Pierce *et al* were able to construct, through medical imaging, image analysis and FEM, a computational model of patient specific blood vessels on which they were then able to apply the residual stress distributions of the arterial tissue layers [57].

All this knowledge of blood vessels can also be applied in cases related to atherosclerosis. One of the cases most studied in the literature in the computational analysis of stents [7, 8]. Computational stent analysis allows for a better comprehension of the stent's effects on the blood vessel, its

progression through time and of improvements on stent design. A different kind of application of computational simulation is for prediction of plaque location. It can be found in a literature works on the usage of FEM to model and predict the initialization and progration of Atherosclerotic plaque on coronary arteries [58]. This work in particular used angiography records of six different patients to create their models and by analysing mechanical parameters of blood circulation (wall shear stress, oscillatory shear index and residence time) achieved a good correlation with the real plaques.

Related to the atherosclerotic plaque itself, several works have characterized its material behaviour [59, 60, 61, 62, 63]. In these studies, one can find both experimental approaches, by use of an circunferential uniaxial mechanical test [61], as well as micro-indentation works with the use of inverse finite elements analysis [59, 60, 63].

In terms of simulation studies focused on the plaque itself only a few can be found in the literature. One of these studies was made by Cunnane *et al* and focused on the influence of the plaque material model on numerical results. In this work the author used FEM to simulate a very simplified model of a diseased artery containing only to circular sections, the artery wall and the atherosclerotic plaque [10]. By the use of two different material models based on femoral plaque tissue and aortic plaque tissue, Cunnane showed that large differences were induced in the numerical results by the use of each material model, concluding that simulations of each vessel should employ vessel-appropriate material models for the plaque [10]. Aside from this, an attempt of modeling the atherosclerotic plaque biomechanical behaviour as an elasto-plastic material was also found in the literature [64]. In that research the author used the NNRPIM method to simulate this behaviour on a single atherosclerotic artery model, being the only work found in the literature that used meshless methods to simulate this tissue.

1.3 Objectives

1. Perform a elasto-plastic analysis of atherosclerotic plaques, using two of the most recent meshless models nowadays, the RPIM and the NNRPIM;

2. Study the effect of tissue calcification and thickening of the atherosclerotic plaque has on the mechanical behaviour of the artery;

3. Draw comparisons between FEM and the meshless methods used.

1.4 Document Structure

This Thesis is composed of seven major chapters: Introduction, Cardiovascular System and Atherosclerosis, Elasto-Plastic Formulation, Preliminary Studies, Atherosclerotic Plaque Analysis, Conclusions and Future Work.

In the first chapter, **Introduction**, an brief introduction on the topic is given, as well as a review on the state of the art of Meshless methods and Numerical Simulation of Atherosclerotic Plaque. Furthermore, the objectives of this work are stated.

In Chapter 2, **Cardio-vascular System and Atherosclerosis**, a brief exposure of the cardio-vascular, arterial and atherosclerosis biology is given. The mechanical properties for the arterial wall tissues and atherosclerotic plaque are also described.

In Chapter 3, **Meshless Methods**, it is given a thorough presentation of the two meshless methods used in this work and their formulation.

In Chapter 4, **Elasto-Plastic Formulation**, the elato-plastic formulation used in this work is present.

In Chapter 5, **Preliminary Studies**, the software used on this thesis is presented and explained. Afterwards, some elastic examples are studied in order to compare results obtained between numerical methods. Finally, a preliminary elasto-plastic study is shown and compared with the expected mechanical behaviour.

In Chapter 6, **Atherosclerotic Plaque Analysis**, the software previously described is used to analyse several models of arteries containing atherosclerotic Plaques. This chapter presents all the results obtained and their discussion.

In Chapter 7, **Conclusions and Future Work**, the main conclusion of this work are stated and some recommendations for future work in this topic are given.

Chapter 2

Cardiovascular System and Atherosclerosis

The cardiovascular system is one of the most important organ system in the human body and atherosclerosis is one of the most common diseases that targets this system. Being those the main focus of this work, it will be given in this chapter a better understanding of the cardiovascular system, the composition of the arterial walls and the processes behind the formation of atherosclerotic tissue. After this, the mechanical properties used for this work are stated as well as the experimental works from which they resulted.

2.1 Cardiovascular System

The Cardiovascular System is an organ system that allows for the transportation of blood cells and nutrients to every cell in the human body and also the collection of all cell residues. The Cardiovascular System is comprised of three different parts: blood, heart and blood vessels.

The human Cardiovascular System has also the characteristic of being a closed system, meaning that the blood never leaves the blood vessel network. The system is composed of two different loops, the pulmonary circulation that takes the blood to the lungs so that it is oxygenated and the systemic circulation where the blood provides oxygen to the rest of body.

The blood is the fluid that it is transported through the cardiovascular system and consists mainly of plasma, erythrocytes, leukocytes and platelets. Each of these components has a purpose, from immune response (leukocytes) to oxygen transportation (erythrocytes) or vase repairing (platelets).

The heart is a muscle located inside the thoracic cage whose function is to pump the blood through the blood vessels. This organ is composed of four cavities (two ventricles and two atriums) connected into two pairs (atrium with ventricle) and four valves that closes each cavity to prevent reflux. Each pair, located on each side of the heart, is responsible for giving thrust to one of the loops of the system, either the pulmonary circulation (right pair) or the systemic circulation (left pair). As the systemic circulation is longer path than the pulmonary circulation, the left side of the

heart is bigger, having a thicker ventricle in order to apply enough pressure to the blood. This organ is controlled by the autonomic nervous system (sympathetic nervous system and parasympathetic nervous system) which controls all the body's unconscious actions.

The blood vessels are the channels through which the blood flows. These vessels are classified according to their characteristics into arteries, veins and capillaries. Arteries are the vessels that receive the blood after it leaves the heart. As the blood has to reach the whole body and then come back to the pump, it needs to be ejected at a high pressure. So, in order to sustain such forces, arteries have a thick muscular wall. The vessels get thinner as one moves away from the heart and blood pressure drops, so that when one reaches the tissues the blood pressure is minimal. At this point the vessels are called capillaries, presenting a very small diameter and a very thin wall to allow for the diffusion of nutrients and residues. Following along the vessels, blood starts returning to the heart, through veins. Veins have a thinner wall when compared to arteries and, given the minimal blood pressure at this point, they present valves along their length to prevent back-flow. These vessels conduct the blood back to the heart, increasing in diameter as they get closer.

2.2 Arteries

2.2.1 Biologic Description

Arterial vessels are composed by three distinct layers called *tunicae*. Those three layers are called *tunicae intima* (inside layer), *tunicae media* (middle layer) and *tunicae adventitia*(outer layer).

The *intima* is composed of a thin endothelial layer over a very thin basal lamina of type IV collagen. This layer works as a semi-permeable membrane, allowing nutrients and chemical signals coming from the blood stream to reach the other blood vessel cells. An example of this permeability is the pressure-regulating agents that the blood passes to the *media* creating an active response by the vessel. Even though it has a very important functional role, given its small thickness, is often neglected when considering each layers contribution for the global mechanical resistance of the artery.

The *media* mainly formed of smooth muscle cells embedded in an extracellular plexus of elastin and collagen (mainly types I and III) combined with an aqueous-base substance containing proteoglycans [9]. This layer can have two different arrangements of their muscle cells, and according to them arteries are classified between *elastic arteries* and *muscular arteries*. Muscular arteries usually present a larger diameter and have a characteristic 'sublayer' of smooth muscle and thin elastic laminae called *lamellar unit*. Given their features this type of arteries is closer to the heart, to sustain the highest pressures.

And the *adventitia*, the outer layer of the vessel, consists of a dense matrix of type I collagen fibers combined with fibroblasts, nerves and elastin. These nerves are the ones responsible for the innervation of the smooth muscle cells present in the outer *media* while fibroblasts produce collagen, thus regulating the connective tissue. This layer presents itself as thick as the media in

muscular arteries, and very thin when examined on elastic arteries. Another particularity of this layer is the appearance of their fibers. At physiological pressure they appear to be ondulated and become progressively straighten as the pressure rises. This characteristic is hypothesised to be a protective mechanism of the vessel to prevent potential ruptures due to acute pressure increases [65].

2.2.2 Mechanical Properties

The understanding of the mechanical behaviour of blood vessels is a topic of research since the end of the 19th century [9].

The first notable characteristic is the existence of residual stresses, both axially and circunferentially, in an unloaded vessel [65]. These residual stresses keep the luminal part of the vessel under compression and the external under tension [65], even though the internal pressure of the vessel equilibrates these forces *in-vivo* [9]. Secondly, there is the anisotropy of the vascular tissue when under a load-free configuration [9]. This is evidenced by a different behaviour of the tissue when analysing the circumferential and the axial direction.

Given its high content of water, between 70 and 80 percent, the vascular wall is taken as incompressible although small fluid movements within the tissue created by stress gradients may exist [9, 65]. Besides this, it is also characteristic a degree of viscoelastic response, as well as hysteresis when under cyclic loads. Another important fact to know is that, after the tissue has been *preconditioned*, it displays a highly repetitive behaviour. Regarding its general mechanical behaviour it is often regarded as hyperelastic [66], even though it may be considered as *pseudoelastic*, as it is elastic but behaving differently in loading and unloading [56, 65].

2.3 Atherosclerosis

Atherosclerosis is defined as a chronic inflammation of the arterial wall that gives rise to the formation of a plaque [67]. The plaque consists of inflammatory cells, a lipid necrotic core, intraplaque haemorrhage and a thin fibrous cap that separates the core from the bloodstream [63]. This fibrous cap can potentially rupture, putting the lipid core in contact with the blood and causing luminal thrombus formation [63]. Atherosclerosis tend to appear at junctions and branches of conduit arteries, sites prone for altered flow patterns. Atherosclerosis begins with the trapping and retention of lipoproteins at lesion prone sites due to an imbalance of Low Density Lipoprotein (LDL) concentration between the tissue and the plasma [65]. Consequently, lipids become trapped in the extracellular matrix at the basal zone of the *intima*. This phenomena is pathogenic, creating an adhesion of leukocytes to the endothelial cells and thus starting the inflammatory response to the plaque formation. This leads to the recruitment of monocytes into the arterial wall that are differentiated into macrophages and, subsequently, foam cells after the ingestion of trapped and modified lipoproteins. Several foam cells within the lesion become activated, inducing the expression of a large number of factors that create an anomalous behaviour on healthy cells that end providing a favourable biochemical environment for the disease progression [65].

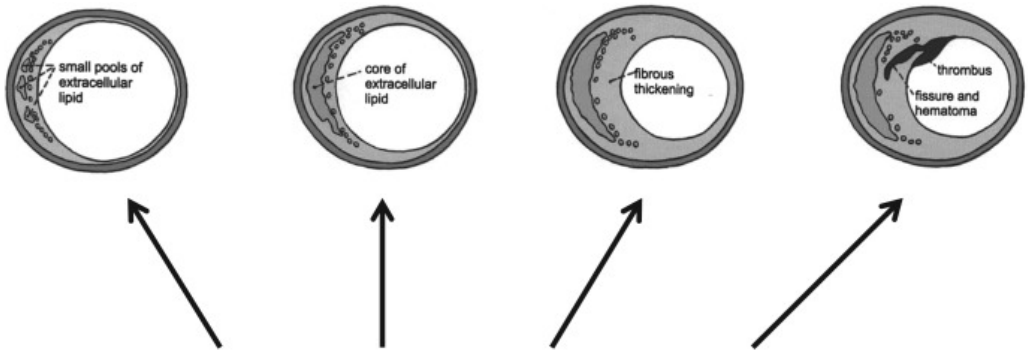

Plaque Type	III	IV	V	VI	VII	VIII
Description	Pre-Atheroma	Atheroma	Fibro-atheroma	Ruptured lesion	Calcified	Fibrous
SMC	-	-/+	+	-/+ or +	-/+	-/+
Collagen	-	-/+	+	-/+ or +	-/+	+
Stiffness	-	-	-/+	- or -/+	+	+
Homogeneity	-/+	-	-	-	-	-/+
Anisotropy	-	-/+	+	-/+ or +	-/+	-/+

Figure 2.1: Relative stiffness, homogeneity and anisotropy of different plaque types, based on plaque content and composition. The cartoons depicting the successive phases of atherosclerosis were adapted from [69]. SMC: smooth muscle cells. The $-$ indicates absence or low amount, + indicates the presence or high amount, and $-/+$ indicates intermediate amount. [62]

Atherosclerotic lesions range from small fatty streak into a ruptured or fibrotic lesion. Taking into account this wide range of lesion, a series of post-mortem pathological studies were made in order to develop a plaque classification scheme [68] being it afterwards perfected using vulnerable plaques focused pathological studies and adopted by the America Heart Association [69]. The classification comprises 8 lesion types that represent the successive stages of atherosclerosis. A summary of some mechanical properties of these stages, based on their composition can be found in Figure 2.1 [62].

2.3.1 Mechanical Behaviour

Experimental data from mechanical characterizations of the atherosclerotic plaque is present the literature [61, 62]. Based on the comparison of the experimental data from the *intima* it was possible to make two main conclusions: (1) all experiments reported a non-linear behaviour of the atherosclerotic plaque; (2) there exist a great dispersion in terms of different studies results.[62]. As it appears not to exist a set of established mechanical properties for this tissue, this work will be based on the work of Sommer *et al.* [65] and Cunnane *et al.* [70].

2.3.1.1 Damaged Arteries Mechanical Properties

Sommer *et al.* performed a study on 107 samples from nine human high-grade stenotic iliac arteries. In this study it was performed cyclic quasi-static uniaxial tension tests in the axial and circumferential direction of 7 different tissues present in the arteries. The samples taken varied from 7 to 17 mm in length, from 2.2 to 5.6 mm in width, and from 0.24 to 1.7 mm in thickness.

This samples were then allowed to equilibrate for 30 to 60 min in a calcium-free physiological 0.9% NaCl solution at 37°. The tissues were pre-conditioned with the execution of five successive loading-unloading cycles for each test and only then underwent the tension test. This was a single cyclic quasi-static uniaxial extension test with continuous recording of tensile force, width and gauge length at a constant crosshead speed of 1mm/min. [65] The results from this tests for the *Adventitia*, *Media*, Damaged *Media*, *Intima*, Damaged *Intima* and *Intima* Fibrous cap can be found on table 2.1.

Table 2.1: Average ultimate tensile stress (kPa) and associated ultimate stretch in the circumferential from all the specimens tested [65]

	Adventitia	Media	Dam. Media	Intima	Intima Fibrous Cap	Dam. Intima
Average σ_{ult}	1031.6	202.0	1073.6	488.6	943.7	776.8
Average λ_{ult}	1.440	1.270	1.115	1.331	1.182	1.107

While the behaviour of this tissues is hyperelastic, their mechanical behaviour can be simplified and approximated by a linear approach. To make this linear-elastic approximation first it is needed to subtract 1 from the stretch values in order to obtain the average strain and afterwards the unidirectional Young's Modulus can be calculated by definition with the following equation:

$$E = \frac{stress}{strain} \tag{2.1}$$

After this process has been done, the mechanical properties of these tissues under a linear elastic model can be found in table 2.2. As all these tissues are incompressible, they were defined as having a Poisson's ratio of 0.45.

Table 2.2: Arterial tissues mechanical Properties

	Adventitia	Media	Dam. Media	Intima	Intima Fibrous Cap	Dam. Intima
E (MPa)	2.3445	0.7481	9.3357	1.476	1.4	7.2598
Poisson's Ratio	0.45	0.45	0.45	0.45	0.45	0.45

2.3.1.2 Atherosclerotic Plaque Mechanical Behaviour

Cunnane *et al.* performed a mechanical study on twenty different samples of atherosclerotic plaques from femoral arteries of fifteen different patients. Immediately after being collected the samples were frozen in phosphate buffer solution at - 20 degrees Celsius.

The samples were tested using a uniaxial tester and video extensometer developed in their laboratory. They were first preconditioned using five cycles of 10% stretch at a displacement rate of 0.1 mm/s and then were elongated until failure at a displacement rate of 30% gauge length per second [70].

Besides this analysis, Cunnane *et al.* also made a Fourier Transform Infra-red Spectroscopy (FTIR) analysis of the plaque luminal surface using attenuated total reflectance (ATR) in order to

characterize the biological content of the tissue. The background spectrum was first removed and the ATR diamond crystal was placed directly into contact with the sample. The spectrums were acquired using absorbance mode with a resolution of 2 cm^{-1} for 16 scans over the range of 4000 to 700 cm^{-1}. By analysing these spectrums, calculating the area under certain characteristical absorvance peaks, the researchers were able to obtain the ratios of lipid to collagen (Li:Col), calcification to collagen (Ca:Col) and calcification to lipids (Ca:Li) in the samples.

Based on the biological characterization of these tissues, the samples were then separated into three different groups, based on their calcification to lipids ratio. The samples with a Ca:Li between 1 and 1.5 were classified as being Lightly Calcified, a Ca:Li ratio between 1.5 and 2 was classified as being Moderately Calcified and a Ca:Li ratio between 2 and 3 was taken as Heavily Calcified. By analysing the results obtained from the mechanical tests a sample was selected from each of these groups as being representative. The mechanical behaviour of these samples can be seen in Figure 2.2.

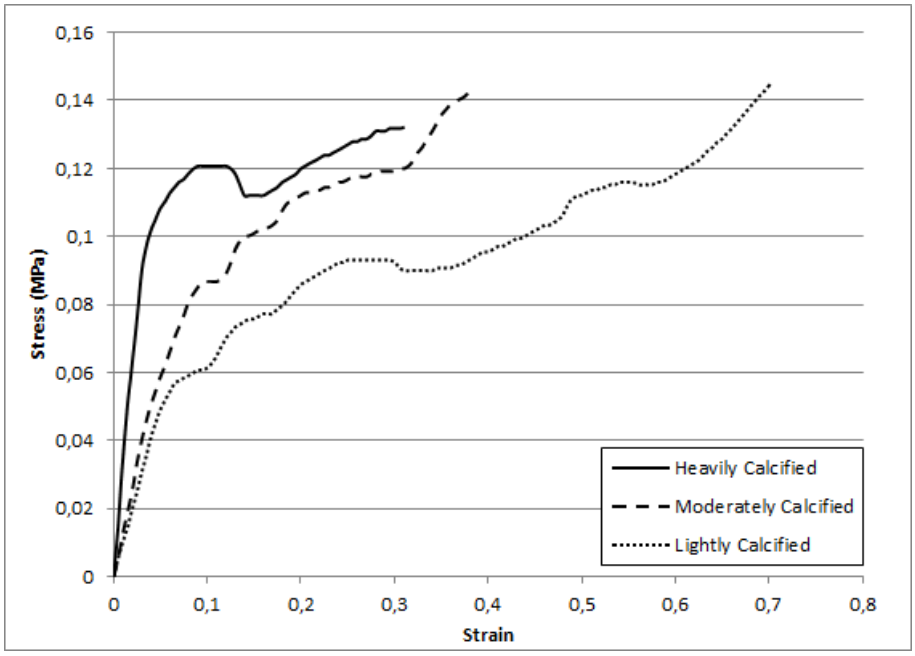

Figure 2.2: Stress vs. Strain plot of the group representative plaque samples

This behaviour could be simplified as elasto-plastic and approximate through a bi-linear function. This approximations can be seen in Figure 2.3.

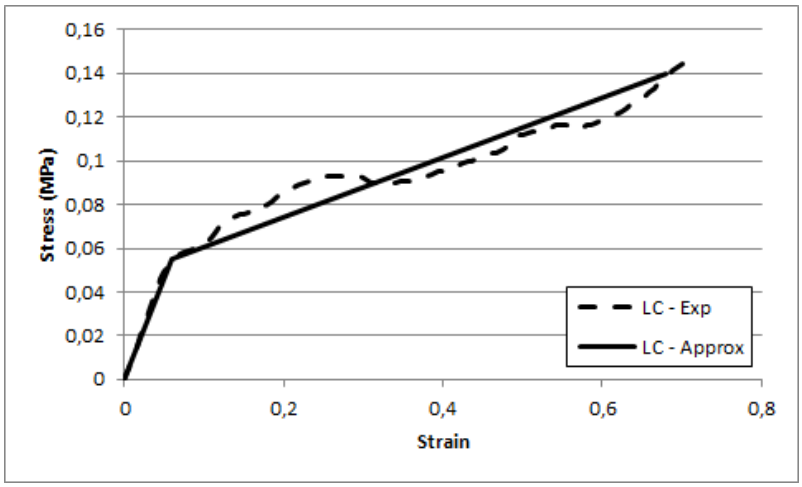

(a) Lightly Calcified

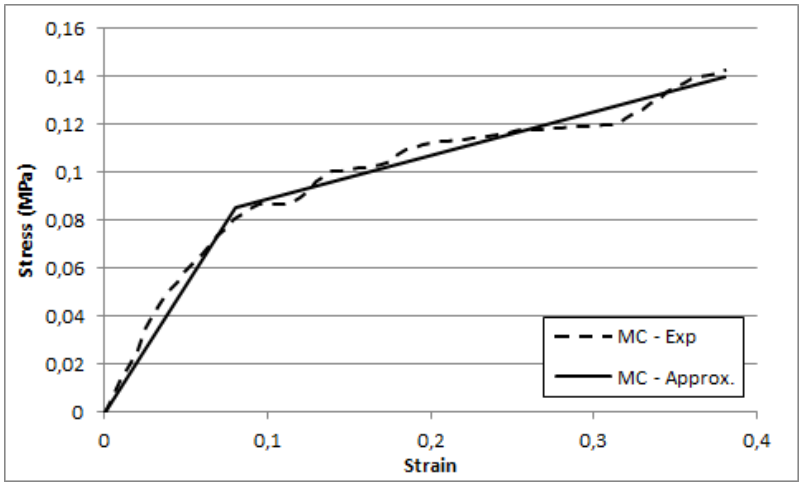

(b) Moderately Calcified

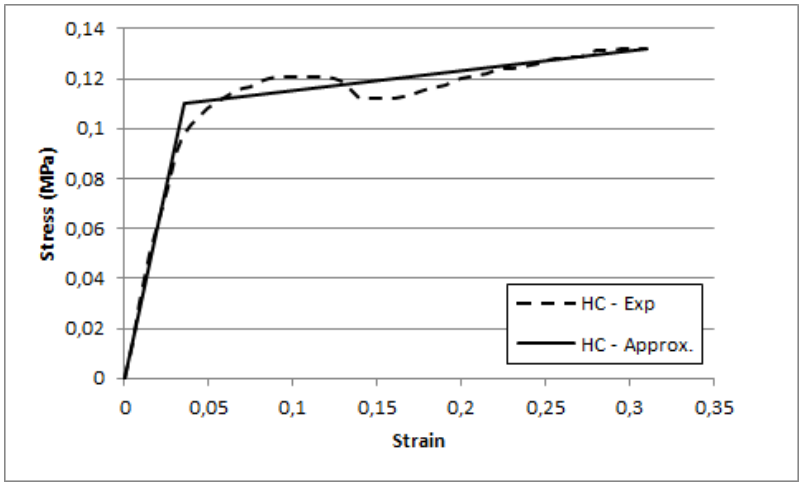

(c) Highly Calcified

Figure 2.3: Bi-linear approximations of Atherosclerotic Mechanical Behaviour

From these bi-linear approximations it were taken the mechanical properties seen in table 2.3.

Table 2.3: Mechanical Properties of the Atherosclerotic Plaque

	Lightly Calcified	Medially Calcified	Highly Calcified
E(MPa)	0.9167	1.0625	3.1429
Et (MPa)	0.1371	0.1833	0.0800
σ_y (MPa)	0.055	0.085	0.110

For the numerical simulations performed in this works it would be also required the Poisson's ratio of the atherosclerotic Plaque. Since that in the work of Cunnane *et al.* no value for this mechanical property, its value was obtained by the law of mixtures [71] to the Poisson's ration, as seen in the following equation:

$$\nu_{plaque} = \nu_{calcification} \times calcification\% + \nu_{lipids} \times lipids\% + \nu_{collagen} \times collagen\% \tag{2.2}$$

where calcification %, lipids % and collagen % represent the fraction of each of the biological components.

For this calculation the collagen and lipids were taken as incompressible and given a Poisson's ratio of 0.45, as seen with the artery's tissues. As for the calcifications those were taken as being similar to hydroxiapatite, one of the most main calcium phosphates present in the the human body, with a Poisson's ratio of 0.27 [72]. The fractions of each component were calculated from the ratios of each of the selected representative samples using the following system of equations:

$$\begin{cases} \frac{\%Lipids}{\%Collagen} = ratio(Li:Col) \\ \frac{\%Calcification}{\%Collagen} = ratio(Ca:Col) \\ \frac{\%Calcification}{\%Lipids} = ratio(Ca:Li) \end{cases} \tag{2.3}$$

The resulting Poisson's Ratio's for each level of calcification in the atherosclerotic plaque can be seen in table 2.4.

Table 2.4: Fractions of Biological Components in each representative sample and resulting Poisson's Ratio

	Lightly Calcified	Moderately Calcified	Heavily Calcified
Calcification	0.1629	0.2092	0.2344
Lipids	0.1252	0.1134	0.0801
Collagen	0.7117	0.6772	0.6854
Poisson's Ratio	0.421	0.412	0.408

Chapter 3

Meshless Methods

For the development of this work two different meshless methods were used: the Radial Point Interpolation Method and the Natural Neighbour Radial Point Interpolation Method. The present chapter will have a brief description of the general meshless method procedure, followed by the explanation of both these methods. By the end of it will also be presented the Radial Point Interpolation functions, which are used in both methods.

3.1 General Meshless Method Procedure

The generality of meshless methods follow the same steps in their algorithms. Firstly, as seen in Figure 3.1.a), the outline on the problem is defined and the essential and natural boundaries are identified. Afterwards the problem is discretized using either an regular or irregular nodal set, as seen in Figure 3.7.b) and c).

The use of different kinds of nodal distributions will have an direct effect on the outcome of the numerical analysis. An irregular mesh while it can often present a lower accuracy on its general results, it can also enhance results on locations with predictable stress concentrations by having a higher nodal density on those locations, as it is seen in the crack of 3.7.c). In order to enhance results on these locations while not compromising the accuracy through out the problem's domain, the best approach is usually to use a regular mesh and to insert extra nodes on those spots. After the problem's domain has been discretized it is necessary to obtain the nodal connectivity. Contrarily to FEM, where the nodal connectivity is established through the element's mesh and the node belonging to the same element interact between themselves, in meshless methods this connectivity must be obtained, for example, by the overlapping of influence domains, as in the RPIM, or the use of influence-cells, as it is seen in the NNRPIM. When it comes to the numerical integration, this is made with a background integration mesh that can either be nodal dependent or nodal independent, having the former a higher accuracy. Nodal dependent meshes, while allowing for the method to be a truly meshless methods (as it only needs the spatial location of its nodes), have the need for a stabilization method in order to achieve accurate results. The necessity for this addition add up to the higher computational costs [73, 74, 75]. Finally the field variables under

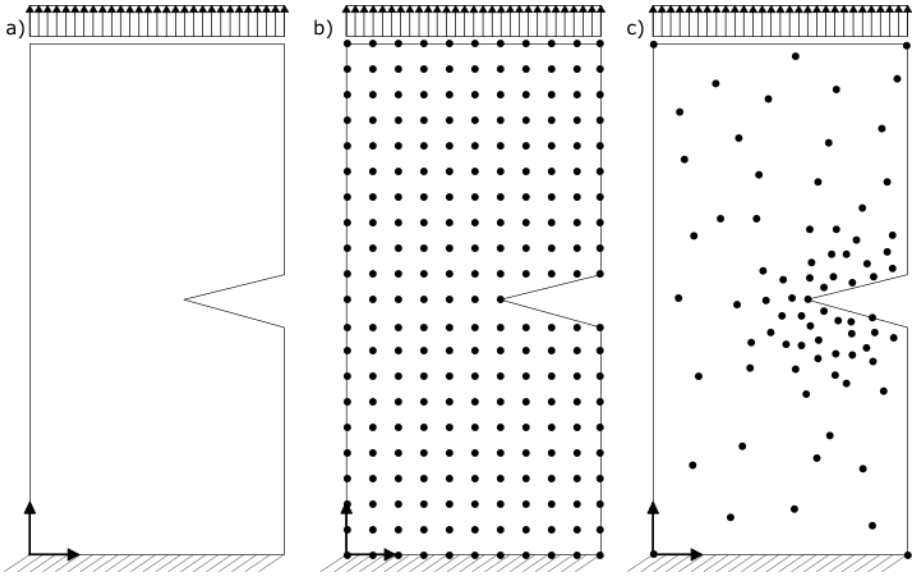

Figure 3.1: a) Problem domain with Essential and Natural boundaries applied. b) Regular nodal discretization. c) Irregular nodal distribution.

study can be calculated with the use of either approximation or interpolation shape functions. In the case of the RPIM and the NNRPIM, interpolation shape function are used that have has base a combination of radial basis functions and polynomial basis functions.

3.2 Radial Point Interpolation Method

3.2.1 Influence-domains and nodal connectivity

As stated in the general meshless procedure, after the problem domain has been discretized with a nodal set it is necessary to define the nodal connectivity of each node.

Before this connectivity can be obtained it is necessary to define areas containing a certain amount of nodes, for any two-dimensional (2D) or three-dimensional (3D) problem, respectively. These areas and volumes are called influence domains and can have either a fixed or variable sized. On Figure 3.2 this is shown for a 2D domain.

The use of fixed size influence-domains can lead, as it is possible to see in Figure 3.8 a), to an uneven number of nodes inside the influence-domains of different nodes. This phenomena can greatly reduce the accuracy of the numerical method and therefore it is advised the use of variable size influence-domains, as it can be seen in 3.2 b). By using this kind of influence-domains it is ensured that they all contain the same amount of nodes, despite the node that it is being analysed, allowing for the construction of shape function with equal levels of complexity. This amount is not dependent on the density of the nodal discretization and after being defined, its value is valid for all domain discretizations within the same analysis. In terms of recommended values, for 2D problems it is recommended in the literature the use of between nine and sixteen nodes, while for 3D problems the recommended number is between twenty-seven and seventy nodes [27, 34, 42].

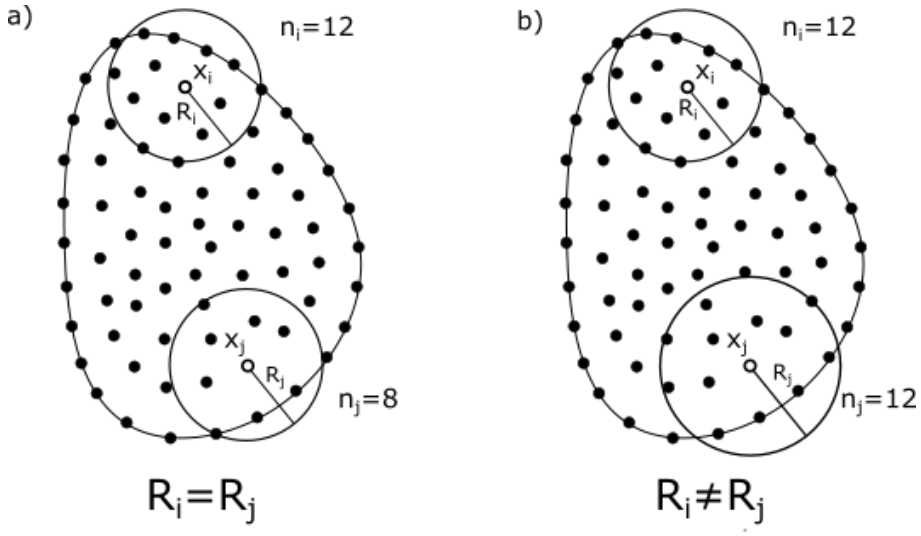

Figure 3.2: a) Fixed size circular influence-domain. b) Variable size circular influence-domain.

3.2.2 Numerical Integration

Following the definition of nodal connectivity, the next step would be the numerical integration. For the integration of the differential equations the RPIM uses the Gauss-Legendre integration scheme being need, as it was stated above, a background integration mesh. For this integration mesh it can be used either the cells created to connect the nodes that discretized the problem's domain (resulting in either quadrilateral or triangular cells), or a regular mesh larger than the domain and whose integration points located outside the domain must be eliminated from the computation. On Figure 3.3 it is possible to see an use of triangular cells in a) and the use of the larger regular mesh in b).

Inside of each cell of the background integration mesh, being it triangular or quadrilateral, it is possible to distribute integration points as seen in Figure 3.3 a) and b).

On tables 3.1 and 3.2 are displayed the locations and weights of the isoparametric integration points for quadrilateral and triangular cells respectively. In Figures 3.4 and 3.5 is it shown the representation of the integration point distribution seen on the tables.

After the integration points have been distributed in the isoparametric shape, the Cartesian coordinates of the integration points are obtained using the following isoparametric interpolation functions:

$$x = \sum_{i=1}^{m} N_i(\xi,\eta)\cdot x_i y = \sum_{i=1}^{m} N_i(\xi,\eta)\cdot y_i \tag{3.1}$$

where m is the number of nodes that define the element and x_i and y_i are the cartesian coordinates of the cells nodes. In Figure 3.6 can be seen a representation of this transformation.

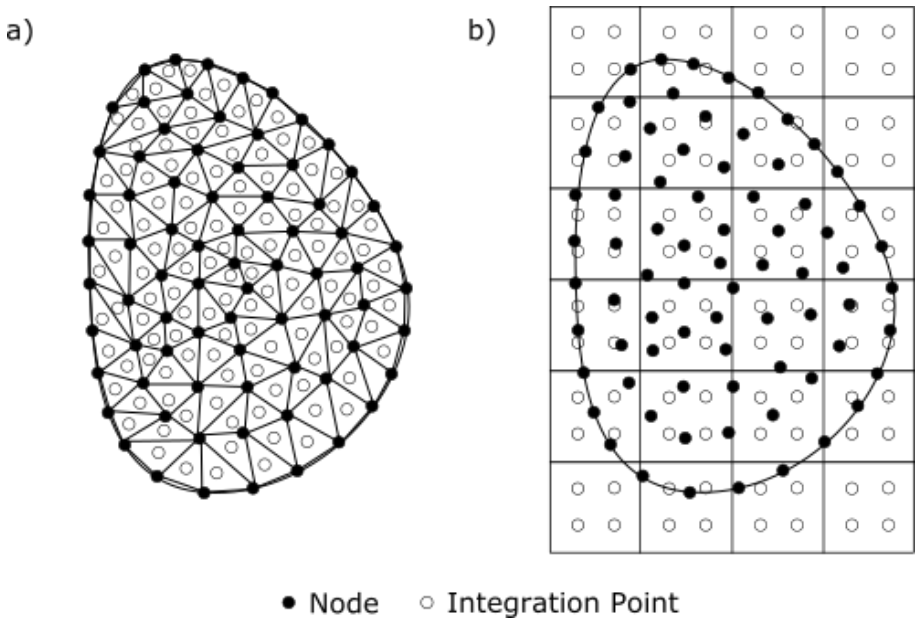

Figure 3.3: a) Triangular "cell" background mesh with 1 integration point. b) Quadrilateral grid background mesh with 4 integration points.

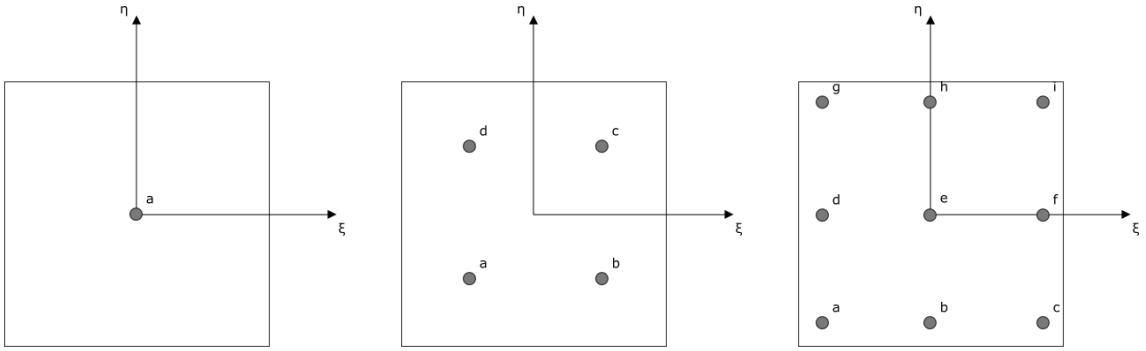

(a) 1 Integration Point (b) 4 Integration Points (c) 9 Integration Points

Figure 3.4: Positioning of integration points for quadrilateral cells

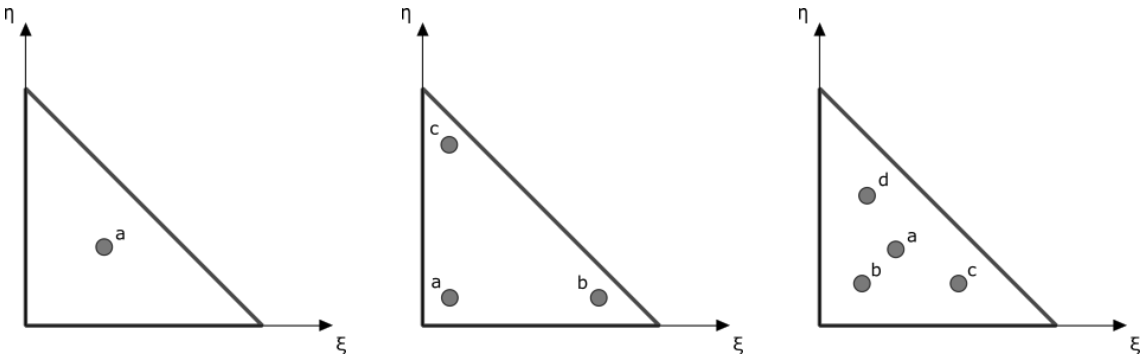

(a) 1 Integration Point (b) 3 Integration Points (c) 4 Integration Points

Figure 3.5: Positioning of integration points for quadrilateral cells

Table 3.1: Integration points coordinates and weights for quadrilateral "cells" [76]

Points	ξ	η	**Weight**
a	0	0	4
a	$-\frac{1}{\sqrt{3}}$	$-\frac{1}{\sqrt{3}}$	1
b	$+\frac{1}{\sqrt{3}}$	$-\frac{1}{\sqrt{3}}$	1
c	$-\frac{1}{\sqrt{3}}$	$+\frac{1}{\sqrt{3}}$	1
d	$+\frac{1}{\sqrt{3}}$	$+\frac{1}{\sqrt{3}}$	1
a	$-\sqrt{\frac{3}{5}}$	$-\sqrt{\frac{3}{5}}$	$\frac{25}{81}$
b	0	$-\sqrt{\frac{3}{5}}$	$\frac{40}{81}$
c	$+\sqrt{\frac{3}{5}}$	$-\sqrt{\frac{3}{5}}$	$\frac{25}{81}$
d	$-\sqrt{\frac{3}{5}}$	0	$\frac{40}{81}$
e	0	0	$\frac{64}{81}$
f	$+\sqrt{\frac{3}{5}}$	0	$\frac{40}{81}$
g	$-\sqrt{\frac{3}{5}}$	$+\sqrt{\frac{3}{5}}$	$\frac{25}{81}$
h	$+\sqrt{\frac{3}{5}}$	$+\sqrt{\frac{3}{5}}$	$\frac{40}{81}$
i	$+\sqrt{\frac{3}{5}}$	$+\sqrt{\frac{3}{5}}$	$\frac{25}{81}$

Table 3.2: Integration points coordinates and weights for triangular "cells" [76]

Points	ξ	η	**Weight**
a	$\frac{1}{3}$	$\frac{1}{3}$	$\frac{1}{2}$
a	$\frac{1}{6}$	$\frac{1}{6}$	$\frac{1}{6}$
b	$\frac{2}{3}$	$\frac{1}{6}$	$\frac{1}{6}$
c	$\frac{1}{6}$	$\frac{2}{3}$	$\frac{1}{6}$
a	$\frac{1}{3}$	$\frac{1}{3}$	$-\frac{27}{96}$
b	$\frac{1}{5}$	$\frac{1}{5}$	$\frac{25}{96}$
c	$\frac{3}{5}$	$\frac{1}{5}$	$\frac{25}{96}$
d	$\frac{1}{5}$	$\frac{3}{5}$	$\frac{25}{96}$

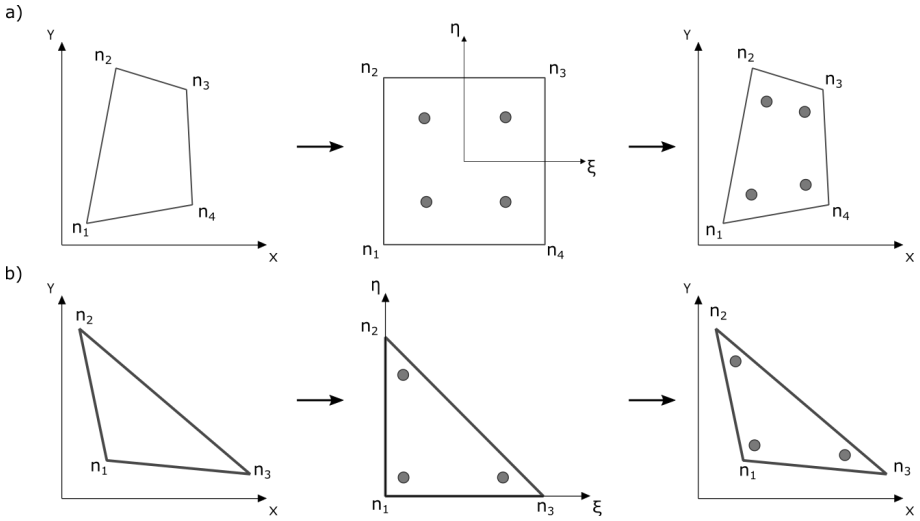

Figure 3.6: a) Transformation of the initial quadrilateral cell into a isoparametric square shape and application of the 2x2 quadrature point rule followed by the return to the initial quadrilateral shape. b) Transformation of the initial triangular cell into a isoparametric triangular shape and application of the 3-point quadrature point rule followed by the return to the initial triangular shape.

The Nodal shape functions (N_i) are define for quadrilaterals as:

$$\begin{aligned} N_1(\xi,\eta) &= \tfrac{1}{4}(1-\xi)(1-\eta) \\ N_2(\xi,\eta) &= \tfrac{1}{4}(1-\xi)(1+\eta) \\ N_3(\xi,\eta) &= \tfrac{1}{4}(1+\xi)(1+\eta) \\ N_4(\xi,\eta) &= \tfrac{1}{4}(1+\xi)(1-\eta) \end{aligned} \tag{3.2}$$

, being for triangles defined as:

$$\begin{aligned} N_1(\xi,\eta) &= 1-\xi-\eta \\ N_2(\xi,\eta) &= \eta \\ N_3(\xi,\eta) &= \xi \end{aligned} \tag{3.3}$$

The integration weight of the integration point is obtained by multiplying the isoparametric weight of correspondent the point with the Jacobian matrix determinant of the respective cell.

$$[J] = \begin{pmatrix} \frac{\partial x}{\partial \xi} & \frac{\partial x}{\partial \eta} \\ \frac{\partial y}{\partial \xi} & \frac{\partial y}{\partial \eta} \end{pmatrix} \tag{3.4}$$

The differential equation integration is finally done using,

$$\int_{-1}^{1}\int_{-1}^{1} f(\mathbf{x})dxdy = \sum_{i=1}^{m}\sum_{i=1}^{n} \omega_i \omega_j f(\mathbf{x}) \tag{3.5}$$

where ω_i and $\omega_j$is the weight in each direction of the integration point $\mathbf{x}$.

This integration method can be extrapolated for three dimensional problems using for this tetrahedral solids instead.

3.3 Natural Neighbour Radial Point Interpolation Method

The NNRPIM is the result of the combination of the Radial Point Interpolators with the Natural Neighbours geometric concept [21]. In this method the concept of influence-domain is exchanged with the concept of "influence-cells". These "influence-cells" are based in the mathematical concepts of the Voronoï diagrams and the Delaunay triangulation to establish the nodal connectivity of each node, *i.e.* the influence-domain of a node is determined by the geometric and spatial relation between the Voronoï cells obtained from the Voronoï diagram of the nodal-distribution [21]. The Delauny triangulation is used to create a node-dependent background integration mesh for the numerical integration of the shape functions. The NNRPIM interpolation functions use the Galerkin weak, constructing them with a similar process to the RPIM.

3.3.1 Natural Neighbours

The natural neighbours concept was firstly introduced by Sibson [47] for data fitting and field smoothing used in NNRPIM for nodal connectivity and creation of the integration mesh.

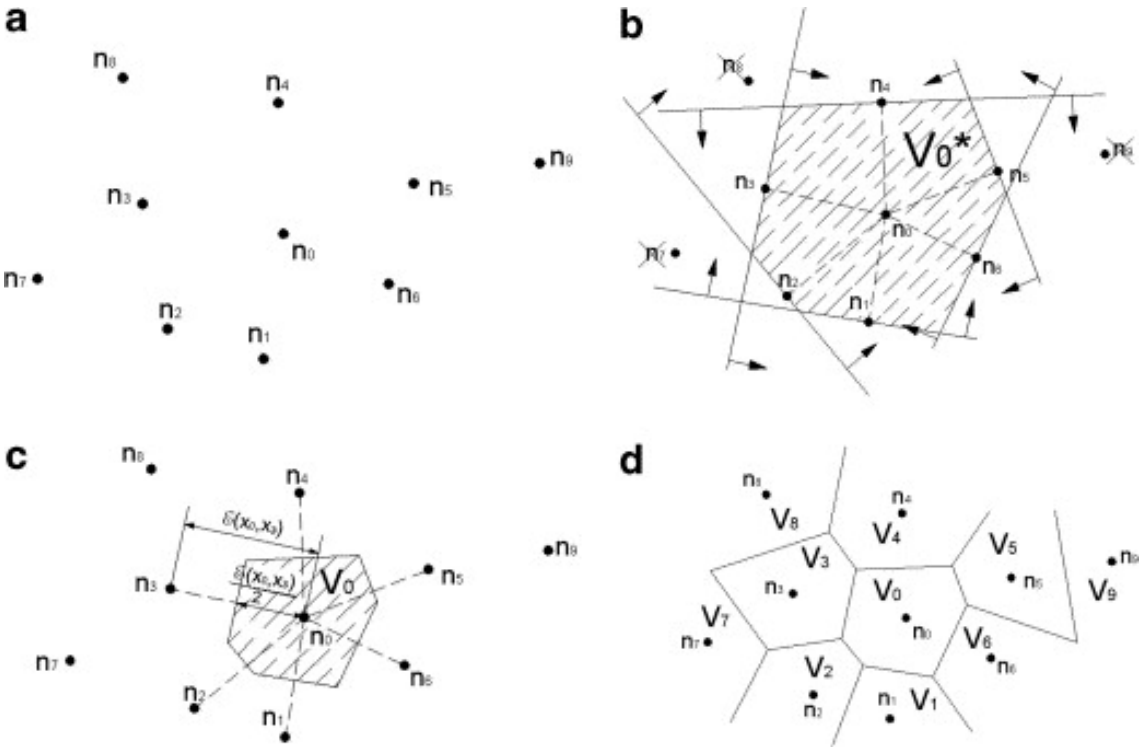

Figure 3.7: a) Potential neighbour nodes of n_0, b) Domain containing neighbour nodes of n_0, c) Voronoï cell for node n_0 and d) Final Voronoï diagram [33]

Consider a nodal set **N** with N distinct nodes defined on an Euclidean space $\Re^2$.

$$\mathbf{N} = \{n_1, n_2, ..., n_N\} \in \Re^2 \tag{3.6}$$

The Voronoï diagram of **N** is the partition of the domain defined by **N** into sub-regions V_i, closed and convex. Each sub-region V_i is associated to the node n_i in a way that all the points inside of V_i are closer to n_i than any other node, n_j.

In Figure 3.7 it is seen the construction of the sub-region V_0. In Figure 3.7 a) one can see the nodal set comprised of the n_0 and its neighbours. From their position V_0* is determined, by the intersection of domains, whose limits are defined by the lines that intersect a potential neighbour node and are normal to the line connecting that node to n_0. The nodes present in the perimeter of this domain are then considered neighbour nodes. From V_0*, as shown in Figure 3.7 c), we may achieve the Voronoï cell V_0, the homothetic form of V_0*. To obtain the remaining Voronoï cells a similar procedure is applied to the other nodes resulting in Figure 3.7 d).

The Delaunay triangulation is obtained by connecting the nodes whose Voronoï cells share common boundaries. Being the Delaunay triangulation the geometrical dual of the Voronoï diagram, it is implied that a Delaunay edge exists if and only if their Voronoï cells have a common edge. A relevant property of the Delauny triangles is the "empty circumcircle criterion" [77]. This criterion states that if a set of nodes $\mathbf{N}_t = \{n_j, n_k, n_l\} \in \mathbf{N}$ forms a Delauny triangle then the circumference formed by the triangle $\mathbf{N}_t$, called natural neighbour circumcircles, contains no other

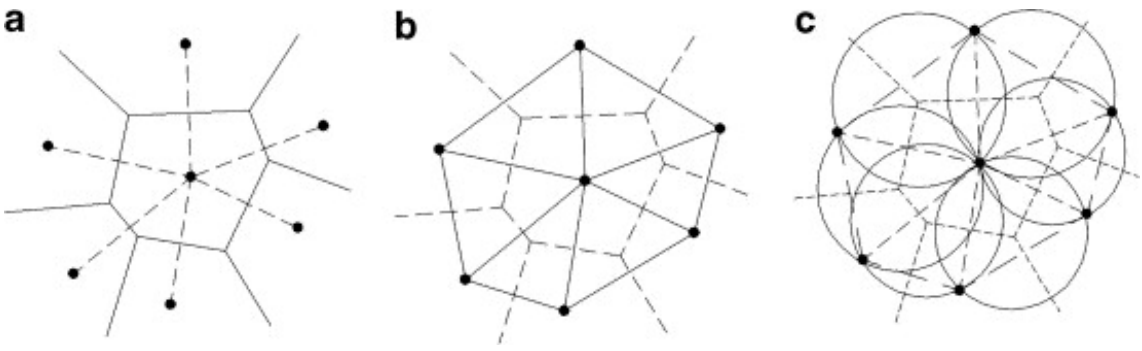

Figure 3.8: (a) Initial Voronoï diagram, (b) Delaunay triangulation and (c) natural neighbour circumcircles [33]

node of the global nodal set **N**. On the center of this circumcircle its found the Voronoï cell vertex (Figure 3.8).

In the NNRPIM the Voronoï diagram is used to create the influence-cells, enforcing the connectivity between the nodes, while the duality between Voronoï cells and Delauny triangles is used to construct a nodal-dependent background integration mesh.

3.3.2 Influence-cells and Nodal Connectivity Determination

In the NNRPIM we are considering the influence-cell, a new concept for nodal conectivity. These cells, constructed based on the Voronoï diagram, work similarly to the influence domains, but instead of nodal-conectivity being defined by the overlapping of influence domains this connectivity is defined by the overlapping of influence-cells. These influence-cells are composed by a set of n nodes that will contribute to the interpolation of the interest point. There are two distinct types of influence-cells that are considered. On one hand, the first degree influence-cell is defined by the interest point natural neighbours, as defined by the Voronoï diagram. On the other hand, the second degree is formed by the same nodes that were considered in the first degree influence-cell, to which are added the respective natural neighbours. Given their size difference it is expected that the use of second-degree influence-cells create better numerical results [21].

3.3.3 Numerical Integration

As previously stated, the numerical integration of the NNRPIM is based in the Delauny triangulation and Voronoï tesselation.

Using the geometrical construction reference above, sub-cells are defined by the partition of Voronoï cells with the lines intersecting the central node and each of the natural neighbours. Depending of the use of irregular or regular meshes, the resulting partition will be quadrilateral or triangular (Figure 3.9). As result the cell is divided into a number of sub-cells equal to the number

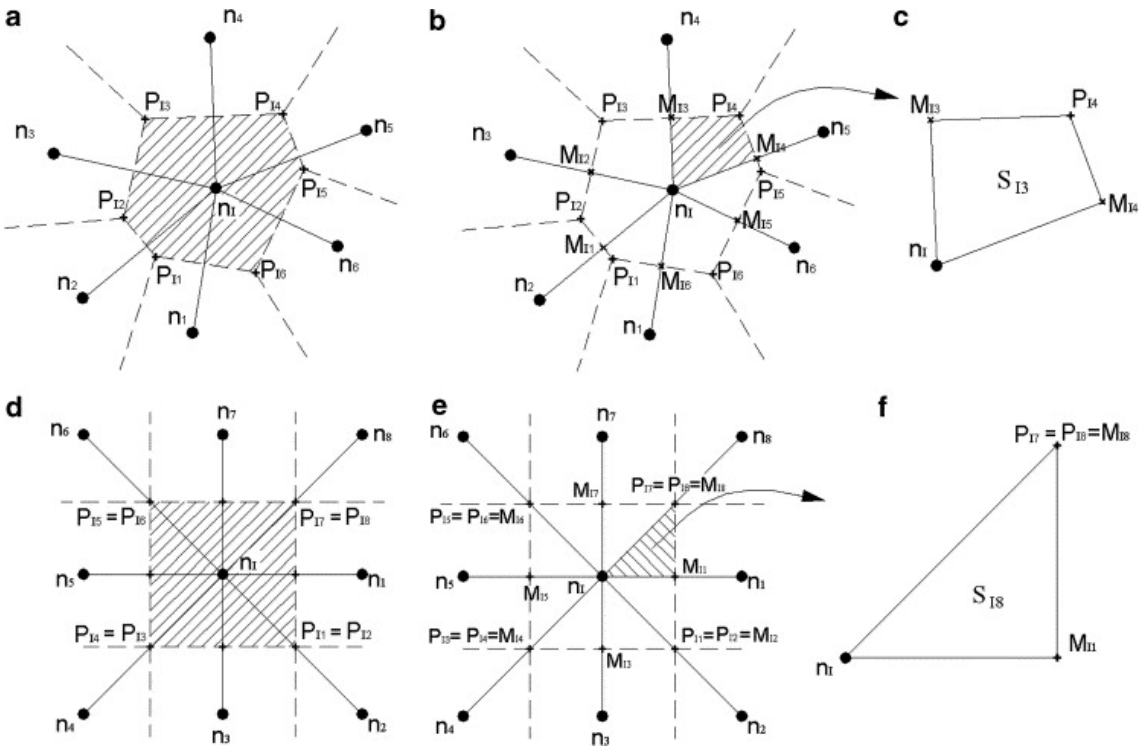

Figure 3.9: (For the irregular mesh (a) Voronoï cell and the respective P intersection points, (b) middle points M and the respective generated quadrilaterals, (c)obtained quadrilateral sub-cell. For the regular mesh, (d) Voronoï cell and the respective P intersection points, (e) middle points M and the respective generated triangles and (f) obtained triangular sub-cell [33]

of neighbour nodes. Consequently the area A_v, the area of the cell, is equal to the sum of the area of each sub-cell, A_i, as defined in the equation:

$$A_v = \sum_{i=1}^{n} A_i, \forall A_i \geq 0 \tag{3.7}$$

If the set of Voronoï cells are a partition, without gaps, of the global domain then the same can be said for the set of sub-cells. The numerical integration is then made using an ordered scheme based on the Gauss-Legendre numerical integration [33].

3.3.3.1 Integration Scheme - order 0

The coordinates of each integration point will be calculated for each sub-cell, as shown in Figure 3.10 a) and d), being their corresponding weight the sub-cell's area. Therefore, the area corresponding to the triangular sub-cell is defined as:

$$A_I\triangle = abs\left(\frac{1}{2}\begin{vmatrix} x2-x1 & y2-y1 \\ x3-x1 & y3-y1 \end{vmatrix}\right) \tag{3.8}$$

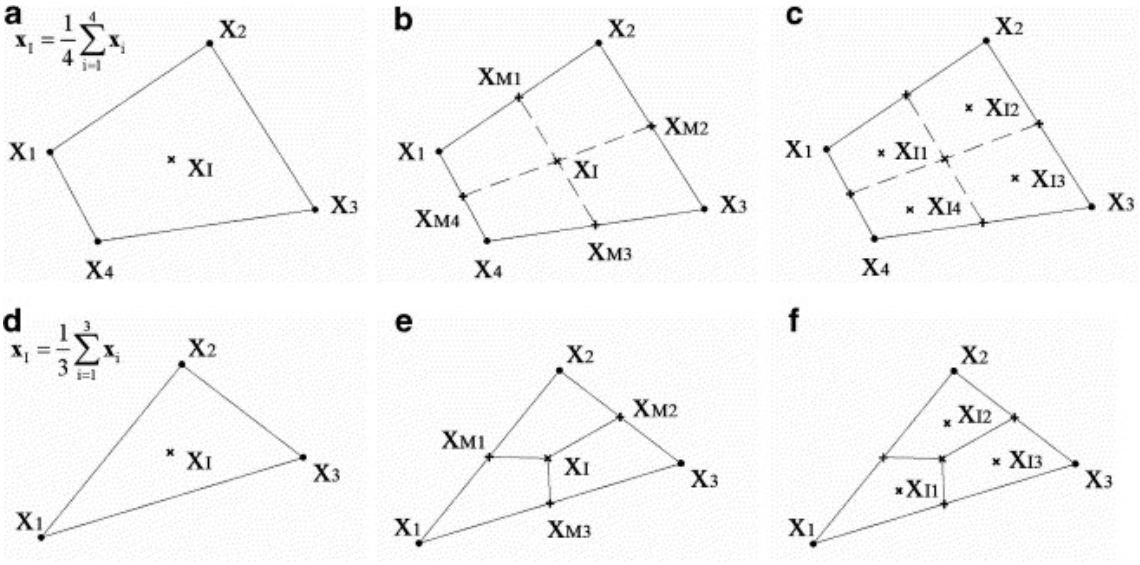

Figure 3.10: (a) Quadrilateral shape and (d) triangular shape and the respective integration points xI, (b) and (e) partition of the initial shape into quadrilaterals, (c) and (f) respective integration points xI. [33]

and the area for the quadrilateral sub-cell:

$$A_{I-square} = abs\left(\frac{1}{2}\begin{vmatrix} x2-x1 & y2-y1 \\ x3-x1 & y3-y1 \end{vmatrix} + \frac{1}{2}\begin{vmatrix} x4-x1 & y4-y1 \\ x3-x1 & y3-y1 \end{vmatrix}\right). \tag{3.9}$$

The procedure is similar to the *1 x 1* integration point Gauss-Legendre scheme for triangular and quadrilateral shapes.

3.3.3.2 Integration Scheme - order 1

For a order 1 integration scheme the geometrical forms described before are again sub-divided, however this subdivision is now only of quadrilateral shapes as seen in Figure 3.10 b) and e). In each of these new sub-divisions the geometrical center is determined, as it consists of the integration, as well as the correspondent weight, obtained by application of the Integration Scheme of order 0.

3.3.3.3 Integration Scheme - order k

Taking into account the quadrilateral shapes that resulted from the Integration Scheme of order 1, a Gauss-Legendre quadrature scheme of *k x k* integration points is applied, Figure 3.11, and being their integration weight defined by:

$$A_I = w_\eta w_\xi \left(\frac{A_{square}}{4}\right) \tag{3.10}$$

where A_{square} is obtained from the Integration Scheme of order 0 for quadrilateral shapes and $w_\eta w_\xi$ are the Gauss quadrature weights for an isoparametric quadrilateral element.

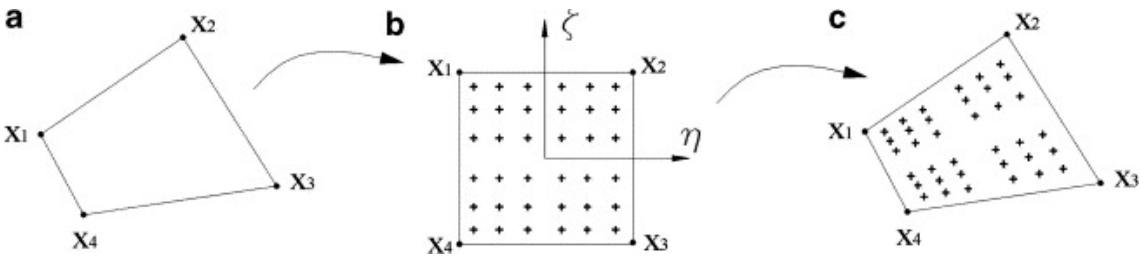

Figure 3.11: (a) Initial quadrilateral, (b) transformation of the initial quadrilateral into an isoparametric square shape and application of the $6*6$ quadrature point rule and (c) return to the initial quadrilateral shape. [33]

The above described 2D integration scheme is directly extended for the 3D space. In this new setting, 3D Voronoï cells from irregular meshes will generate hexahedrons, while cells from regular meshes will be sub-divided into tetrahedrons. Afterwards all the integration schemes can be obtained by recreating the 2D procedure.

3.4 Shape Functions

In terms of Shape Functions both the RPIM and the NNRPIM use the same methodology, combining two known methods, the moving least-square aproximants (MLS)[78] and the radial point interpolators (RPI) [42, 43].

Assuming a function $u(x)$ defined in the domain Ω, which is discretized by a set of N nodes. It is considered that only the nodes inside the influence-cell of the point of interest x_I have effect over $u(x_I)$ and so the value of $u(x_I)$ at the point of interest x_I is calculated by:

$$u(x_I) = \sum_{i=1}^{n} R_i(x_I)a_i(x_I) + \sum_{j=1}^{m} p_j(x_I)b_j(x_I) = \left\{R^T(x_I), p^T(x_I)\right\} \begin{Bmatrix} a \\ b \end{Bmatrix} \tag{3.11}$$

where $R_i(x_I)$ is the Radial Basis Function (RBF), n is the number of nodes inside the influence-cell of x_I, $p_j(x_I)$ defines the m monomials of the polynomial basis and $a_i(x_I)$ and $b_j(x_I)$ are the respectively associated non-constant coefficients. In vector form, these can be represented by:

$$\mathbf{R}(x_I) = \{R_1(x_I), R_2(x_I), ..., R_n(x_I)\}^T \tag{3.12}$$

$$\mathbf{p}(x_I) = \{p_1(x_I), p_2(x_I), ..., p_m(x_I)\}^T \tag{3.13}$$

$$\mathbf{a}(x_I) = \{a_1(x_I), a_2(x_I), ..., a_n(x_I)\}^T \tag{3.14}$$

$$\mathbf{b}(x_I) = \{b_1(x_I), b_2(x_I), ..., b_m(x_I)\}^T \tag{3.15}$$

To guaranty a stable function, the number of monomials of the polynomial basis *(m)* should be inferior than the number of nodes present in the point of interest influence-cell *(n)*.

Although the initial purpose of the addition of a polynomial basis into the radial point interpolator function formulation was to ensure its consistency, it was afterwards found [33] that this addition was not required. These conclusions were reached by not finding a significant change when comparing results from RPI functions with a constant polynomial basis and RPI functions without any polynomial basis function. This allows for equation 3.11 to be simplified to:

$$\mathbf{u}(x_I) = \mathbf{R}^T(x_I)\mathbf{a}(x_I) \tag{3.16}$$

In the RBF the variable is the distance between the relevant node x_I and the neighbour node x_i, represented as r_{Ii}. In 3D space its value can be obtained by:

$$r_{Ii} = \sqrt{(x_I - x_i)^2 + (y_I - y_i)^2 + (z_I - z_i)^2} \tag{3.17}$$

The NNRPIM uses a different formulation of the RBF based in the multiquadric (MQ) function proposed by Hardy [79]. The formulation of the MQ-RBF is as follows:

$$R(r_{Ii}) = (r_{Ii}^2 + c^2)^p \tag{3.18}$$

where c and p are two parameters whose optimal values were determined as 0.0001 and 1.0001, respectively[80]. These values allow the RPI to have the delta Kronecker property and, as aforementioned, an easier definition of the boundary conditions. Consequently, the newly obtained equation is:

$$\mathbf{u}_s = \mathbf{R}_Q\mathbf{a} \tag{3.19}$$

where $\mathbf{u}_s$ is defined by:

$$\mathbf{u}_s = \{u_1, u_2, ..., u_n\}^T \tag{3.20}$$

and the moment matrix of the RBF, $\mathbf{R}_Q$, is given by:

$$\mathbf{R}_Q = \begin{pmatrix} R(r_{11}) & R(r_{12}) & ... & R(r_{1n}) \\ R(r_{21}) & R(r_{22}) & ... & R(r_{2n}) \\ \vdots & \vdots & & \vdots \\ R(r_{n1}) & R(r_{n2}) & ... & R(r_{nn}) \end{pmatrix} \tag{3.21}$$

Since according to its definition this equality will verify $r_{ji} = r_{ij}$ and consequently $R(r_{ji}) = R(r_{ij})$ will also be verified. Therefore the previous matrix will be symmetrical. Then, by substitution in equation 3.16:

$$\mathbf{u}(x_I) = \mathbf{R}^T(x_I)\mathbf{R}_Q\mathbf{u}_s = \varphi(x_I)\mathbf{u}_s \tag{3.22}$$

Finally, the value of the interpolation function on the point of interest $\varphi(x_I)$, can then be achieved by using:

$$\varphi(x_I) = \mathbf{R}^T(x_I)\mathbf{R}_Q = \{\varphi_1(x_I), \varphi_2(x_I), ..., \varphi_n(x_I)\} \tag{3.23}$$

3.5 Galerkin Weak Form

The Strong Form is the name given to the differential equations that model each studied phenomena. The ideal scenario would be to always get an exact solution from a equation system based on the Strong Form. Still, the generalization of strong form to account for demands of complex problems is a difficult task to achieve. Therefore, it is often chosen to use the Weak Form formulation since a much more stable algebric equation system allowing for more precise solutions [81]. In the case of the NNRPIM, it uses the Galerkin Weak Form.

Consider a body described by a domain $\Omega \subset \Re^2$ and bounded by Γ, where $\Gamma \in \Omega : \Gamma_u \cup \Gamma_t = \Gamma \wedge \Gamma_u \cap \Gamma_t = \emptyset$, being Γ_u the body's essential boundaries and Γ_t its natural boundaries. The equilibrium equations governing the linear elastostatic problem are defined as $\nabla\mathbf{\Lambda} + \mathbf{b} = 0$ in Ω, where ∇ is the divergence operator, $\mathbf{\Lambda}$ the Cauchy stress tensor for a kinematically admissible displacement field $\mathbf{u}$ and $\mathbf{b}$ the body force per unit volume. The boundary are obtained by $\mathbf{\Lambda n} = \bar{\mathbf{t}}$ on Γ_t and $\mathbf{u} = \bar{\mathbf{u}}$ on Γ_u, being $\bar{\mathbf{u}}$ the prescribed displacement on the essential boundary Γ_u, $\bar{\mathbf{t}}$ the traction on the natural boundary Γ_t and $\mathbf{n}$ the unit outward normal to the boundary of domain Ω. With use of the Voigt notation and assuming the Galerkin method for linear elasticity, the weak form for the discrete problem can be written as,

$$\delta L = \int_\Omega \delta\boldsymbol{\varepsilon}^T \boldsymbol{\sigma} d\Omega - \int_\Omega \delta\mathbf{u}^T \mathbf{b} d\Omega - \int_{\Gamma_t} \delta\mathbf{u}^T \bar{\mathbf{t}} d\Gamma_t = 0 \tag{3.24}$$

Where $\boldsymbol{\varepsilon}$ is the strain vector defined as $\boldsymbol{\varepsilon} = \mathbf{Lu}$, being $\mathbf{L}$ the following differential operator:

$$\mathbf{L} = \begin{bmatrix} \frac{\partial}{\partial x} & 0 & \frac{\partial}{\partial y} \\ 0 & \frac{\partial}{\partial y} & \frac{\partial}{\partial x} \end{bmatrix}^T \tag{3.25}$$

The direct correlation of the stress field with the strain field is possible using Hooke's Law: $\boldsymbol{\sigma} = \mathbf{c}\boldsymbol{\varepsilon} = \mathbf{cLu}$. Where $\mathbf{c}$ is the material constitutive matrix, obtained by inversion of the compliance elasticity matrix, $\mathbf{c} = \mathbf{s}^{-1}$. The compliance elasticity matrix $\mathbf{s}$ for the general anisotropic material case for the plane stress and plane strain formulations is defined by:

$$\mathbf{s}_{stress} = \begin{bmatrix} \frac{1}{E_{11}} & -\frac{\nu_{21}}{E_{22}} & 0 \\ -\frac{\nu_{12}}{E_{11}} & \frac{1}{E_{22}} & 0 \\ 0 & 0 & \frac{1}{G_{12}} \end{bmatrix} \tag{3.26}$$

$$\mathbf{s}_{strain} = \begin{bmatrix} \frac{1-\nu_{31}\nu_{13}}{E_{11}} & -\frac{\nu_{21}+\nu_{31}\nu_{23}}{E_{22}} & 0 \\ -\frac{\nu_{12}+\nu_{312}\nu_{13}}{E_{11}} & \frac{1-\nu_{32}\nu_{23}}{E_{22}} & 0 \\ 0 & 0 & \frac{1}{G_{12}} \end{bmatrix} \tag{3.27}$$

Being E_{ij} the elasticity modulus, ν_{ij} the material Poisson coefficient and G_{ij} the distortion modulus in the material direction i and j.

For simplicity it will only be detailed the 2D Galerkin Weak form formulation. In a 2D problem considering the plane strain or the plane stress assumptions each node x_i discretizing the problem domain has two degrees of freedom: $\mathbf{u}_i = \{u_i, v_i\}$. Thus, in order to interpolate the virtual displacement at the interest point x_I, the interpolation equation can be written as,

$$\delta\mathbf{u}(x_I) = \delta\mathbf{u}_I = \mathbf{I}\begin{Bmatrix}\Phi_I\\ \Phi_I\end{Bmatrix}\delta\mathbf{u}_s = \begin{bmatrix}\varphi_I(x_I) & 0 & \cdots & \varphi_n(x_I) & 0\\ 0 & \varphi_I(x_I) & \cdots & 0 & \varphi_n(x_I)\end{bmatrix}\begin{Bmatrix}\delta u_I\\ \delta v_I\\ \vdots\\ \delta u_n\\ \delta v_n\end{Bmatrix} = \mathbf{H}_I\delta\mathbf{u}_s \quad (3.28)$$

with I a 2×2 identity matrix. Substituting $\boldsymbol{\varepsilon} = \mathbf{L}\mathbf{u}$ in the first term of equation 3.24 and considering the previous equation it is possible to formulate:

$$\int_\Omega \delta\boldsymbol{\varepsilon}^T\boldsymbol{\sigma}d\Omega = \int_\Omega (\mathbf{L}\delta\mathbf{u})^T\mathbf{c}(\mathbf{L}\mathbf{u})d\Omega = \int_\Omega (\mathbf{L}\mathbf{H}_I\delta\mathbf{u}_s)^T\mathbf{c}(\mathbf{L}\mathbf{H}_I\delta\mathbf{u}_s)d\Omega = \quad (3.29)$$

$$= \int_\Omega \delta\mathbf{u}_s^T\mathbf{B}_I^T\mathbf{c}\mathbf{B}_I\mathbf{u}_s d\Omega = \delta\mathbf{u}_s^T\int_\Omega \mathbf{B}_I^T\mathbf{c}\mathbf{B}_I d\Omega\mathbf{u} \quad (3.30)$$

where $\mathbf{B}_I$ is the resultant deformation matrix defined for the n nodes constituting the influence-cell of interest point $\mathbf{x}_I$,

$$\mathbf{B}_I = \begin{bmatrix}\frac{\partial\varphi_1(\mathbf{x}_I)}{\partial x} & 0 & \frac{\partial\varphi_2(\mathbf{x}_I)}{\partial x} & 0 & \cdots & \frac{\partial\varphi_n(\mathbf{x}_I)}{\partial x} & 0\\ 0 & \frac{\partial\varphi_1(\mathbf{x}_I)}{\partial y} & 0 & \frac{\partial\varphi_2(\mathbf{x}_I)}{\partial y} & \cdots & 0 & \frac{\partial\varphi_n(\mathbf{x}_I)}{\partial y}\\ \frac{\partial\varphi_1(\mathbf{x}_I)}{\partial y} & \frac{\partial\varphi_1(\mathbf{x}_I)}{\partial x} & \frac{\partial\varphi_2(\mathbf{x}_I)}{\partial y} & \frac{\partial\varphi_2(\mathbf{x}_I)}{\partial x} & \cdots & \frac{\partial\varphi_n(\mathbf{x}_I)}{\partial y} & \frac{\partial\varphi_n(\mathbf{x}_I)}{\partial x}\end{bmatrix} \quad (3.31)$$

Performing an analogous procedure on the second and third terms of equation 3.24 it can be obtained the following force vectors,

$$\int_\Omega \delta\mathbf{u}^T\mathbf{b}d\Omega = \int_\Omega (\mathbf{H}_I\delta\mathbf{u}_s)^T\mathbf{b}d\Omega = \delta\mathbf{u}_s^T\int_\Omega \mathbf{H}_I^T\mathbf{b}d\Omega \quad (3.32)$$

$$\int_{\Gamma_t} \delta\mathbf{u}^T\bar{\mathbf{t}}d\Gamma_t = \int_{\Gamma_t} (\mathbf{H}_I\delta\mathbf{u}_s)^T\bar{\mathbf{t}}d\Gamma_t = \delta\mathbf{u}_s^T\int_{\Gamma_t} \mathbf{H}_I^T\bar{\mathbf{t}}d\Gamma_t \quad (3.33)$$

Finally, equation 3.24 can be re-written as,

$$\partial L = \delta\mathbf{u}_s^T\underbrace{\int_\Omega \mathbf{B}_I^T\mathbf{c}\mathbf{B}_I d\Omega\mathbf{u}}_{\mathbf{K}} - \delta\mathbf{u}_s^T\underbrace{\int_\Omega \mathbf{H}_I^T\mathbf{b}d\Omega}_{\mathbf{f}_b} - \delta\mathbf{u}_s^T\underbrace{\int_{\Gamma_t} \mathbf{H}_I^T\bar{\mathbf{t}}d\Gamma_t}_{\mathbf{f}_t} \quad (3.34)$$

The eqatuin system can be written in the matrix form as $\mathbf{K}\mathbf{u} = \mathbf{f}$, where $\mathbf{K}$ is the stiffness matrix, $\mathbf{u}$ is the displacement field vector and $\mathbf{f}$ is the vector of applied forces defined as $\mathbf{f} = \mathbf{f}_b + \mathbf{f}_t$. As the

RPI shape function possess the delta Kronecker property, the essential boundary conditions may be applied directly to the stiffness matrix [33]. After the displacement field has been determined by solving the linear equation system $\mathbf{K}^{-1}\mathbf{f} = \mathbf{u}$, the strain in an interest point $\mathbf{x}_I \in \Omega$ can be obtained with use of $\boldsymbol{\varepsilon}(\mathbf{x}_I) = \mathbf{L}\mathbf{u}(\mathbf{x}_I)$. Afterwards it is then possible to determine the stress field by considering Hooke's Law, $\boldsymbol{\sigma}(\mathbf{x}_I) = \mathbf{c}(\mathbf{x}_I)\boldsymbol{\varepsilon}(\mathbf{x}_I)$. In order to determine the strain energy density field for the considered load it is used the stress field and the strain field. The strain energy field at any interest point $\mathbf{x}_I$ is determined with,

$$U(\mathbf{x}_I) = \frac{1}{2}\int_{\Omega} \boldsymbol{\sigma}(\mathbf{x}_I)^T \boldsymbol{\varepsilon}(\mathbf{x}_I) d\Omega_I \tag{3.35}$$

In addition, it can be obtained the three principal stresses $\sigma(\mathbf{x}_I)_i$ for each interest point $\mathbf{x}_I$, $\det(\boldsymbol{\Lambda}(\mathbf{x}_I) - \sigma(\mathbf{x}_I)_i\mathbf{I}) = 0$, and the three principal directions $\mathbf{n}(\mathbf{x}_I)_i$: $(\boldsymbol{\Lambda}(\mathbf{x}_I) - \sigma(\mathbf{x}_I)_i\mathbf{I})\mathbf{n}(\mathbf{x}_I)_i = 0$, with $\boldsymbol{\Lambda}(\mathbf{x}_I)$ the Cauchy stress tensor obtained for the interest point and $\mathbf{I}$ being a 2×2 identity matrix. The three principal stresses $\sigma(\mathbf{x}_I)_i$ can then be used to obtain the von Mises effective stress by applying the following expression:

$$\bar{\sigma}(\mathbf{x}_I) = \sqrt{\frac{1}{2}((\sigma(\mathbf{x}_I)_1 - \sigma(\mathbf{x}_I)_2)^2 + (\sigma(\mathbf{x}_I)_2 - \sigma(\mathbf{x}_I)_3)^2 + (\sigma(\mathbf{x}_I)_3 - \sigma(\mathbf{x}_I)_1)^2)} \tag{3.36}$$

Chapter 4

Elasto-Plastic Formulation

The Atherosclerotic plaque, as many other organic tissues, has a very complex mechanical behaviour. In this work, as it has been stated before, this mechanical behaviour will be simplified to a elasto-plastic model using a bi-linear approximation. In this chapter it will be address the definition of an elastic-plastic material, the elsto-plastic formulation used for this work and the non-linear solution method used to solve the equations derived from this formulation.

4.1 Elasto-Plastic Definition

A material with an elasto-plastic behaviour is, as the name states, one who possesses both elastic and plastic properties. An elastic material is one that after being deformed from forces applied to it, if those forces cease to exist it returns to its original size. On the other hand, a plastic material is one whose deformations that the material undergoes due the application of forces (beyond the material elastic limit) are non-reversible.

On Figure 4.1 it can be seen a stress-strain curve of a typical elasto-plastic behaviour. If it would simply have a linear-elastic behaviour, as it is applied more stress it would be linearly deformed and follow the dotted line until Point A. As it is a elasto-plastic material it will show an elastic behaviour until a certain point were, if surpassed it will start to experience plastic deformation. This threshold level is called the Yield Stress and it is marked on the Figure as σ_y.

By going over this threshold the strain increases more rapidly than in the elastic region and any deformation that exists passed this point will be non-reversible. This can be seen as after the material is taken until Point B it does not return to the origin but to point 0*. At this stage the material has experienced a phenomena called hardening, where the material will need increasingly higher stresses in order to have further plastic deformation. In this case, this material will only experience further plastic-deformation after reaching Point B, being this its new Yield Point.

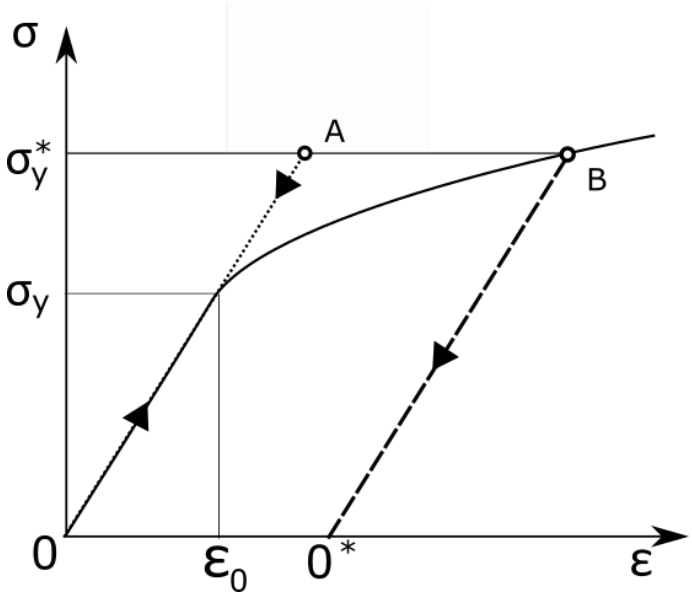

Figure 4.1: Stress-strain curve (A- Linear Elastic Behaviour; B- Elasto-Plastic Behaviour)

4.2 Elasto-Plastic Formulation

In order to characterize the non-linear behaviour of an elasto-plastic material it is necessary to define the mathematical law for the plastic component of the deformation. To do so, three aspects should be addressed:

- a yield criterion, showing the stress level in terms of the stress tensor and indicating the beginning of the plastic regime;
- a flow rule, characterizing how the deformation relates to stress after plastification;
- and a hardening rule, describing any interdependency between the yield criterion and the plastic deformation [82].

The beginning of the plastic regime is defined by the yield criterion. The Yield Criterion is usually defined as:

$$F(\boldsymbol{\sigma}, k) = f(\boldsymbol{\sigma}) - \sigma_y(k) = 0 \tag{4.1}$$

with $\boldsymbol{\sigma}$ being the stress tensor and k being the hardening parameter. The yield function is shown as the scalar function $f(\boldsymbol{\sigma})$ and the yield stress, the stress limit for the elastic regime, is shown as $\sigma_y(k)$.

This Criterion defines that if the material's stress state at any given point leads to $f(\boldsymbol{\sigma}) < \sigma_y(k)$, then the material at that point is governed by the linear equations of the theory of elasticity [83].

If, by the contrary, $f(\boldsymbol{\sigma}) = \sigma_y(k)$ then the point its yielding and it will start to experience plastic deformations. In this work it was used the Von Mises yield Criterion [84] that is defined as,

$$f(\boldsymbol{\sigma}) = \bar{\sigma} = \frac{\sqrt{2}}{2}\left[(\sigma_{xx}-\sigma_{yy})^2 + (\sigma_{yy}-\sigma_{zz})^2 + (\sigma_{zz}-\sigma_{xx})^2 + 6(\tau_{xy}^2+\tau_{yz}^2+\tau_{zx}^2)\right]^{0.5} \tag{4.2}$$

This yield function can be worked with, resulting the the following expression:

$$f(\boldsymbol{\sigma}) = \bar{\sigma} = \left[\sigma_{xx}^2+\sigma_{yy}^2+\sigma_{zz}^2+\sigma_{xx}\sigma_{yy}+\sigma_{yy}\sigma_{zz}+\sigma_{zz}\sigma_{xx}+3\tau_{xy}^2+3\tau_{yz}^2+3\tau_{zx}^2\right]^{0.5} \tag{4.3}$$

The flow rule, as mentioned before, is the mathematical formulation that will express which will be the relation of strain and stress after the Yield Criterion as been met. In this work it was considered an associated flow rule, in this case the Prandtl-Reuss flow rule. This flow rule is defined as:

$$d\boldsymbol{\varepsilon}_p = d\lambda \frac{\partial f}{\partial \boldsymbol{\sigma}} = d\lambda \mathbf{a} \tag{4.4}$$

where $d\lambda$ is the plastic rate multiplier and $\boldsymbol{a}$ is the flow vector, normal to the adopted yield function, f, defined before. The flow vector can be presented as $a = \partial f/\partial \boldsymbol{\sigma}$, where

$$\mathbf{a} = \left\{ \frac{\partial f}{\partial \sigma_{xx}} \quad \frac{\partial f}{\partial \sigma_{yy}} \quad \frac{\partial f}{\partial \sigma_{zz}} \quad \frac{\partial f}{\partial \sigma_{xy}} \quad \frac{\partial f}{\partial \sigma_{yz}} \quad \frac{\partial f}{\partial \sigma_{zx}} \right\}^T \tag{4.5}$$

From Hooke's Law the following relation between the stress rate $\boldsymbol{\sigma}$ and the elastic strain rate $d\boldsymbol{\varepsilon}_e$ is assumed:

$$d\boldsymbol{\sigma} = \mathbf{c} d\boldsymbol{\varepsilon}_e = \mathbf{c}(d\boldsymbol{\varepsilon} - d\boldsymbol{\varepsilon}_p) \tag{4.6}$$

in which $d\boldsymbol{\varepsilon}$ is the total strain rate and $d\boldsymbol{\varepsilon}_p$ is the plastic strain rate. By considering the Prandtl-Reuss flow rule and assuming that the yield surface ($F(\boldsymbol{\sigma}, k)$) only depends on the magnitude of the applied principal stresses and of the hardening parameter k, the previous equation can be rewritten as

$$d\boldsymbol{\sigma} = \mathbf{c}(d\boldsymbol{\varepsilon} - d\lambda \mathbf{a}) \tag{4.7}$$

As the stress must not go pass the yield surface in order to occur plastic flow, the following relation is defined:

$$dF = \frac{\partial f}{\partial \boldsymbol{\sigma}} d\boldsymbol{\sigma} - \frac{\partial \sigma_Y}{\partial k} = \mathbf{a}^T d\boldsymbol{\sigma} - A d\lambda = 0 \tag{4.8}$$

where A is an hardening parameter dependent on the hardening rule [82]. This parameter is defined by,

$$A = \frac{1}{d\lambda}\frac{\partial \sigma_Y}{\partial k}dk \tag{4.9}$$

By applying equation 4.7 on equation 4.8 it is obtained:

$$d\lambda = \frac{\mathbf{a}^T \mathbf{c} d\boldsymbol{\varepsilon}}{\mathbf{a}^T \mathbf{c}\mathbf{a} + A} \tag{4.10}$$

With the introduction of the value of $d\lambda$ into the equation 4.6, the stress rate can be written as:

$$d\boldsymbol{\sigma} = \mathbf{c}d\boldsymbol{\varepsilon} - \frac{\mathbf{a}^T \mathbf{c} d\boldsymbol{\varepsilon}}{\mathbf{a}^T \mathbf{c}\mathbf{a} + A} \cdot \mathbf{c}\mathbf{a} = (\mathbf{c} - \frac{\mathbf{c}\mathbf{a}\mathbf{a}^T \mathbf{c}}{\mathbf{a}^T \mathbf{c}\mathbf{a} + A})d\boldsymbol{\varepsilon} = \mathbf{c}_t d\boldsymbol{\varepsilon} \tag{4.11}$$

in which $\mathbf{c}_t$ is the tangential constitutive matrix. In this work the work hardening hypothesis is employed [82] considering the associated flow rule in order to define explicitly the hardening parameter A. As all of the materials studied in this work will be used as having a linear elastic-linear plastic plastic hardening behaviour, the hardening parameter A can be defined as [82]:

$$A = \frac{E_{To}}{1 - \frac{E_{To}}{E_o}} \tag{4.12}$$

where E_o is the elastic modulus and E_{To} the tangential modulus in the reference direction.

In this work the material behaviour is modelled as an incremental relation between the incremental stress vector and the strain increment. The "backward-Euler" procedure [85] was considered in order to force the stress back to the yield surface.

As for the calculation of the non-linear solution, this was done resorting to the Newton-Rapson initial stiffness method [82]. Using this algorithm the stiffness matrix is only calculated for the first iteration of the first increment. A diagram of the algorithm implemented in the software used for this work can be seen in Figure 4.2.

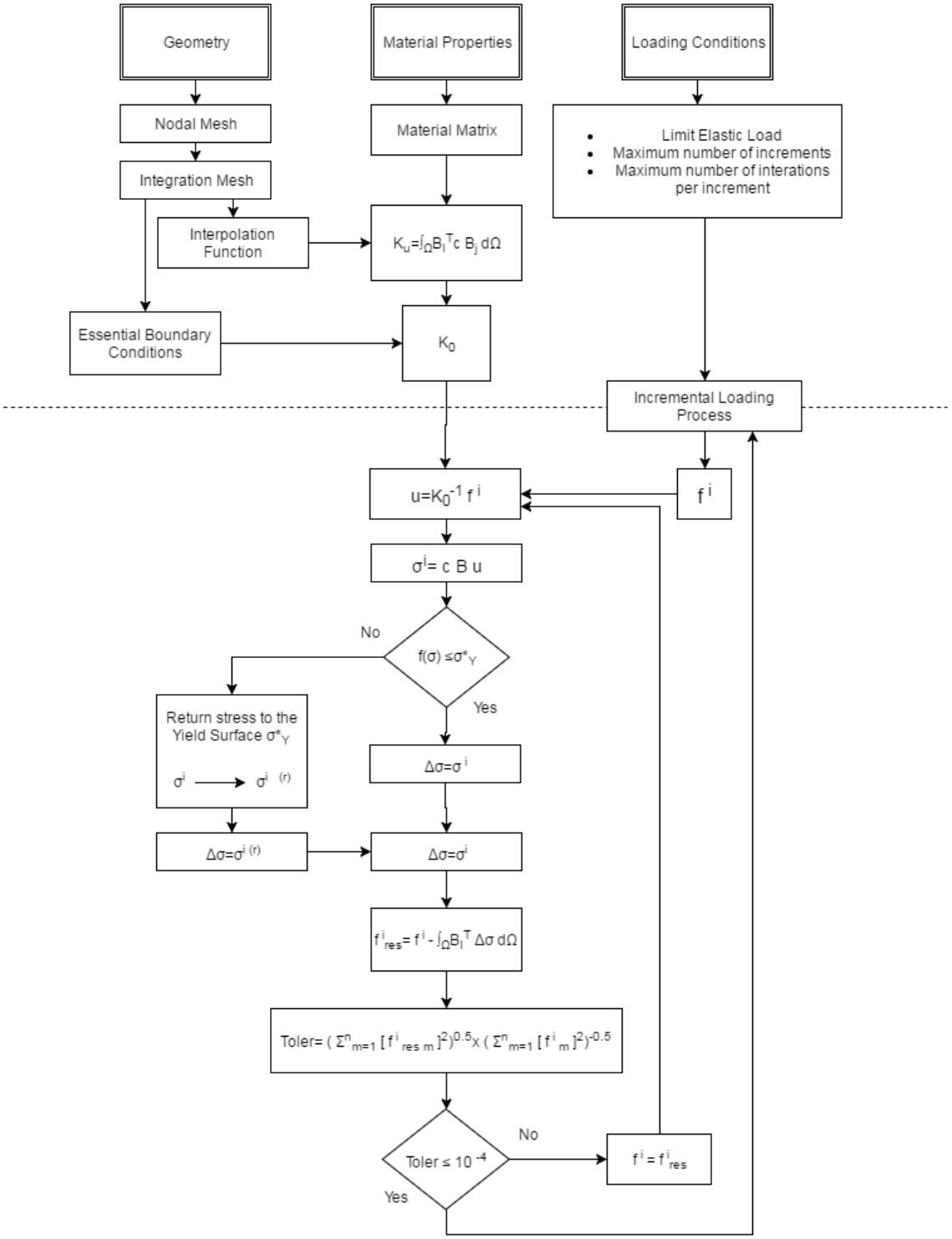

Figure 4.2: Newton-Rapson based non-linear solution algorithm (adapted from [86])

Chapter 5

Preliminary Studies

Before analysing 2D and 3D models of arteries with Atherosclerotic Plaque, several preliminary studies were made. The first objective of these studies was to analyse the convergence of the RPIM and the NNRPIM when compared with FEM. The second objective was to stablish the mechanical properties for the Atherosclerotic Plaque from experimental data present in the literature and afterwards validate the accuracy of our simulations of this material. In this chapter it is shown a brief introduction of the software used throughout this work, the convergence study made to validate the numerical methods and the study of the accuracy of Atherosclerotic Plaque simulations.

5.1 Finite Element Meshless Method Analysis Software - FEMAS

FEMAS is a meshless computational framework developed at FEUP since 2014 by Prof. Jorge Belinha. It is an original code implemented in the commercial software MATLAB that uses the meshless formulations presented in Chapter 3 and the non-linear elasto-plastic analysis presented in Chapter 4. Through a graphical user interface (GUI), this software allows for an easy construction of numerical models and their analysis using several different discretization techniques.

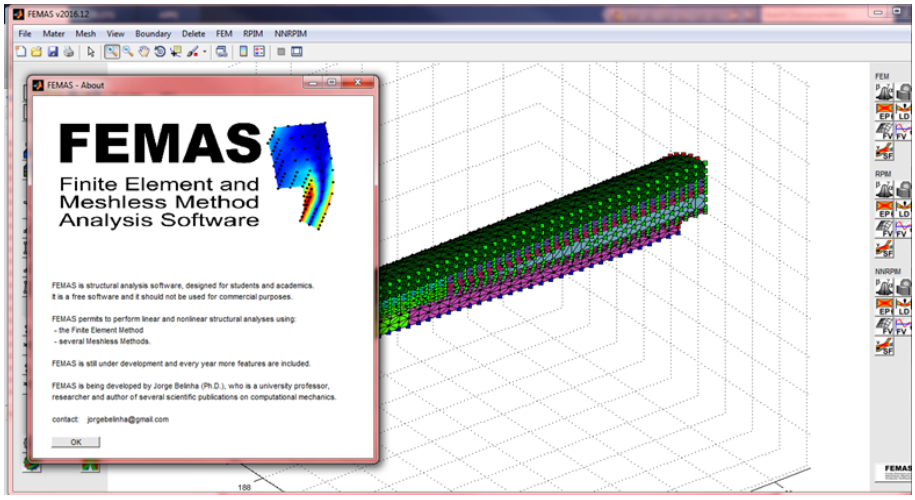

Figure 5.1: FEMAS Graphical User Interface

In terms of numerical analysis, FEMAS allows for the use of the RPIM, the NNRPIM and the FEM (this last method implemented for comparison purposes) and currently allows for the following analysis:

- Linear Static Linear-Elastic;
- Non-Linear Elasto-Plastic;
- Non-Linear Large Deformations;
- Crack opening path;
- Free Vibration;
- Forced Vibration;
- Buckling;
- Static Fluid flow.

This framework is capable of performing simulations with isotropic and anisotropic materials, as well as, making analysis both in 3D and 2D settings, using for this the classical three-dimensional deformation theory and the plane stress and plane strain two-dimensional deformation theory, respectively. FEMAS allows for the autonomous construction of the numerical models, allowing the user to control the nodal discretization, material disposition and location of essential and boundary conditions. All these tasks can be performed directly in the software without the need to use any external CAD software. Nonetheless, meshes can also be created using other CAD software and imported into FEMAS. For a linear elastic static analysis, FEMAS's workflow can be divided into three different stages: pre-processing, processing and post-processing. A brief explanation of this workflow can be found in Figure 5.2. All the examples and simulation shown in this work were made using the aforementioned software.

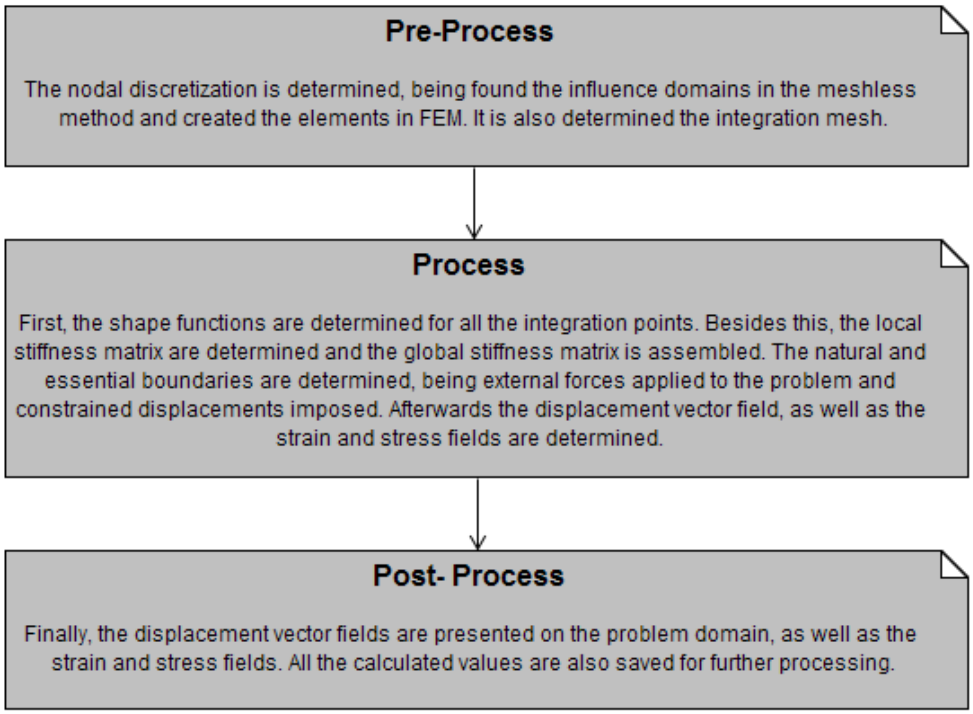

Figure 5.2: Diagram of the different phases in the FEMAS workflow

5.2 Convergence Study

A convergence study was made to define which would be the level of discretization needed in order to obtain the most accurate results in the following numerical simulations. For this convergence study three different situations were analysed: compression, confined compression and shear force. These three situations were studied both as 2D problems as well as 3D problems. The results obtained with the meshless methods were compared with the solution obtained from FEM. The FEM analysis was also done using two different kinds of elements, for 2D analysis it was used triangular elements made with three (2D-T3) and six (2D-T6) nodes and for the 3D analysis it was used tetrahedral elements with four (3D-T4) and ten (3D-T10) nodes. This allowed also for the comparison of two different kinds of FEM analysis. In all the analysis, both meshless and FEM, the nodes location was coincident.

In order to study the convergence of the methods several different meshes were used for each example, being each one of them more refined than the other following a rule of 2^n. For the 2D analysis it was used a square model with a side equal to one meter. This model was discretized with 9, 25, 81, 289 and 1089 nodes for each of the methods except for the FEM analysis with 6 nodes, where the analysis started directly with 25 nodes. This can be seen in Figure 5.3.

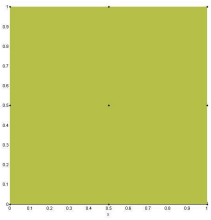

(a) 9 nodes

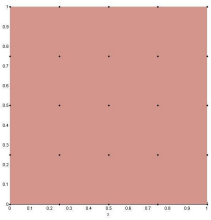

(b) 25 nodes

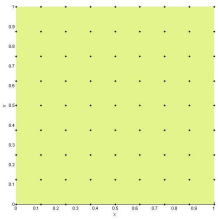

(c) 81 nodes

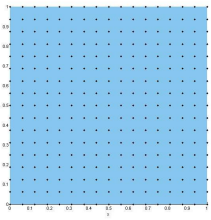

(d) 289 nodes

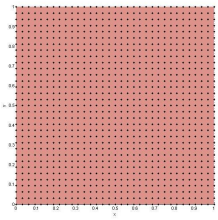

(e) 1089 nodes

Figure 5.3: 2D Nodal Distributions

For the 3D analysis it was used a cubical model with a side equal to one meter. This model was discretized with 27, 125, 729 and 4913 nodes for each of the methods except for the FEM analysis with 10 nodes, where the analysis started directly with 125 nodes. This can be seen in Figure 5.4.

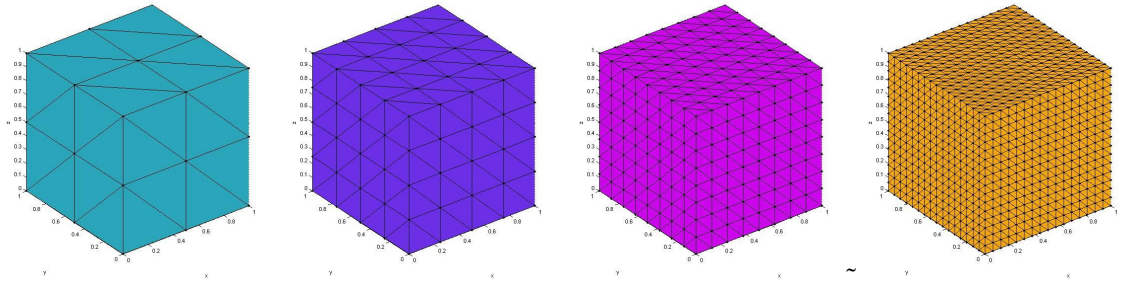

(a) 27 nodes (b) 125 nodes (c) 729 nodes (d) 4913 nodes

Figure 5.4: 3D Nodal Distributions (The FEM elements are also shown to help visualization)

All examples were considered as having a Young's Modulus of 1000 Pa and a Poisson's ratio of 0.3. For the RPIM and the NNRPIM analysis it was used the parameters present on Table 5.1 and 5.2.

Table 5.1: RPIM Parameters

RPIM	
2D	**3D**
Nodes in the influence-domain: **27**	Nodes in the influence-domain: **27**
c = **1,42**	c = **1,42**
p = **1,03**	p = **1,03**
Polynomial Basis: **Linear**	Polynomial Basis: **Linear**
Integration points: **1 per triangle**	Integration points: **1 per tetrahedron**

Table 5.2: NNRPIM Parameters

NNRPIM	
2D	**3D**
c = **0.0001**	c = **0.0001**
p = **0.9999**	p = **0.9999**
Influence-cell: **Second Order**	Influence-cell: **Second Order**
Polynomial Basis: **Constant**	Polynomial Basis: **Constant**
Integration points: **1 per sub-cell**	Integration points: **1 per sub-cell**

5.2.1 2D Square Compression

For this example it was considered a solid domain $\omega \in \Re^2$ with a form of a square of side 1 meter. To this solid domain it was applied the following constrains: $u, v = 0 : \forall x \in \Re^2 \wedge y = 0$ with $\mathbf{u} = (u, v)$. An uniform force of 1 N was also applied for $\forall x \in \Re^2 \wedge y = 1$ with the direction (x,y)= (0,1). A representation of this setting can be seen in Figure 5.5.

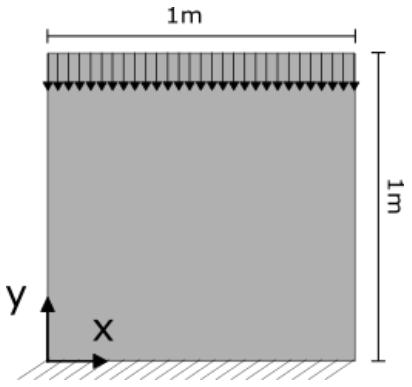

Figure 5.5: Square Plate under uniform compression

In this problem it was analysed the displacement in Oy, the Von Mises Stress, σ_{xx} and σ_{yy}. In Figure 5.6 it is possible to see how each of this variables change as it discretization of the problem increases. On those graphs, the value for the displacement in Oy was obtained at (x,y)=(0.5, 1) and all the Stresses were obtained from (x,y)=(0.5, 0.5).

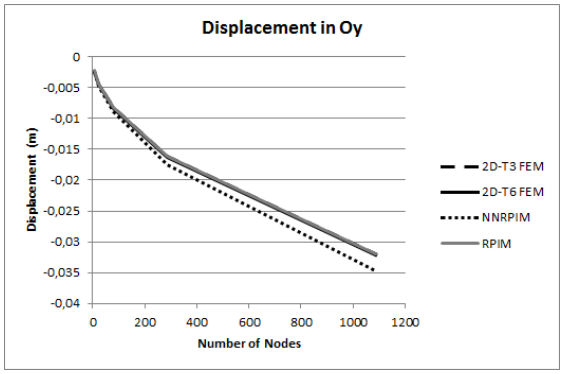

(a) Displacement in Oy

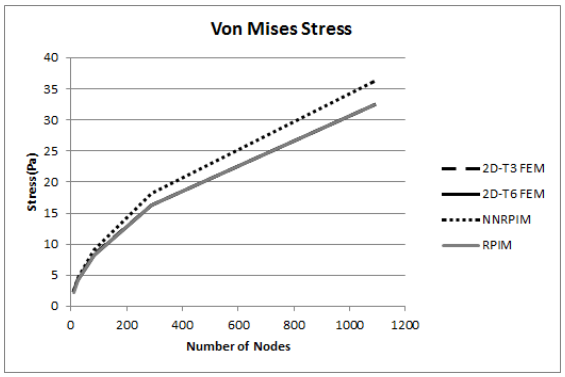

(b) Von Mises Stress

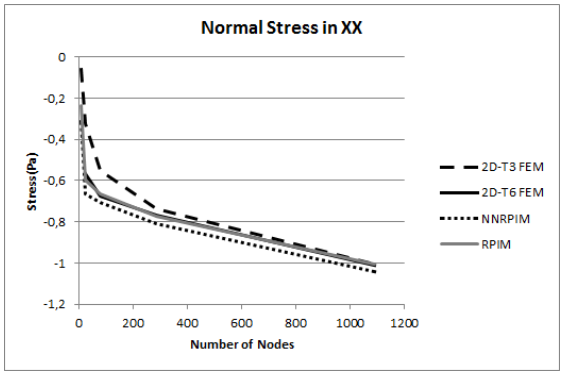

(c) Normal Stress in XX (σ_{xx})

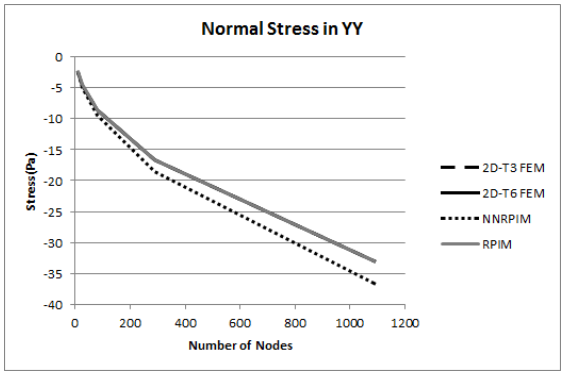

(d) Normal Stress in YY (σ_{yy})

Figure 5.6: 2D Square Compression Displacement and Stresses

Looking at the results we can clearly see that all the numerical methods follow the same tendency in all of the analysed variables, as the discretization of the problem increases, still the results have not still converged in a final converged value. Even so it is possible to see similar results and progressions in these variables. These similarities can also be seen in the distribution of Von Mises Stress Field, Figure 5.7. The Von Mises Stress Fields shown are the ones obtained with the highest level of discretization.

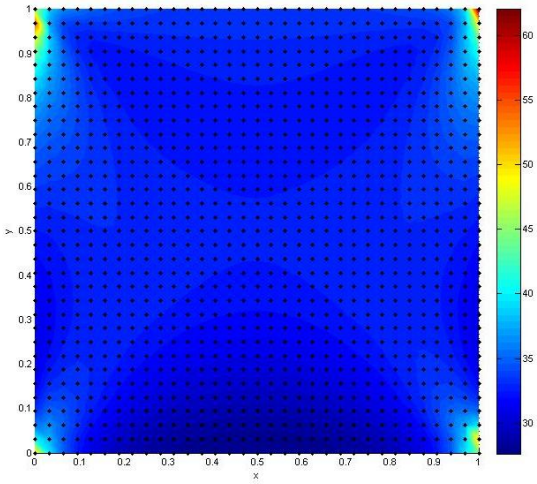

(a) FEM 2D-T3

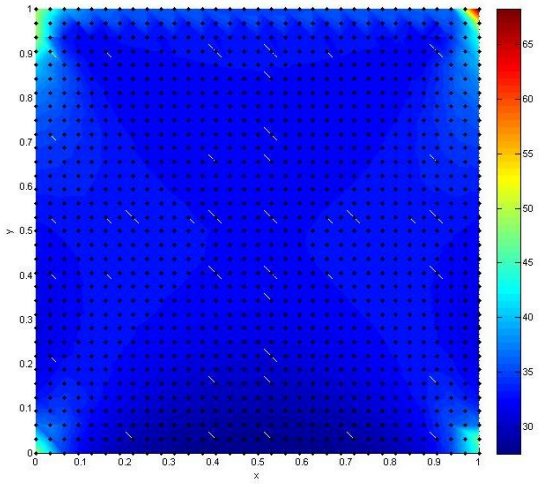

(b) FEM 2D-T6

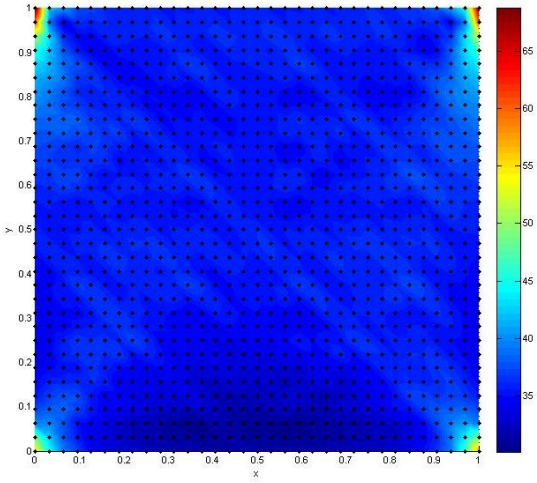

(c) RPIM

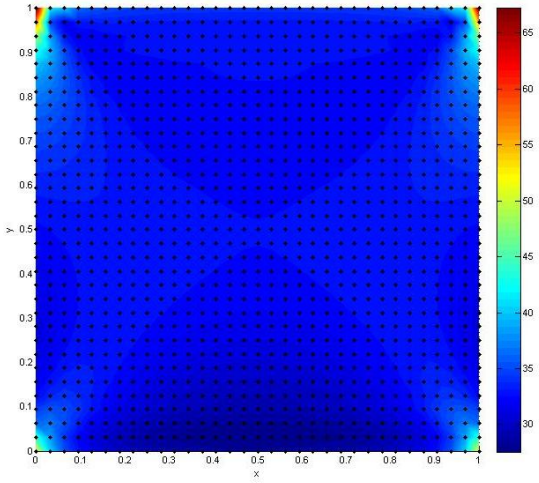

(d) NNRPIM

Figure 5.7: 2D Compression Square Plate - Von Mises Stress Field (Axis Units: 0.1 m)

5.2.2 3D Cube Compression

For this example it was taken into consideration a solid domain $\omega \in \Re^3$ with a shape of cube with size = 1m. This solid, similarly to the previous example, had the following constrains: $u,v,w = 0 : \forall x,y \in \Re^3 \wedge z = 0$ with $\mathbf{u} = (u,v,w)$. An uniform force of 1 N was applied to the solid for $\forall x,y \in \Re^3 \wedge z = 1$ with the direction (x,y,z)= (0,0,1).

In this problem it was analysed the displacement in Oz, the Von Mises Stress, σ_{xx}, σ_{yy}, σ_{zz}, τ_{xy}, τ_{yz} and τ_{zx} . In Figure 5.9 it is possible to see how each of this variables change as it discretization of the problem increases. On those graphs, the value for the displacement in Oz was obtain from

the central point at (x,y,z)=(0.5, 0.5 ,1) and all the stresses were obtained from the central point of the squared plate (x,y,z)=(0.5, 0.5 ,1).

Looking at the results in Figure 5.9, we can clearly see that all the numerical methods follow the same tendency in all the variables analysed as the discretization of the problem increases. It is also possible to see that the results have all converged, except for FEM with 4 nodes in τ_{zx} . In most of the variables analysed the numerical method appear to have almost converged at around 1000 nodes. This convergence between all the numerical methods can also be seen in the similarities between the distribution of Von Mises Stress Field, as seen in Figure 5.8. In this Figure it is possible to see the distribution of Von Mises Stress Field in the simulation with the higher discretization with a cross section of the cube at y=0.5.

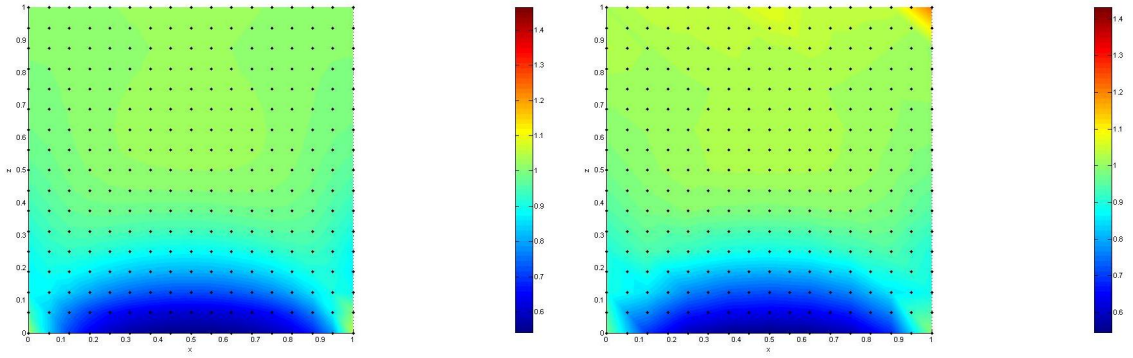

(a) FEM 2D-T3

(b) FEM 2D-T6

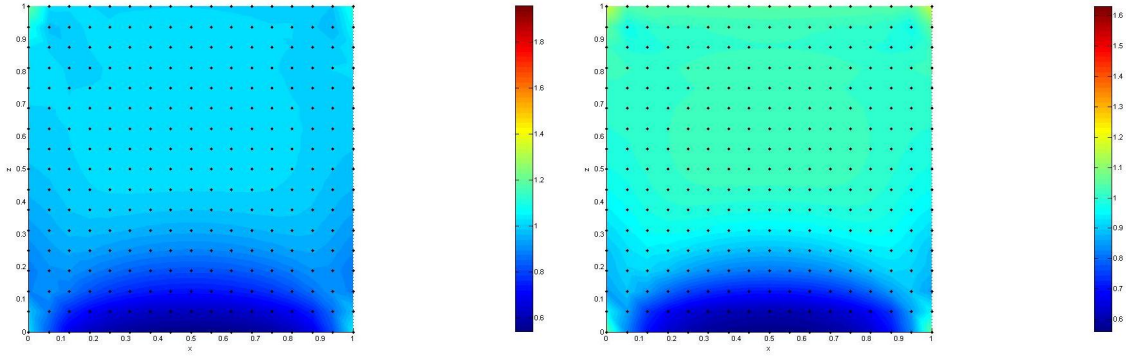

(c) RPIM

(d) NNRPIM

Figure 5.8: 3D Cube Compression - Von Mises Stress Field (Axis Units; 0.1 m)

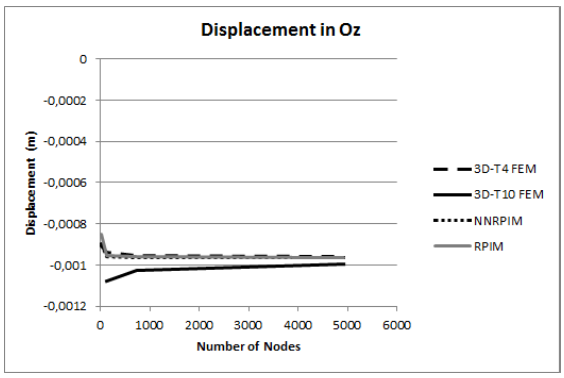

(a) Displacement in Oz

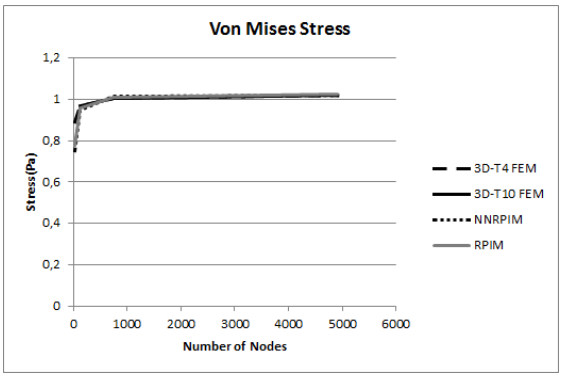

(b) Von Mises Stress

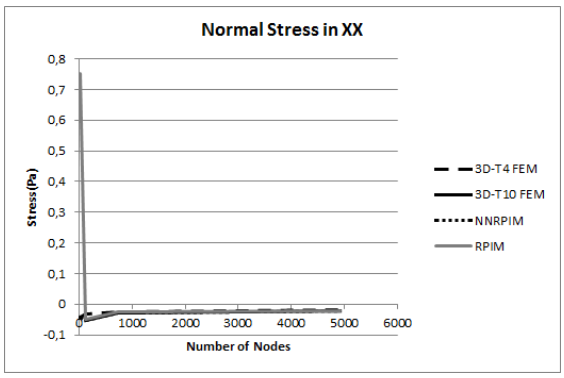

(c) Normal Stress in XX (σ_{xx})

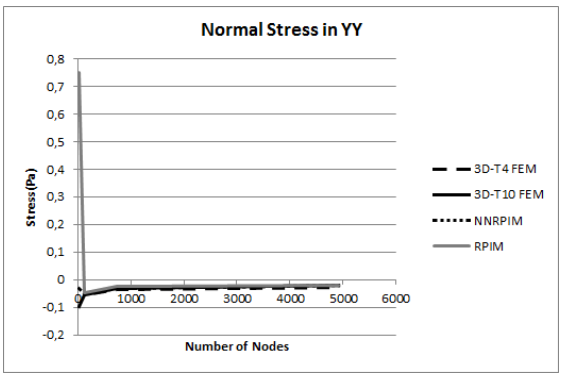

(d) Normal Stress in YY (σ_{yy})

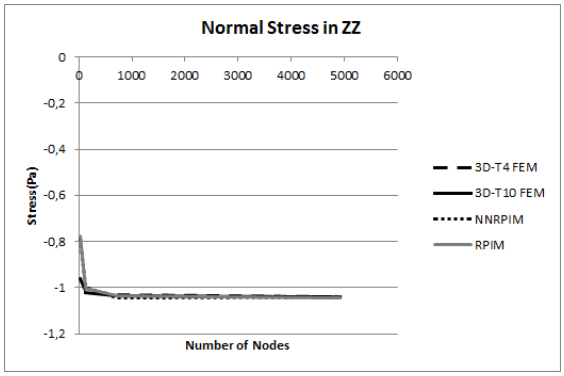

(e) Normal Stress in ZZ (σ_{zz})

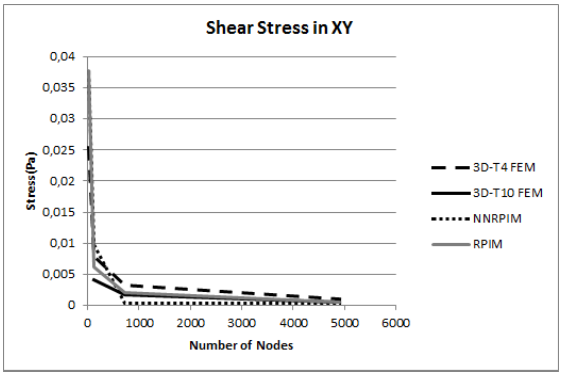

(f) Shear Stress in XY (τ_{xy})

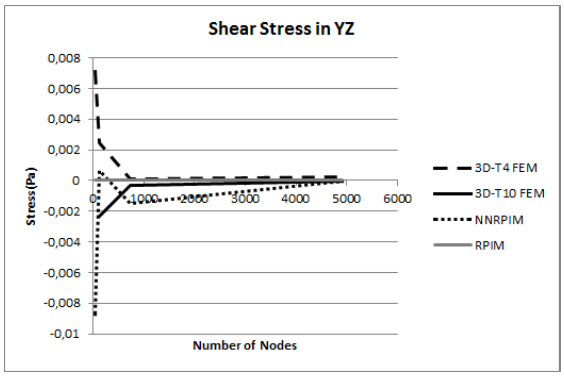

(g) Shear Stress in YZ (τ_{yz})

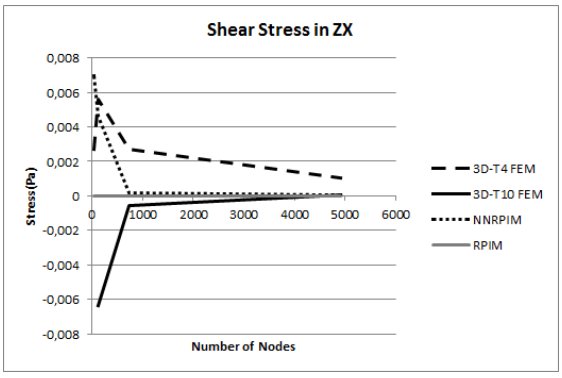

(h) Shear Stress in ZX (τ_{zx})

Figure 5.9: 3D Cube Compression Displacement and Stresses

5.2.3 2D Square Confined Compression

For this example it was considered a solid domain $\omega \in \Re^2$ with a form of a square of side 1 meter. To this solid domain it was applied the following constrains: $u = 0 : \forall x \in \Re^2 \wedge y = 0$ and $v = 0 : \forall x \in \Re^2 \wedge (y = 0 \vee y = 1)$ with $\mathbf{u} = (u, v)$. An uniform force of 1 N was applied at $\forall x \in \Re^2 \wedge y = 1$ with the direction (x,y)= (0,1). A representation of this setting can be seen in Figure 5.10.

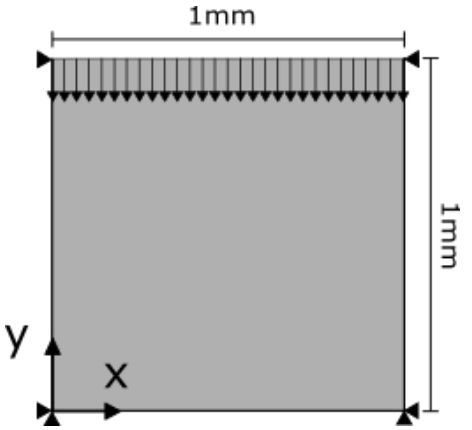

Figure 5.10: Square Plate under uniform compression

In this problem it was analysed the displacement in Oy, the Von Mises Stress, σ_{xx} and σ_{yy} . In Figure 5.11 it is possible to see how each of this variables change as it discretization of the problem increases. On those graphs, the value for the displacement in Oy was obtain at (x,y)=(0.5, 1) and all the Stresses were obtained from (x,y)=(0.5, 0.5).

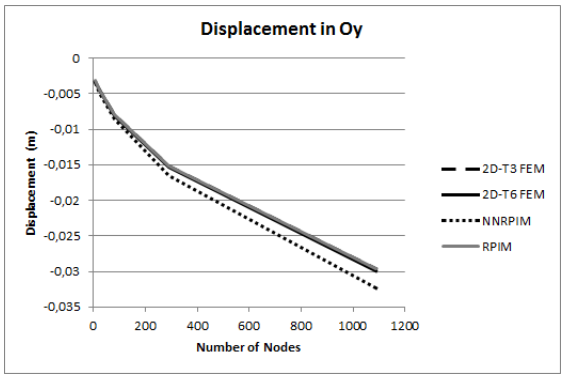

(a) Displacement in Oy

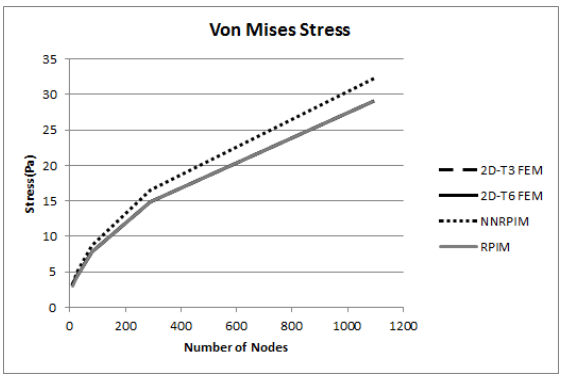

(b) Von Mises Stress

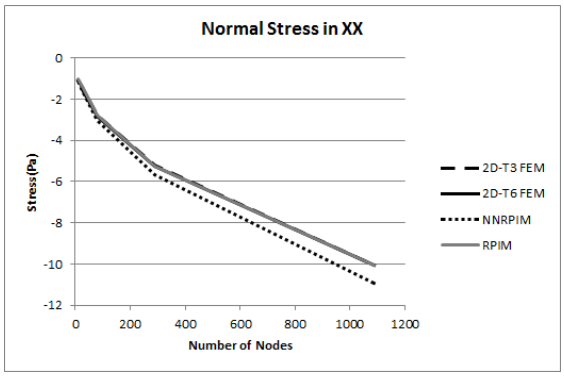

(c) Normal Stress in XX (σ_{xx})

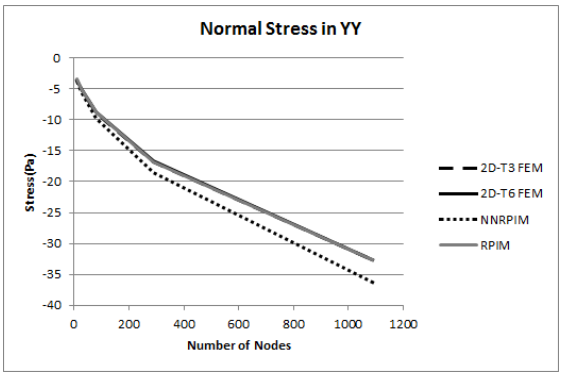

(d) Normal Stress in YY (σ_{yy})

Figure 5.11: 2D Square Confined Compression Displacement and Stress

As seen in the previous examples, all the numerical methods follow the same tendency in all the variables analysed as the discretization of the problem increases. It is also possible to see that the results have not still converged in a value, but they are starting to. Although they have not yet converged all the variables analysed show similar results for all numerical methods. These similarities between all the numerical methods can also be seen in the distribution of Von Mises Stress Field, as seen in Figure 5.12. The Von Mises Stress Fields shown are the ones obtained with the highest level of discretization.

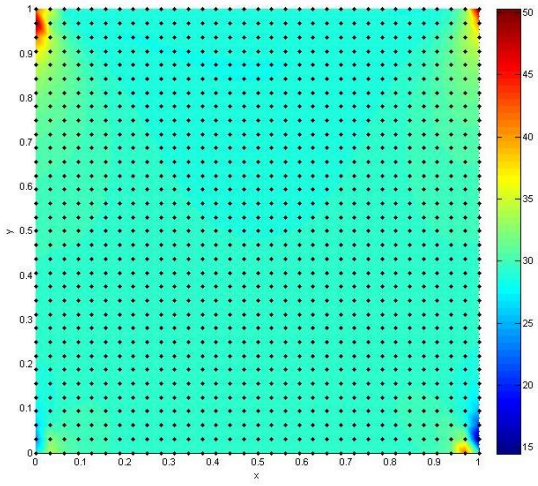

(a) FEM 2D-T3

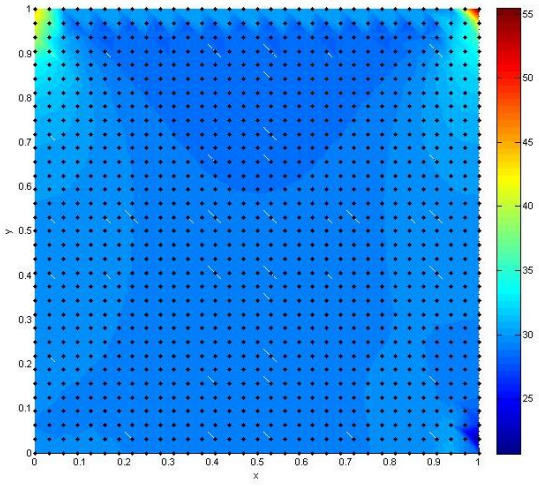

(b) FEM 2D-T6

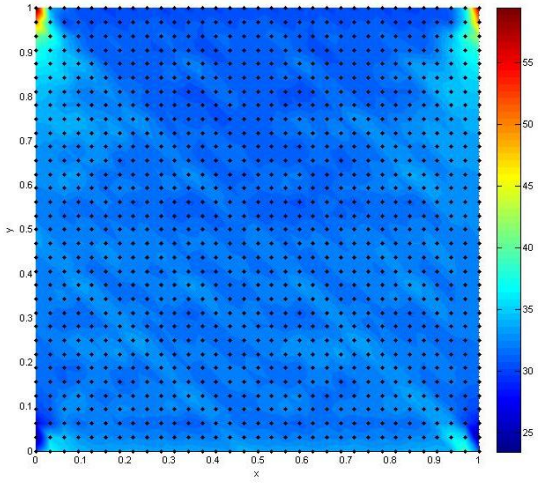

(c) RPIM

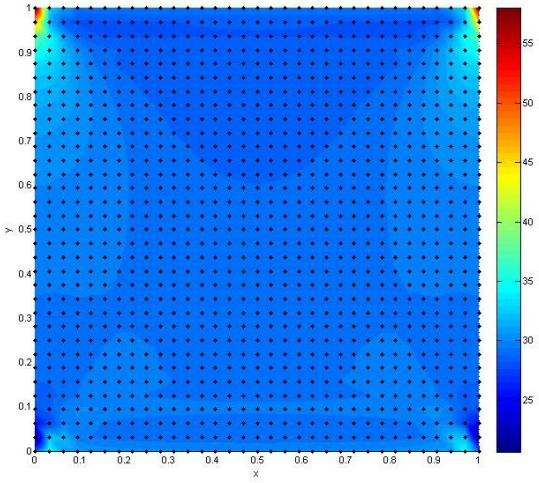

(d) NNRPIM

Figure 5.12: 2D Square Confined Compression - Von Mises Stress Field (Axis Units: 0.1 m)

5.2.4 3D Cube Confined Compression

For this example it was taken into consideration a solid domain $\omega \in \Re^3$ with a shape of cube with size = 1m. This solid, similarly to the previous example, had the following constrains: $w = 0 : \forall x, y \in \Re^3 \wedge z = 0$, $\mathbf{u} = 0 : \forall y, z \in \Re^3 \wedge x = 0$ and $v = 0 : \forall x, z \in \Re^3 \wedge y = 0$ with $u = (u, v, w)$. It was applied to this solid a uniform force of 1 N at $\forall x, y \in \Re^3 \wedge z = 1$ with the direction (x,y,z)= (0,0,1).

In this problem it was analysed the displacement in Oz, the Von Mises Stress, σ_{xx}, σ_{yy}, σ_{zz}, τ_{xy}, τ_{yz} and τ_{zx} . In Figure 5.14 it is possible to see how each of this variables change as it discretization of the problem increases. On those graphs, the value for the displacement in Oz was obtain from

the central point at (x,y,z)=(0.5, 0.5 ,1) and all the stresses were obtained from the central point of the squared plate (x,y,z)=(0.5, 0.5 ,1).

Looking at the results we can clearly see that all the numerical methods follow the same tendency in all the variables analysed as the discretization of the problem increases. It is also possible to see that the results have all the numerical methods converged being, in most of the variables analysed, this convergence seen at around 1000 nodes. This convergence between all the numerical methods can also be seen in the similarities between the distribution of Von Mises Stress Field, as seen in Figure 5.13. In this figure it is possible to see the distribution of Von Mises Stress Field in the simulation with the higher discretization at a cross section of the cube, at the plane y=0.5. By analysing this figures we can see that while throughout the solid all the stresses are similar, in the FEM analysis we have some outliers near the corners of the solid, hence its difference in color scale with the other numerical methods.

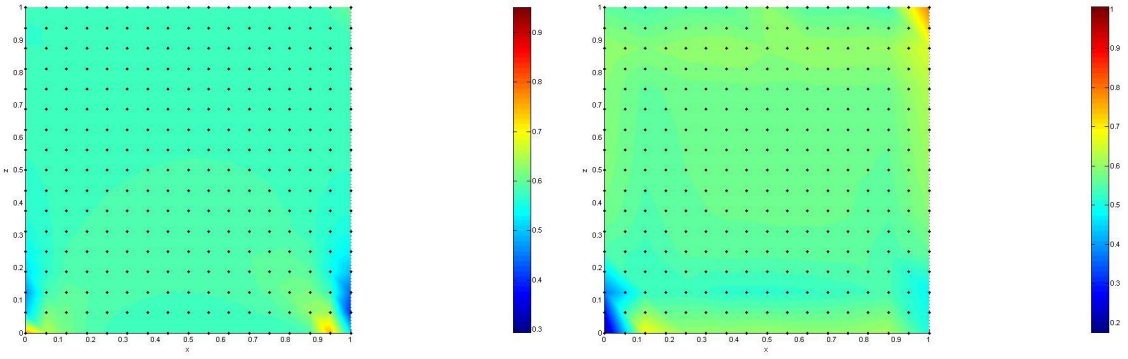

(a) FEM 2D-T3

(b) FEM 2D-T6

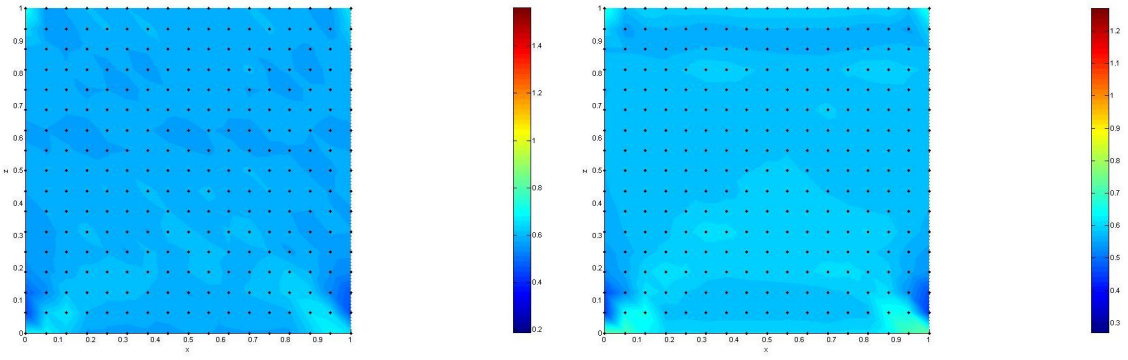

(c) RPIM

(d) NNRPIM

Figure 5.13: 3D Cube Confined Compression - Von Mises Stress Field (Axis Units:0.1 m)

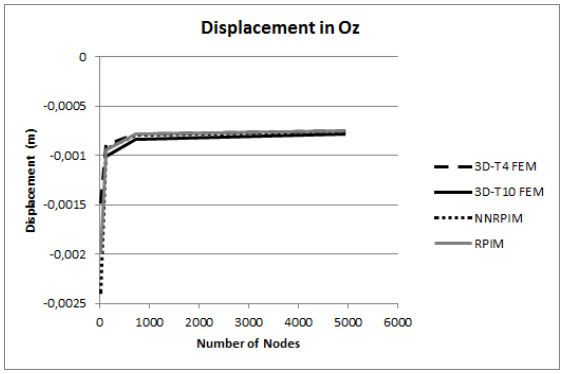

(a) Displacement in Oz

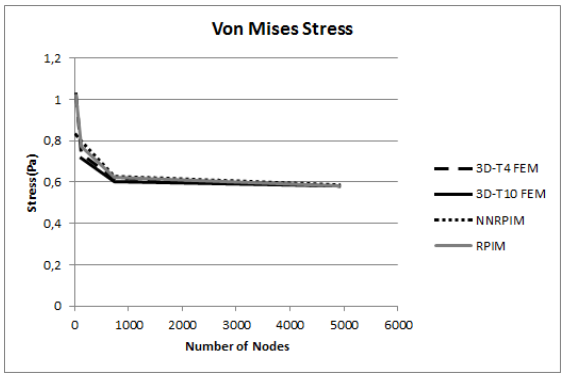

(b) Von Mises Stress

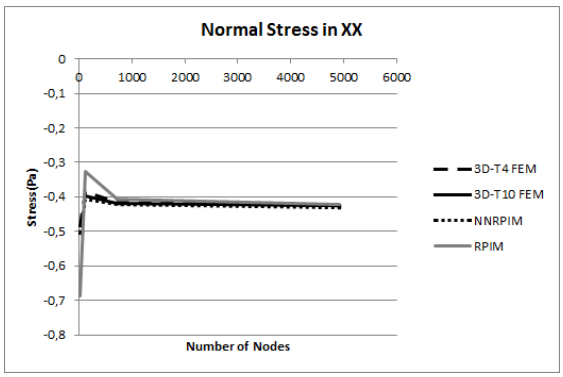

(c) Normal Stress in XX (σ_{xx})

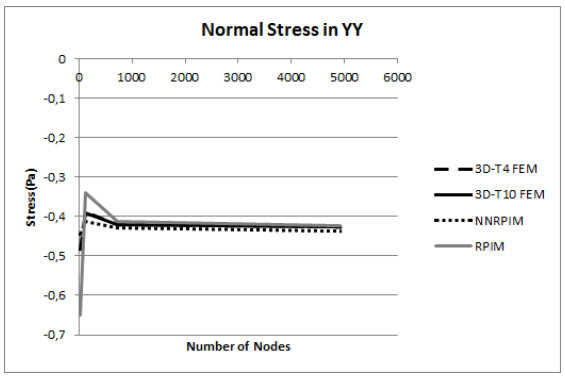

(d) Normal Stress in YY (σ_{yy})

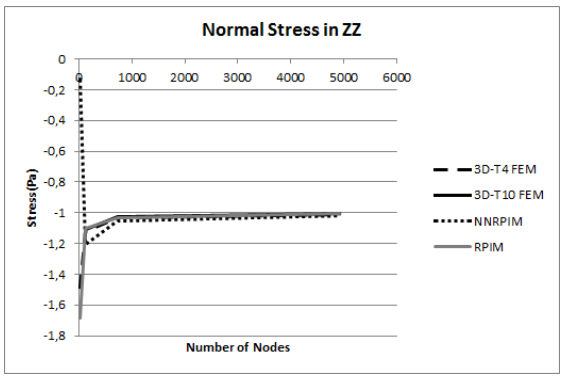

(e) Normal Stress in ZZ (σ_{zz})

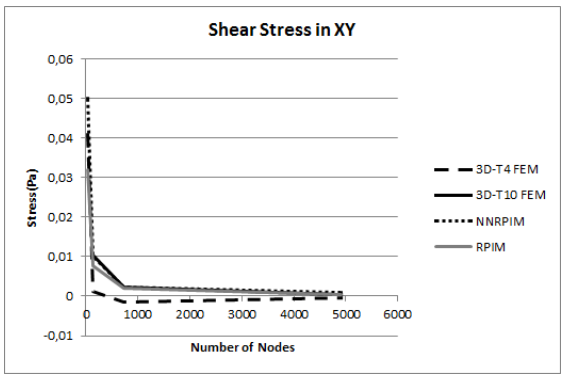

(f) Shear Stress in XY (τ_{xy})

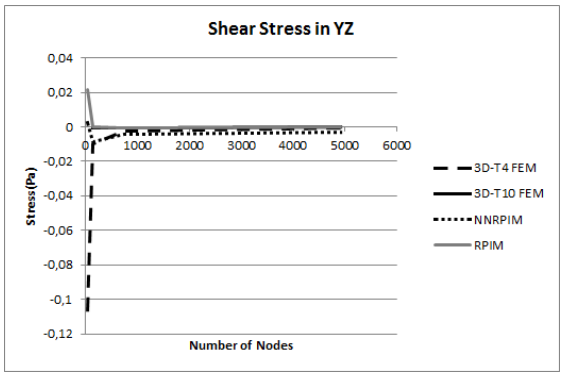

(g) Shear Stress in YZ (τ_{yz})

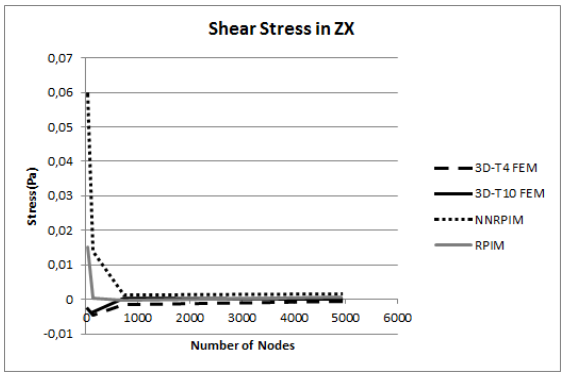

(h) Shear Stress in ZX (τ_{zx})

Figure 5.14: 3D Cube Confined Compression Displacement and Stresses

5.2.5 2D Square - Shear Force

For this example it was considered a solid domain $\omega \in \Re^2$ with a form of a square of side 1 meter. To this solid domain it was applied the following constrains: $u, v = 0 : \forall x \in \Re^2 \wedge y = 0$ with $\mathbf{u} = (u, v)$. It was also applied an uniform force of 1 N at $\forall x \in \Re^2 \wedge y = 1$ with the direction (x,y)= (1,0). A representation of this setting can be seen in Figure 5.15.

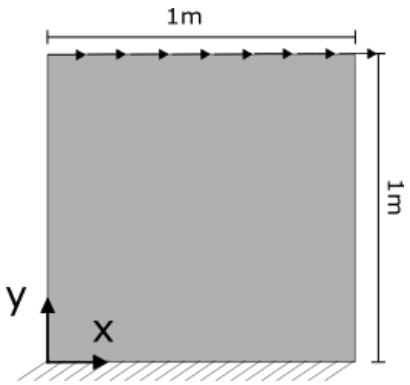

Figure 5.15: Square Plate under an uniform shear force

In this problem it was analysed the displacement in Ox, the Von Mises Stress and τ_{xy}. In Figure 5.16 it is possible to see how each of this variables change as it discretization of the problem increases. On those graphs, the value for the displacement in Ox was obtain at (x,y)=(0.5, 1) and all the stresses were obtained from (x,y)=(0.5, 0.5).

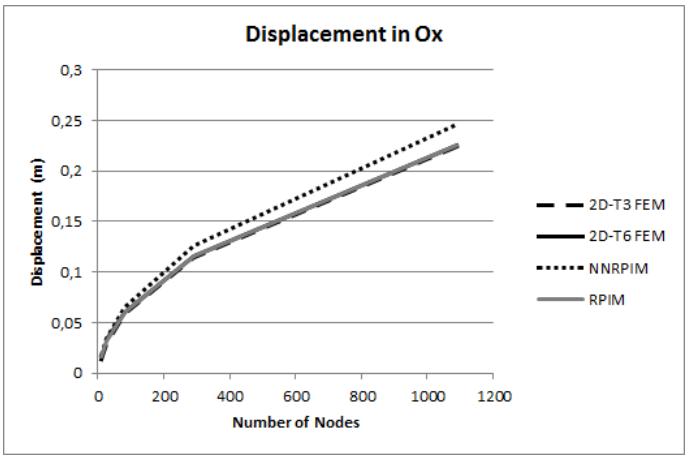

(a) Displacement in Ox

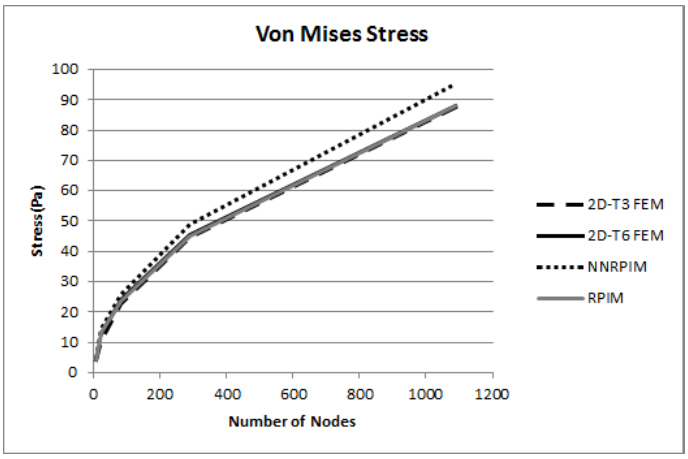

(b) Von Mises Stress

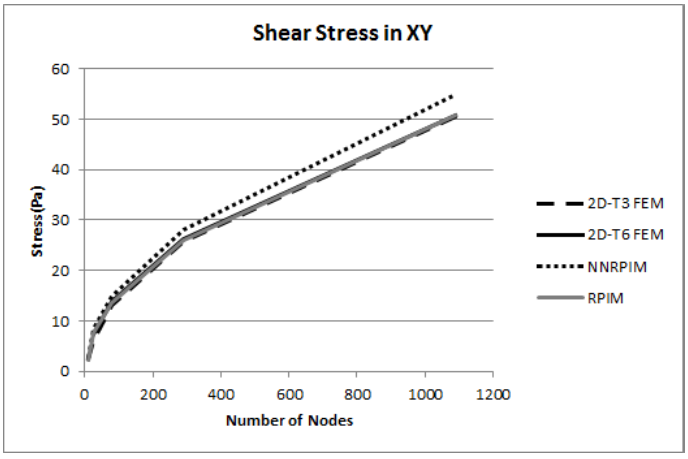

(c) Shear Stress in XY (τ_{xy})

Figure 5.16: 2D Square with Shear Force - Displacement and Stresses

As in the previous 2D examples, the results clearly show that all the numerical methods follow the same tendency in all of the analysed variables as the discretization of the problem increases. while the results have not still converged in a value until this point, it is possible to see similar

results and progressions in these variables. These similarities between all the numerical methods can also be seen in the distribution of Von Mises Stress Field, as seen in Figure 5.17. The Von Mises Stress Fields shown are the ones obtained with the highest level of discretization.

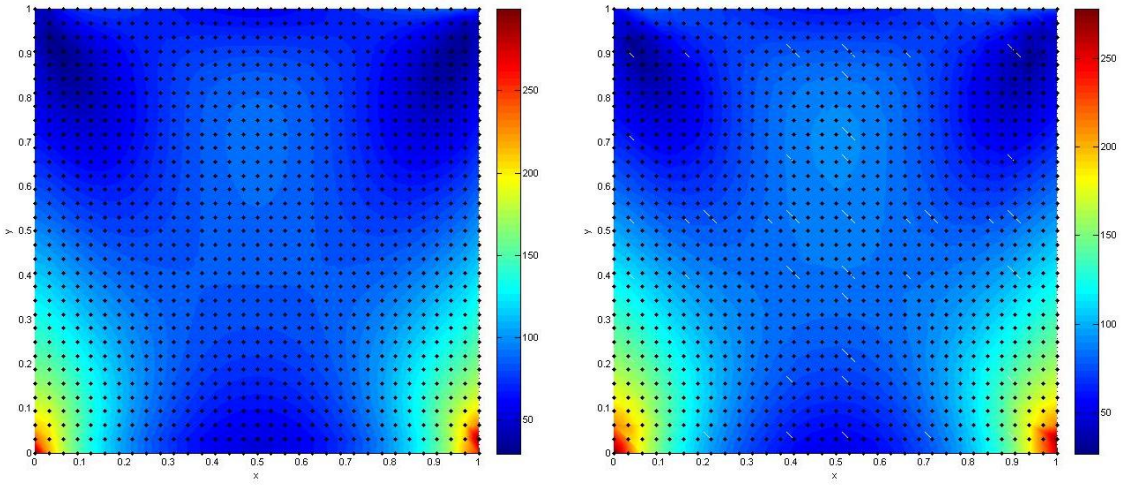

(a) FEM 2D-T3

(b) FEM 2D-T6

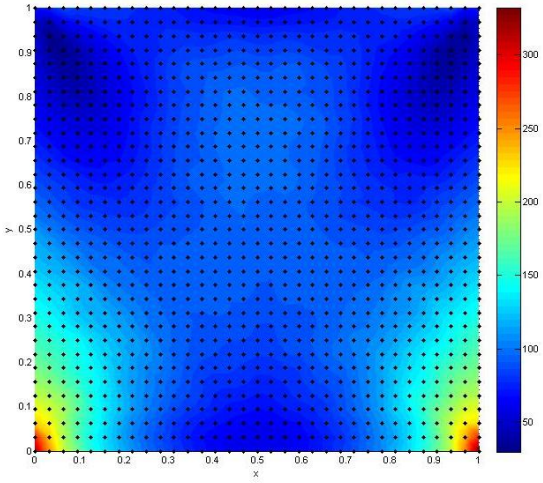

(c) RPIM

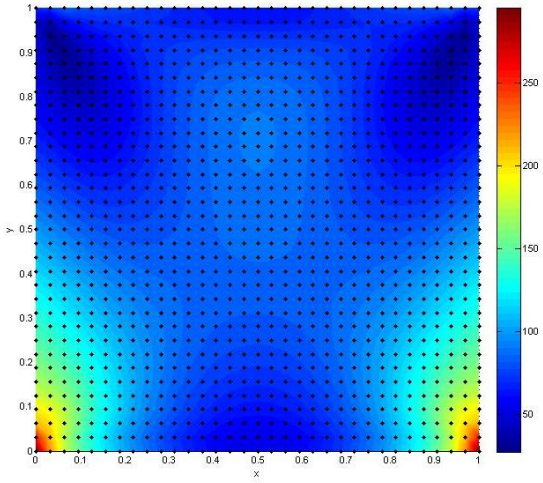

(d) NNRPIM

Figure 5.17: 2D Square with Shear Force - Von Mises Stress Field (Axis Units: 0.1 m)

5.2.6 3D Cube -Shear Force

For this example it was taken into consideration a solid domain $\omega \in \Re^3$ with a shape of cube with size = 1m. This solid, similarly to the previous example, had the following constrains: $u,v,w = 0 : \forall x,y \in \Re^3 \wedge z = 0$ with $\mathbf{u} = (u,v,w)$. It was applied to this solid a uniform force of 1 N at $\forall x,y \in \Re^3 \wedge z = 1$ with the direction (x,y,z)= (0,0,1).

In this problem it was analysed the displacement in X, the Von Mises Stress, σ_{xx}, σ_{yy}, σ_{zz}, τ_{xy}, τ_{yz} and τ_{zx} . In Figure 5.19 it is possible to see how each of this variables change as it discretization of the problem increases. On those graphs, the value for the displacement in Z was obtain from the central point at (x,y,z)=(0.5, 0.5 ,1) and all the stresses were obtained from the central point of the squared plate (x,y,z)=(0.5, 0.5 ,1).

Looking at the results we can clearly see that all the numerical methods follow the same tendency in all the variables analysed as the discretization of the problem increases. It is also possible to see that almost all the results have all the numerical methods converged being, in most of the variables analysed, this convergence seen at around 1000 nodes. In the case of the FEM analysis with 4 nodes elements (3D-T4), we can see that it does not converge as quickly as the FEM analysis with 10 nodes elements or the meshless methods. This convergence between all the numerical methods can also be seen in the similarities between the distribution of Von Mises Stress Field, as seen in Figure 5.18. In this figure it is possible to see the distribution of Von Mises Stress Field in the simulation with the higher discretization at a cross section of the cube, at the plane y=0.5.

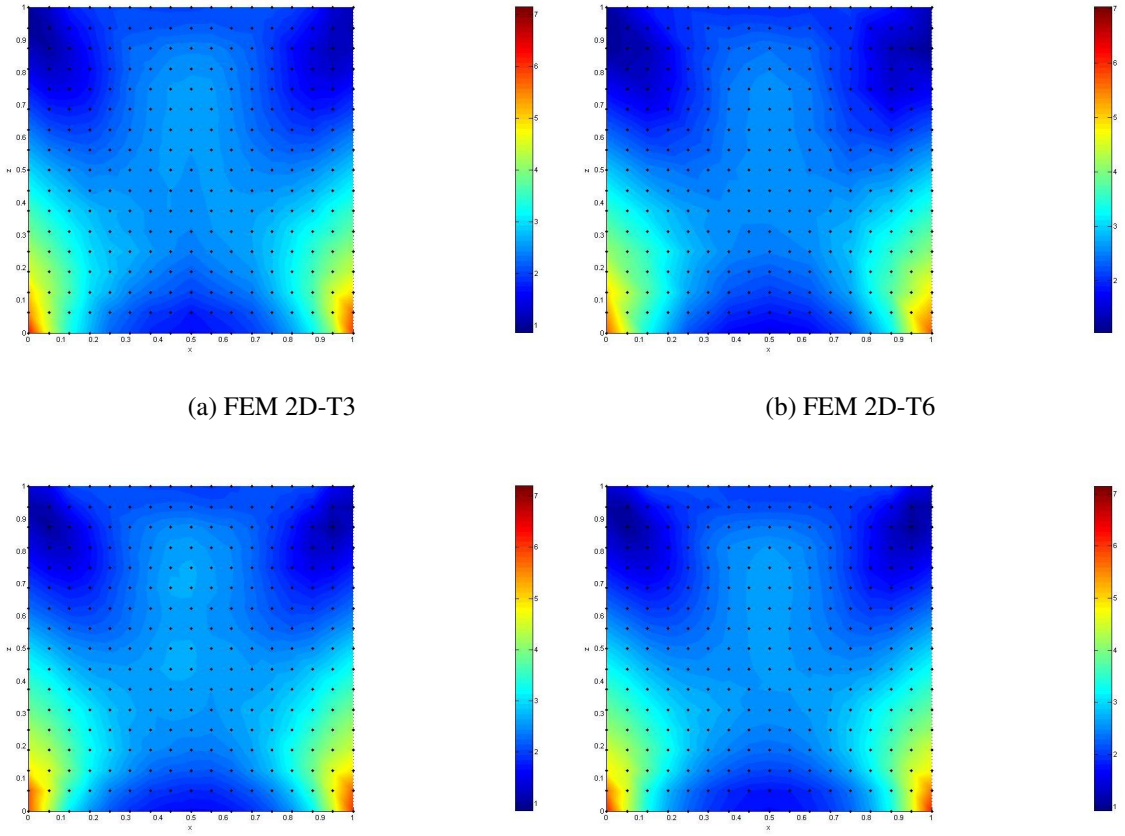

(a) FEM 2D-T3

(b) FEM 2D-T6

(c) RPIM

(d) NNRPIM

Figure 5.18: 3D Cube with Shear Force - Von Mises Stress Field (Axis Units: 0.1 m)

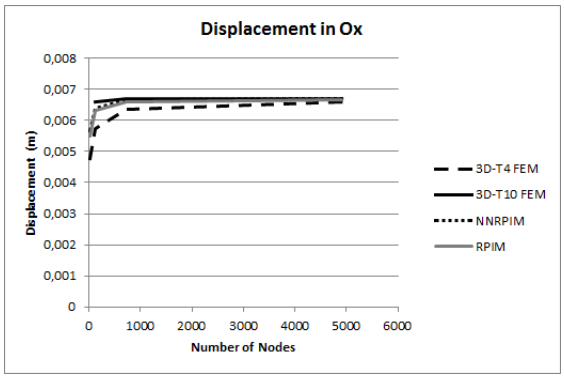

(a) Displacement in Ox

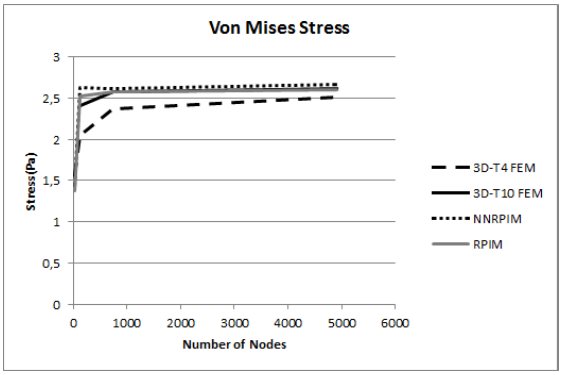

(b) Von Mises Stress

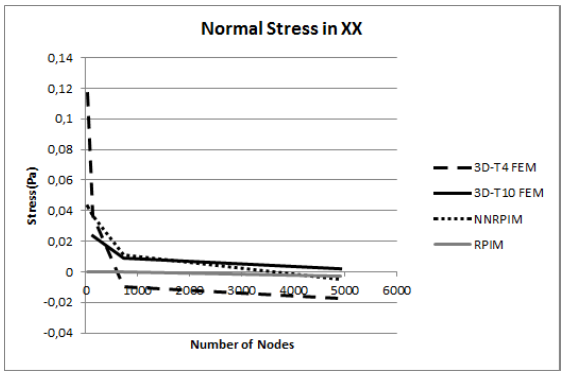

(c) Normal Stress in XX (σ_{xx})

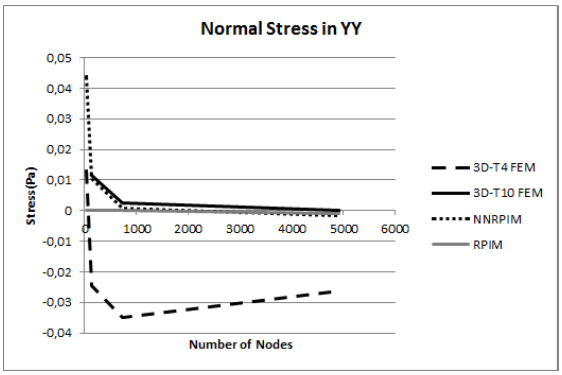

(d) Normal Stress in YY (σ_{yy})

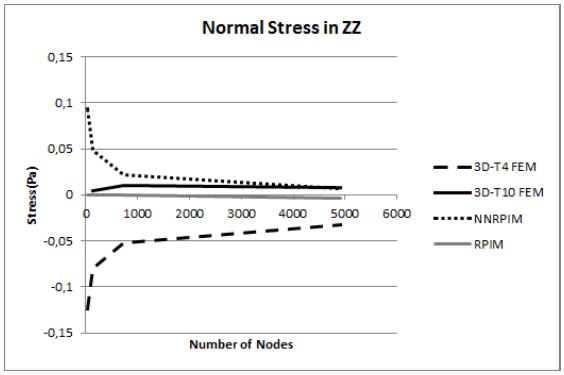

(e) Normal Stress in ZZ (σ_{zz})

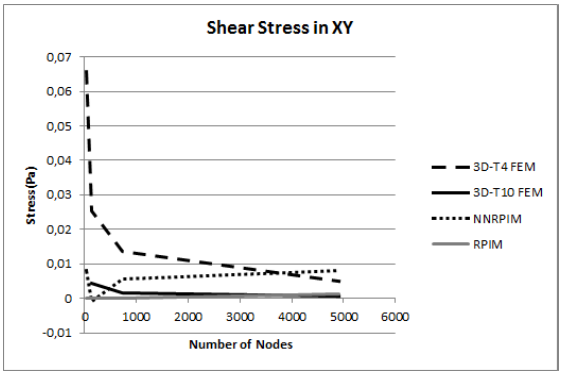

(f) Shear Stress in XY (τ_{xy})

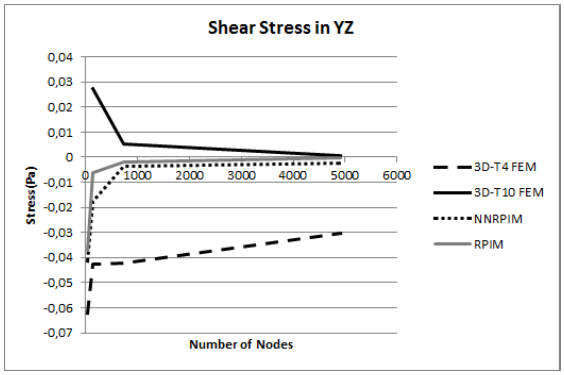

(g) Shear Stress in YZ (τ_{yz})

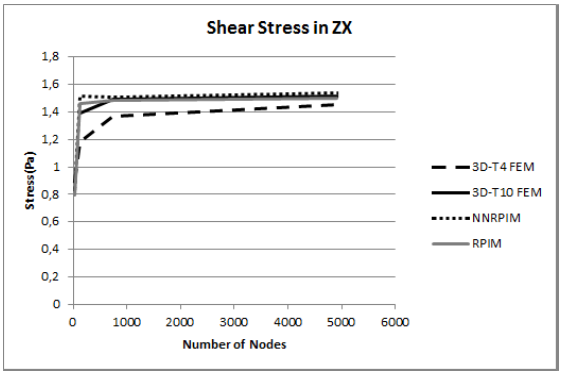

(h) Shear Stress in ZX (τ_{zy})

Figure 5.19: 3D Cube with Shear Force - Displacement and Stresses

5.2.7 Conclusions

With the analysis of all the examples shown before it is concluded that the meshless methods analysed present very similar results to FEM. The 2D Convergence study did not reach the nodal discretization necessary for the studied variables to converge, yet the study could not be taken further as number of nodes in the following mesh would not be supported by the used hardware. In the following 2D examples it was either used the highest discretization square mesh studied, in analysis were it was used a square domain, or used the highest number of nodes supported by the hardware, in the analysis made with different meshes. As for the 3D Convergence study the analysed variables reached convergence with a discretization level of around one thousand nodes.

5.3 Elasto-Plastic Simulation of Atherosclerotic Plaque Material

Before it was possible to simulate an artery containing atherosclerotic plaque, first it was required to test the accuracy of the simulation for this tissue. This study was analysed as a 2D problem under two different settings: compression and confined compression, similarly to the convergence study. The results obtained with the numerical methods were compared between them and also with the theoretical bi-linear approximation. Similarly to the convergence study two different FEM analysis were made, one with triangular elements with 3 nodes (2D-T3) and one with triangular elements with 6 nodes (2D-T6). The mesh used was a squared regular mesh with 1089 nodes, as it was the level of discretization that showed the best results in the convergence study. The parameters used for the RPIM and NNRPIM analysis were the same as for the previous study (Table 5.1 and Table 5.2).

For each of the two configurations it was made one example using each of the three material properties for the atherosclerotic plaque defined for this work: Lightly Calcified, Medially Calcified or Highly Calcified. The values were calculated in Chapter 2 and can be seen in Table 5.3, with a representation of the bi-linear approximation in Figure 5.20.

Table 5.3: Mechanical Properties of the Atherosclerotic Plaque

	Lightly Calcified	Medially Calcified	Highly Calcified
E(MPa)	0.9167	1.0625	3.1429
Et (MPa)	0.1371	0.1833	0.0800
σ_y (MPa)	0.055	0.085	0.110
ν	0.421	0.412	0.408

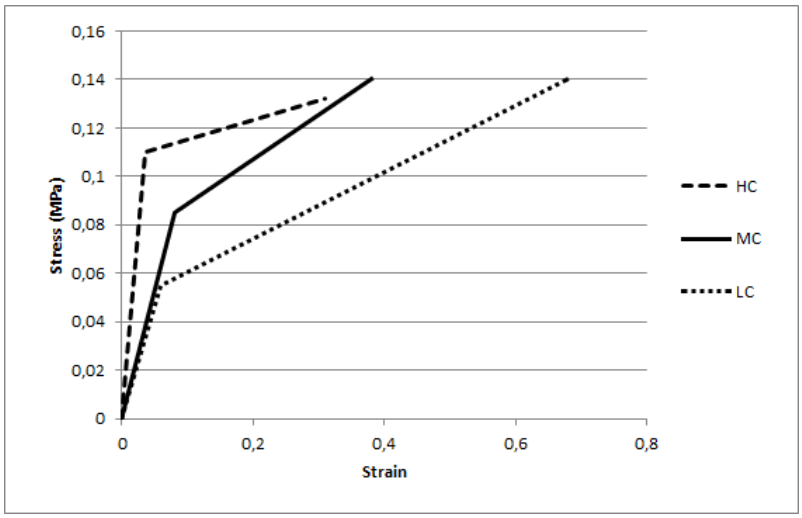

Figure 5.20: Theoretical Bi-linear Aproximation of Atherosclerotic Plaque Elasto-Plastic Behaviour

5.3.1 2D Compression

For this simulation it was taken into consideration a solid domain $\omega \in \Re^2$ with a shape of cube with side equal to 1m. This solid had the following constrains: $u, v = 0 : \forall x, y \in \Re^2 \wedge y = 0$ with $u = (u, v)$. This solid was compressed at $\forall x, y \in \Re^3 \wedge z = 1$ with the direction (x,y)= (0,1).

After the non-linear analysis was made, in each of the algorithm increments it was analysed the Von Mises Stress and the Effective Strain on the point (x,y)=(0.5,0.5).

5.3.1.1 Lightly Calcified

In Figure 5.21 it can be seen the stress-strain lines obtained from the each of the numerical methods and also the bi-linear approximation.

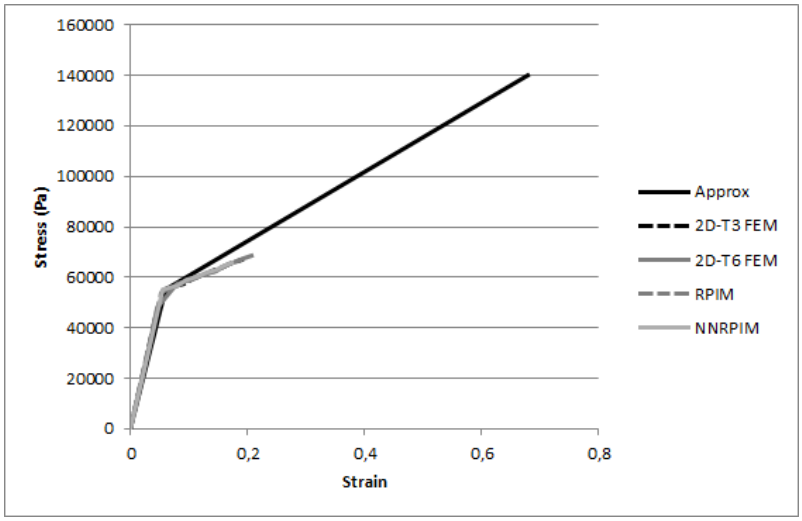

Figure 5.21: Elasto-Plastic Simulation Results - Compression - Lightly Calcified

As it can be seen, there is a very good overlaying between all of the results obtained from the numerical simulations, being it difficult to distinguish some of the numerical methods. When comparing these results with the bi-linear approximation it is seen a very good accuracy of the results in the elastic segment, while the numerical methods appear to start to sway away from the approximation on the plastic segment.

5.3.1.2 Medially Calcified

In Figure 5.22 it can be seen the stress-strain lines obtained from the each of the numerical methods and also the bi-linear approximation.

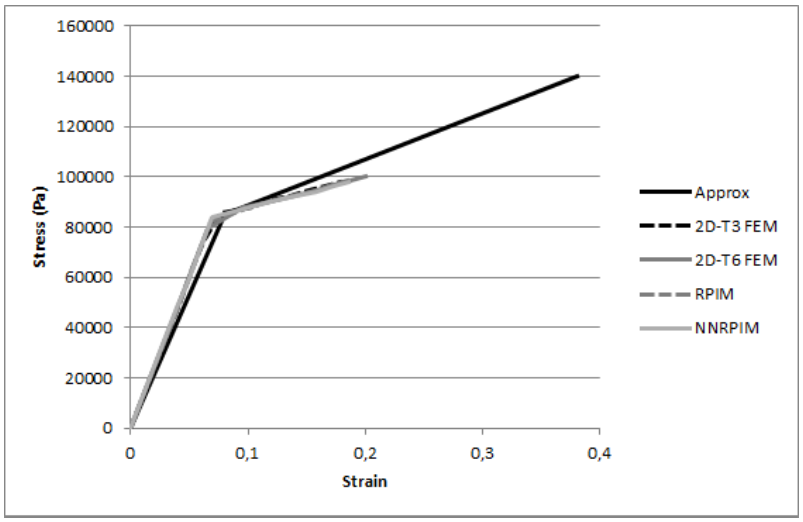

Figure 5.22: Elasto-Plastic Simulation Results - Compression - Medially Calcified

There is a very good overlaying between all of the results obtained from the numerical simulations, being it difficult to distinguish some of the numerical methods. When comparing these results with the bi-linear approximation it appears to be a small deviation of the results in the elastic segment and, as seen in the lightly calcified compression simulation, the numerical methods results appear sway away from the approximation on the plastic segment.

5.3.1.3 Highly Calcified

In Figure 5.23 it can be seen the stress-strain lines obtained from the each of the numerical methods and also the bi-linear approximation.

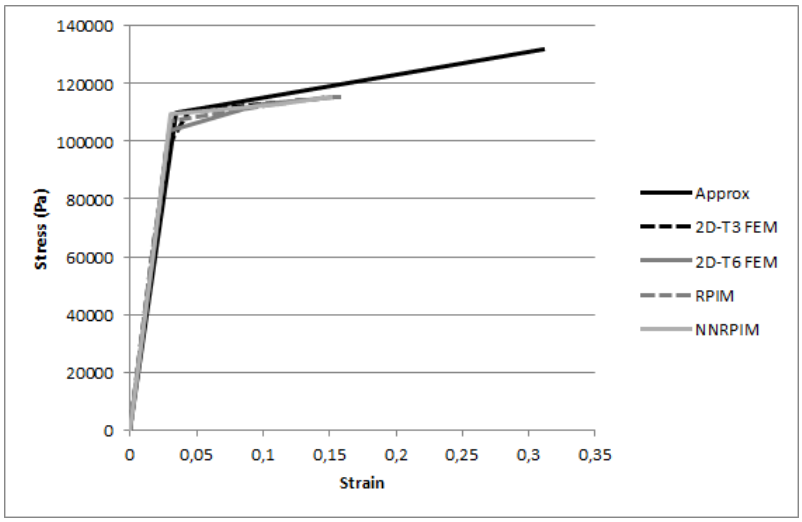

Figure 5.23: Elasto-Plastic Simulation Results - Compression - Highly Calcified

As the figure shows, there is a very good overlaying between all of the results obtained from the numerical simulations, being it difficult to distinguish some of the numerical methods. When comparing these results with the bi-linear approximation it appears to be a good overlay of the results in the elastic segment and, as seen in the previous examples, the numerical methods results appear to deviate lightly from the approximation on the plastic segment.

5.3.2 2D Confined Compression

For this simulation it was taken into consideration a solid domain $\omega \in \Re^2$ with a shape of cube with side equal to 1m. This solid had the following constrains: $u = 0 : \forall x \in \Re^2 \wedge y = 0$ and $v = 0 : \forall x \in \Re^2 \wedge (y = 0 \vee y = 1)$ with $\mathbf{u} = (u, v)$. This solid was compressed at $\forall x, y \in \Re^3 \wedge z = 1$ with the direction (x,y)= (0,1).

After the non-linear analysis was made, in each of the algorithm increments it was analysed the Von Mises Stress and the Effective Strain on the point (x,y)=(0.5,0.5).

5.3.2.1 Lightly Calcified

In Figure 5.24 it can be seen the stress-strain lines obtained from the each of the numerical methods and also the bi-linear approximation.

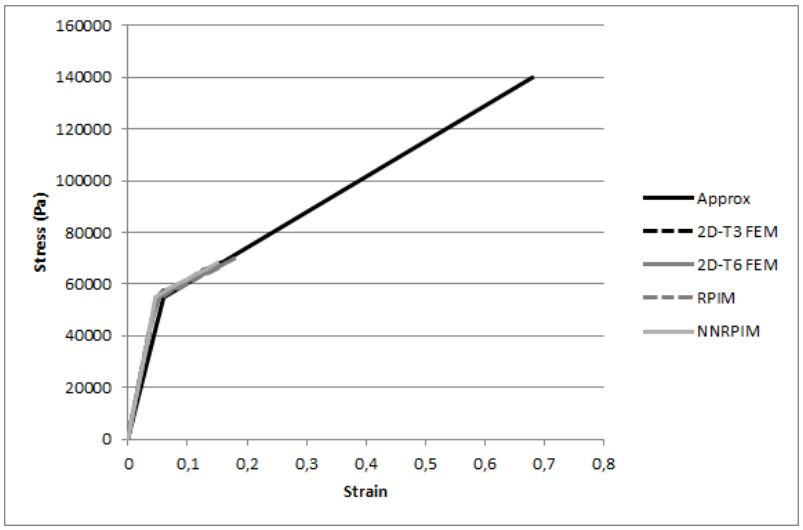

Figure 5.24: Elasto-Plastic Simulation Results - Confined Compression - Lightly Calcified

The results show a very good overlaying between all the numerical methods, being it difficult to distinguish some of the them. When comparing these results with the bi-linear approximation it is seen a very good accuracy of the results in both the plastic segment and elastic segment.

5.3.2.2 Medially Calcified

In Figure 5.25 it can be seen the stress-strain lines obtained from the each of the numerical methods and also the bi-linear approximation.

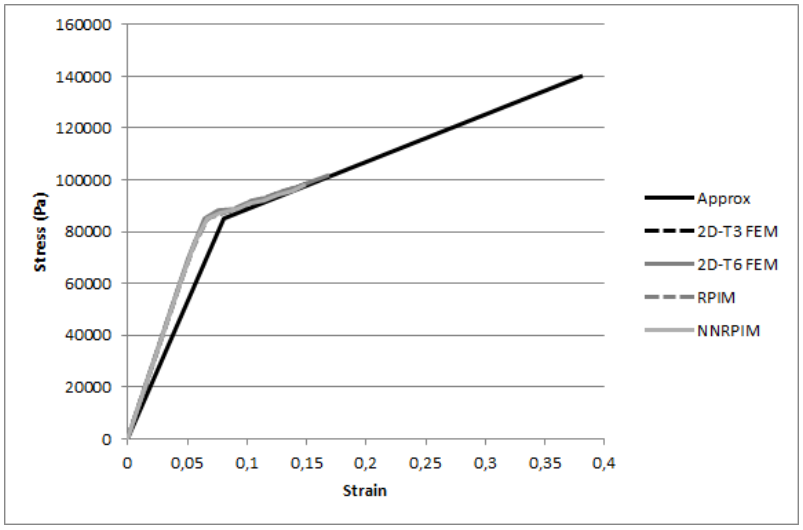

Figure 5.25: Elasto-Plastic Simulation Results - Confined Compression - Medially Calcified

As in the previous analysis, there is a very good overlaying between all of the results obtained from the numerical simulations, being it difficult to distinguish some of the numerical methods. In terms of the overlay of the numerical methods results with the bi-linear approximation, it is seen

a very good accuracy of the results in the plastic segment, while they have small deviation away from the approximation on the elastic segment.

5.3.2.3 Highly Calcified

In Figure 5.26 it can be seen the stress-strain lines obtained from the each of the numerical methods and also the bi-linear approximation.

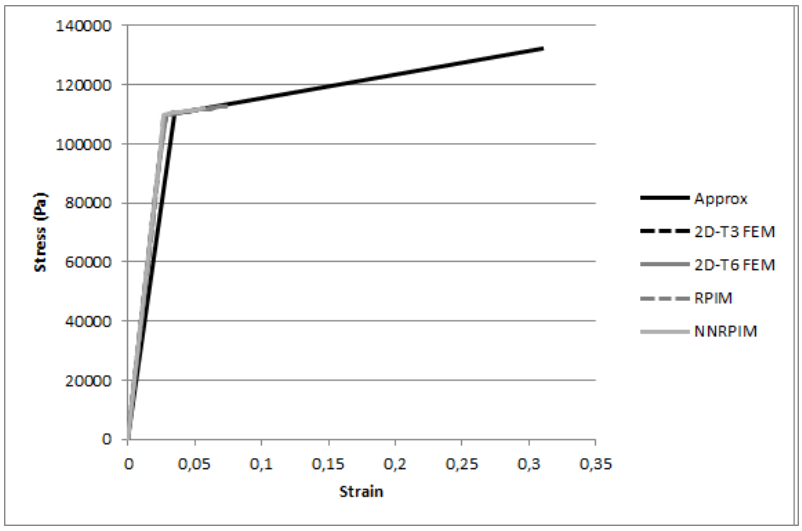

Figure 5.26: Elasto-Plastic Simulation Results - Confined Compression - Highly Calcified

As it has been shown in previous examples, there is a very good overlaying between all of the results obtained from the numerical simulations, being it difficult to distinguish the numerical methods. In terms of the overlay of the numerical methods results with the bi-linear approximation, it is seen a very good accuracy of the results in the plastic segment, while they have small deviation away from the approximation on the plastic segment.

5.3.3 Conclusions

When analysing all the data from all this examples it can be said that all the numerical methods were consistent, showing a very good overlay between them in all the simulations. In terms of the two different constrains that were tested, while in there is a good overlay in all the examples, the confined compression constrains, given the small deviation on the elastic part and good adjustment on the plastic segment, appear to have the better results and so provide a better approximation of the experimental data.

Chapter 6

Atherosclerotic Plaque Analysis

The Atherosclerotic plaque is a tissue created from the deposition of organic substances on arteries and from the immune response those substances generate. It is a tissue with mechanical properties distinct from the artery and that, as a result of the disease's progression, stiffens the arterial walls and provokes stenosis. The current chapter will address the formulation of the problem at hand and how it was formulated. Afterwards it will continue with the analysis of several 2D models showing different stages of the disease and finish with its comparison with results obtained from two different 3D models.

6.1 Problem Description

In this analysis it is going to be taken into account several models of arteries depicting different stages of the disease. Theses models, besides the atherosclerotic plaque, will contain the three characteristic layers of the artery (*adventitia*, *media* and *intima*) and also areas of damaged *media*, damaged *intima* and *intima* fibrous cap. The damaged *intima* and damaged *media* tissues will be located in the area between the *adventitia* and the atherosclerotic plaque. As for the *intima* fibrous cap, this will be the tissue that will stay between the atherosclerotic plaque and the lumen. In Figure 6.1, it can be seen a graphical representation of a typical artery with atherosclerosis base in the literature [65].

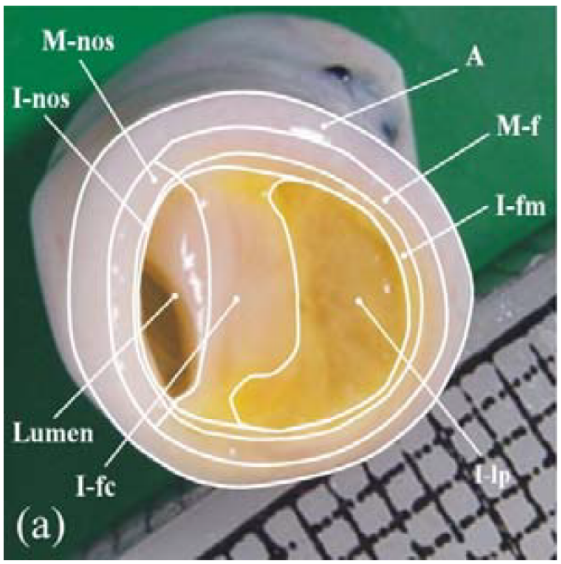

(a) Atherosclerotic Artery [65]

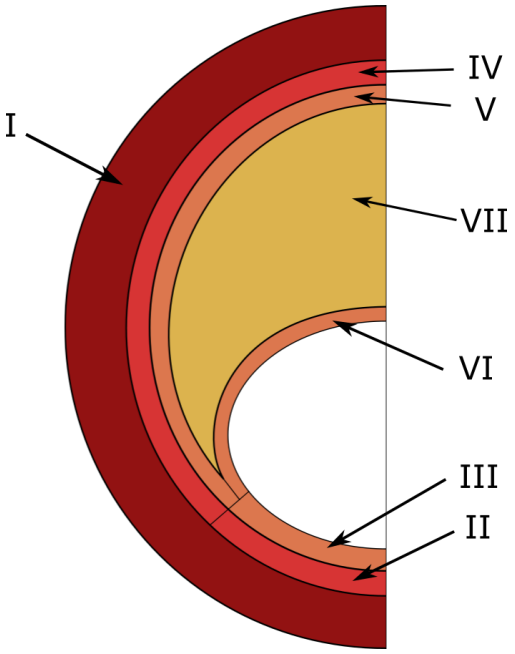

(b) Schematic representation of an Atherosclerotic Artery. I- *Adventitia*; II- *Media*; III- *Intima*; IV- Damaged *Media*; V- Damaged *Intima*; VI- *Intima* Fibrous Cap; VII- Atherosclerotic Plaque

Figure 6.1: Atherosclerotic Artery Examples

As for the artery's dimension, since all the atherosclerotic plaque mechanical data was from femoral arteries, its diameter was taken as 9mm [87]. In terms of the thickness of the layers of the arterial wall, as it revealed to be difficult to find values from femoral arteries, this values were also based in information from carotid arteries and thickness relations between layers [88, 89]. The *adventitia* was defined as having the same thickness as the complex *intima-media* (0.75 mm) and the *media* and *intima* as having the same thickness (0.375 mm). While in reality the *intima* is much thinner than the *media*, it was define in this way as a simplification in order to reduce problems that could happen with its discretization.

In the literature it can be seen that the atherosclerotic plaque can present different configurations, having just some speckled calcifications or a larger diffuse tissue [90], and so four different configurations were tested in the 2D elasto-plastic analysis. A first model with a thin segmented plaque, a second model with a continuous thin plaque and a third and fourth models showing increasing levels of stenosis. A diagram of all these models can be seen in Figure 6.2.

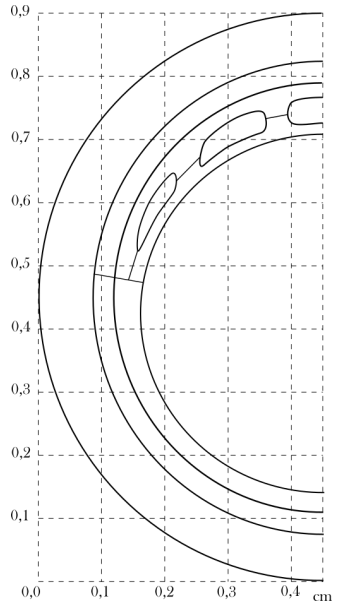

(a) 2D Model I - Segmented Plaque)

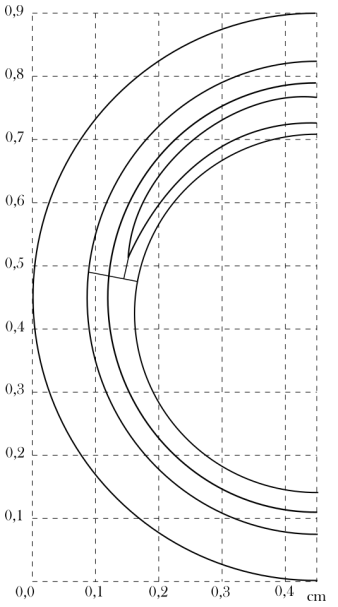

(b) 2D Model II - Thin Plaque

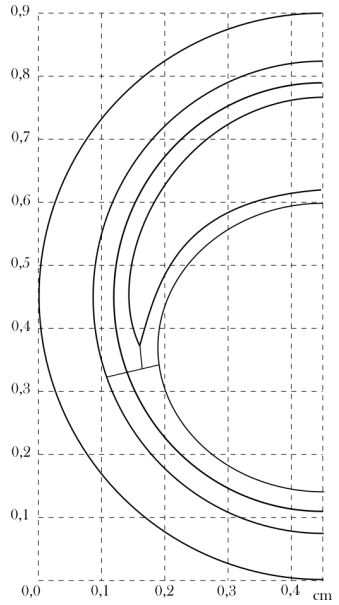

(c) 2D Model III - Medium Thickness Plaque

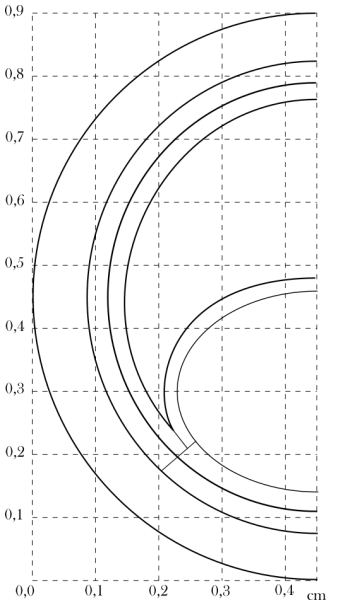

(d) 2D Model IV - High Thickness Plaque

Figure 6.2: Diagrams of the 2D atherosclerotic arteries models

The models created only represent half of an artery, being applied to them symmetry conditions at x=4.5. In all the 2D numerical simulations, besides the symmetry constrains, the point (x,y)=(4.5,0) was also fixed and an uniform static force was applied into the lumen of the artery.

For the 3D Elasto-plastic analysis there were created two different models representing a continuous atherosclerotic plaque with two different levels of stenosis, one third and two thirds. To created these models a profile of the arteries was created and revolved ninety degrees, being it afterwards tested under symmetry conditions. The profile of the two models can be seen in Figure

6.3.

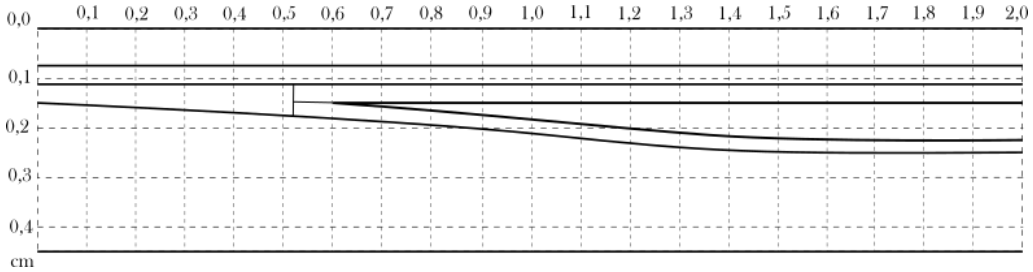

(a) 3D Model I - 1/3 Stenosis)

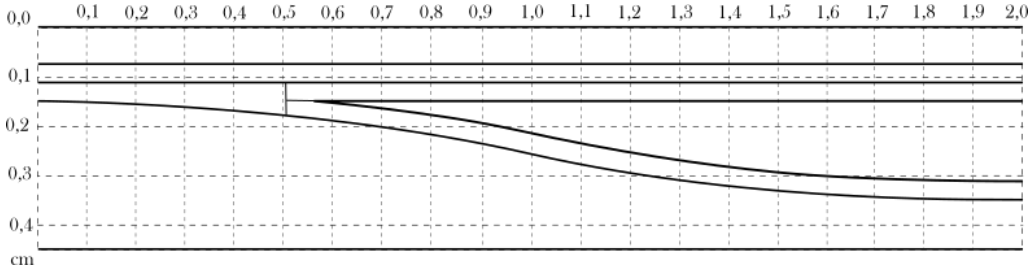

(b) 3D Model II - 2/3 Stenosis

Figure 6.3: Diagrams of profile for the 3D atherosclerotic arteries models - Ozx view

All models were analysed using the RPIM, the NNRPIM, the FEM with triangular elements of 3 nodes for the 2D models and the FEM with tetrahedral elements of 4 nodes for the 3D models. Besides this, all the models were also analysed with each of the atherosclerotic plaque mechanical properties referenced before. The mechanical properties of the tissues present in these analysis are defined as stated in Chapter 2.

6.2 2D Elasto-Plastic Analysis

6.2.1 2D Model I

For this example it was taken into consideration a solid domain $\omega \in \Re^2$ representing a atherosclerotic artery containing a thin segmented plaque. It was applied to the domain symmetry constrains and fixed the node (x,y)=(4.5,0). The numerical model was designed using 3908 nodes and was analysed using three different numerical methods (FEM, RPIM and NNRPIM). An image of the nodal distribution used can be seen in Figure 6.4

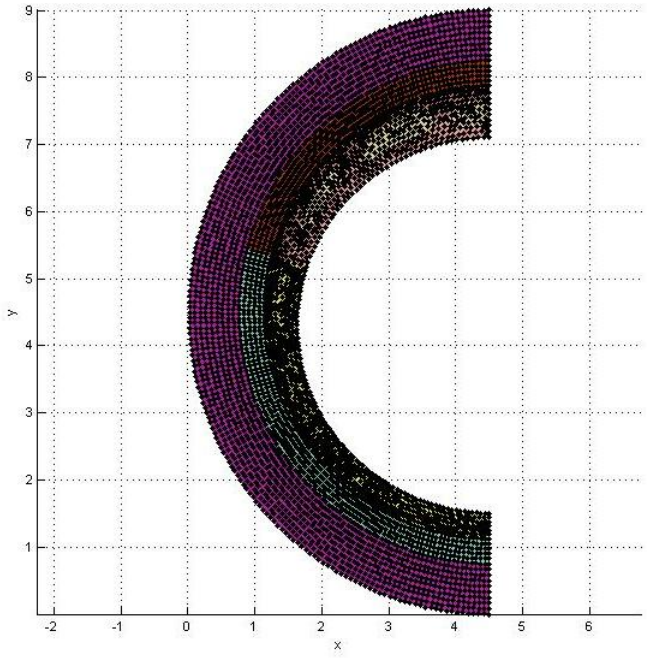

Figure 6.4: 2D Model of Artery with Atherosclerotic Plaque - Stage I (Axis Units: 1 mm)

The von Mises Stress field and Effective Plastic Strain Field were analysed for each of the atherosclerotic plaque set of material properties. Besides this, it was also analysed the displacement in Oy in specific interface nodes between tissues. The location of these nodes can be seen in the diagram of Figure 6.22. The displacement seen was analysed against the pressure applied in the artery's lumen.

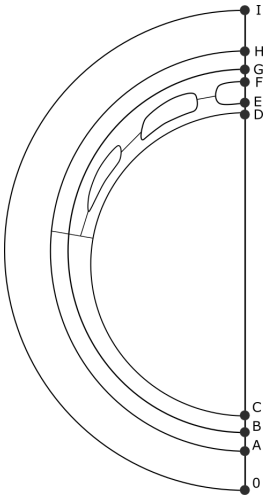

Figure 6.5: 2D Model Stage I - Points location

6.2.1.1 Lightly Calcified

The following plots represent the relation between the internal luminal pressure and the displacement seen in points C, D, E and F.

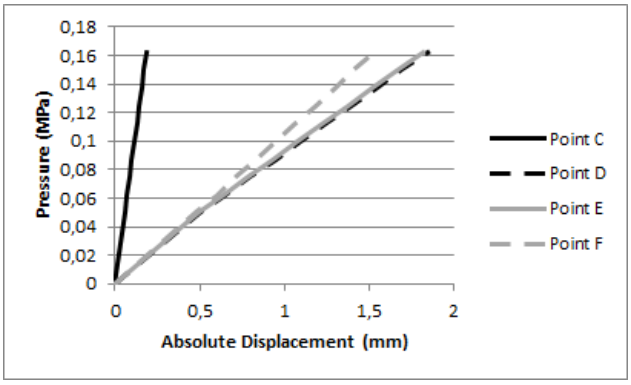

(a) Displacement obtained using FEM

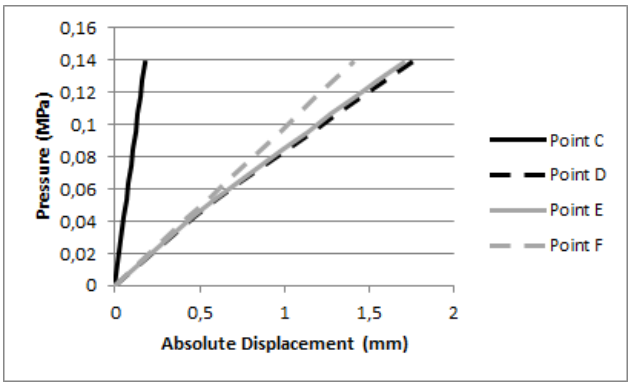

(b) Displacement obtained using RPIM

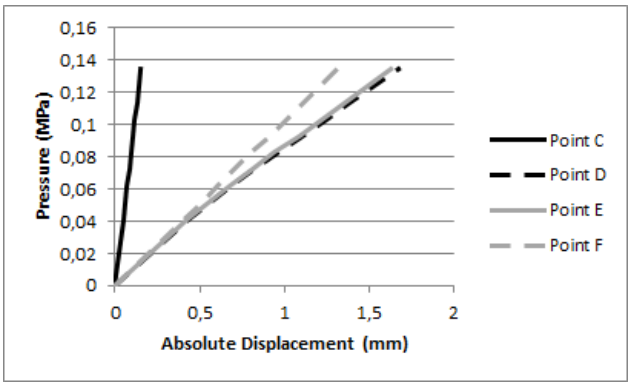

(c) Displacement obtained using NNRPIM

Figure 6.6: 2D Model I - Lightly Calcified - Displacement in Oy vs. Luminal Pressure

The following von Mises Stress Fields and Effective Plastic Strain Fields were also obtained. It can be seen 3 different stages of the plastic deformation progression starting when the Yield Pressure was met.

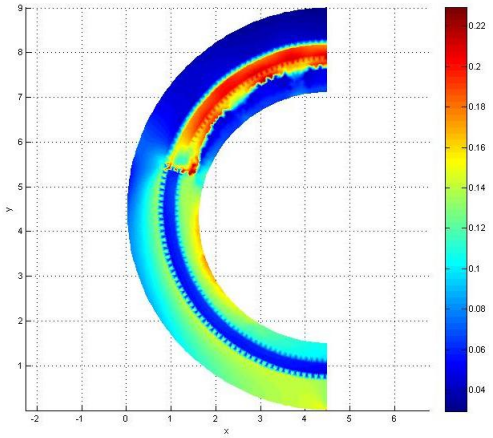

(a) von Mises Tension - Luminal Pressure = 0.05 MPa (color bar up to 0.22 MPa)

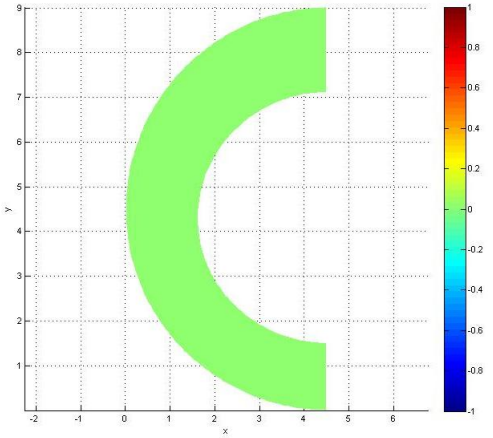

(b) Effective Plastic Strain - Luminal Pressure = 0.05 MPa (no significant values)

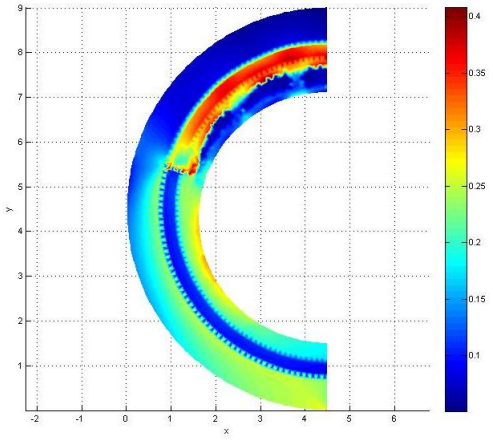

(c) von Mises Tension - Luminal Pressure = 0.09 MPa (color bar up to 0.4 MPa)

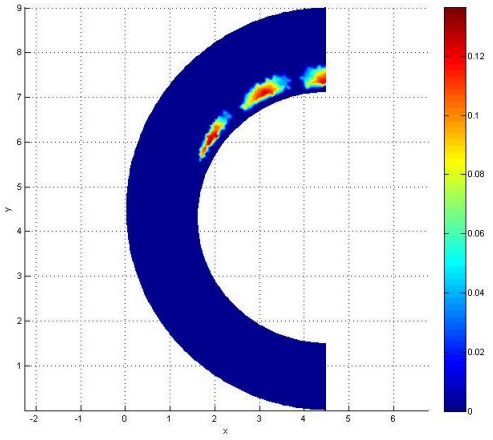

(d) Effective Plastic Strain - Luminal Pressure = 0.09 MPa (color bar up to 0.12)

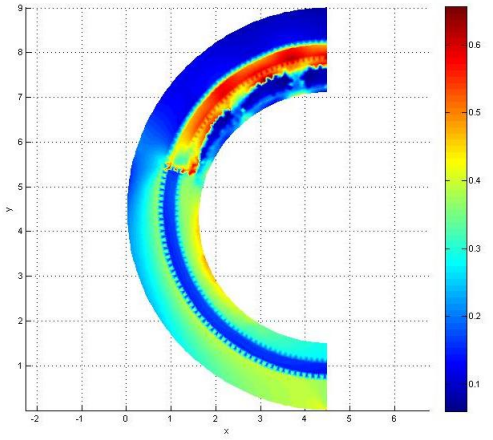

(e) von Mises Tension - Luminal Pressure = 0.135 MPa (color bar up to 0.6 MPa)

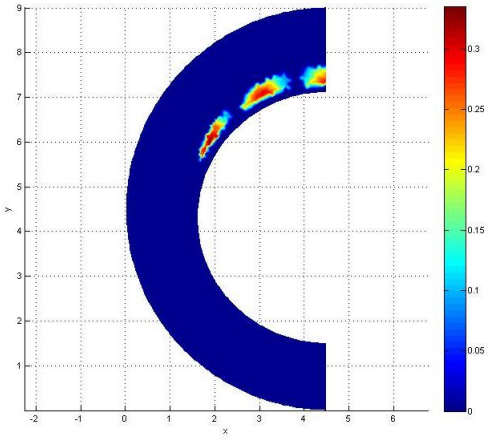

(f) Effective Plastic Strain - Luminal Pressure = 0.135 MPa (color bar up to 0.3)

Figure 6.7: 2D Artery Model I - Lightly Calcified Atherosclerotic Plaque - FEM (Axis Units: 1 mm)

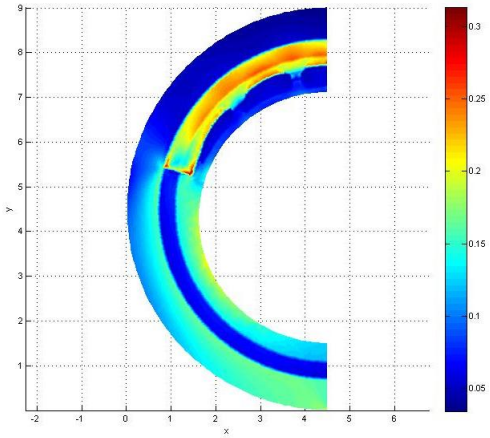

(a) von Mises Tension - Luminal Pressure = 0.05 MPa (color bar up to 0.3 MPa)

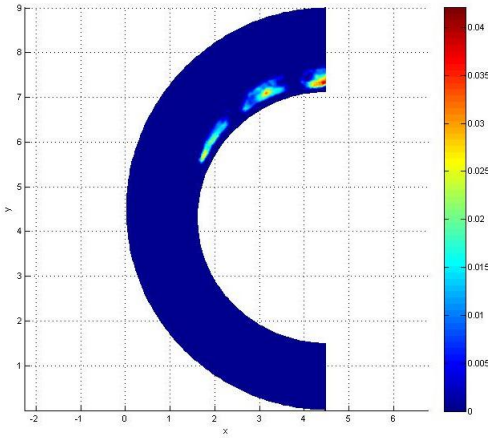

(b) Effective Plastic Strain - Luminal Pressure = 0.05 MPa (color bar up to 0.04)

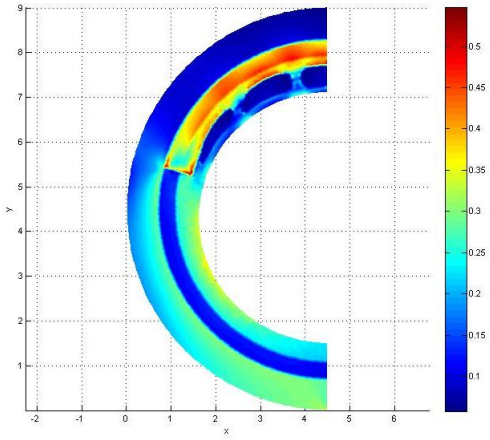

(c) von Mises Tension - Luminal Pressure = 0.09 MPa (color bar up to 0.5 MPa)

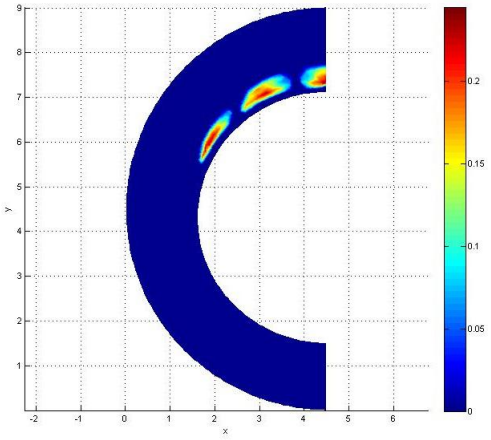

(d) Effective Plastic Strain - Luminal Pressure = 0.09 MPa (color bar up to 0.2)

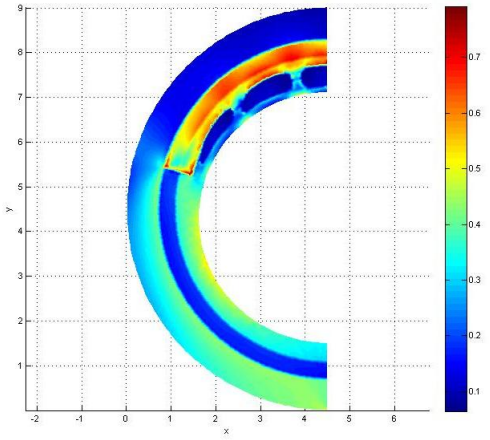

(e) von Mises Tension - Luminal Pressure = 0.135 MPa (color bar up to 0.7 MPa)

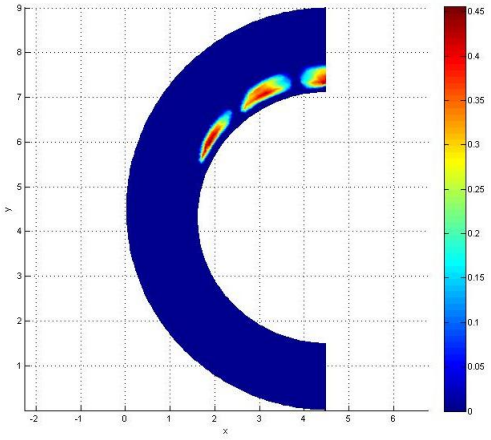

(f) Effective Plastic Strain - Luminal Pressure = 0.135 MPa (color bar up to 0.45)

Figure 6.8: 2D Artery Model I - Lightly Calcified Atherosclerotic Plaque - RPIM (Axis Units: 1 mm)

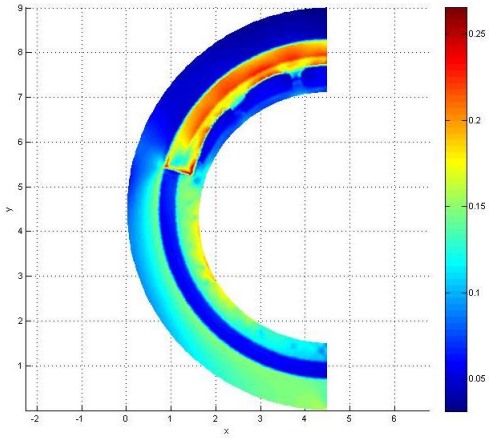

(a) von Mises Tension - Luminal Pressure = 0.05 MPa (color bar up to 0.25 MPa)

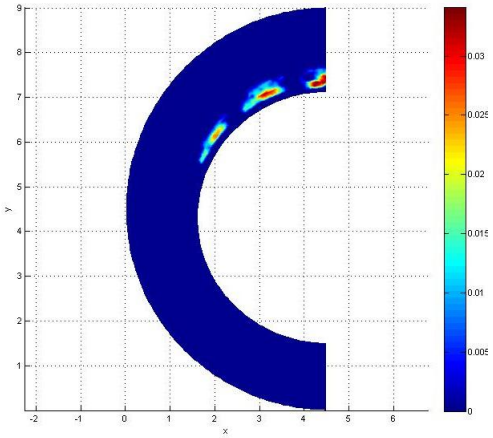

(b) Effective Plastic Strain - Luminal Pressure = 0.05 MPa (color bar up to 0.03)

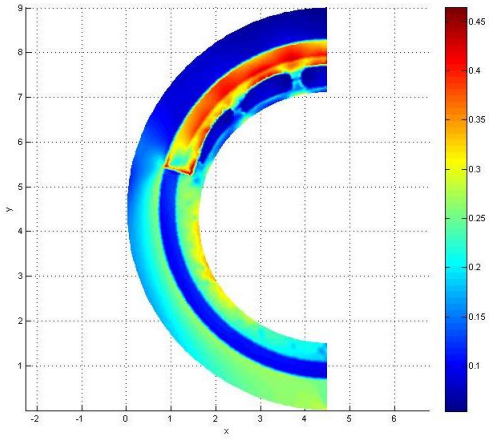

(c) von Mises Tension - Luminal Pressure = 0.09 MPa (color bar up to 0.45 MPa)

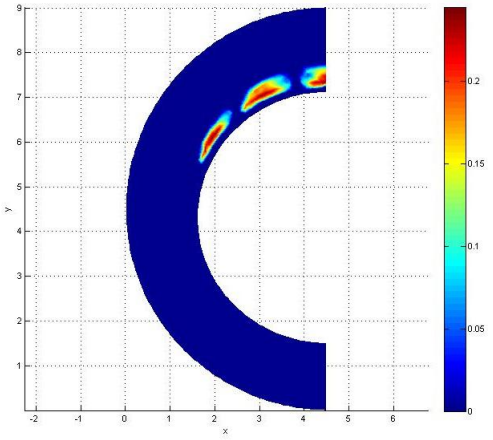

(d) Effective Plastic Strain - Luminal Pressure = 0.09 MPa (color bar up to 0.2)

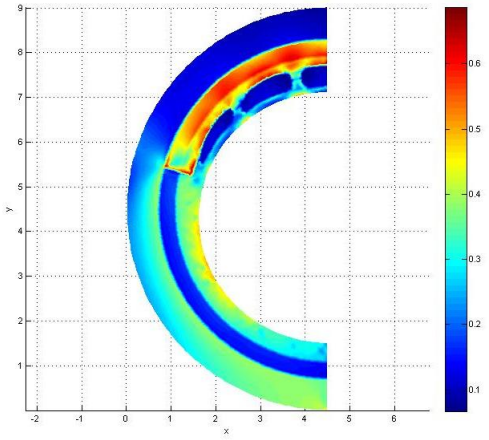

(e) von Mises Tension - Luminal Pressure = 0.135 MPa (color bar up to 0.6 MPa)

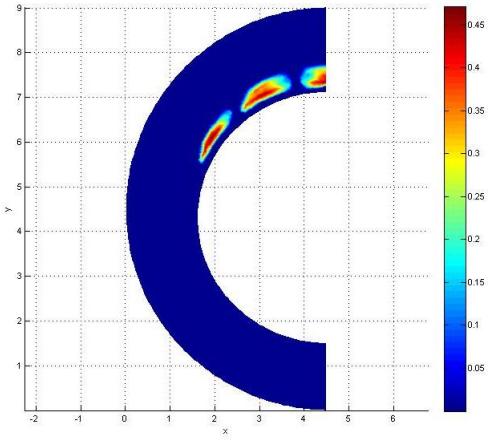

(f) Effective Plastic Strain - Luminal Pressure = 0.135 MPa (color bar up to 0.45)

Figure 6.9: 2D Artery Model I - Lightly Calcified Atherosclerotic Plaque - NNRPIM (Axis Units: 1 mm)

6.2.1.2 Moderately Calcified

The following plots represent the relation between the internal luminal pressure and the displacement seen in points C, D, E and F.

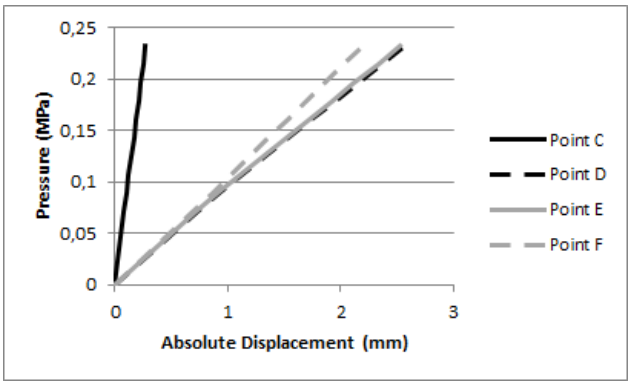

(a) Displacement obtained using FEM

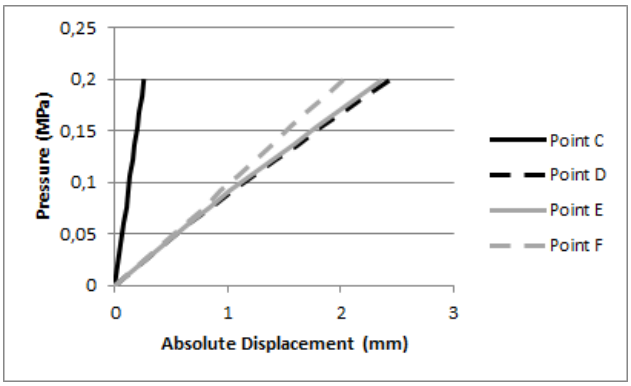

(b) Displacement obtained using RPIM

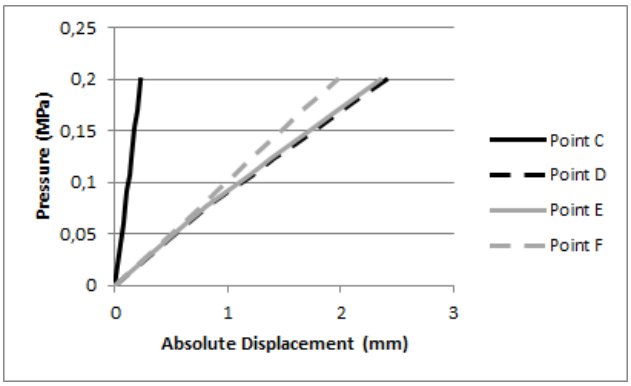

(c) Displacement obtained using NNRPIM

Figure 6.10: 2D Model I - Moderately Calcified - Displacement in Oy vs. Luminal Pressure

The following von Mises Stress Fields and Effective Plastic Strain Fields were also obtained. It can be seen 3 different stages of the plastic deformation progression starting when the Yield Pressure was met.

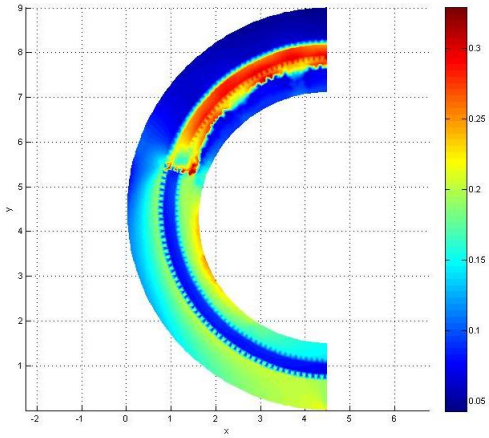

(a) von Mises Tension - Luminal Pressure = 0.75 MPa (color bar up to 0.3 MPa)

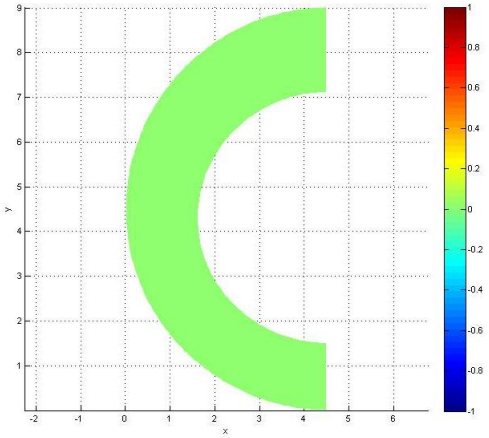

(b) Effective Plastic Strain - Luminal Pressure = 0.075 MPa (no significant values)

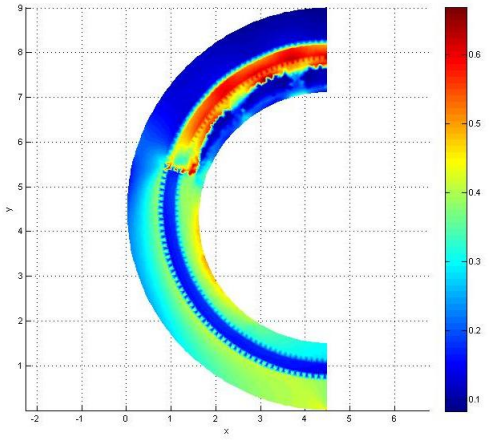

(c) von Mises Tension - Luminal Pressure = 0.14 MPa (color bar up to 0.6 MPa)

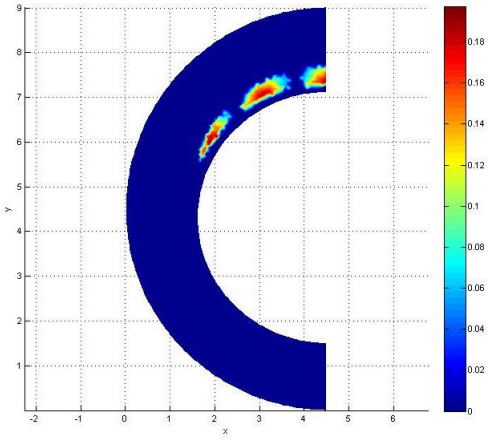

(d) Effective Plastic Strain - Luminal Pressure = 0.14 MPa (color bar up to 0.18)

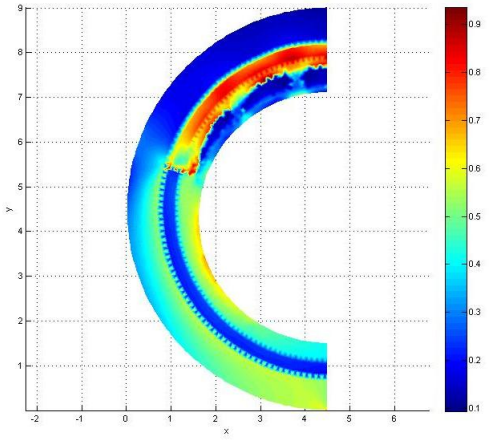

(e) von Mises Tension - Luminal Pressure = 0.2 MPa (color bar up to 0.9 MPa)

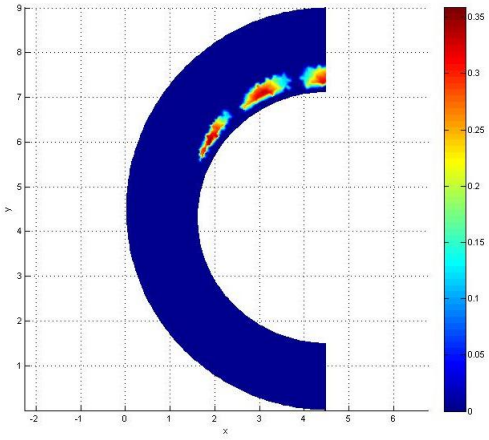

(f) Effective Plastic Strain - Luminal Pressure = 0.2 MPa (color bar up to 0.35)

Figure 6.11: 2D Artery Model I - Medially Calcified Atherosclerotic Plaque - FEM (Axis Units: 1 mm)

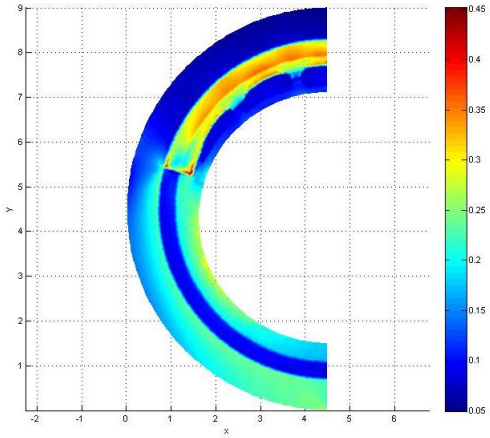

(a) von Mises Tension - Luminal Pressure = 0.75 MPa (color bar up to 0.45 MPa)

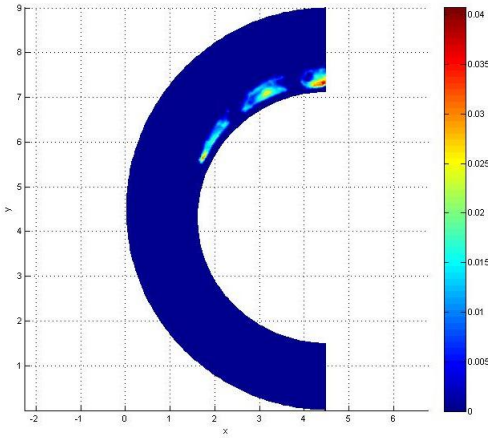

(b) Effective Plastic Strain - Luminal Pressure = 0.075 MPa (color bar up to 0.04)

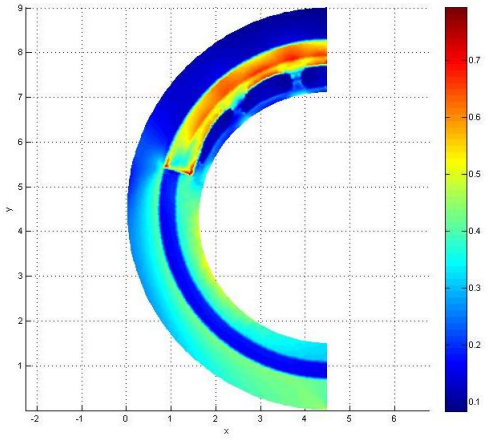

(c) von Mises Tension - Luminal Pressure = 0.14 MPa (color bar up to 0.7 MPa)

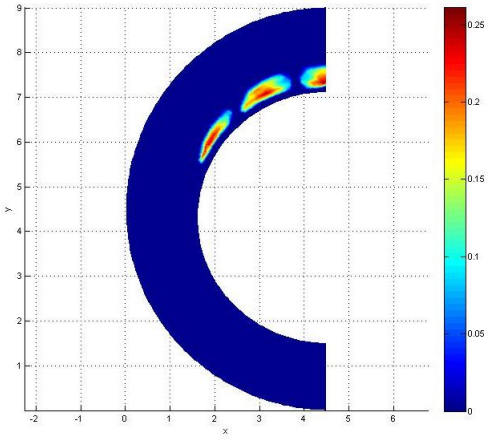

(d) Effective Plastic Strain - Luminal Pressure = 0.14 MPa (color bar up to 0.25)

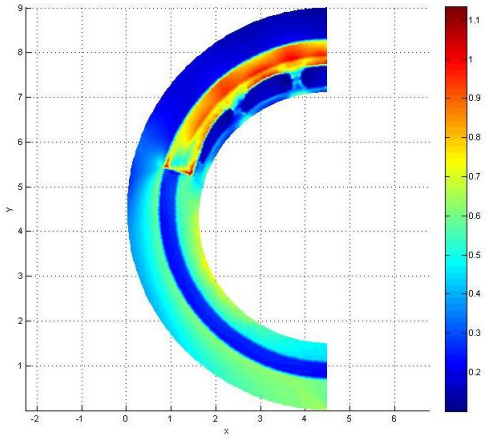

(e) von Mises Tension - Luminal Pressure = 0.2 MPa (color bar up to 1.1 MPa)

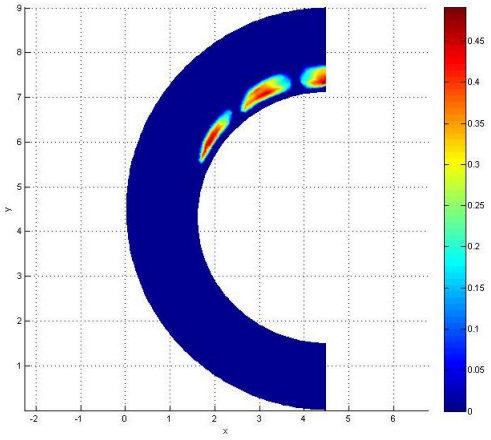

(f) Effective Plastic Strain - Luminal Pressure = 0.2 MPa (color bar up to 0.45)

Figure 6.12: 2D Artery Model I - Medially Calcified Atherosclerotic Plaque - RPIM (Axis Units: 1 mm)

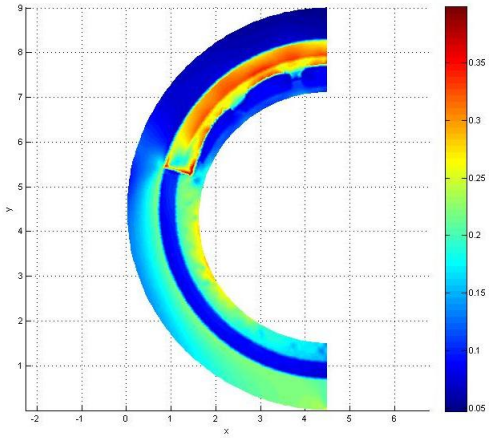

(a) von Mises Tension - Luminal Pressure = 0.75 MPa (color bar up to 0.35 MPa)

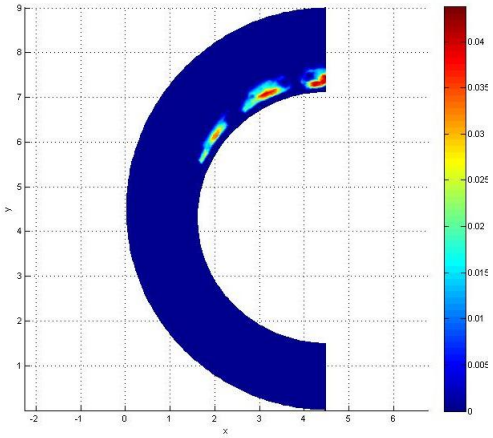

(b) Effective Plastic Strain - Luminal Pressure = 0.075 MPa (color bar up to 0.04)

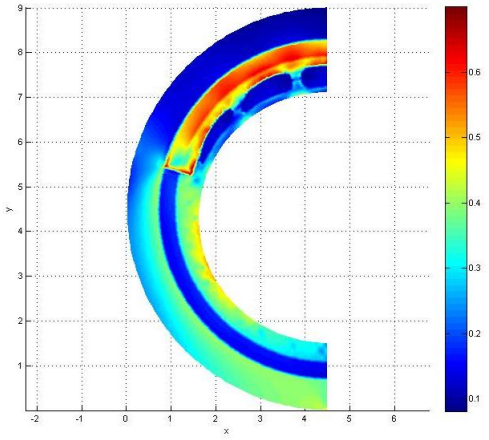

(c) von Mises Tension - Luminal Pressure = 0.14 MPa (color bar up to 0.6 MPa)

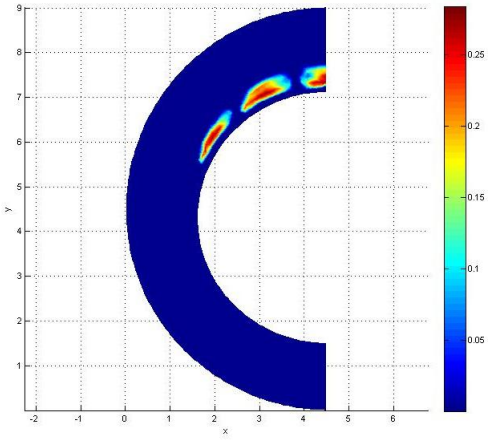

(d) Effective Plastic Strain - Luminal Pressure = 0.14 MPa (color bar up to 0.25)

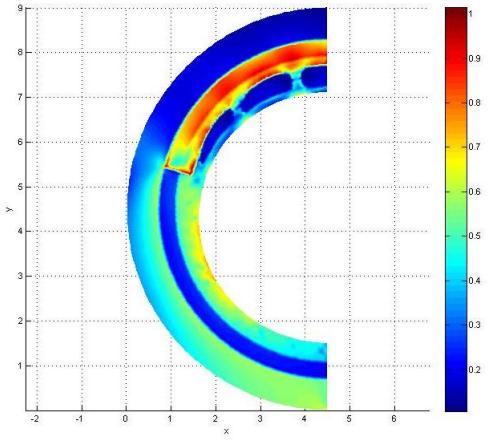

(e) von Mises Tension - Luminal Pressure = 0.2 MPa (color bar up to 1 MPa)

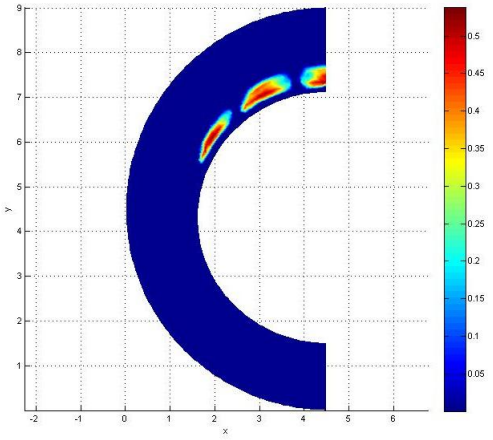

(f) Effective Plastic Strain - Luminal Pressure = 0.2 MPa (color bar up to 0.5)

Figure 6.13: 2D Artery Model I - Medially Calcified Atherosclerotic Plaque - NNRPIM (Axis Units: 1 mm)

6.2.1.3 Heavily Calcified

The following plots represent the relation between the internal luminal pressure and the displacement seen in points C, D, E and F.

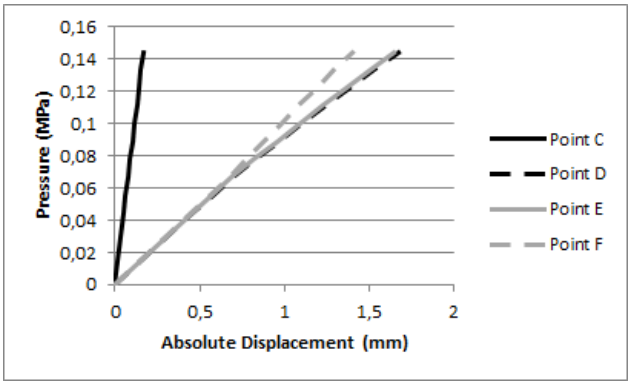

(a) Displacement obtained using FEM

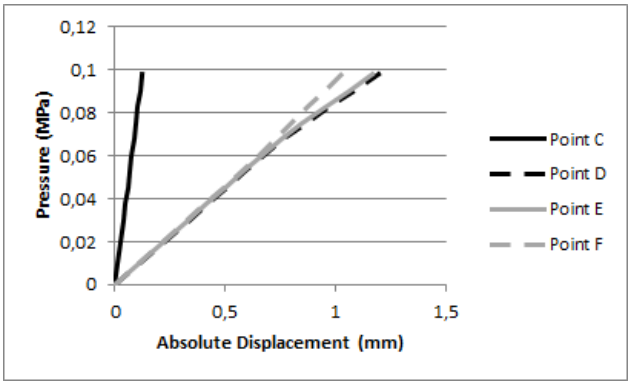

(b) Displacement obtained using RPIM

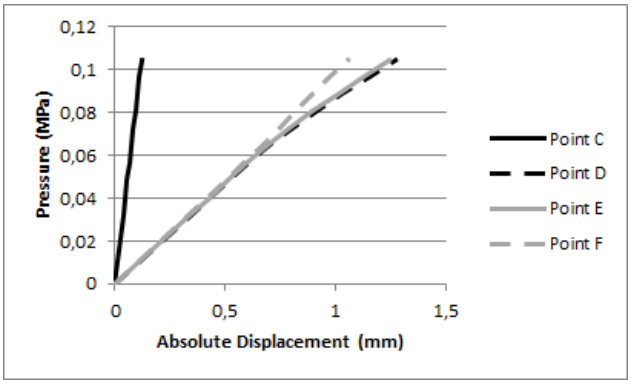

(c) Displacement obtained using NNRPIM

Figure 6.14: 2D Model I - Heavily Calcified - Displacement in Oy vs. Luminal Pressure

The following von Mises Stress Fields and Effective Plastic Strain Fields were also obtained. It can be seen 3 different stages of the plastic deformation progression starting when the Yield Pressure was met.

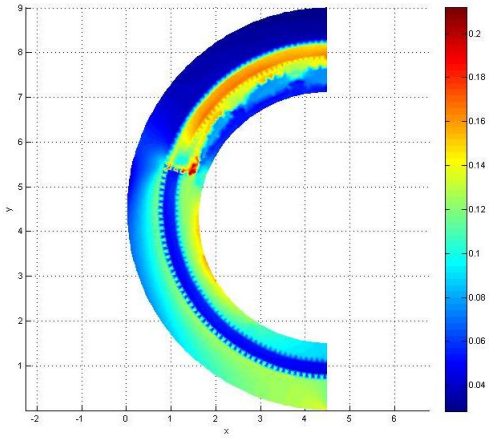

(a) von Mises Tension - Luminal Pressure = 0.45 MPa (color bar up to 0.2 MPa)

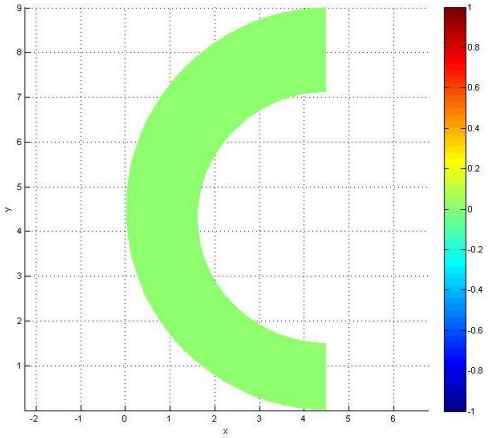

(b) Effective Plastic Strain - Luminal Pressure = 0.045 MPa (no significant values)

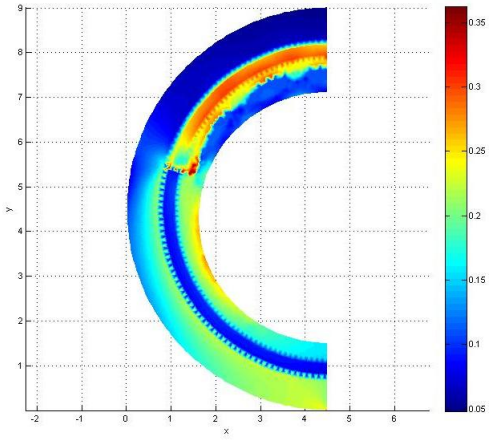

(c) von Mises Tension - Luminal Pressure = 0.075 MPa (color bar up to 0.35 MPa)

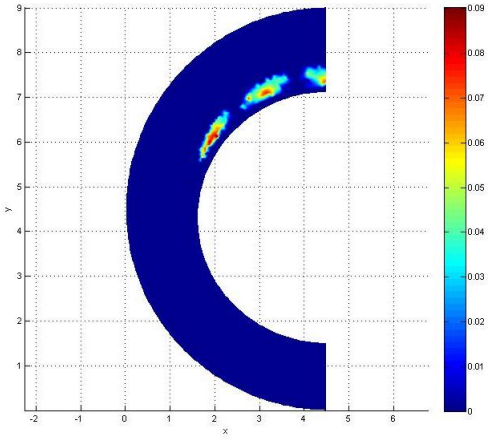

(d) Effective Plastic Strain - Luminal Pressure = 0.075 MPa (color bar up to 0.09)

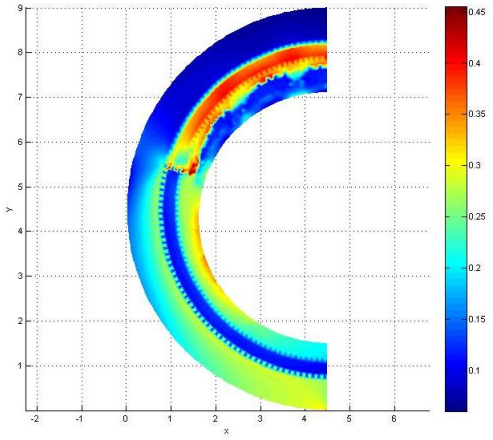

(e) von Mises Tension - Luminal Pressure = 0.1 MPa (color bar up to 0.4 5MPa)

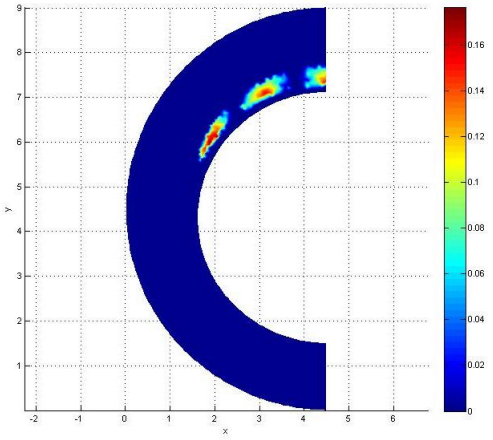

(f) Effective Plastic Strain - Luminal Pressure = 0.1 MPa (color bar up to 0.16)

Figure 6.15: 2D Artery Model I - Highly Calcified Atherosclerotic Plaque - FEM (Axis Units: 1 mm)

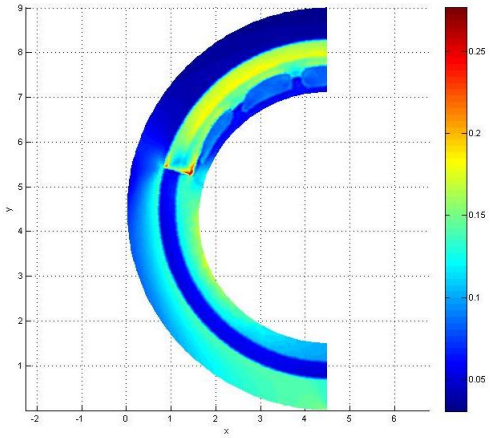

(a) von Mises Tension - Luminal Pressure = 0.45 MPa (color bar up to 0.25 MPa)

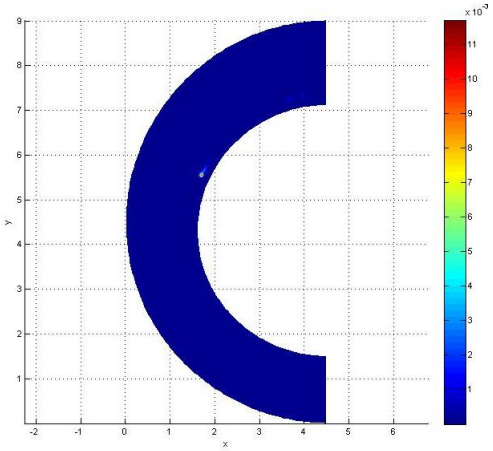

(b) Effective Plastic Strain - Luminal Pressure = 0.045 MPa (color bar up to 0.011)

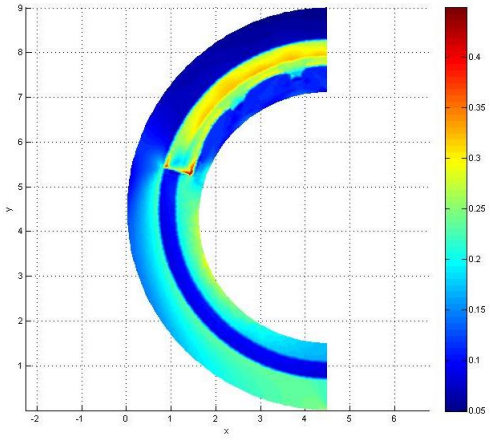

(c) von Mises Tension - Luminal Pressure = 0.075 MPa (color bar up to 0.4 MPa)

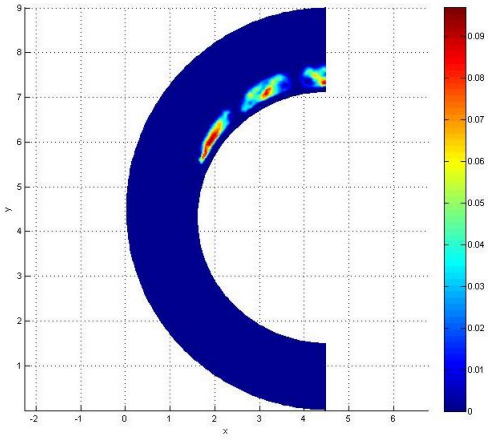

(d) Effective Plastic Strain - Luminal Pressure = 0.075 MPa (color bar up to 0.09)

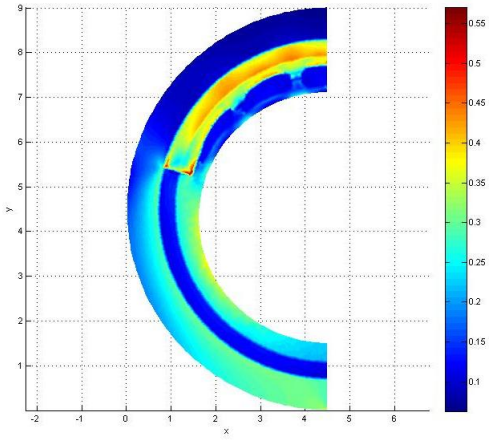

(e) von Mises Tension - Luminal Pressure = 0.1 MPa (color bar up to 0.55 MPa)

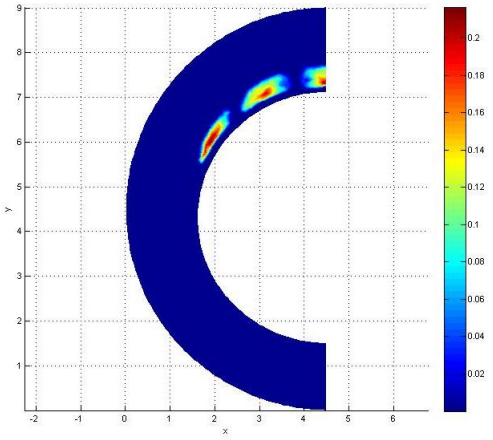

(f) Effective Plastic Strain - Luminal Pressure = 0.1 MPa (color bar up to 0.2)

Figure 6.16: 2D Artery Model I - Highly Calcified Atherosclerotic Plaque - RPIM (Axis Units: 1 mm)

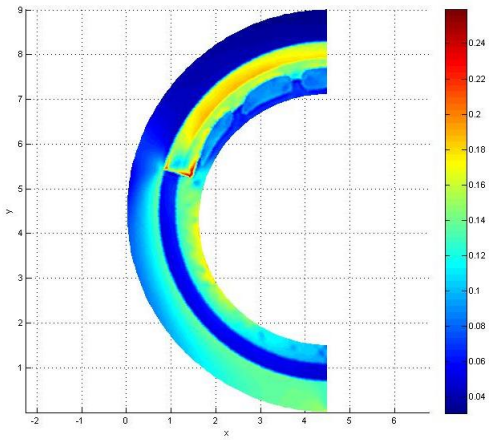

(a) von Mises Tension - Luminal Pressure = 0.45 MPa (color bar up to 0.24 MPa)

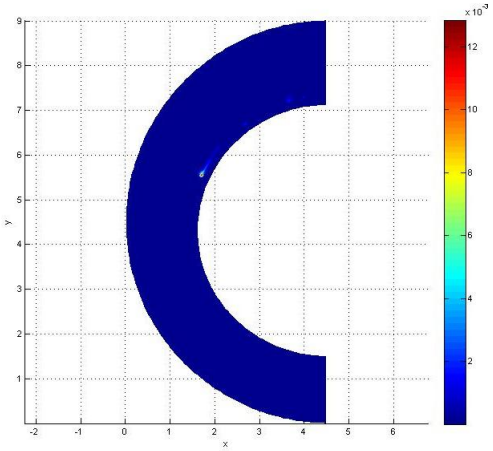

(b) Effective Plastic Strain - Luminal Pressure = 0.045 MPa (color bar up to 0.012)

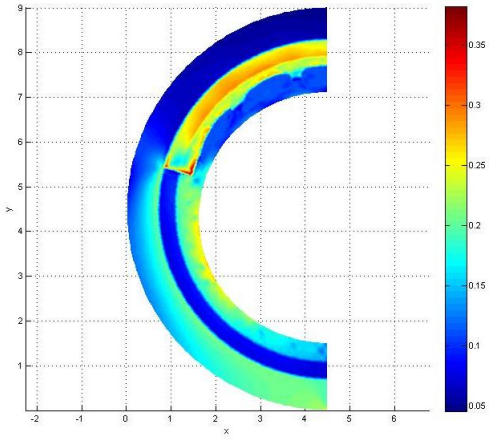

(c) von Mises Tension - Luminal Pressure = 0.075 MPa (color bar up to 0.35 MPa)

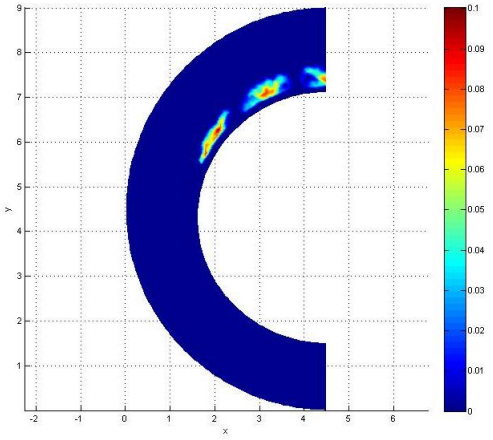

(d) Effective Plastic Strain - Luminal Pressure = 0.075 MPa (color bar up to 0.1)

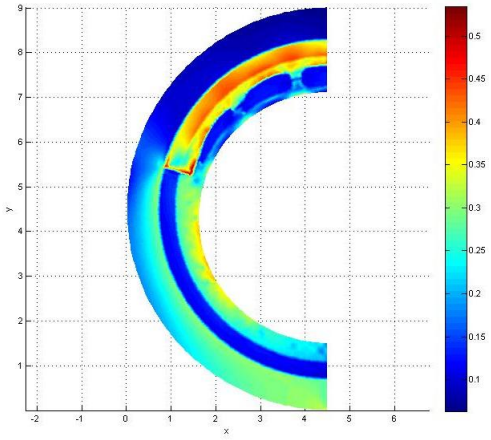

(e) von Mises Tension - Luminal Pressure = 0.1 MPa (color bar up to 0.5 MPa)

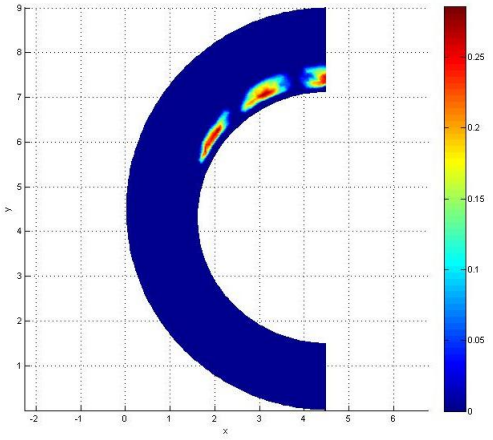

(f) Effective Plastic Strain - Luminal Pressure = 0.1 MPa (color bar up to 0.25)

Figure 6.17: 2D Artery Model I - Highly Calcified Atherosclerotic Plaque - NNRPIM (Axis Units: 1 mm)

6.2.1.4 Discussion

It is possible to see in Figures 6.6, 6.10 and 6.14, that points whose displacement is only affected by elastic materials, as it is the case of points C and F, show a linear displacement relation with the luminal pressure. In comparison to these, points D and E whose displacement is affected by the atherosclerotic plaque show a non-linear progression as the pressure increases.

In Figure 6.18 it can be seen a comparison of the effects of each level of calcification on the displacement of point E. The results appear to be similar between methods showing a small deviation between them starting at around 0.06 MPa. While this results do not show very clearly the effect of atheroscletotic plaque material properties, this can be seen when analysing the distance between point E and F, seen in Figure 6.19. From the measurements of the E-F distance is seen increase in stiffness of the material as the level of calcification increases and also the change in the behaviour as the material started to suffer plastic deformations. This can be supported by the Effective Plastic Strain fields shown before for each set of material properties in Figures 6.7, 6.8, 6.9, 6.11, 6.12, 6.13, 6.15, 6.16 and 6.17.

If it taken into account a normal systolic blood pressure (0.01867 MPa) [91], the highest pressure experienced on a cardiac cycle, the results show that none of the atherosclerotic plaques would experience plastic deformations.

As for the von Mises Tension fields, they show a accumulation of stress in the interface between the damaged *media* and the healthy *media*. It is important to state that this behaviour is an effect of the sudden change of material properties between the tissues, where in a real artery this transition would be smoothed. Even so, it can also be seen in these fields an accumulation of tensions in the *intima*'s luminal wall that is an effect of the high pressures the arteries has been subjected in order for the atherosclerotic plaque to suffer plastic deformation.

In terms of the performance of the numerical methods, the results are coherent and similar between them. In Figure 6.20 it can be seen a comparison of the displacement of point E obtained from three numerical methods with each set of material properties. As the plot show, there is a good overlay between the RPIM and NNRPIM, while it appears to exist a small deviation when compared to the FEM results.

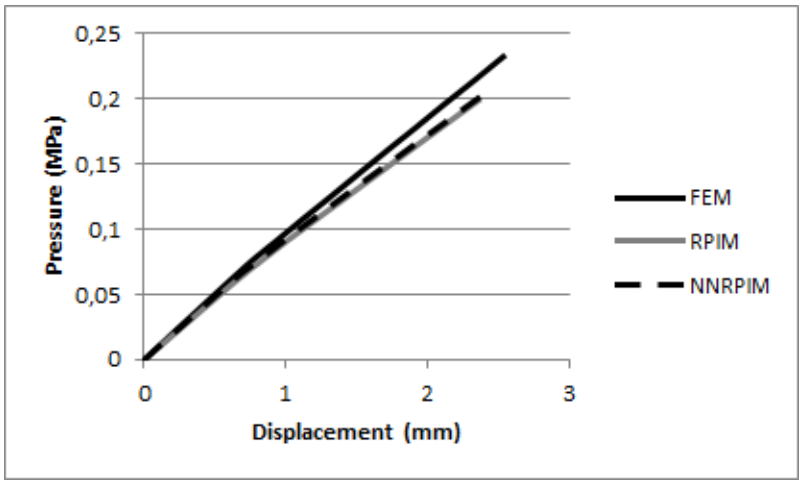

(a) Displacement obtained using FEM

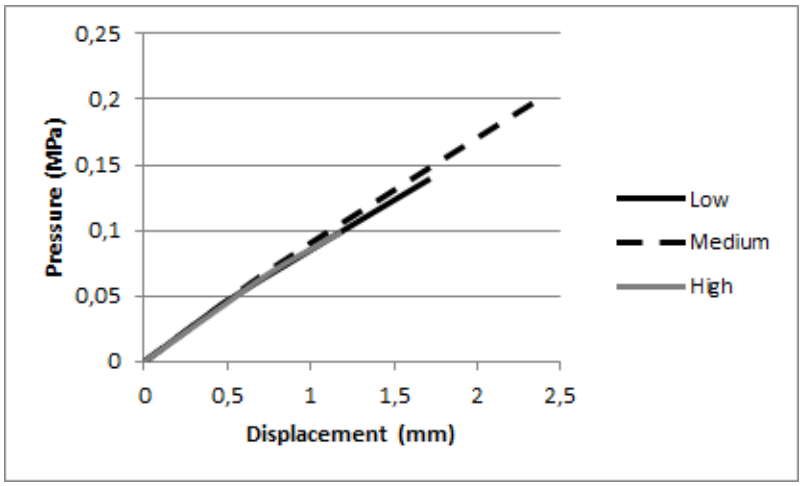

(b) Displacement obtained using RPIM

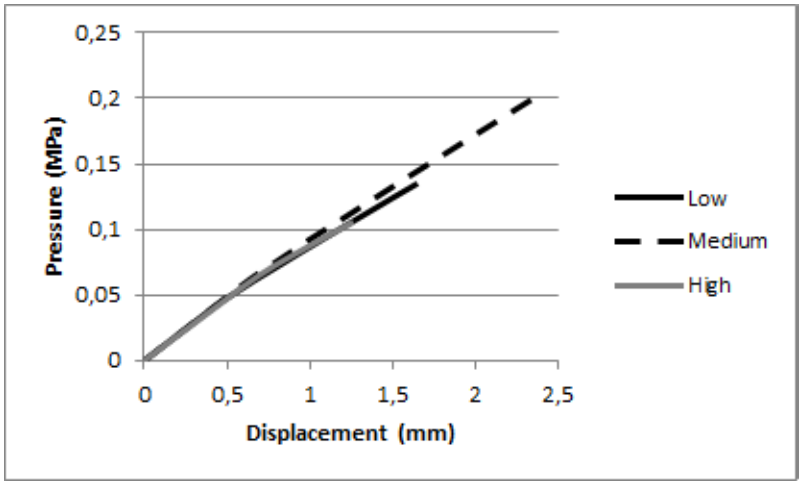

(c) Displacement obtained using NNRPIM

Figure 6.18: 2D Model I - Comparison of Displacements of Point E in different levels of calcification

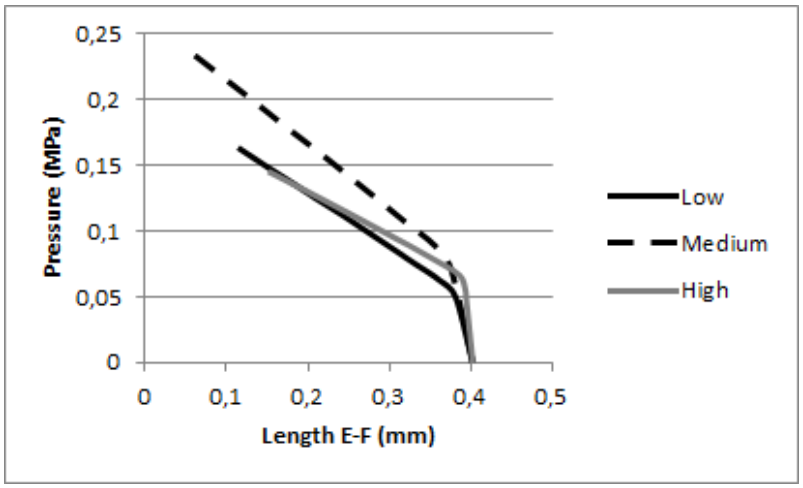

(a) Displacement obtained using FEM

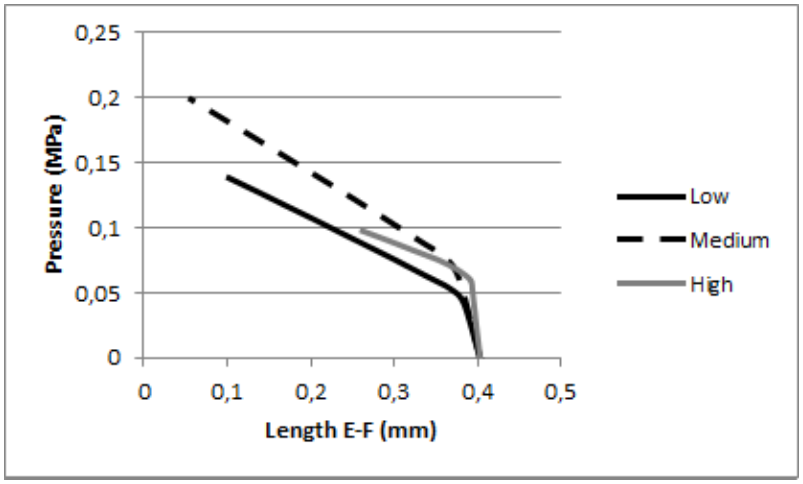

(b) Displacement obtained using RPIM

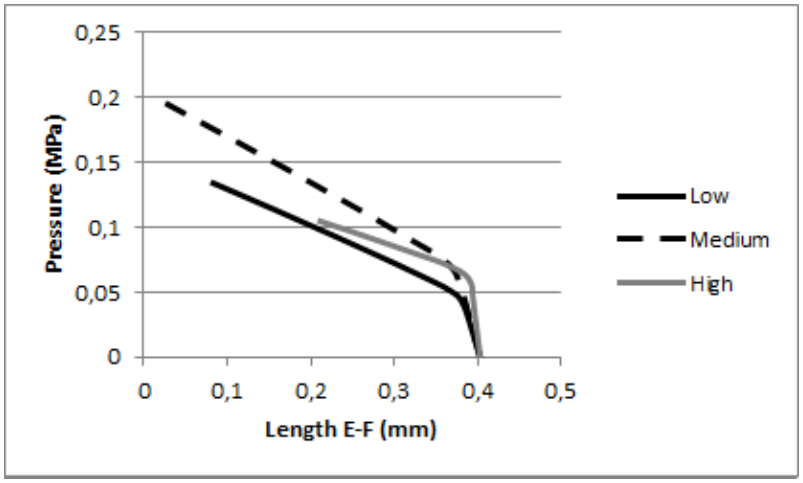

(c) Displacement obtained using NNRPIM

Figure 6.19: 2D Model I - Comparison of length of segment FE

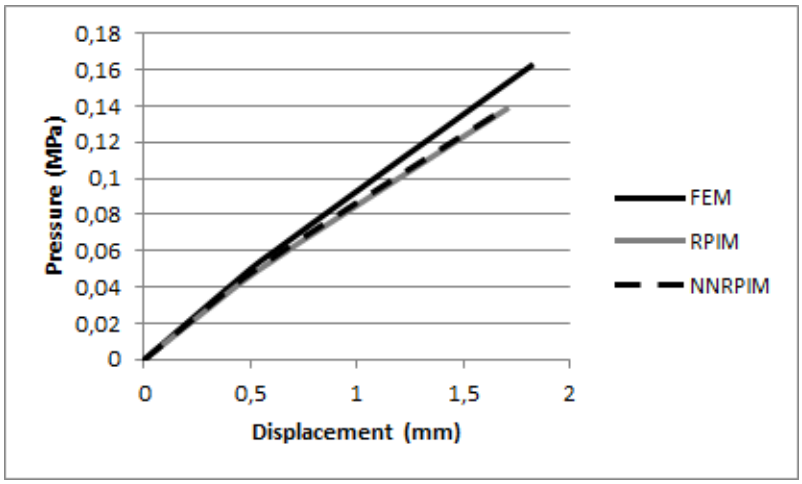

(a) Displacement obtained with the Lightly Calcified material properties

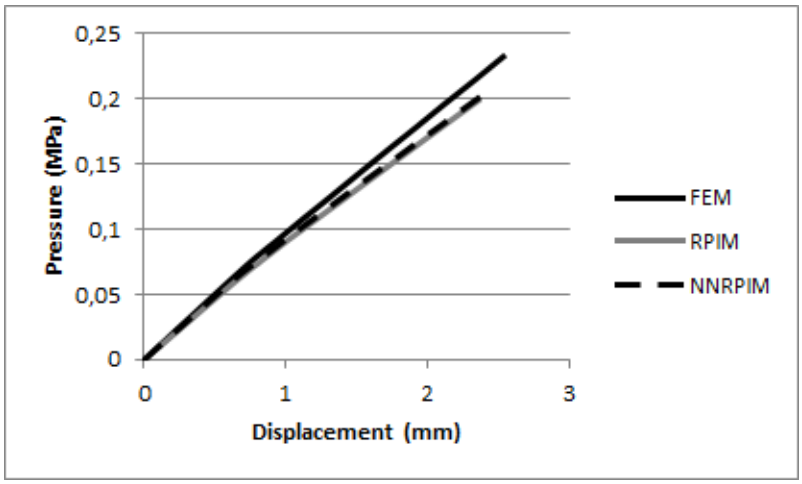

(b) Displacement obtained with the Moderately Calcified material properties

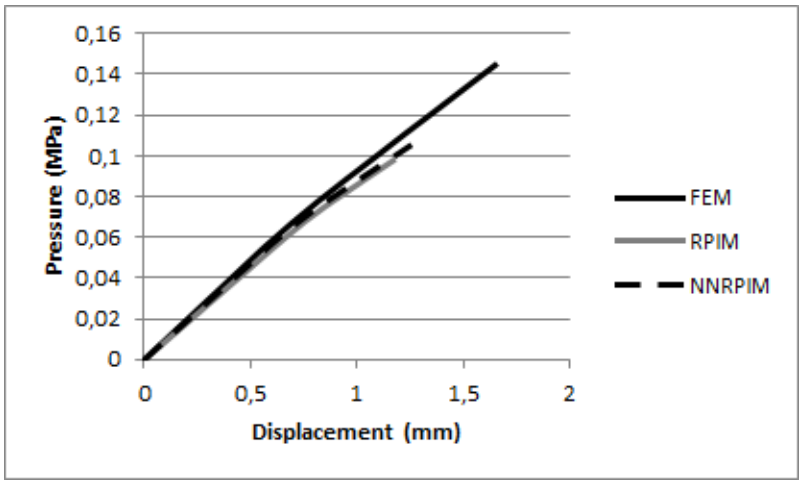

(c) Displacement obtained with the Heavily Calcified material properties

Figure 6.20: 2D Model I - Comparison of displacement of point E with different numerical methods

6.2.2 2D Model II

For this example it was taken into consideration a solid domain $\omega \in \Re^2$ representing a atherosclerotic artery containing a thin segmented plaque. It was applied to the domain symmetry constrains and fixed the node (x,y)=(4.5,0). The numerical model was designed using 4097 nodes and was analysed using three different numerical methods (FEM, RPIM and NNRPIM). An image of the nodal distribution used can be seen in Figure 6.21

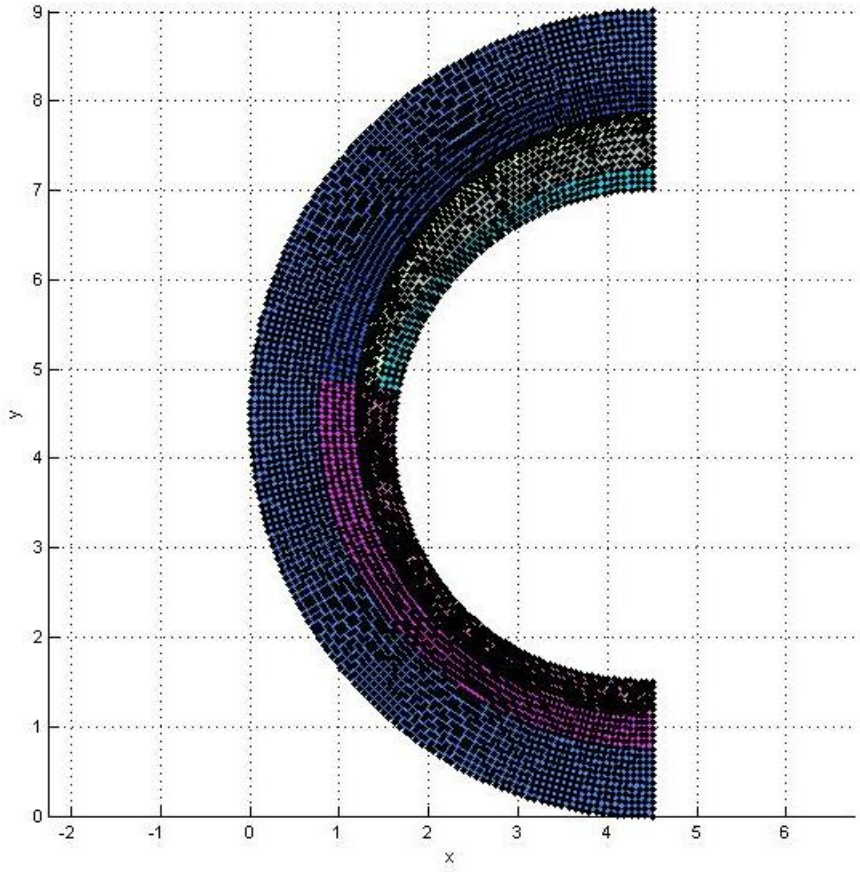

Figure 6.21: 2D Model of Artery with Atherosclerotic Plaque - Stage II (Axis Units: 1 mm)

The von Mises Stress field and Effective Plastic Strain Field were analysed for each of the atherosclerotic plaque set of material properties. Besides this, it was also analysed the displacement in Oy in specific interface nodes between tissues. The location of these nodes can be seen in the diagram of Figure 6.22. The displacement seen was analysed against to the pressure applied in the artery's lumen.

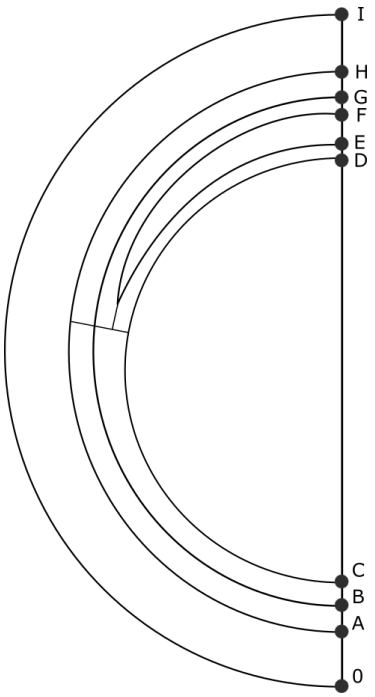

Figure 6.22: 2D Model Stage II - Points location

6.2.2.1 Lightly Calcified

The following plots represent the relation between the internal luminal pressure and the displacement seen in points C, D, E and F.

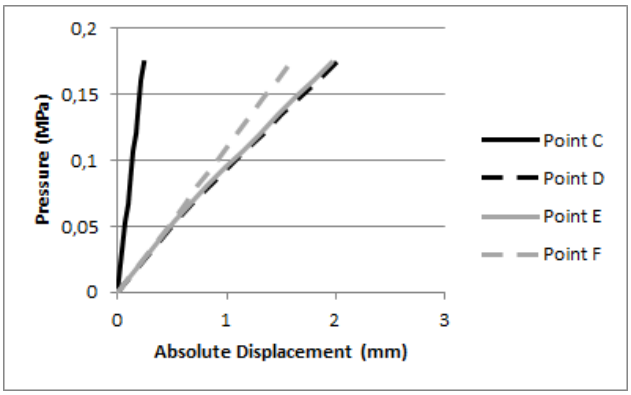

(a) Displacement obtained using FEM

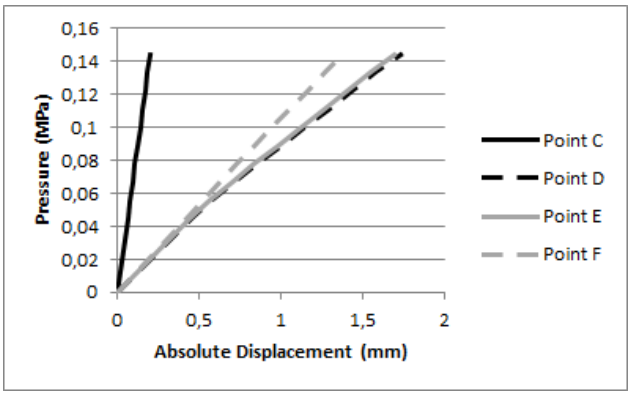

(b) Displacement obtained using RPIM

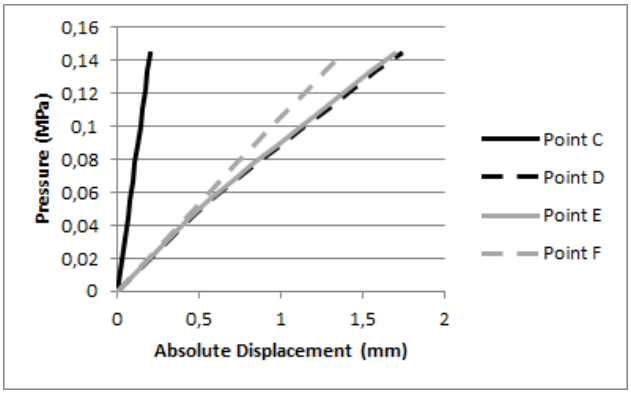

(c) Displacement obtained using NNRPIM

Figure 6.23: 2D Model II - Lightly Calcified - Displacement in Oy vs. Luminal Pressure

The following von Mises Stress Fields and Effective Plastic Strain Fields were also obtained. It can be seen 3 different stages of the plastic deformation progression starting when the Yield Pressure was met.

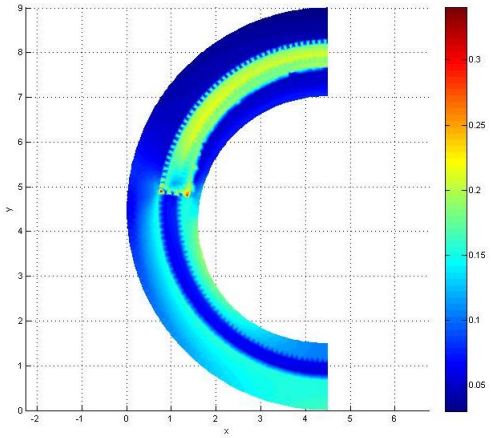

(a) von Mises Tension - Luminal Pressure = 0.055 MPa (color bar up to 0.3 MPa)

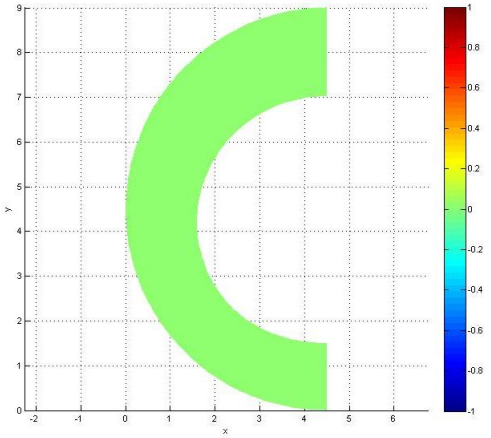

(b) Effective Plastic Strain - Luminal Pressure = 0.055 MPa (no significant values)

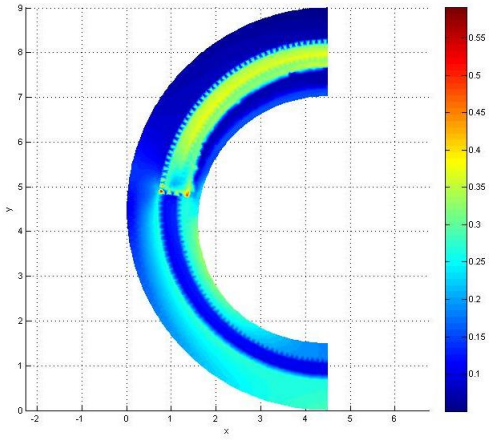

(c) von Mises Tension - Luminal Pressure = 0.09 MPa (color bar up to 0.55 MPa)

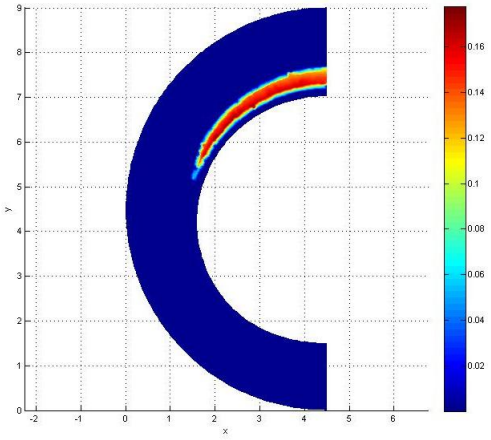

(d) Effective Plastic Strain - Luminal Pressure = 0.09 MPa (color bar up to 0.16)

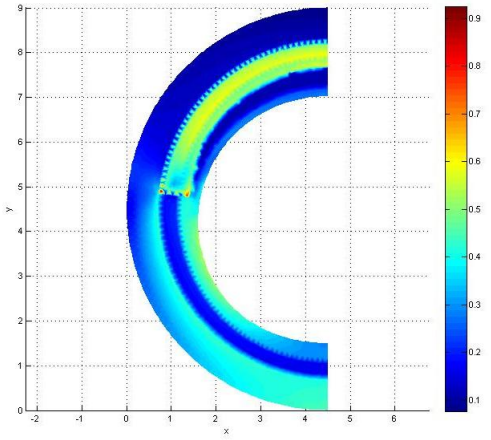

(e) von Mises Tension - Luminal Pressure = 0.145 MPa (color bar up to 0.9 MPa)

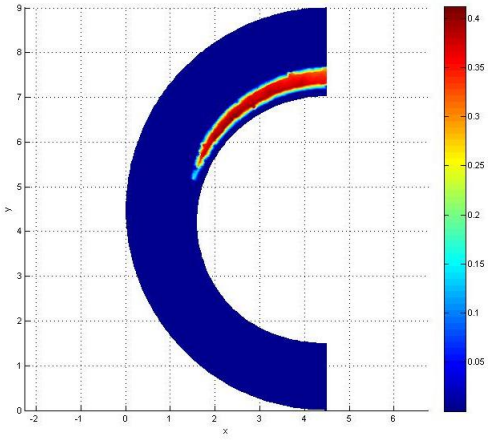

(f) Effective Plastic Strain - Luminal Pressure = 0.145 MPa (color bar up to 0.4)

Figure 6.24: 2D Artery Model II - Lightly Calcified Atherosclerotic Plaque - FEM (Axis Units: 1 mm)

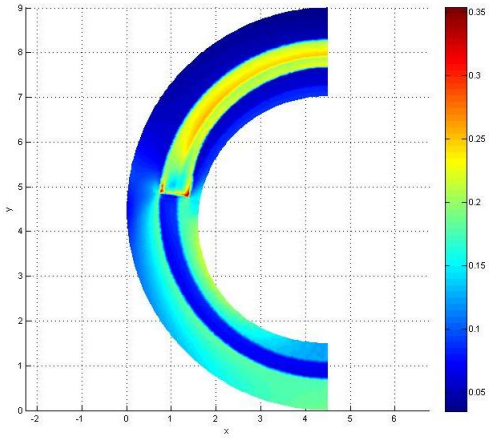

(a) von Mises Tension - Luminal Pressure = 0.05 MPa (color bar up to 0.35 MPa)

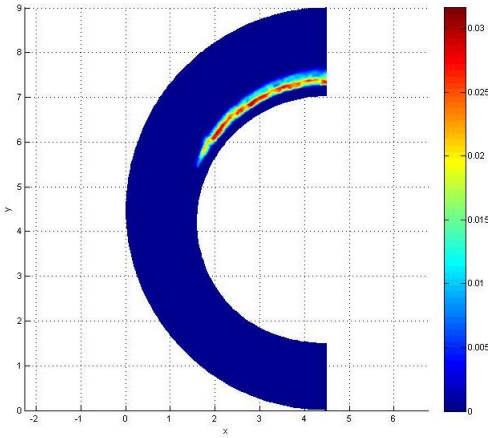

(b) Effective Plastic Strain - Luminal Pressure = 0.05 MPa (color bar up to 0.03)

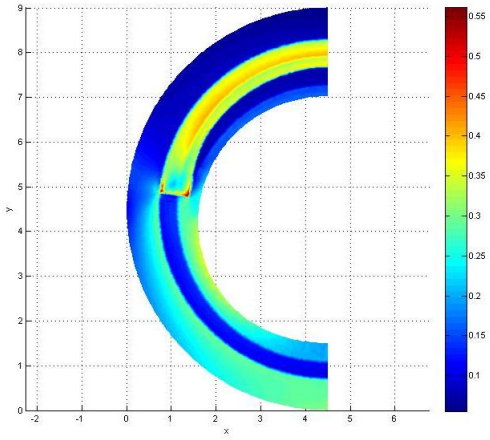

(c) von Mises Tension - Luminal Pressure = 0.09 MPa (color bar up to 0.55 MPa)

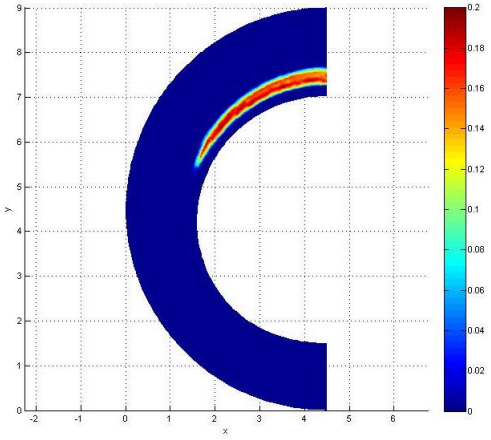

(d) Effective Plastic Strain - Luminal Pressure = 0.09 MPa (color bar up to 0.2)

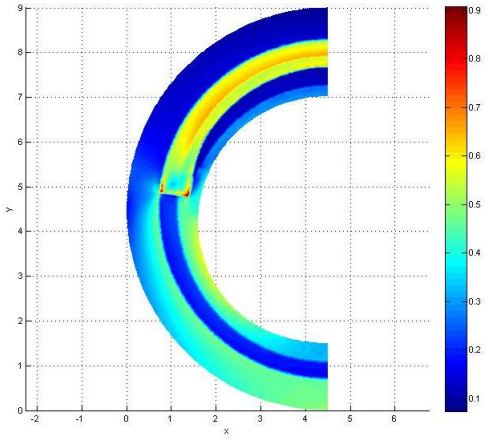

(e) von Mises Tension - Luminal Pressure = 0.145 MPa (color bar up to 0.9 MPa)

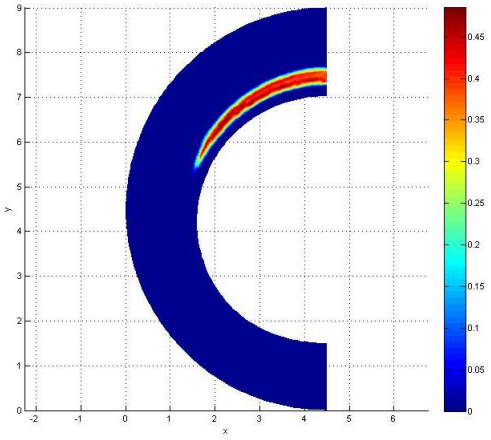

(f) Effective Plastic Strain - Luminal Pressure = 0.145 MPa (color bar up to 0.45)

Figure 6.25: 2D Artery Model II - Lightly Calcified Atherosclerotic Plaque - RPIM (Axis Units: 1 mm)

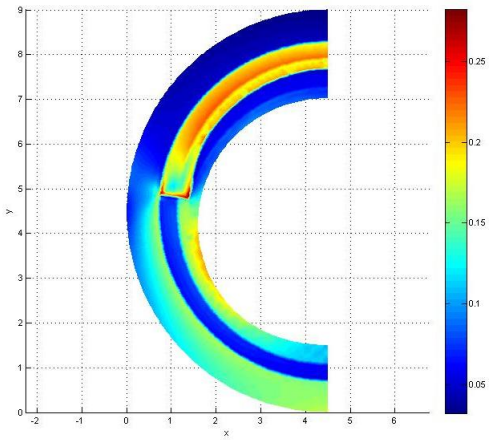

(a) von Mises Tension - Luminal Pressure = 0.05 MPa (color bar up to 0.25 MPa)

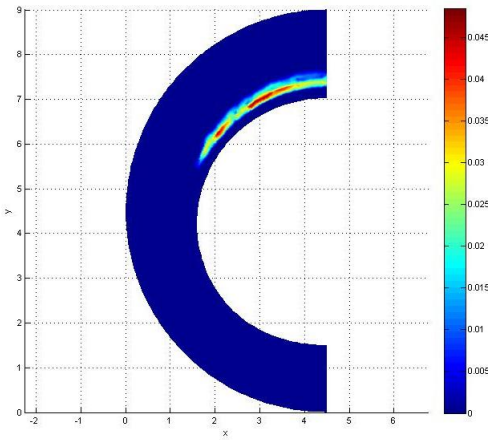

(b) Effective Plastic Strain - Luminal Pressure = 0.05 MPa (color bar up to 0.045)

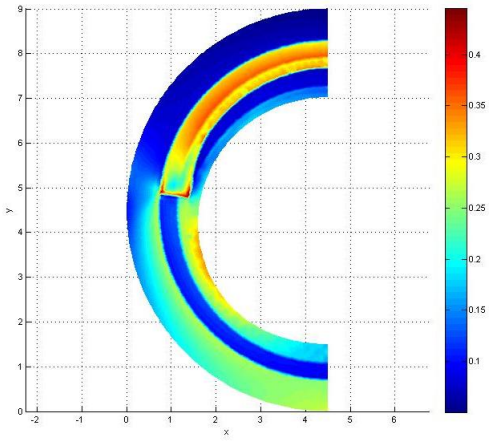

(c) von Mises Tension - Luminal Pressure = 0.09 MPa (color bar up to 0.4 MPa)

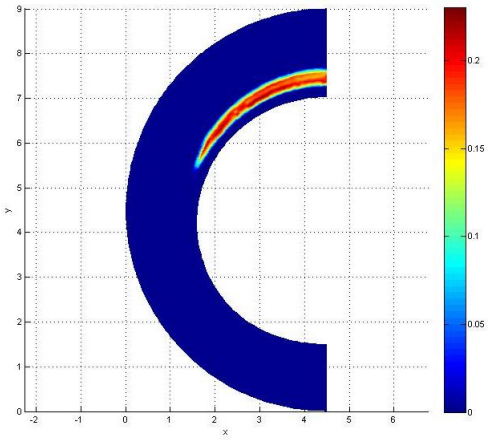

(d) Effective Plastic Strain - Luminal Pressure = 0.09 MPa (color bar up to 0.2)

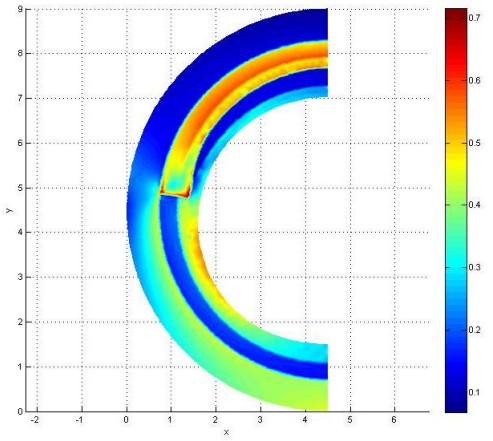

(e) von Mises Tension - Luminal Pressure = 0.145 MPa (color bar up to 0.7 MPa)

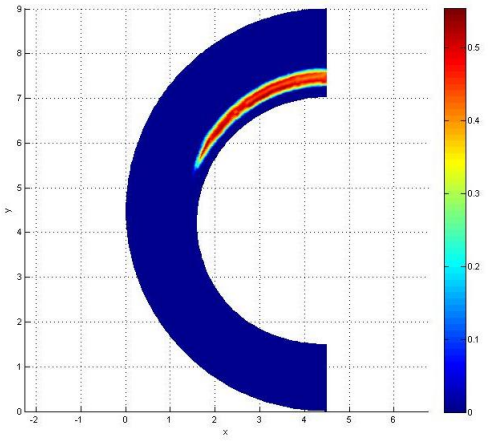

(f) Effective Plastic Strain - Luminal Pressure = 0.145 MPa (color bar up to 0.5)

Figure 6.26: 2D Artery Model II - Lightly Calcified Atherosclerotic Plaque - NNRPIM (Axis Units: 1 mm)

6.2.2.2 Moderately Calcified

The following plots represent the relation between the internal luminal pressure and the displacement seen in points C, D, E and F.

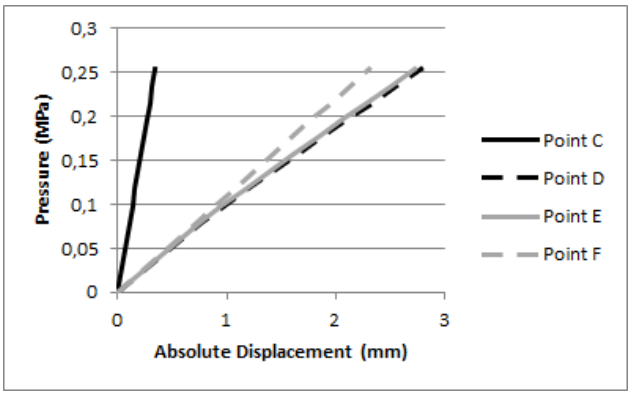

(a) Displacement obtained using FEM

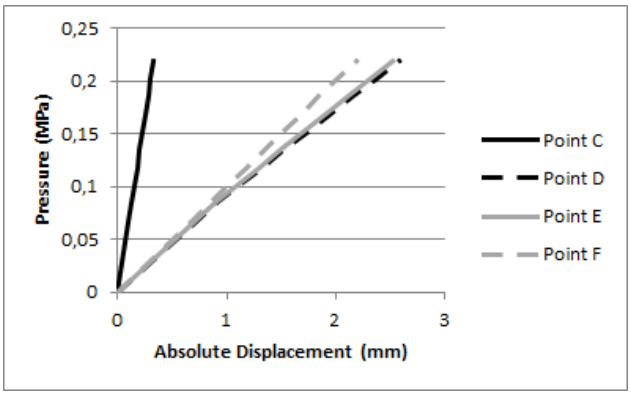

(b) Displacement obtained using RPIM

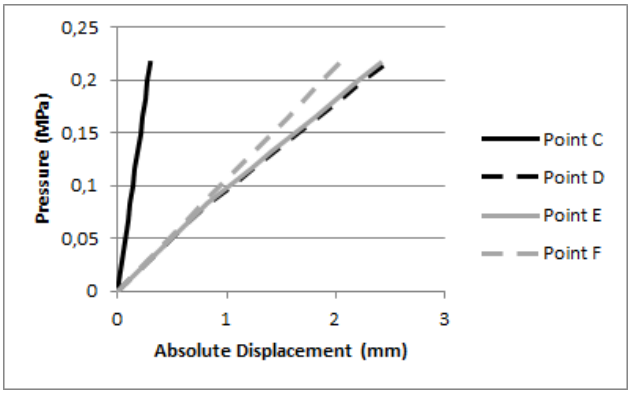

(c) Displacement obtained using NNRPIM

Figure 6.27: 2D Model I - Moderately Calcified - Displacement int Oy vs. Luminal Pressure

The following von Mises Stress Fields and Effective Plastic Strain Fields were also obtained. It can be seen 3 different stages of the plastic deformation progression starting when the Yield Pressure was met.

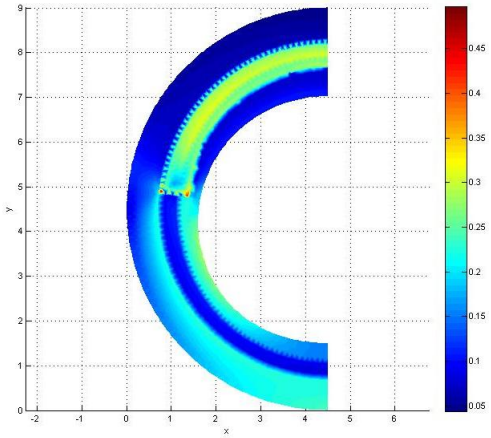

(a) von Mises Tension - Luminal Pressure = 0.08 MPa (color bar up to 0.45 MPa)

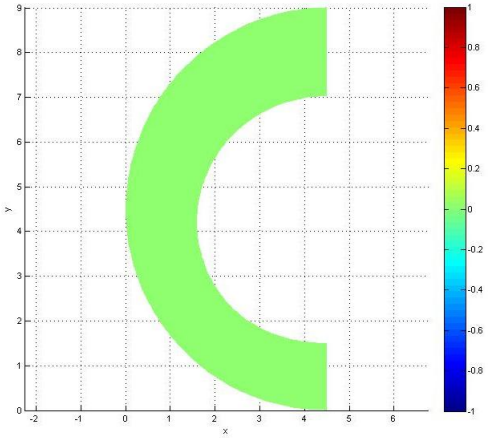

(b) Effective Plastic Strain - Luminal Pressure = 0.08 MPa (no significant values)

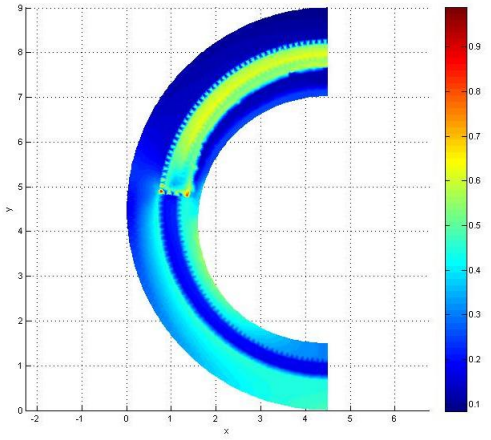

(c) von Mises Tension - Luminal Pressure = 0.15 MPa (color bar up to 0.9 MPa)

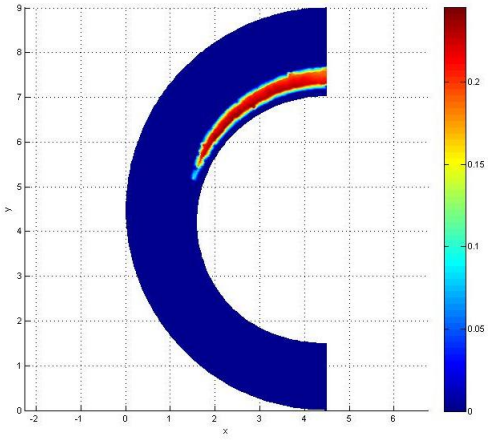

(d) Effective Plastic Strain - Luminal Pressure = 0.15 MPa (color bar up to 0.2)

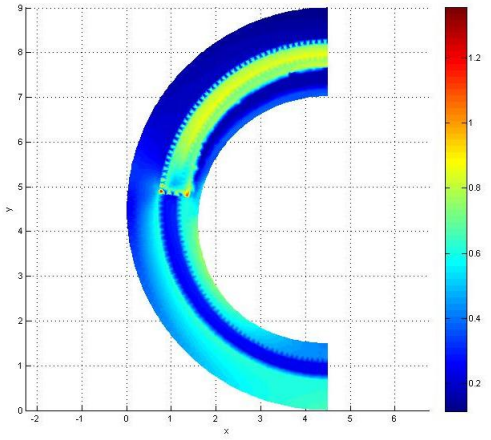

(e) von Mises Tension - Luminal Pressure = 0.22 MPa (color bar up to 1.2 MPa)

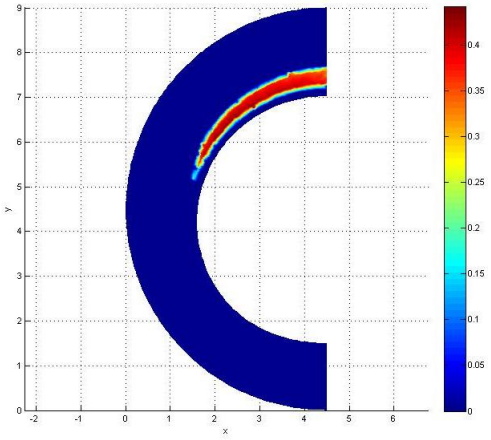

(f) Effective Plastic Strain - Luminal Pressure = 0.22 MPa (color bar up to 0.4)

Figure 6.28: 2D Artery Model II - Medially Calcified Atherosclerotic Plaque - FEM (Axis Units: 1 mm)

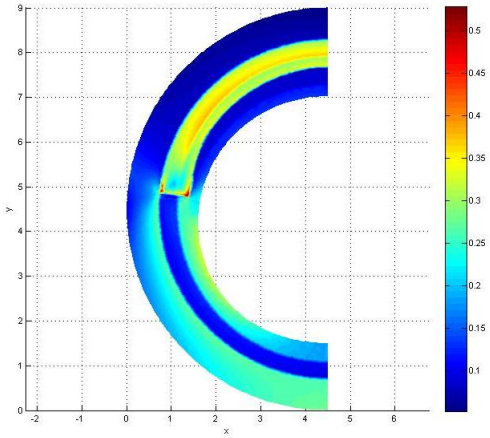

(a) von Mises Tension - Luminal Pressure = 0.08 MPa (color bar up to 0.5 MPa)

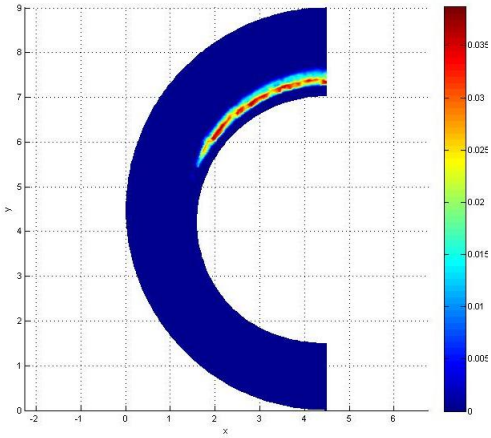

(b) Effective Plastic Strain - Luminal Pressure = 0.08 MPa (color bar upto 0.035)

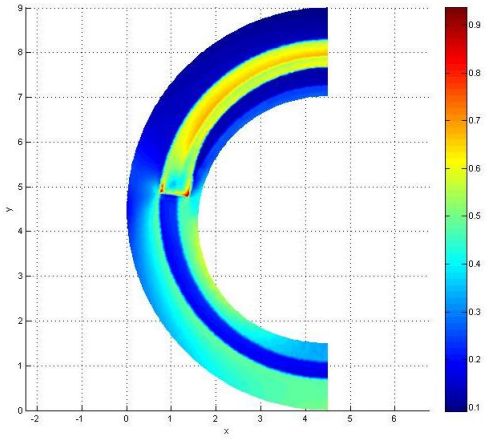

(c) von Mises Tension - Luminal Pressure = 0.15 MPa (color bar up to 0.9 MPa)

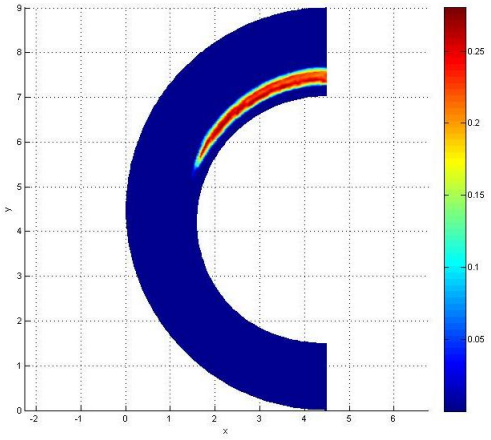

(d) Effective Plastic Strain - Luminal Pressure = 0.15 MPa (color bar up to 0.25)

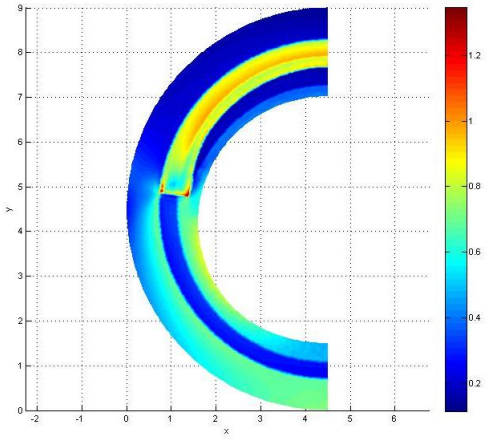

(e) von Mises Tension - Luminal Pressure = 0.22 MPa (color bar up to 1.2 MPa)

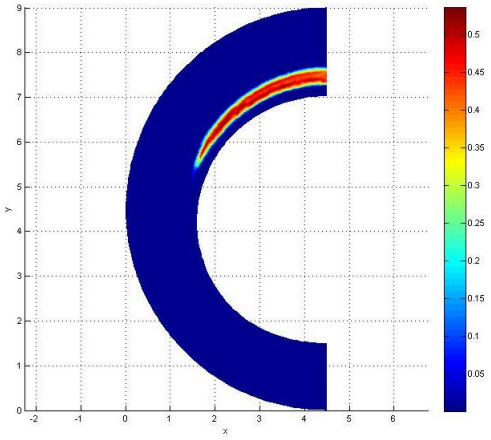

(f) Effective Plastic Strain - Luminal Pressure = 0.22 MPa (color bar up to 0.5)

Figure 6.29: 2D Artery Model II - Medially Calcified Atherosclerotic Plaque - RPIM (Axis Units: 1 mm)

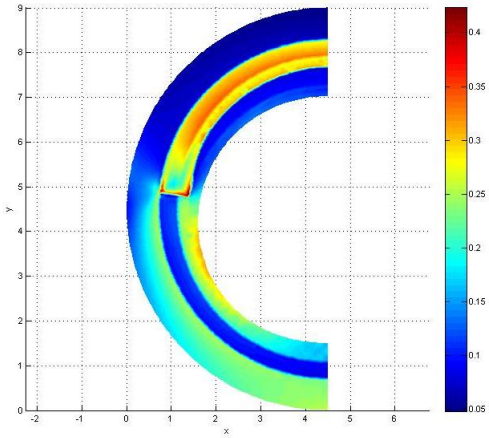

(a) von Mises Tension - Luminal Pressure = 0.08 MPa (color bar up to 0.4 MPa)

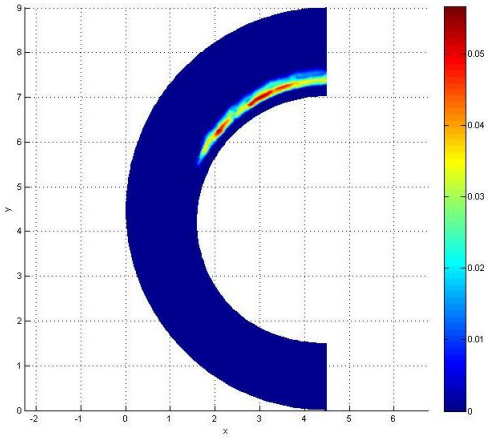

(b) Effective Plastic Strain - Luminal Pressure = 0.08 MPa (color bar upto 0.05)

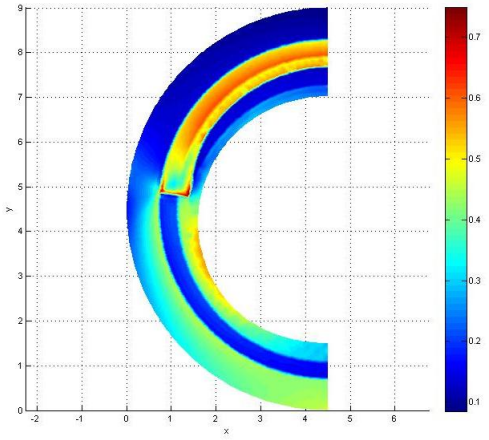

(c) von Mises Tension - Luminal Pressure = 0.15 MPa (color bar up to 0.7 MPa)

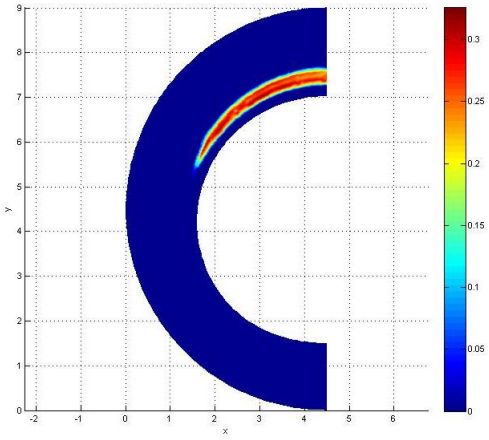

(d) Effective Plastic Strain - LuminalLuminal Pressure = 0.15 MPa (color bar up to 0.3)

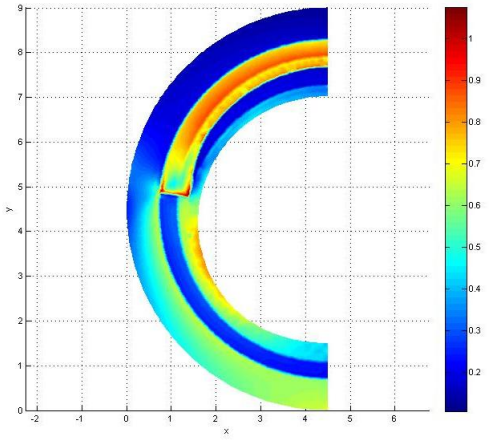

(e) von Mises Tension - Lumen Pressure = 0.22 MPa (color bar up to 1 MPa)

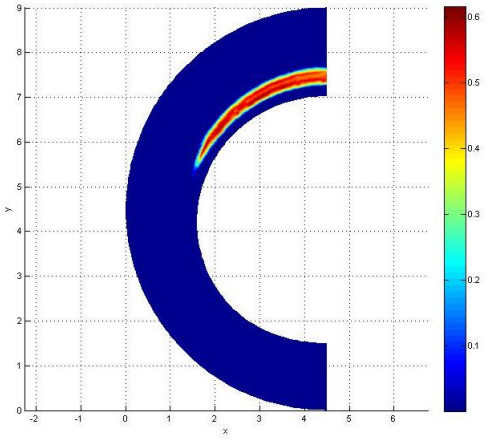

(f) Effective Plastic Strain - Luminal Pressure = 0.22 MPa (color bar up to 0.6)

Figure 6.30: 2D Artery Model II - Medially Calcified Atherosclerotic Plaque - NNRPIM (Axis Units: 1 mm)

6.2.2.3 Heavily Calcified

The following plots represent the relation between the internal luminal pressure and the displacement seen in points C, D, E and F.

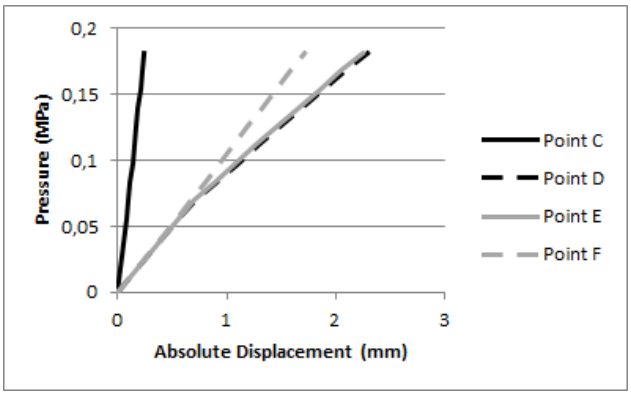

(a) Displacement obtained using FEM

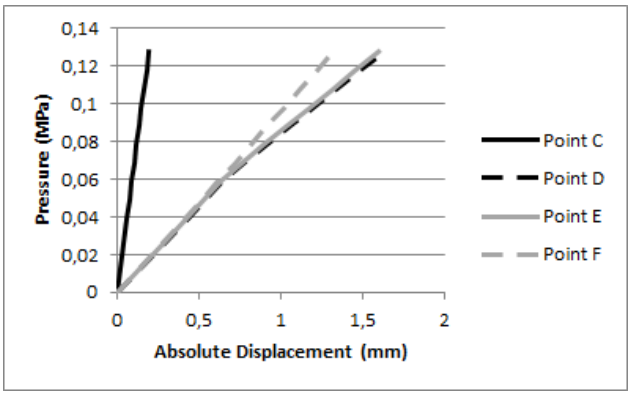

(b) Displacement obtained using RPIM

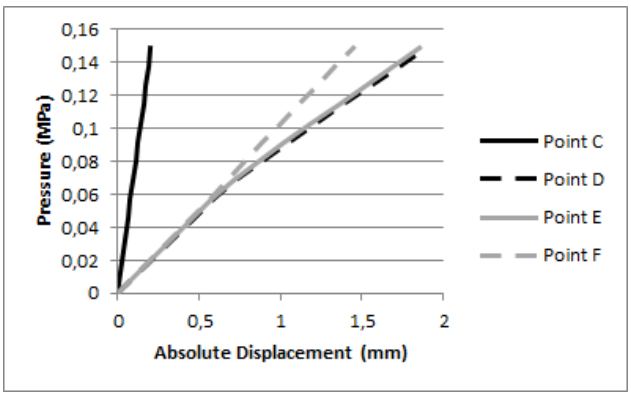

(c) Displacement obtained using NNRPIM

Figure 6.31: 2D Model II - Heavily Calcified - Displacement in Oy vs. Luminal Pressure

The following von Mises Stress Fields and Effective Plastic Strain Fields were also obtained. It can be seen 3 different stages of the plastic deformation progression starting when the Yield Pressure was met.

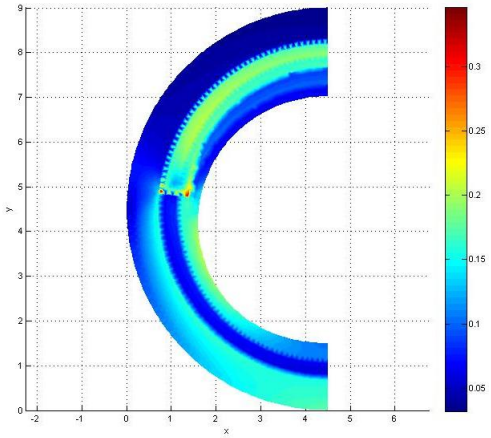

(a) von Mises Tension - Luminal Pressure = 0.055 MPa (color bar up to 0.3 MPa)

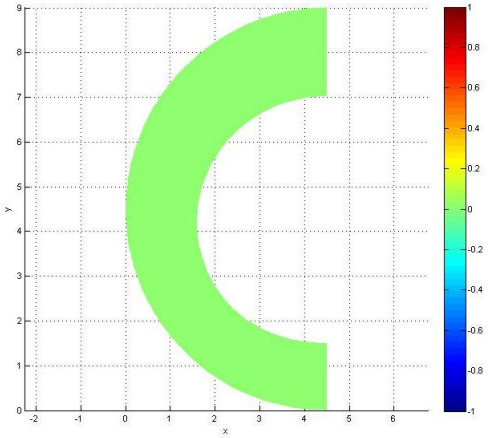

(b) Effective Plastic Strain - Luminal Pressure = 0.055 MPa (no significant values)

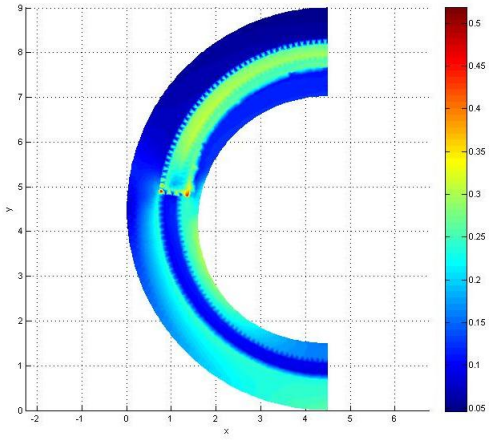

(c) von Mises Tension - Luminal Pressure = 0.08 MPa (color bar up to 0.5 MPa)

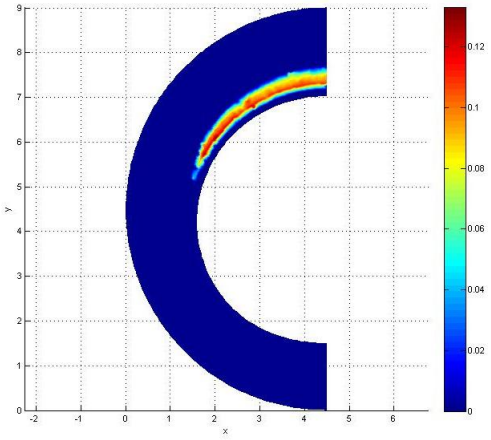

(d) Effective Plastic Strain - Luminal Pressure = 0.08 MPa (color bar up to 0.12)

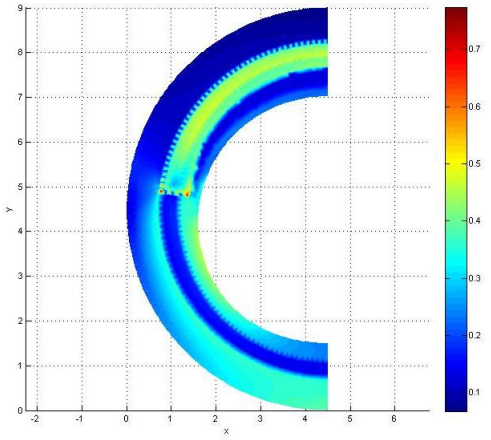

(e) von Mises Tension - Luminal Pressure = 0.125 MPa (color bar up to 0.7 MPa)

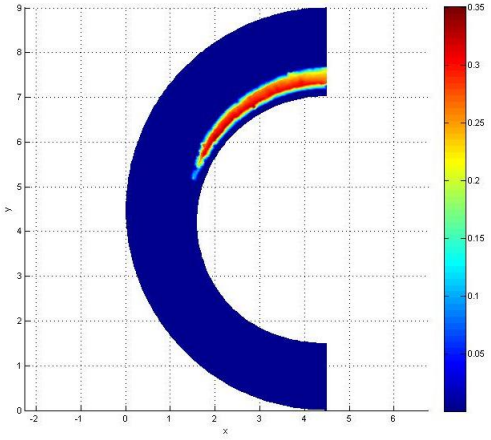

(f) Effective Plastic Strain - Luminal Pressure = 0.125 MPa (color bar up to 0.35)

Figure 6.32: 2D Artery Model II - Highly Calcified Atherosclerotic Plaque - FEM (Axis Units: 1 mm)

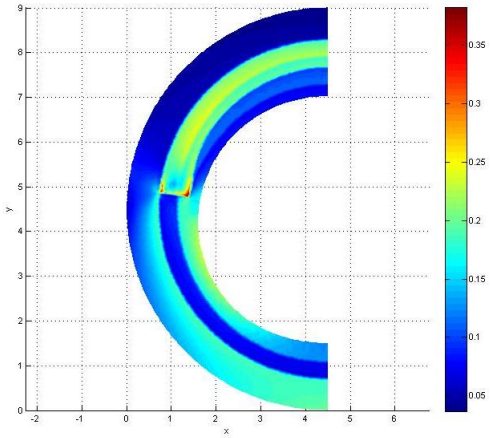

(a) von Mises Tension - Luminal Pressure = 0.055 MPa (color bar up to 0.35 MPa)

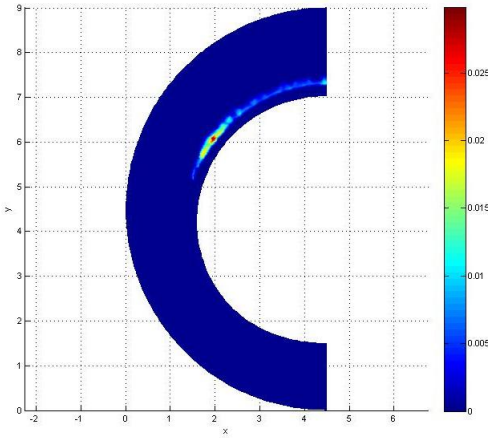

(b) Effective Plastic Strain - Luminal Pressure = 0.055 MPa (color bar up to 0.025)

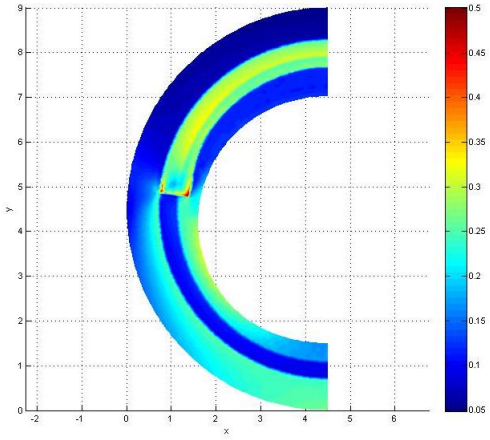

(c) von Mises Tension - Luminal Pressure = 0.08 MPa (color bar up to 0.5 MPa)

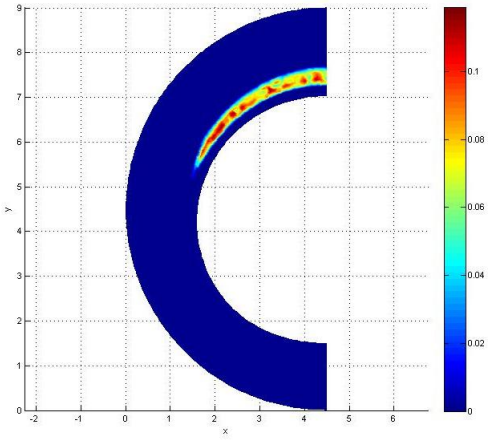

(d) Effective Plastic Strain - Luminal Pressure = 0.08 MPa (color bar up to 0.1)

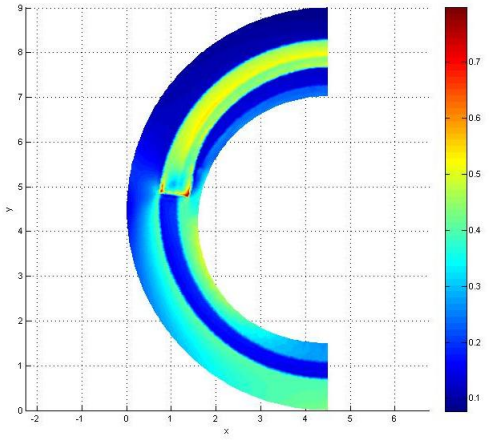

(e) von Mises Tension - Luminal Pressure = 0.125 MPa (color bar up to 0.7 MPa)

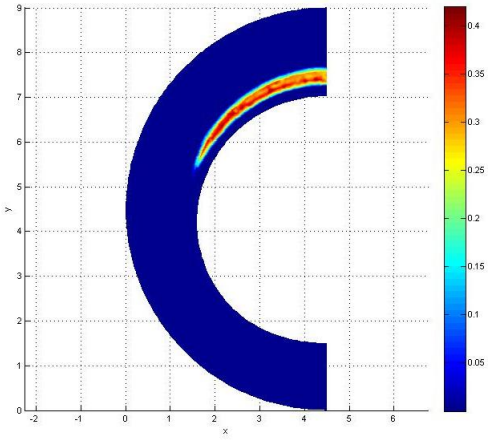

(f) Effective Plastic Strain - Luminal Pressure = 0.125 MPa (color bar up to 0.4)

Figure 6.33: 2D Artery Model II - Highly Calcified Atherosclerotic Plaque - RPIM (Axis Units: 1 mm)

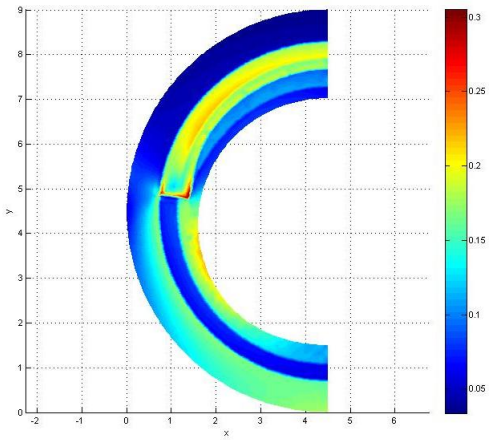

(a) von Mises Tension - Luminal Pressure = 0.055 MPa (color bar up to 0.3 MPa)

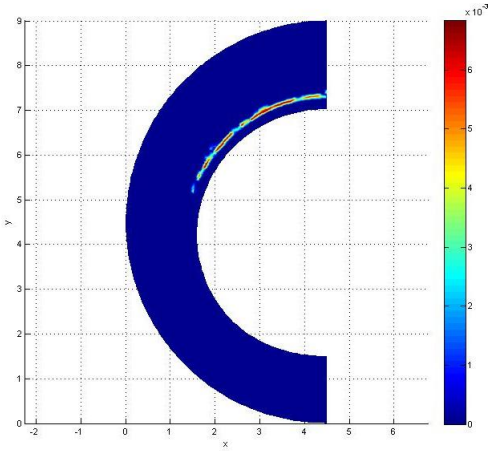

(b) Effective Plastic Strain - Luminal Pressure = 0.055 MPa (color bar up to 0.006)

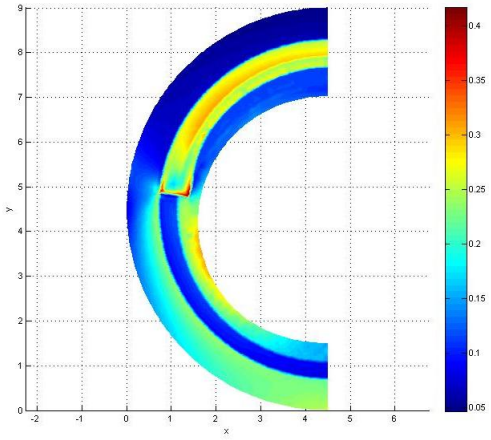

(c) von Mises Tension - Luminal Pressure = 0.08 MPa (color bar up to 0.4 MPa)

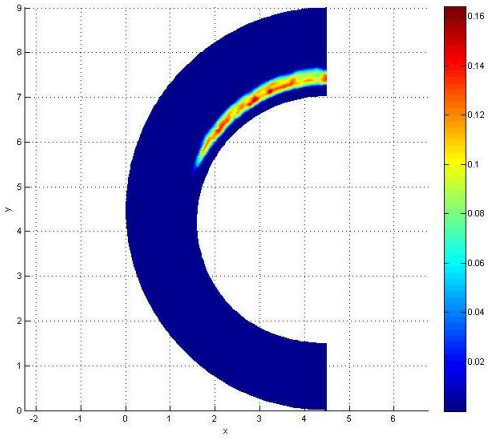

(d) Effective Plastic Strain - Luminal Pressure = 0.08 MPa (color bar up to 0.16)

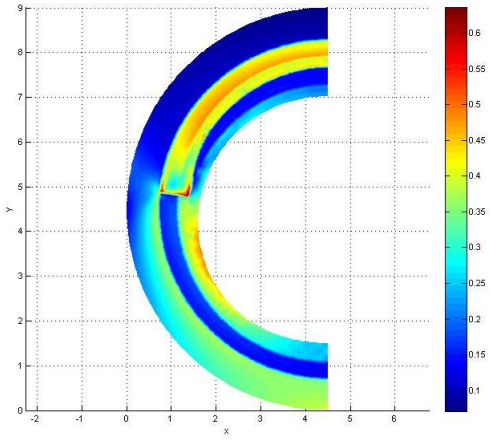

(e) von Mises Tension - Luminal Pressure = 0.125 MPa (color bar up to 0.6 MPa)

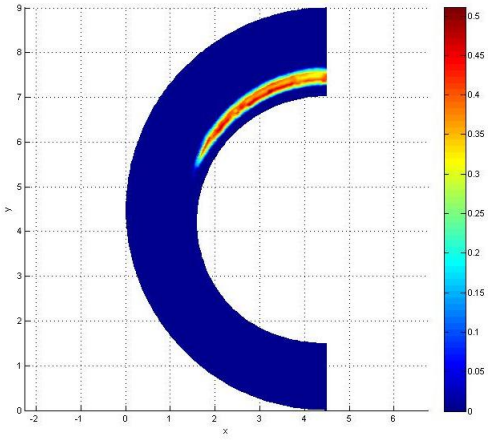

(f) Effective Plastic Strain - Luminal Pressure = 0.125 MPa (color bar up to 0.5)

Figure 6.34: 2D Artery Model II - Highly Calcified Atherosclerotic Plaque - NNRPIM (Axis Units: 1 mm)

6.2.2.4 Discussion

As in the previous model, Figures 6.23, 6.27 and 6.31 show the variation of the displacement in Oy as the luminal pressure rises. In these one can see a linear relation between the variables for points C and F, as their displacement is only affected by elastic materials. In comparison, points D and E whose displacement is affected by the atherosclerotic plaque show a non-linear progression as the pressure increases.

In Figure 6.35 it is compared the effects of each level of calcification on the displacement of point E. The results appear to be consistent among the numerical methods showing a small deviation between them starting around 0.06 MPa. While this results do not show the effect of atherosclerotic plaque material properties, they are more clearly seen with the analisys of the distance between point E and F, seen in Figure 6.36. The variation on this distance showed an increase in the material's stiffness as the level of calcification increases, as well as the expected change in behaviour as the material entered in plastic regime. This plastic state can also be seen in the Effective Plastic Strain fields shown before, in Figures 6.24, 6.25, 6.26, 6.28, 6.29, 6.30, 6.32, 6.33 and 6.34. As with the previous model, at normal systolic blood pressure (0.01867 MPa) [91] none of the atherosclerotic plaques would experience plastic deformations.

The von Mises Tension fields present, as seen in the previous example, a accumulation of tension in the interface between the damaged *media* and the healthy *media*. This behaviour is an effect of the sudden change of material properties between the tissues, which is not realistic. On the other hand the accumulation of tensions in the *intima*'s luminal wall is an effect of the high pressures the arteries was being subjected in order for the atherosclerotic plaque to suffer plastic deformation.

The three numerical methods results are coherent and similar between them. In Figure 6.37 it can be seen a comparison of the displacement of point E obtained from three numerical methods with each set of material properties. As the plot show, there is a good overlay between all numerical methods being it almost perfect on the analysis with the Moderately Calcified Plaque.

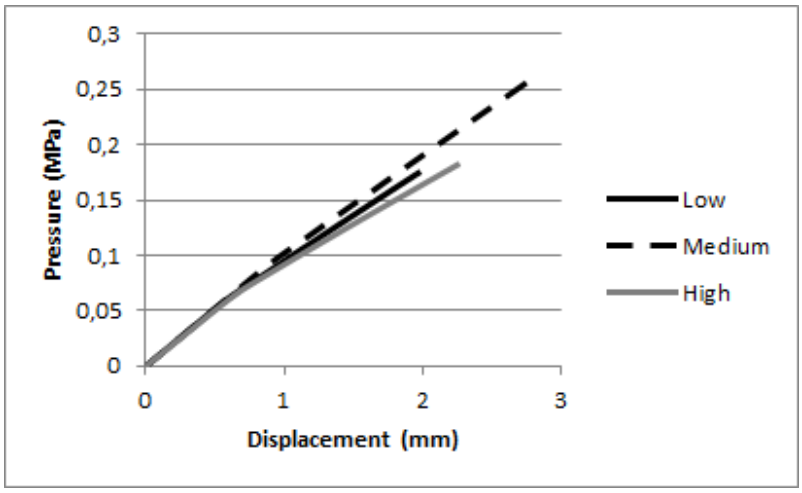

(a) Displacement obtained using FEM

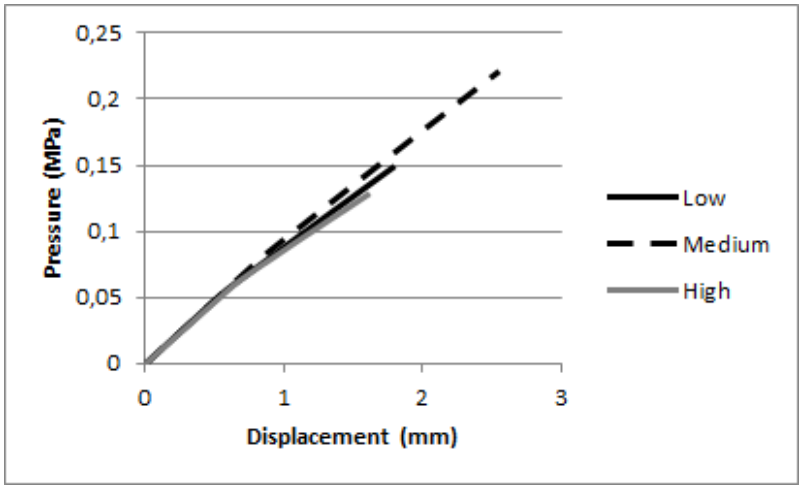

(b) Displacement obtained using RPIM

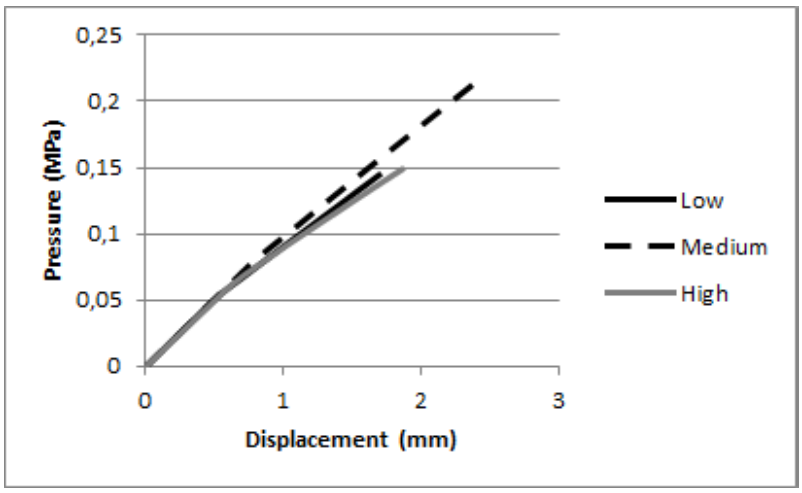

(c) Displacement obtained using NNRPIM

Figure 6.35: 2D Model II - Comparison of Displacements of Point E in different levels of calcification

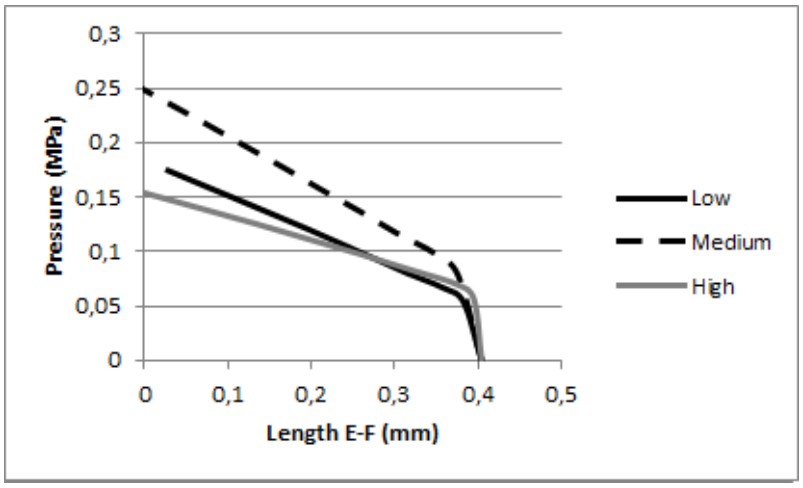

(a) Displacement obtained using FEM

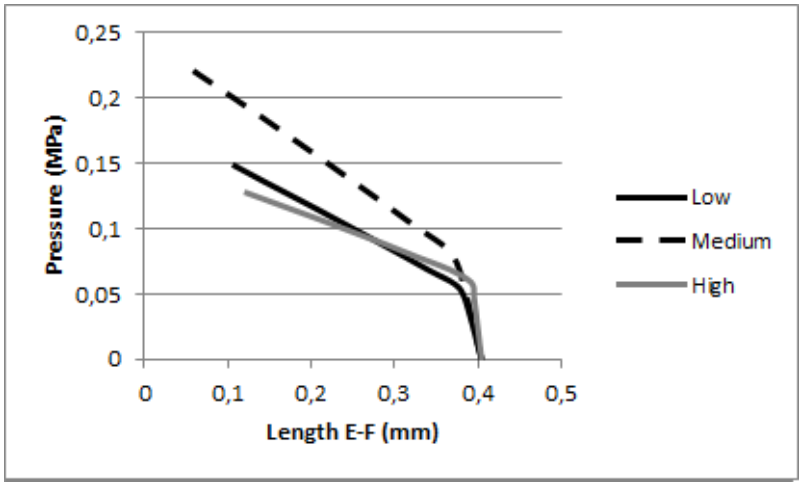

(b) Displacement obtained using RPIM

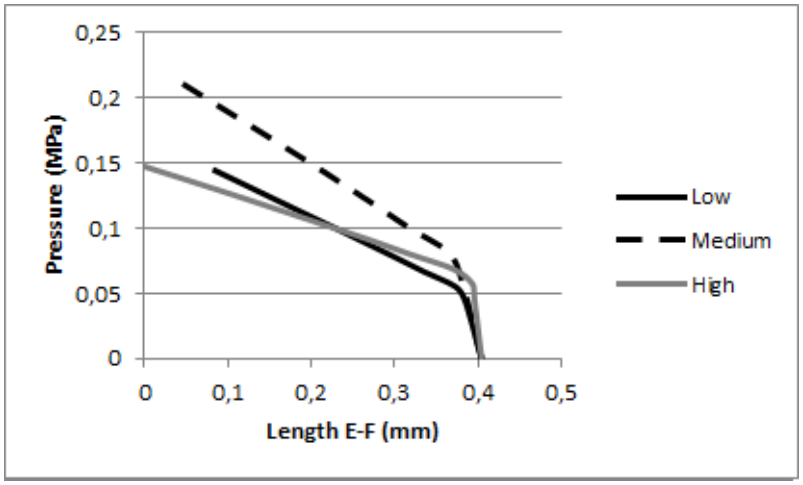

(c) Displacement obtained using NNRPIM

Figure 6.36: 2D Model II - Comparison of length of segment FE

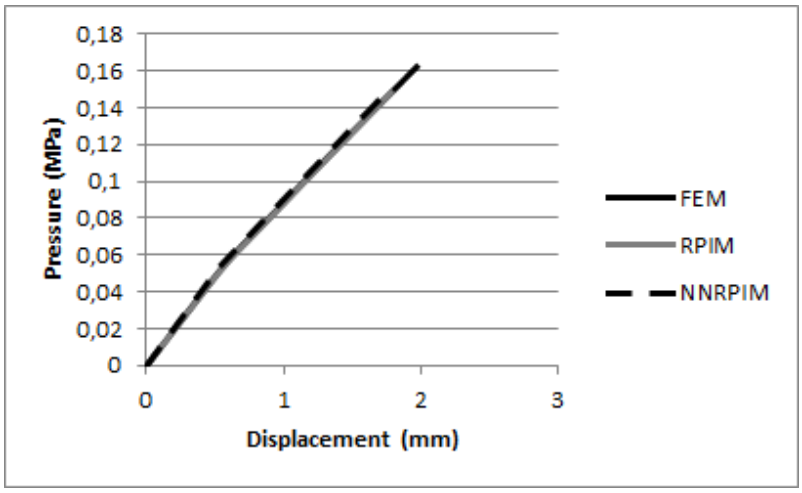

(a) Displacement obtained with the Lightly Calcified material properties

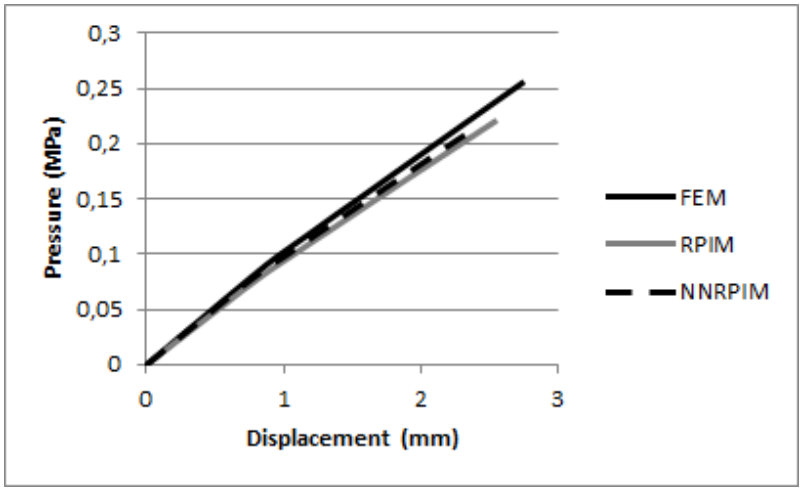

(b) Displacement obtained with the Moderately Calcified material properties

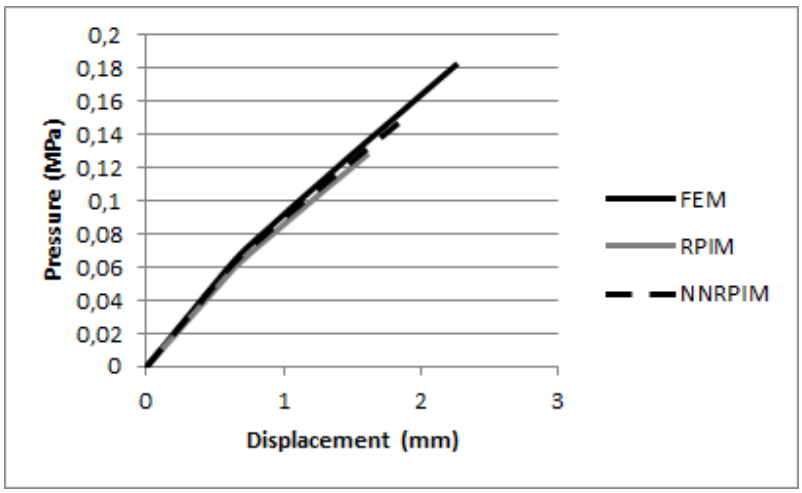

(c) Displacement obtained with the Heavily Calcified material properties

Figure 6.37: 2D Model II - Comparison of displacement of point E with different numerical methods

6.2.3 2D Model III

For this example it was taken into consideration a solid domain $\omega \in \Re^2$ representing a atherosclerotic artery containing a thin segmented plaque. It was applied to the domain symmetry constrains and fixed the node (x,y)=(4.5,0). The numerical model was designed using 4097 nodes and was analysed using three different numerical methods (FEM, RPIM and NNRPIM). An image of the nodal distribution used can be seen in Figure 6.38

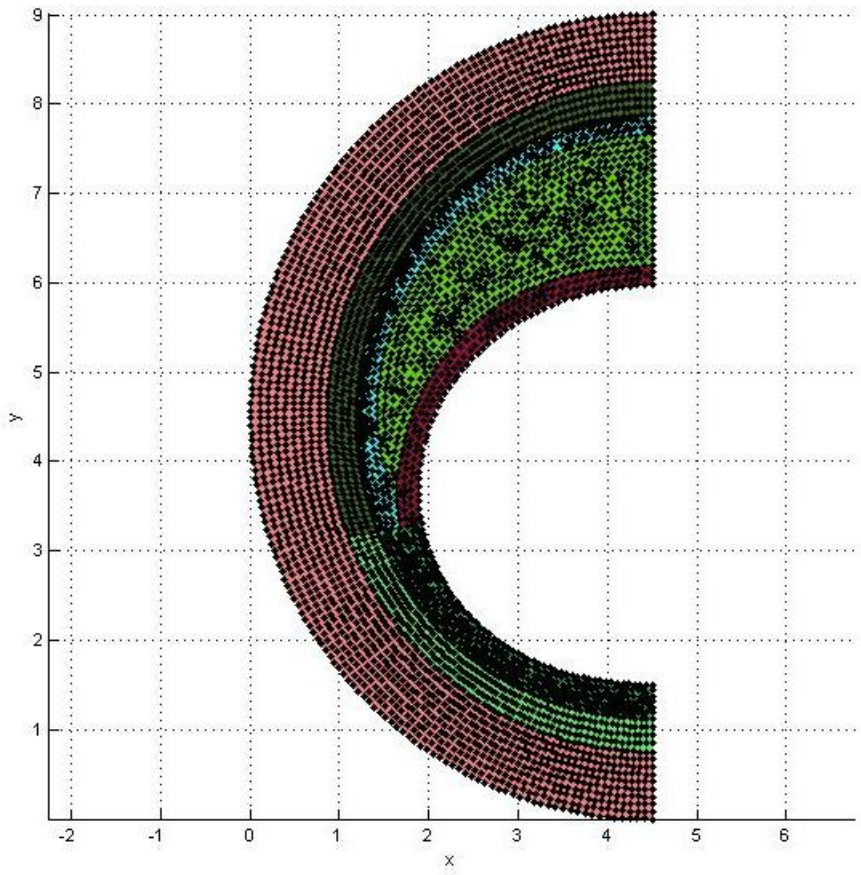

Figure 6.38: 2D Model of Artery with Atherosclerotic Plaque - Stage III (Axis Units: 1 mm)

The von Mises Stress field and Effective Plastic Strain Field were analysed for each of the atherosclerotic plaque set of material properties. Besides this, it was also analysed the displacement in Oy in specific interface nodes between tissues. The location of these nodes can be seen in the diagram of Figure 6.39. The displacement seen was analysed against to the pressure applied in the artery's lumen.

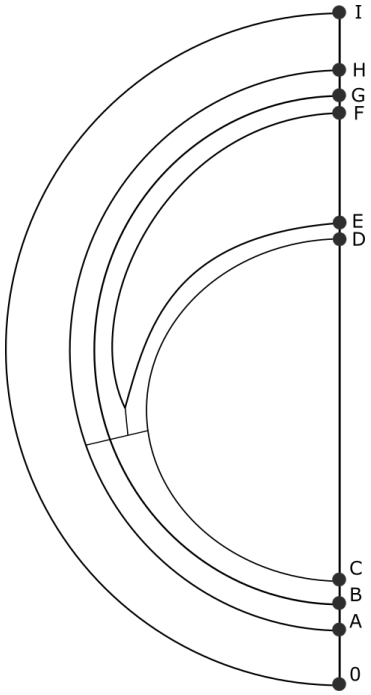

Figure 6.39: 2D Model Stage III - Points location

6.2.3.1 Lightly Calcified

The following plots represent the relation between the internal luminal pressure and the displacement seen in points C, D, E and F.

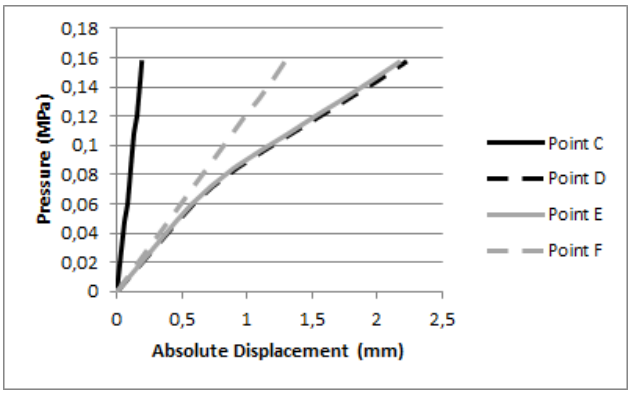

(a) Displacement obtained using FEM

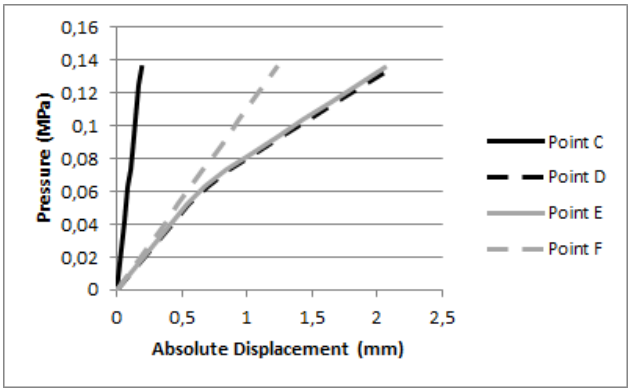

(b) Displacement obtained using RPIM

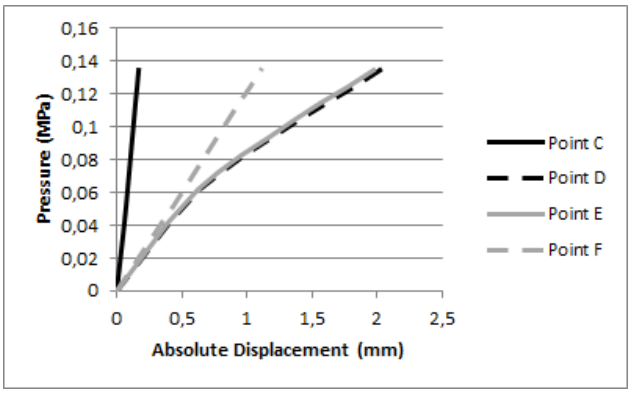

(c) Displacement obtained using NNRPIM

Figure 6.40: 2D Model III - Lightly Calcified - Displacement in Oy vs. Luminal Pressure

The following von Mises Stress Fields and Effective Plastic Strain Fields were also obtained. It can be seen 3 different stages of the plastic deformation progression starting when the Yield Pressure was met.

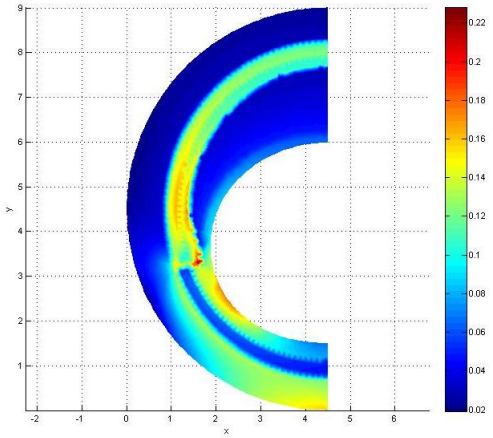

(a) von Mises Tension - Luminal Pressure = 0.05 MPa (color bar up to 0.22 MPa)

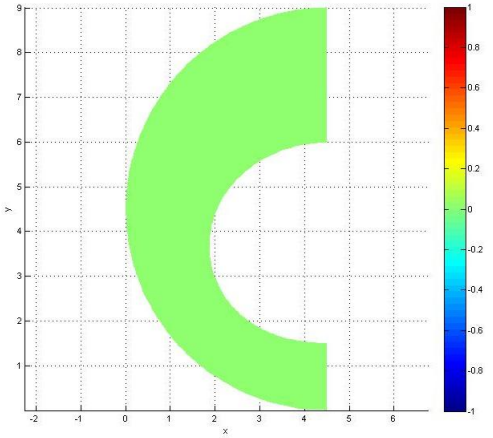

(b) Effective Plastic Strain - Luminal Pressure = 0.05 MPa (no significant values)

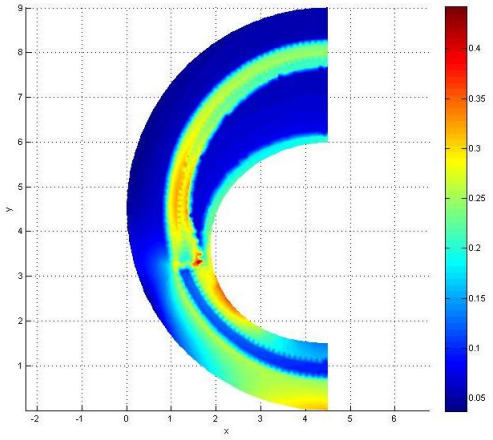

(c) von Mises Tension - Luminal Pressure = 0.095 MPa (color bar up to 0.4 MPa)

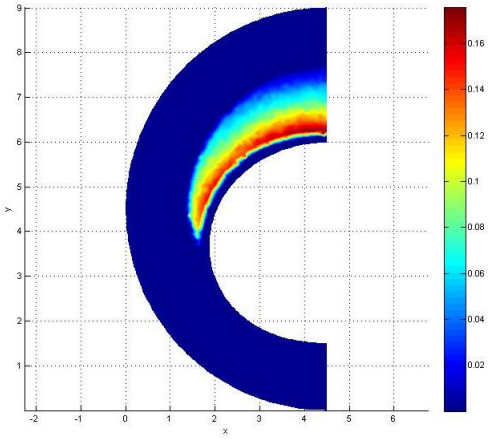

(d) Effective Plastic Strain - Luminal Pressure = 0.095 MPa (color bar up to 0.16)

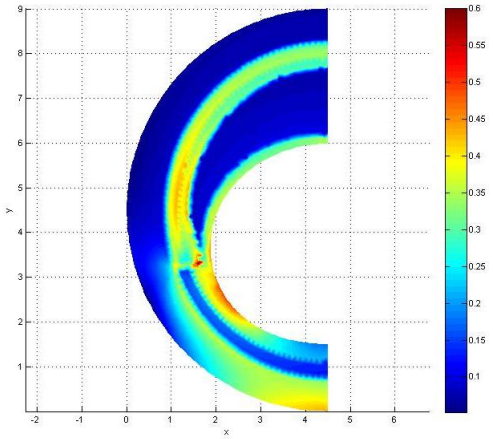

(e) von Mises Tension - Luminal Pressure = 0.135 MPa (color bar up to 0.6 MPa)

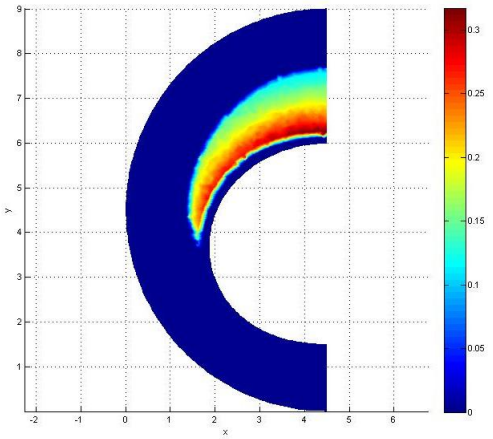

(f) Effective Plastic Strain - Luminal Pressure = 0.135 MPa (color bar up to 0.3)

Figure 6.41: 2D Artery Model III - Lightly Calcified Atherosclerotic Plaque - FEM (Axis Units: 1 mm)

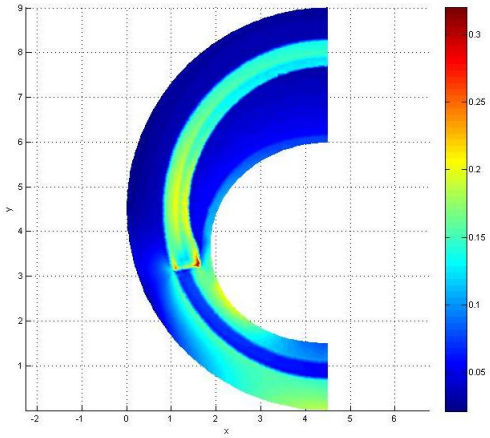

(a) von Mises Tension - Luminal Pressure = 0.05 MPa (color bar up to 0.3 MPa)

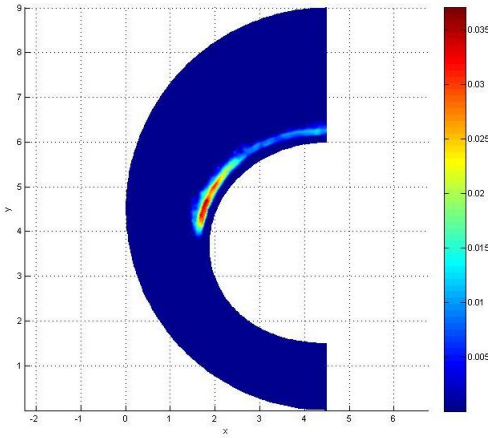

(b) Effective Plastic Strain - Luminal Pressure = 0.05 MPa (color bar up to 0.035)

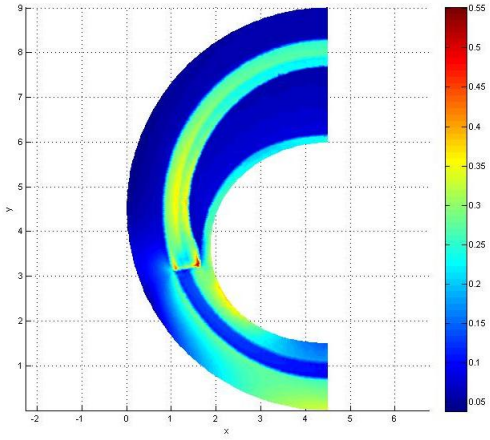

(c) von Mises Tension - Luminal Pressure = 0.095 MPa (color bar up to 0.55 MPa)

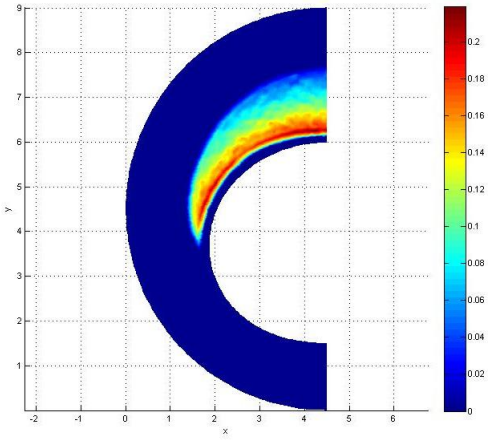

(d) Effective Plastic Strain - Luminal Pressure = 0.095 MPa (color bar up to 0.2)

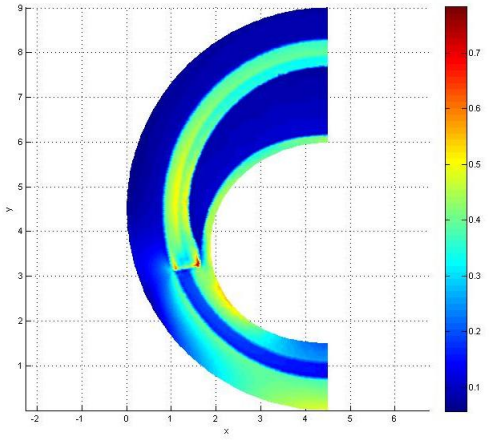

(e) von Mises Tension - Luminal Pressure = 0.135 MPa (color bar up to 0.7 MPa)

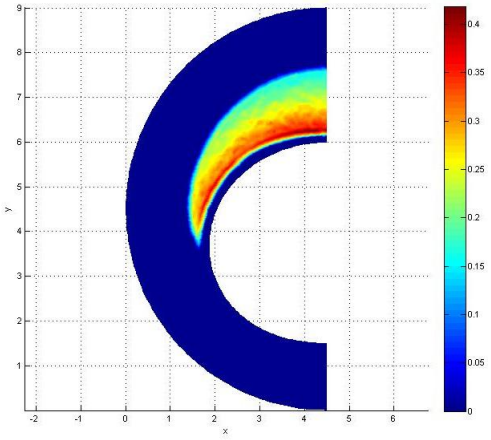

(f) Effective Plastic Strain - Luminal Pressure = 0.135 MPa (color bar up to 0.4)

Figure 6.42: 2D Artery Model III - Lightly Calcified Atherosclerotic Plaque - RPIM (Axis Units: 1 mm)

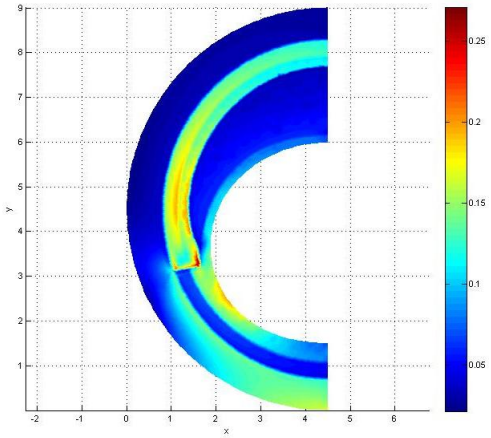

(a) von Mises Tension - Luminal Pressure = 0.05 MPa (color bar up to 0.25 MPa)

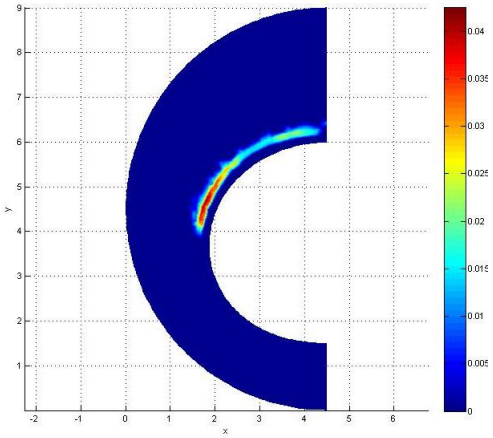

(b) Effective Plastic Strain - Luminal Pressure = 0.05 MPa (color bar up to 0.04)

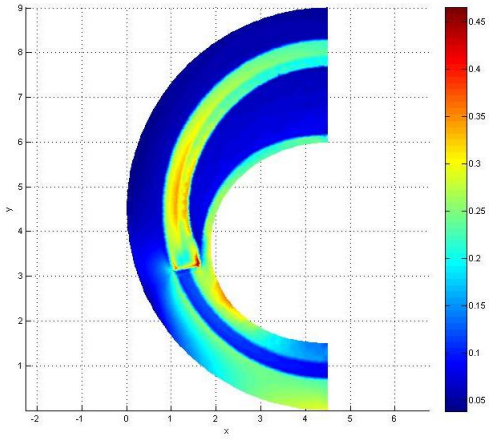

(c) von Mises Tension - Luminal Pressure = 0.095 MPa (color bar up to 0.45 MPa)

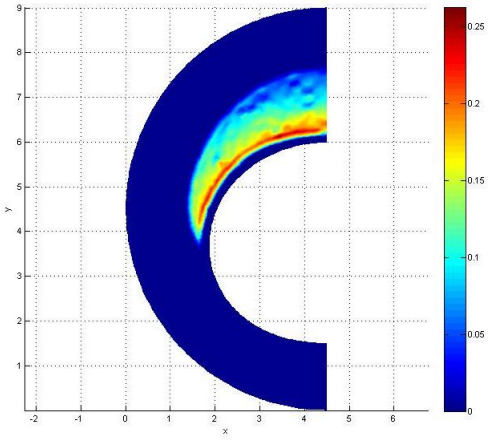

(d) Effective Plastic Strain - Luminal Pressure = 0.095 MPa (color bar up to 0.25)

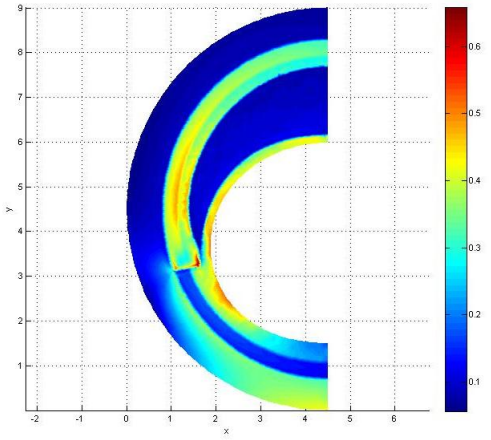

(e) von Mises Tension - Luminal Pressure = 0.135 MPa (color bar up to 0.6 MPa)

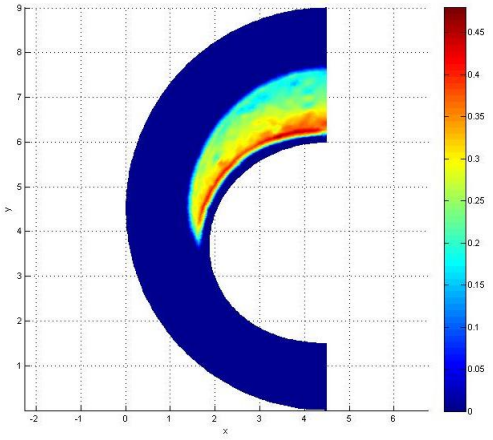

(f) Effective Plastic Strain - Luminal Pressure = 0.135 MPa (color bar up to 0.45)

Figure 6.43: 2D Artery Model III - Lightly Calcified Atherosclerotic Plaque - NNRPIM (Axis Units: 1 mm)

6.2.3.2 Moderately Calcified

The following plots represent the relation between the internal luminal pressure and the displacement seen in points C, D, E and F.

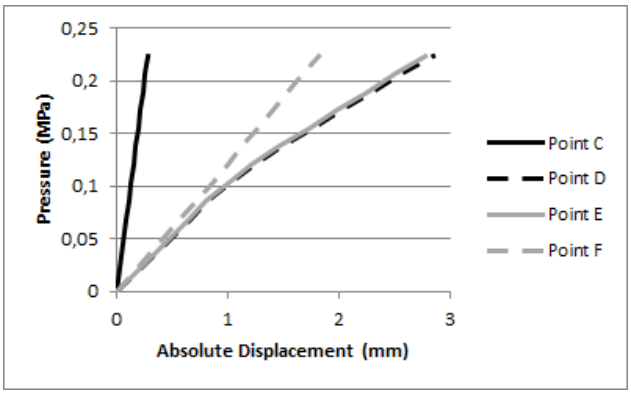

(a) Displacement obtained using FEM

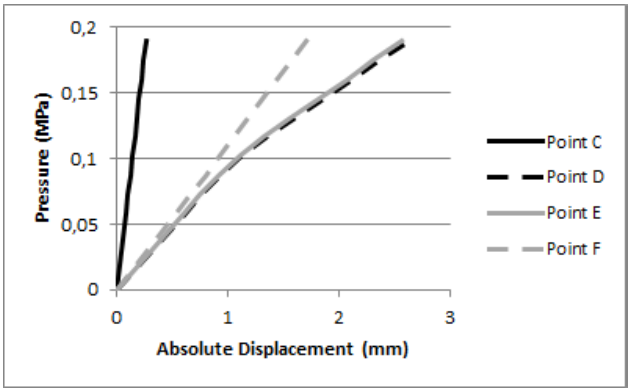

(b) Displacement obtained using RPIM

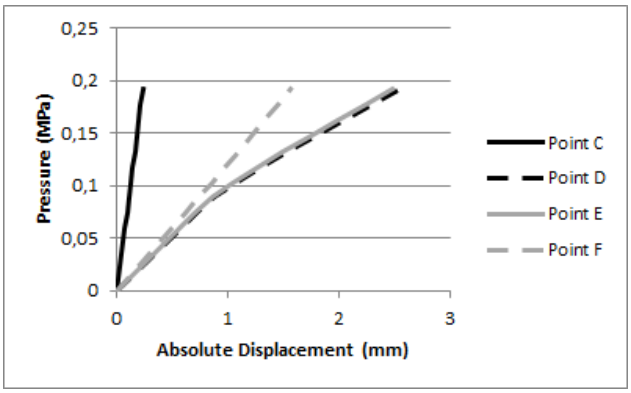

(c) Displacement obtained using NNRPIM

Figure 6.44: 2D Model III - Moderately Calcified - Displacement in Oy vs. Luminal Pressure

The following von Mises Stress Fields and Effective Plastic Strain Fields were also obtained. It can be seen 3 different stages of the plastic deformation progression starting when the Yield Pressure was met.

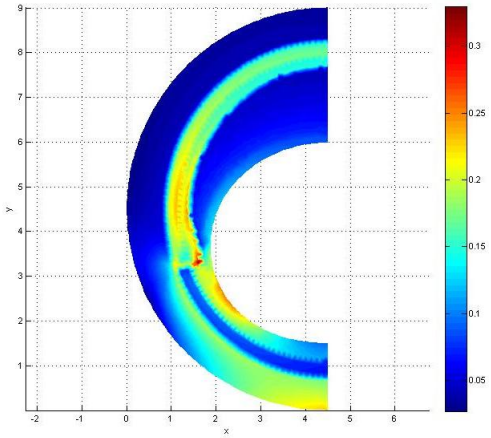

(a) von Mises Tension - Luminal Pressure = 0.07 MPa (color bar up to 0.3 MPa)

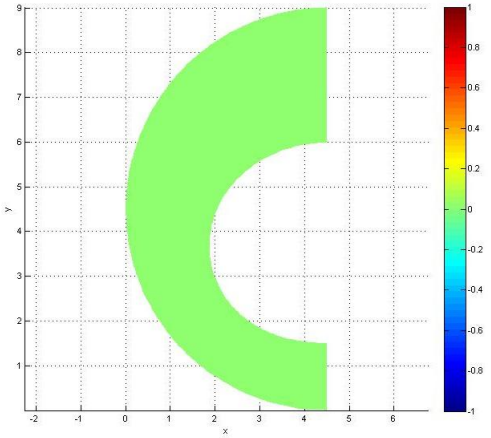

(b) Effective Plastic Strain - Luminal Pressure = 0.07 MPa (no significant values)

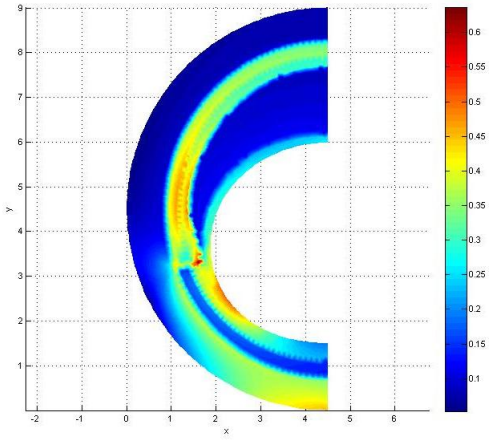

(c) von Mises Tension - Luminal Pressure = 0.13 MPa (color bar up to 0.6 MPa)

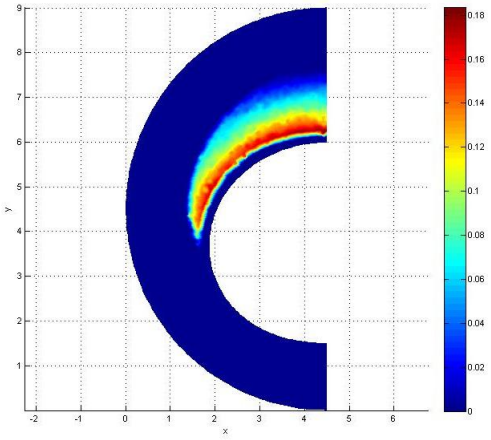

(d) Effective Plastic Strain - Luminal Pressure = 0.13 MPa (color bar up to 0.18)

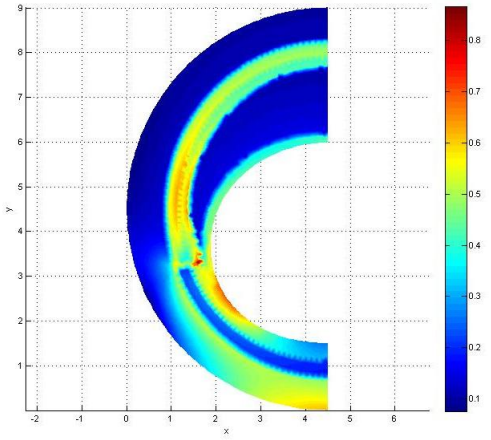

(e) von Mises Tension - Luminal Pressure = 0.19 MPa (color bar up to 0.8 MPa)

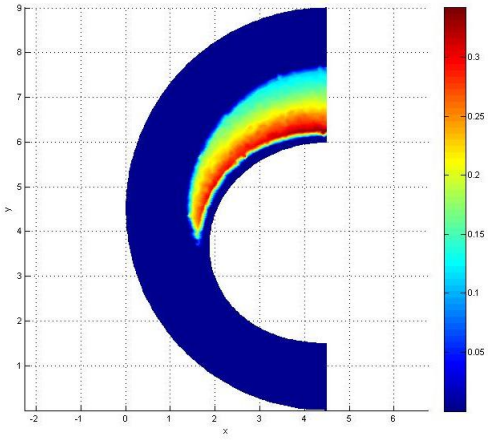

(f) Effective Plastic Strain - Luminal Pressure = 0.19 MPa (color bar up to 0.3)

Figure 6.45: 2D Artery Model III - Medially Calcified Atherosclerotic Plaque - FEM (Axis Units: 1 mm)

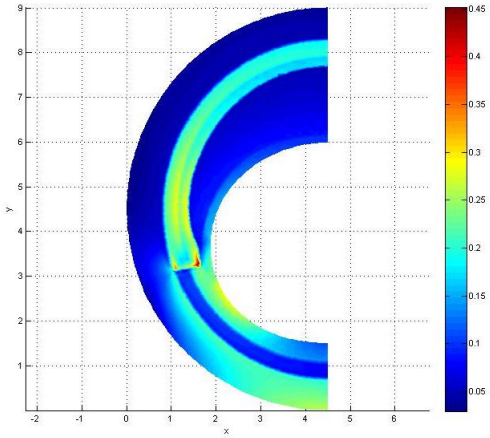

(a) von Mises Tension - Luminal Pressure = 0.07 MPa (color bar up to 0.45 MPa)

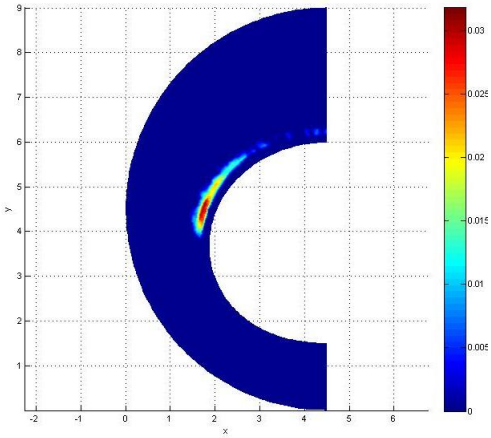

(b) Effective Plastic Strain - Luminal Pressure = 0.07 MPa (color bar up to 0.03)

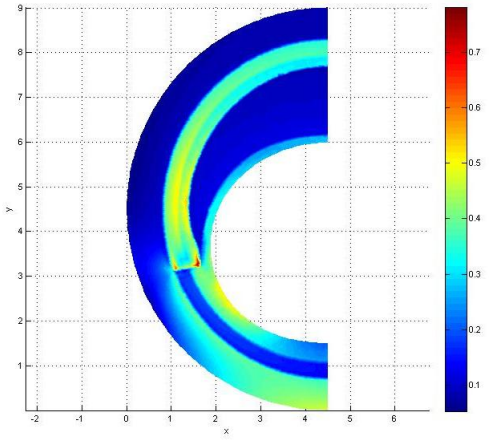

(c) von Mises Tension - Luminal Pressure = 0.13 MPa (color bar up to 0.7 MPa)

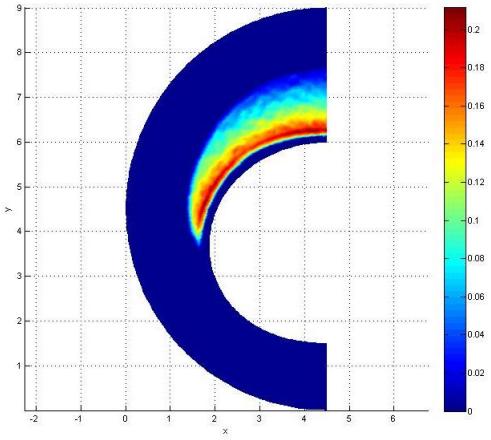

(d) Effective Plastic Strain - Luminal Pressure = 0.13 MPa (color bar up to 0.2)

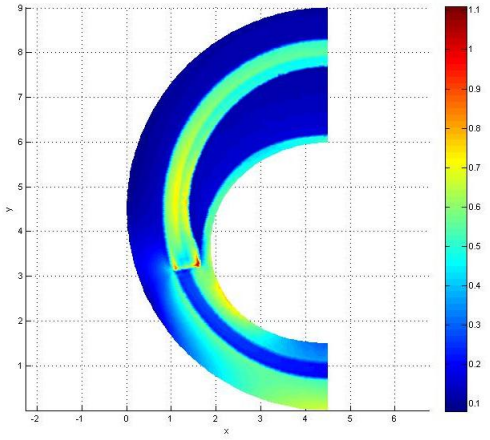

(e) von Mises Tension - Luminal Pressure = 0.19 MPa (color bar up to 1.1 MPa)

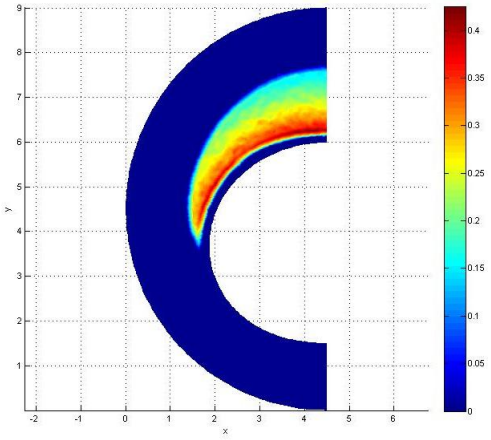

(f) Effective Plastic Strain - Luminal Pressure = 0.19 MPa (color bar up to 0.4)

Figure 6.46: 2D Artery Model III - Medially Calcified Atherosclerotic Plaque - RPIM (Axis Units: 1 mm)

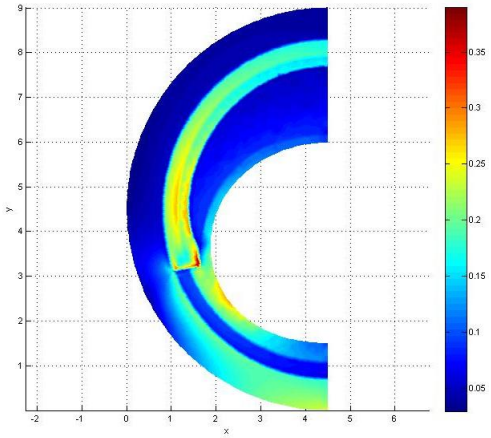

(a) von Mises Tension - Luminal Pressure = 0.07 MPa (color bar up to 0.35 MPa)

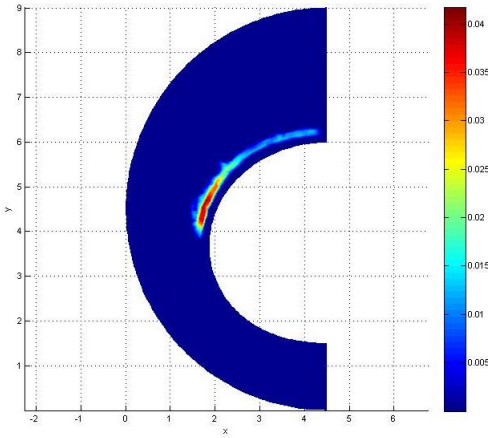

(b) Effective Plastic Strain - Luminal Pressure = 0.07 MPa (color bar up to 0.04)

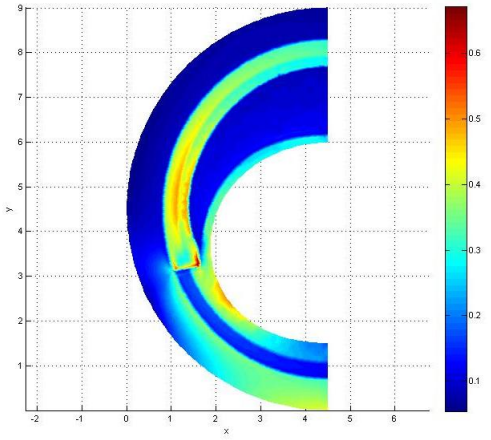

(c) von Mises Tension - Luminal Pressure = 0.13 MPa (color bar up to 0.6 MPa)

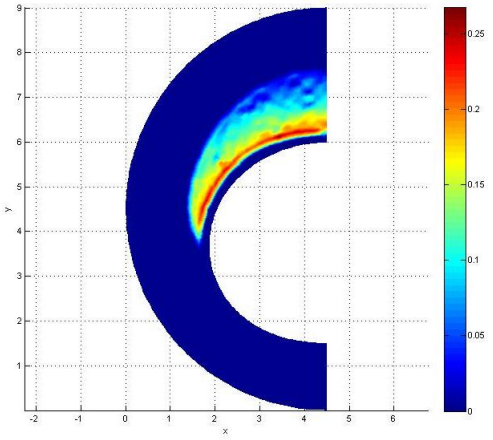

(d) Effective Plastic Strain - Luminal Pressure = 0.13 MPa (color bar up to 0.25)

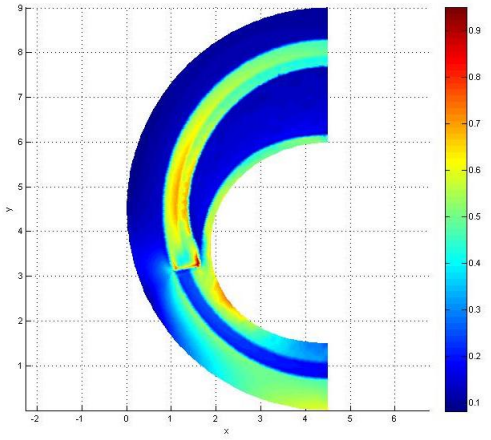

(e) von Mises Tension - Luminal Pressure = 0.19 MPa (color bar up to 0.9 MPa)

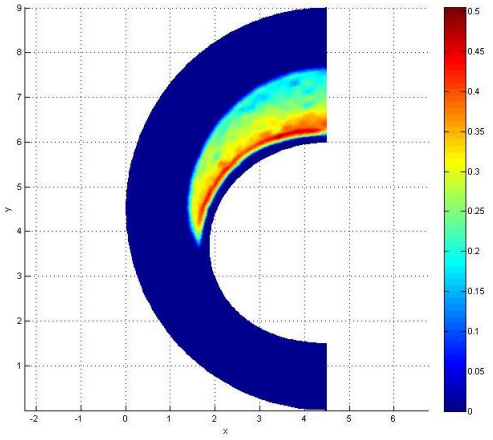

(f) Effective Plastic Strain - Luminal Pressure = 0.19 MPa (color bar up to 0.5)

Figure 6.47: 2D Artery Model III - Medially Calcified Atherosclerotic Plaque - NNRPIM (Axis Units: 1 mm)

6.2.3.3 Heavily Calcified

The following plots represent the relation between the internal luminal pressure and the displacement seen in points C, D, E and F.

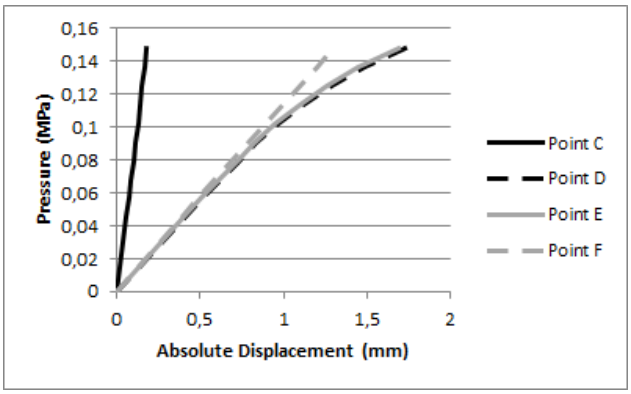

(a) Displacement obtained using FEM

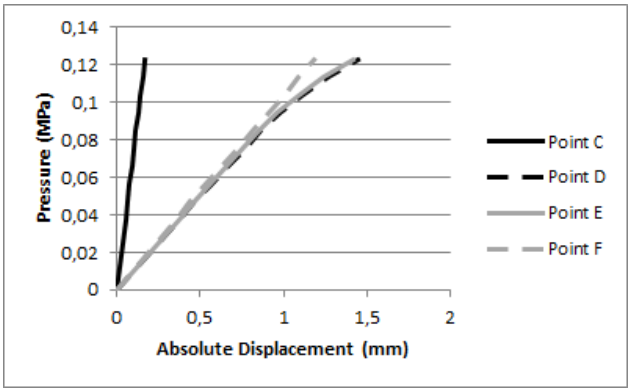

(b) Displacement obtained using RPIM

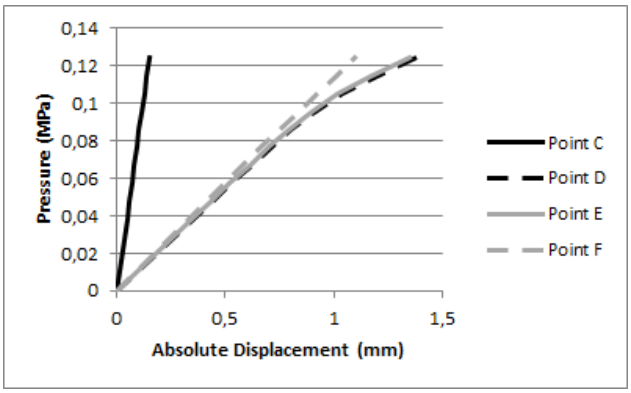

(c) Displacement obtained using NNRPIM

Figure 6.48: 2D Model III - Heavily Calcified - Displacement in Oy vs. Luminal Pressure

The following von Mises Stress Fields and Effective Plastic Strain Fields were also obtained. It can be seen 3 different stages of the plastic deformation progression starting when the Yield Pressure was met.

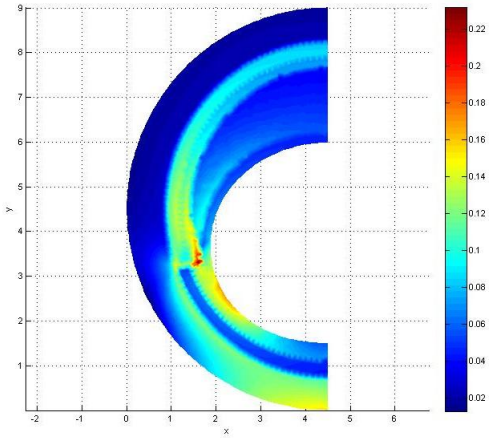

(a) von Mises Tension - Luminal Pressure = 0.045 MPa (color bar up to 0.22 MPa)

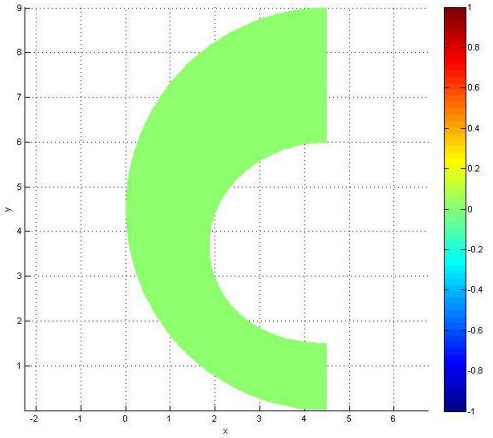

(b) Effective Plastic Strain - Luminal Pressure = 0.045 MPa (no significant values)

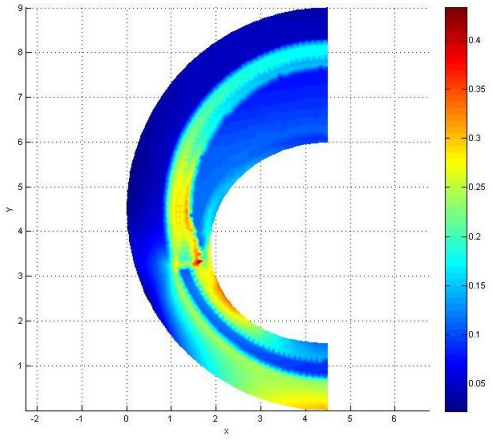

(c) von Mises Tension - Luminal Pressure = 0.085 MPa (color bar up to 0.4 MPa)

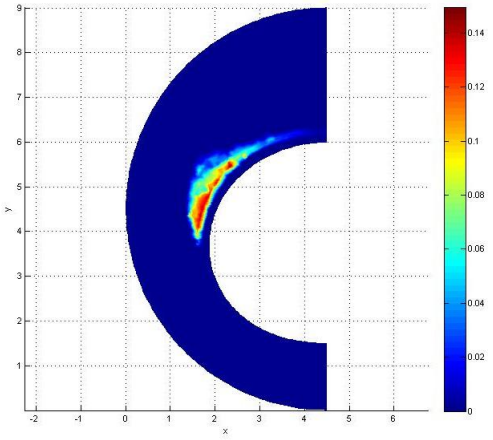

(d) Effective Plastic Strain - Luminal Pressure = 0.085 MPa (color bar up to 0.14)

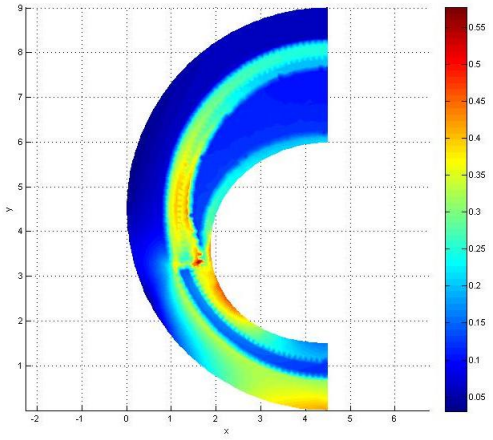

(e) von Mises Tension - Luminal Pressure = 0.125 MPa (color bar up to 0.55 MPa)

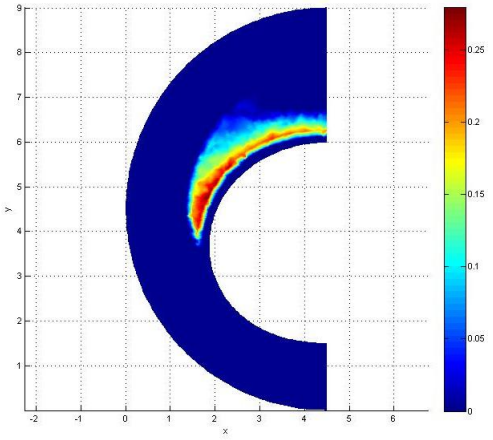

(f) Effective Plastic Strain - Luminal Pressure = 0.125 MPa (color bar up to 0.25)

Figure 6.49: 2D Artery Model III - Highly Calcified Atherosclerotic Plaque - FEM (Axis Units: 1 mm)

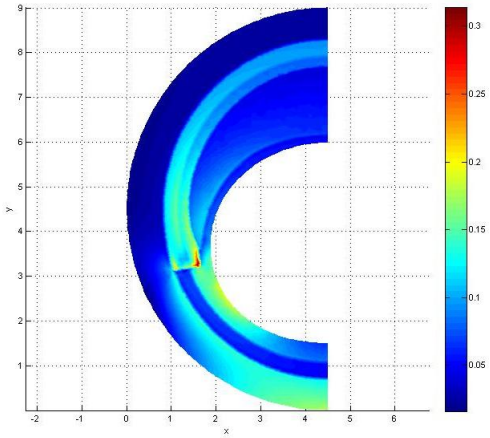

(a) von Mises Tension - Luminal Pressure = 0.045 MPa (color bar up to 0.3 MPa)

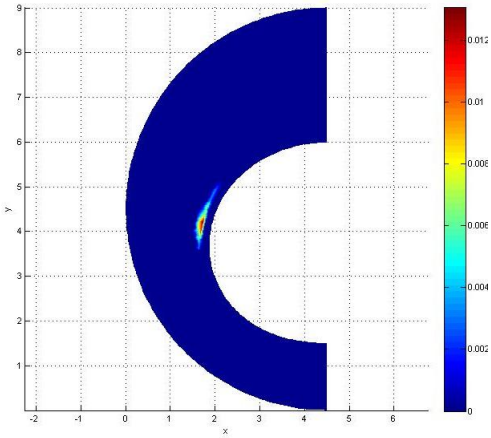

(b) Effective Plastic Strain - Luminal Pressure = 0.045 MPa (color bar up to 0.012)

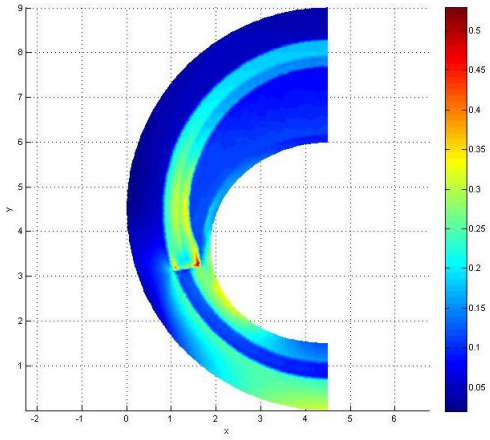

(c) von Mises Tension - Luminal Pressure = 0.085 MPa (color bar up to 0.5 MPa)

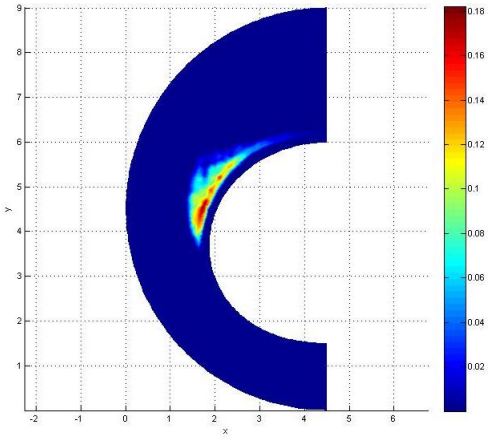

(d) Effective Plastic Strain - Luminal Pressure = 0.085 MPa (color bar up to 0.18)

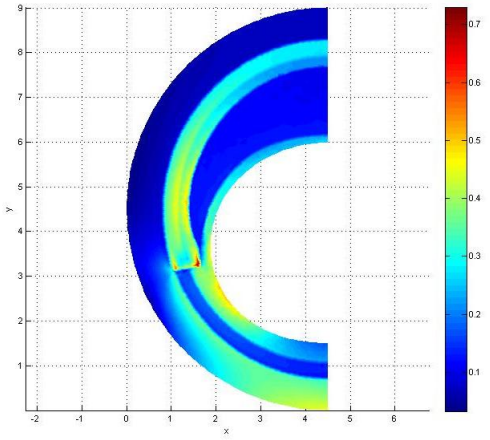

(e) von Mises Tension - Luminal Pressure = 0.125 MPa (color bar up to 0.7 MPa)

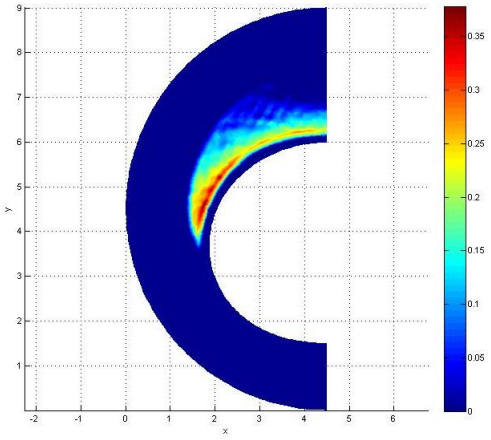

(f) Effective Plastic Strain - Luminal Pressure = 0.125 MPa (color bar up to 0.35)

Figure 6.50: 2D Artery Model III - Highly Calcified Atherosclerotic Plaque - RPIM (Axis Units: 1 mm)

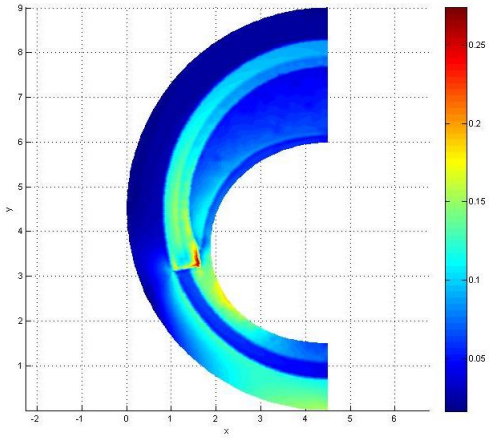

(a) von Mises Tension - Luminal Pressure = 0.045 MPa (color bar up to 0.25 MPa)

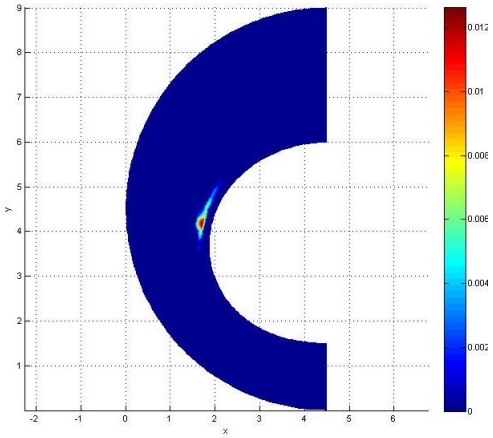

(b) Effective Plastic Strain - Luminal Pressure = 0.045 MPa (color bar up to 0.012)

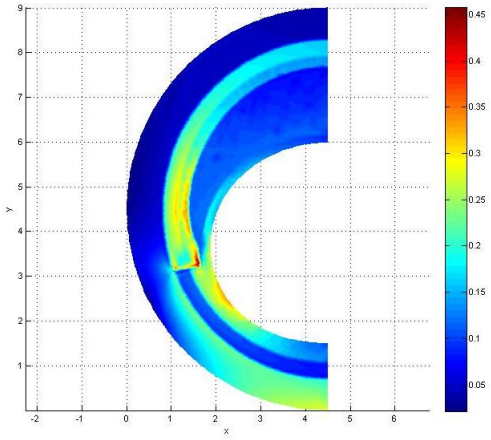

(c) von Mises Tension - Luminal Pressure = 0.085 MPa (color bar up to 0.45 MPa)

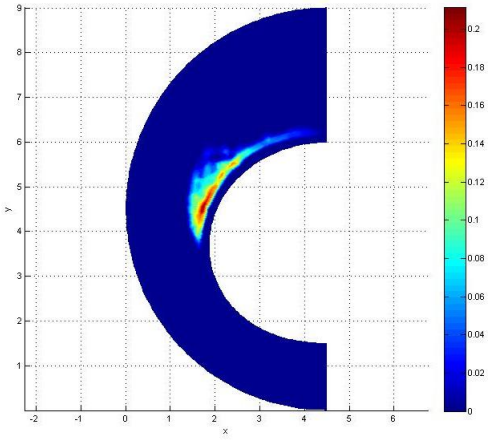

(d) Effective Plastic Strain - Luminal Pressure = 0.085 MPa (color bar up to 0.2)

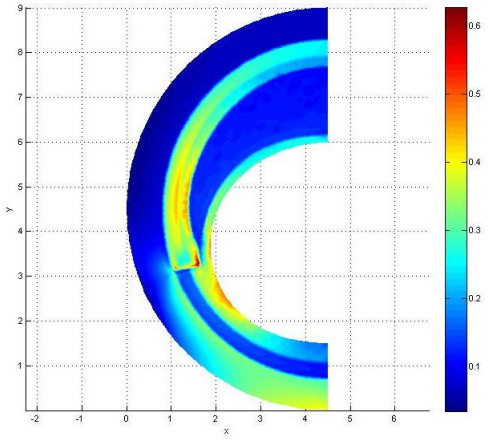

(e) von Mises Tension - Luminal Pressure = 0.125 MPa (color bar up to 0.6 MPa)

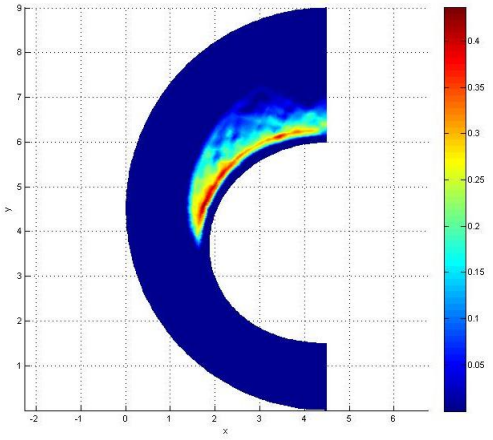

(f) Effective Plastic Strain - Luminal Pressure = 0.125 MPa (color bar up to 0.4)

Figure 6.51: 2D Artery Model III - Highly Calcified Atherosclerotic Plaque - NNRPIM (Axis Units: 1 mm)

6.2.3.4 Discussion

In Figures 6.40, 6.44 and 6.48, it can be seen that points whose displacement is only affected by elastic materials, as it is the case of point C and F, show a linear displacement relation with the luminal pressure. Similarly to previous examples, points D and E have their movement affected by the atherosclerotic plaque and , as this model presents a thicker plaque, they start to show more clear non-linear progression in their displacement as the pressure increases. By comparison of these graphs, as shown in Figure 6.52, it is possible to see that the atherosclerotic plaque differences in yield stress start to be seen more distinctly. The Lightly Calcified plaque starts to yield at around 0.06 MPa and the Medially and Heavily Calcified Plaques start to show that change at around 0.1 MPa.

The analysis of the distance between point E and F evidences this even further, seen in Figure 6.53. The results clearly show an increase in the stiffness of the material as the level of calcification increases. In this case the results show, at it would be expect, the yield point of the lightly, moderately and heavily calcified plaques at around 0.055 MPa, 0.085 MPa and 0.11 MPa, respectivily. As with the previous models, at normal systolic blood pressure (0.01867 MPa) [91] none of the atherosclerotic plaques would experience plastic deformations.

In the von Mises Stress Fields and the Effective Plastic Strain Fields images (Figures 6.41, 6.42, 6.43, 6.45, 6.46, 6.47, 6.49, 6.50 and 6.51) it can be seen that, as it should be expected, the tensions inside the atherosclerotic plaque are higher near the lumen, showing also a higher level of plastic deformation. It can also be see in the fields obtained from the heavily calcified plaque that the plastic deformations appear to start the lateral side of the plaque were the thickness is smaller and as the pressure rises start to affect a more central area. As with the previous examples the von Mises Tension fields show a non-realistic accumulation of tension in the interface between the damaged *media* and the healthy *media*.

In Figure 6.54 it can be seen a comparison of the displacement of point E obtained from three numerical methods with each set of material properties. As it can be seen with the previous examples, the results are coherent and similar between them.

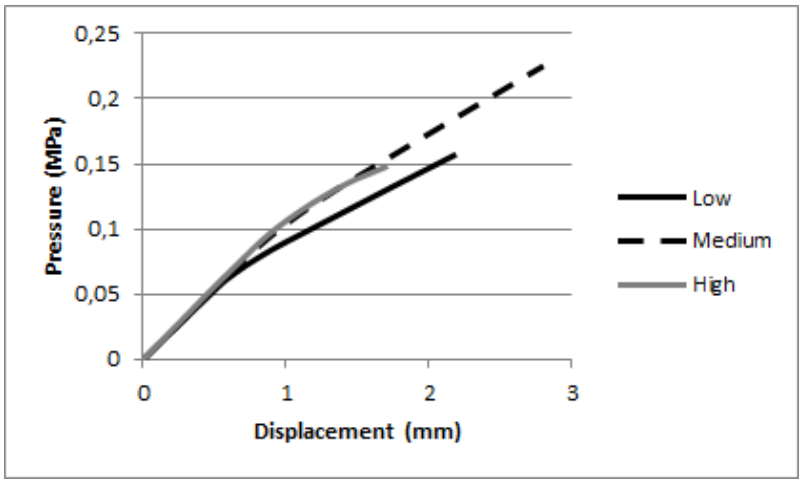

(a) Displacement obtained using FEM

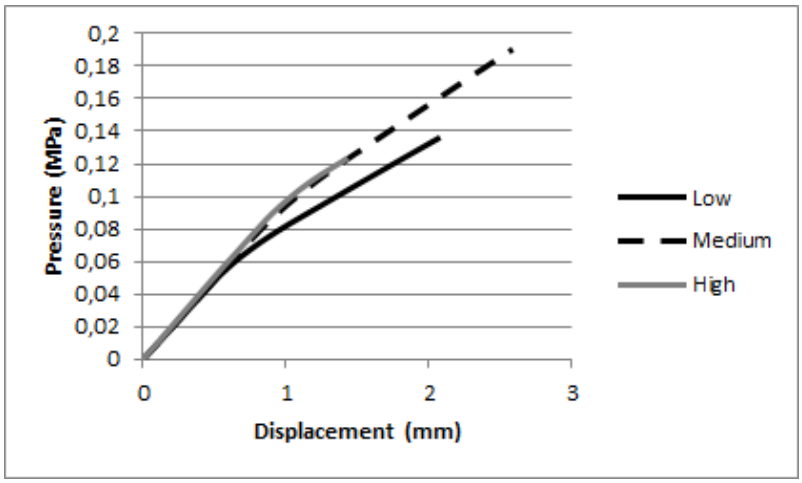

(b) Displacement obtained using RPIM

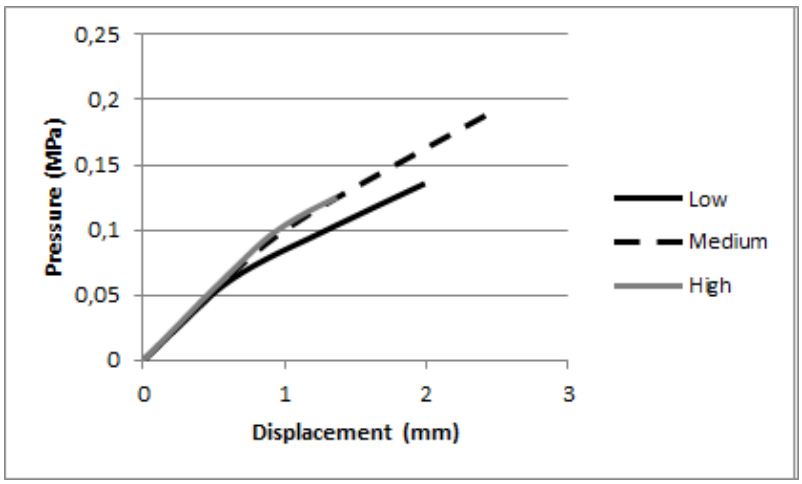

(c) Displacement obtained using NNRPIM

Figure 6.52: 2D Model III - Comparison of Displacements of Point E in different levels of calcification

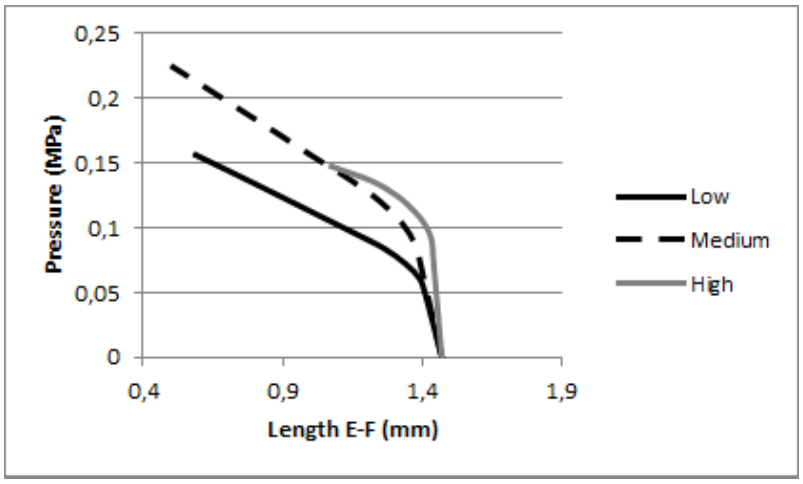

(a) Displacement obtained using FEM

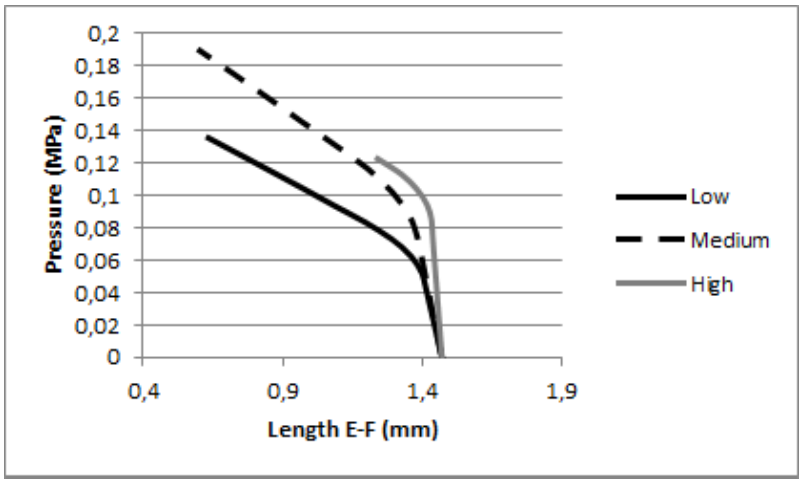

(b) Displacement obtained using RPIM

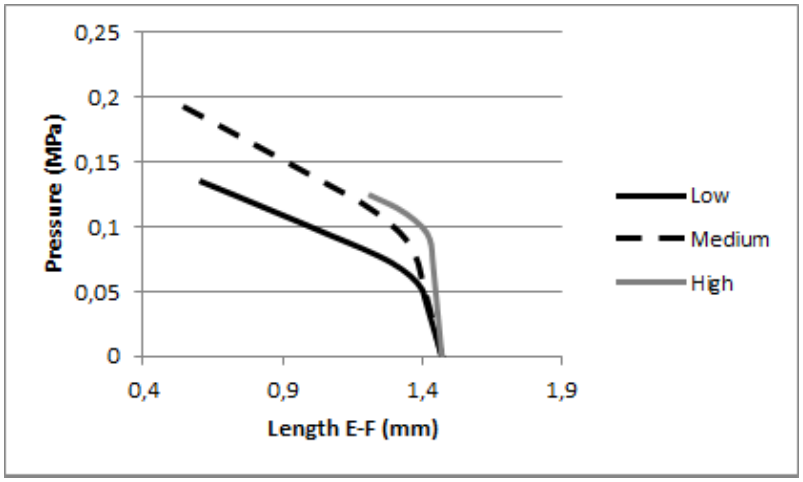

(c) Displacement obtained using NNRPIM

Figure 6.53: 2D Model III - Comparison of length of segment FE

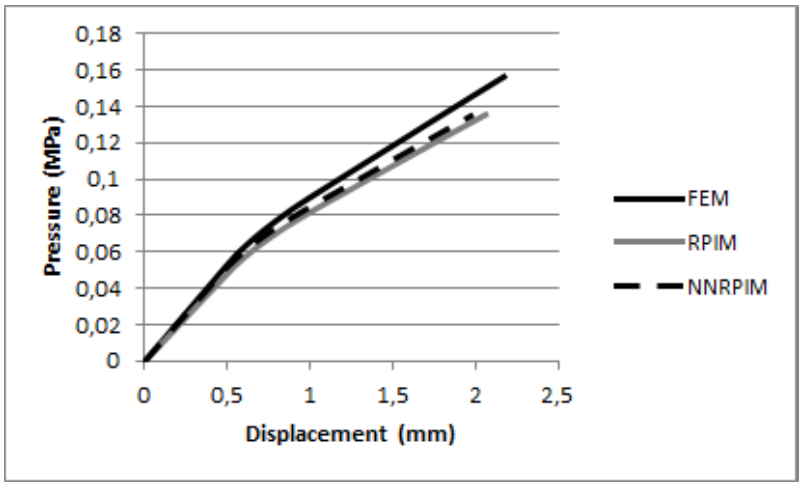

(a) Displacement obtained with the Lightly Calcified material properties

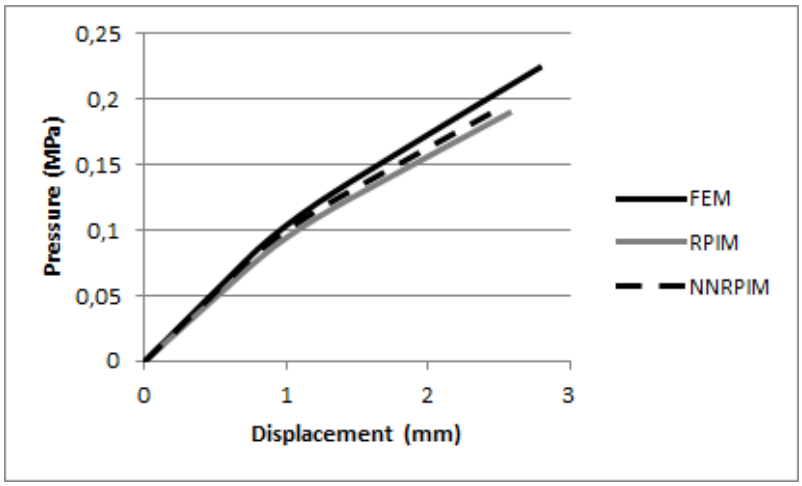

(b) Displacement obtained with the Moderately Calcified material properties

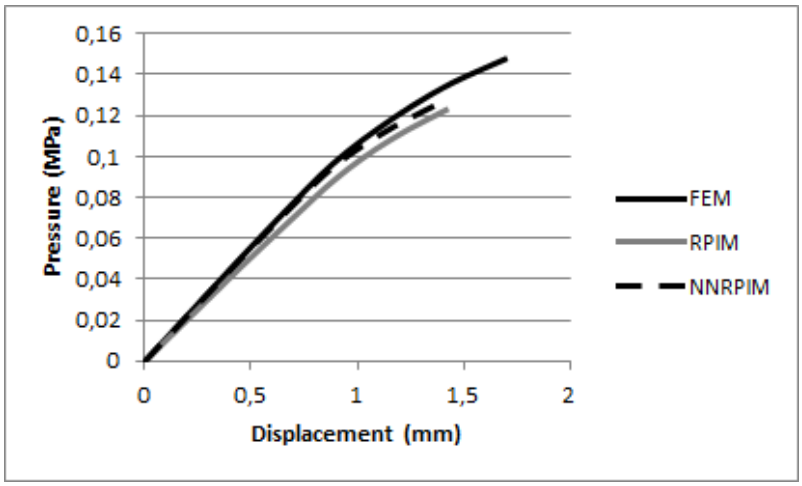

(c) Displacement obtained with the Heavily Calcified material properties

Figure 6.54: 2D Model III - Comparison of displacement of point E with different numerical methods

6.2.4 2D Model IV

For this example it was taken into consideration a solid domain $\omega \in \Re^2$ representing a atherosclerotic artery containing a thin segmented plaque. It was applied to the domain symmetry constrains and fixed the node (x,y)=(4.5,0). The numerical model was designed using 4097 nodes and was analysed using three different numerical methods (FEM, RPIM and NNRPIM). An image of the nodal distribution used can be seen in Figure 6.55

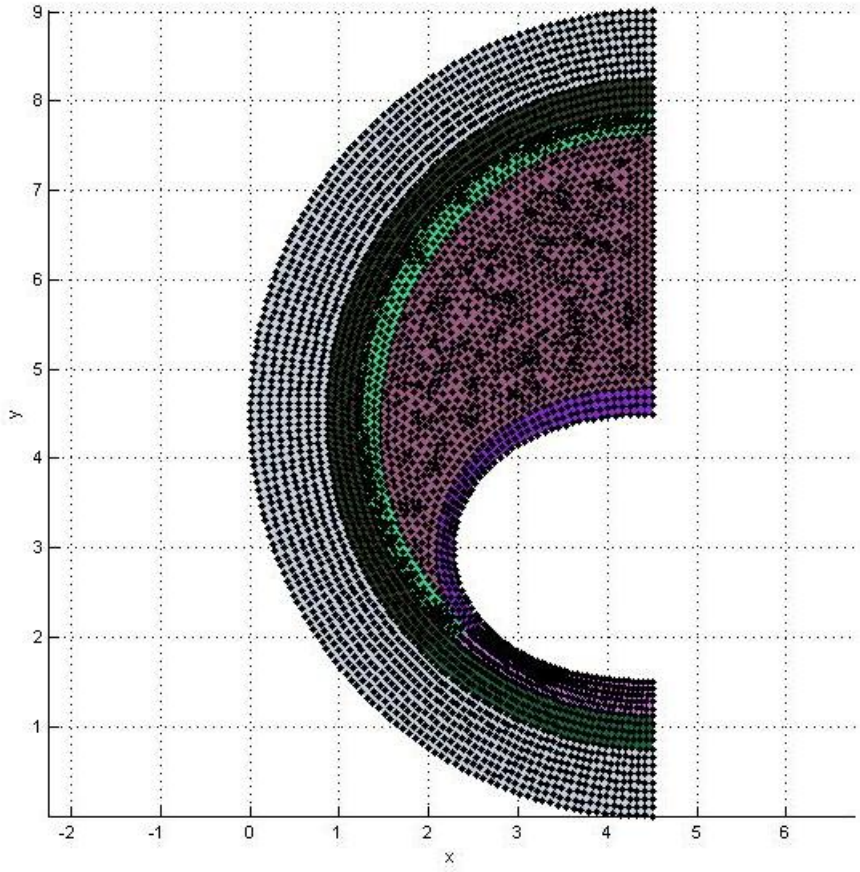

Figure 6.55: 2D Model of Artery with Atherosclerotic Plaque - Stage IV (Axis Units: 1 mm)

The von Mises Stress field and Effective Plastic Strain Field were analysed for each of the atherosclerotic plaque set of material properties. Besides this, it was also analysed the displacement in Y in specific interface nodes between tissues. The location of these nodes can be seen in the diagram of Figure 6.56. The displacement seen was analysed against to the pressure applied in the artery's lumen.

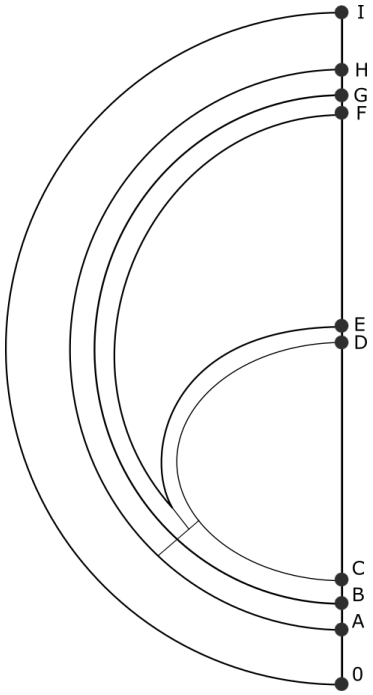

Figure 6.56: 2D Model Stage IV - Points location

6.2.4.1 Lightly Calcified

The following plots represent the relation between the internal luminal pressure and the displacement seen in points C, D, E and F.

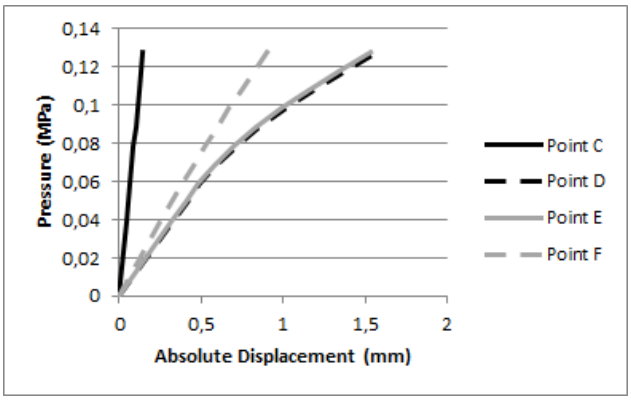

(a) Displacement obtained using FEM

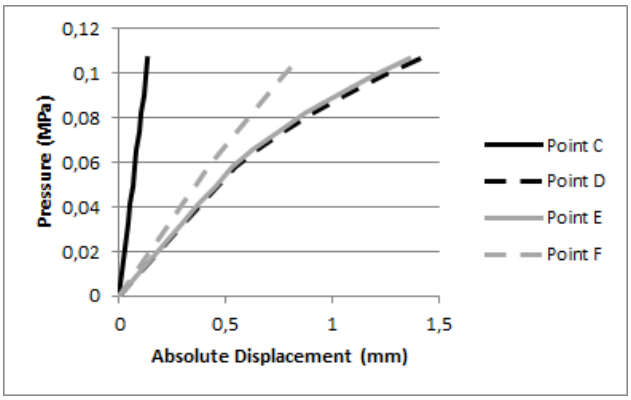

(b) Displacement obtained using RPIM

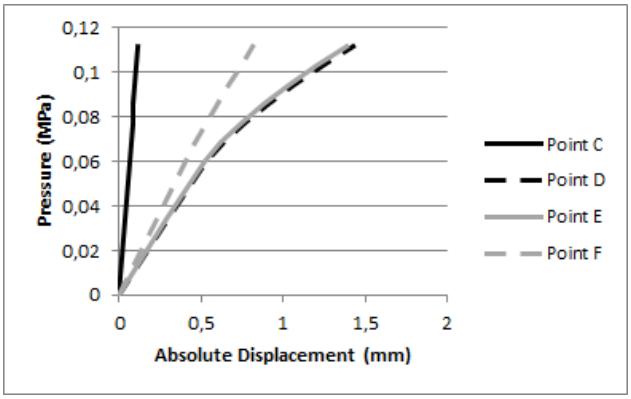

(c) Displacement obtained using NNRPIM

Figure 6.57: 2D Model IV - Lightly Calcified - Displacement in Oy vs. Luminal Pressure

The following von Mises Stress Fields and Effective Plastic Strain Fields were also obtained. It can be seen 3 different stages of the plastic deformation progression starting when the Yield Pressure was met.

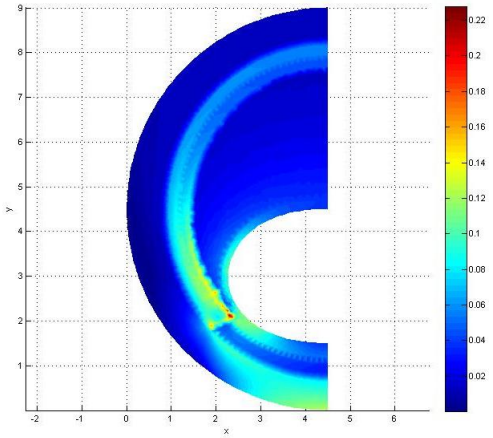

(a) von Mises Tension - Luminal Pressure = 0.04 MPa (color bar up to 0.22 MPa)

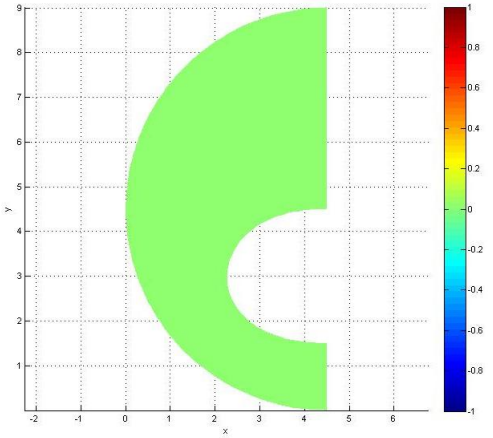

(b) Effective Plastic Strain - Luminal Pressure = 0.04 MPa (no significant values)

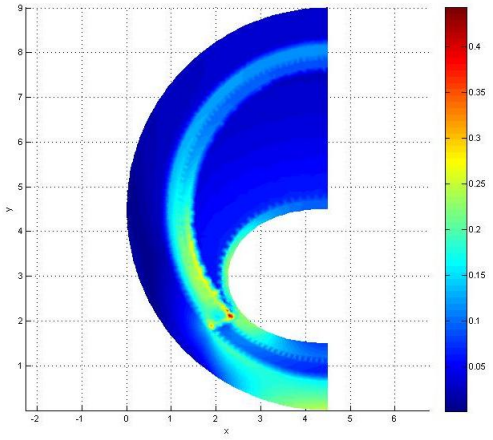

(c) von Mises Tension - Luminal Pressure = 0.075 MPa (color bar up to 0.4 MPa)

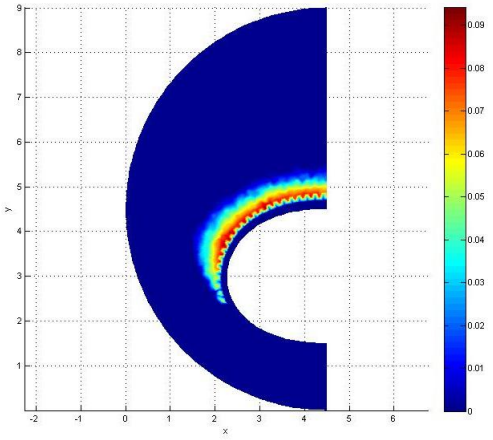

(d) Effective Plastic Strain - Luminal Pressure = 0.075 MPa (color bar up to 0.09)

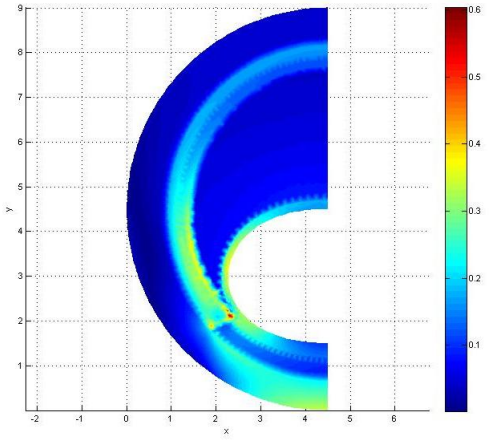

(e) von Mises Tension - Luminal Pressure = 0.105 MPa (color bar up to 0.6 MPa)

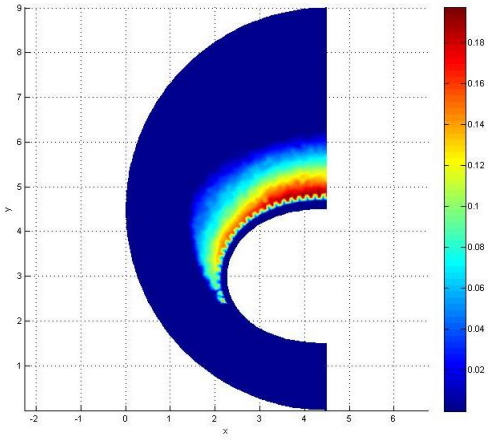

(f) Effective Plastic Strain - Luminal Pressure = 0.105 MPa (color bar up to 0.18)

Figure 6.58: 2D Artery Model IV - Lightly Calcified Atherosclerotic Plaque - FEM (Axis Units: 1 mm)

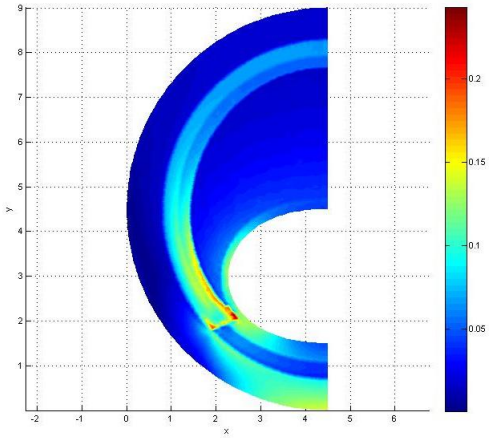

(a) von Mises Tension - Luminal Pressure = 0.04 MPa (color bar up to 0.2 MPa)

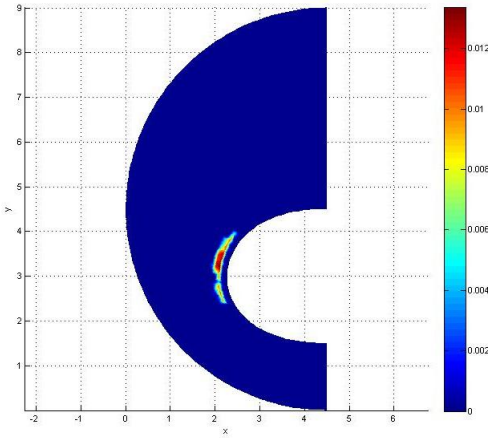

(b) Effective Plastic Strain - Luminal Pressure = 0.04 MPa (color bar up to 0.012)

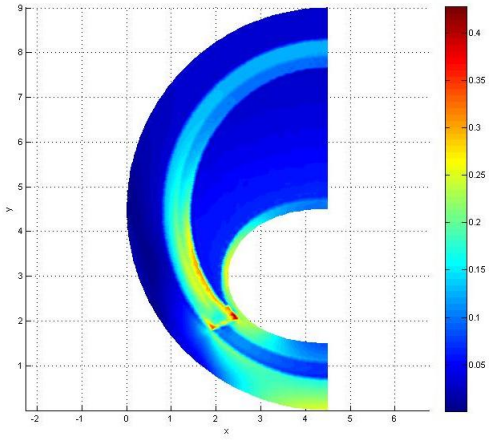

(c) von Mises Tension - Luminal Pressure = 0.075 MPa (color bar up to 0.4 MPa)

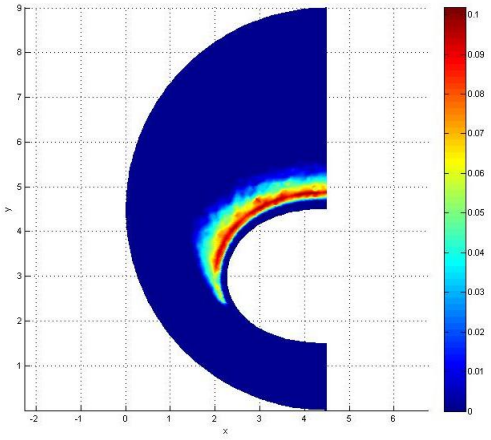

(d) Effective Plastic Strain - Luminal Pressure = 0.075 MPa (color bar up to 0.1

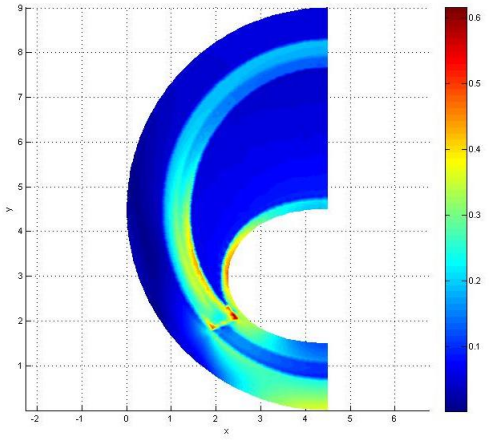

(e) von Mises Tension - Luminal Pressure = 0.105 MPa (color bar up to 0.6 MPa)

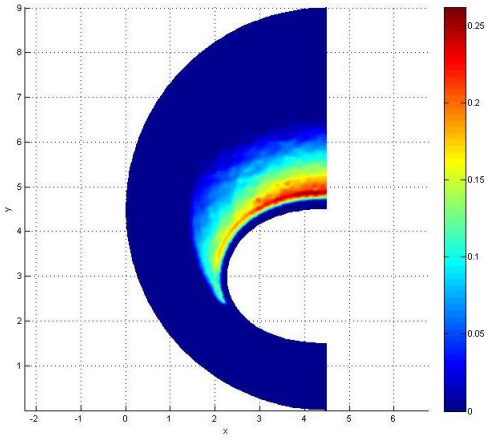

(f) Effective Plastic Strain - Luminal Pressure = 0.105 MPa (color bar up to 0.25)

Figure 6.59: 2D Artery Model IV - Lightly Calcified Atherosclerotic Plaque - RPIM (Axis Units: 1 mm)

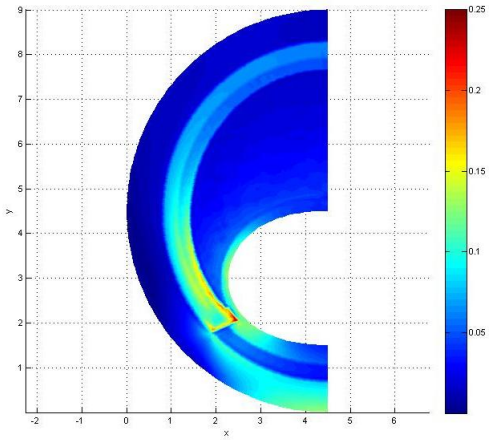

(a) von Mises Tension - Luminal Pressure = 0.04 MPa (color bar up to 0.25 MPa)

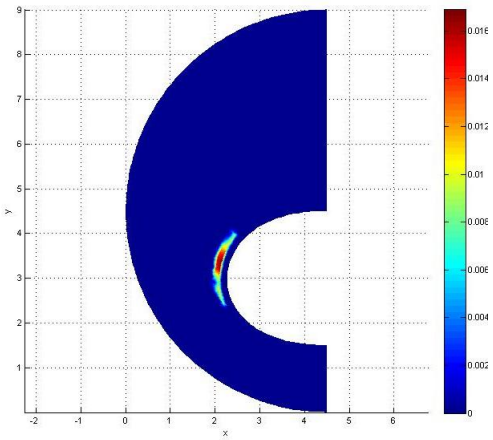

(b) Effective Plastic Strain - Luminal Pressure = 0.04 MPa (color bar up to 0.016)

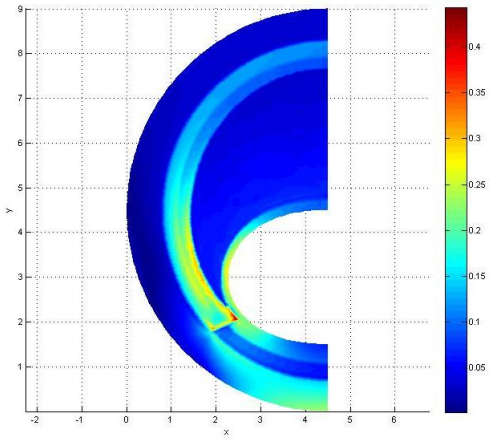

(c) von Mises Tension - Luminal Pressure = 0.075 MPa (color bar up to 0.4 MPa)

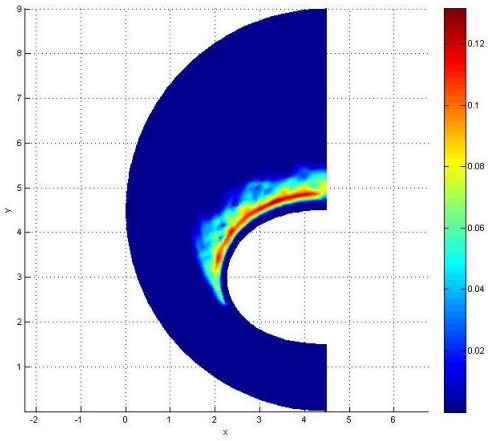

(d) Effective Plastic Strain - Luminal Pressure = 0.075 MPa (color bar up to 0.12

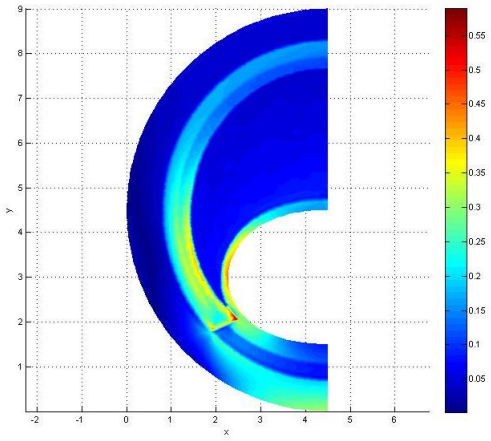

(e) von Mises Tension - Luminal Pressure = 0.105 MPa (color bar up to 0.55 MPa)

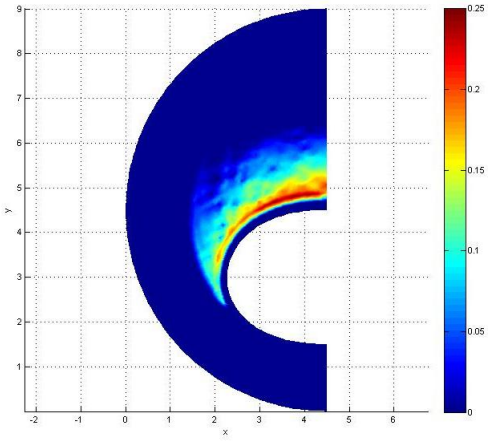

(f) Effective Plastic Strain - Luminal Pressure = 0.105 MPa (color bar up to 0.25)

Figure 6.60: 2D Artery Model IV - Lightly Calcified Atherosclerotic Plaque - NNRPIM (Axis Units: 1 mm)

6.2.4.2 Moderately Calcified

The following plots represent the relation between the internal luminal pressure and the displacement seen in points C, D, E and F.

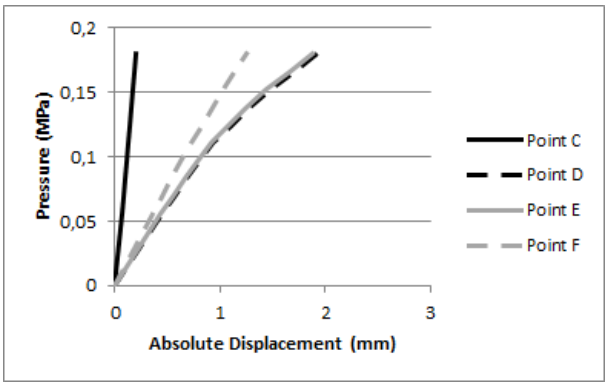

(a) Displacement obtained using FEM

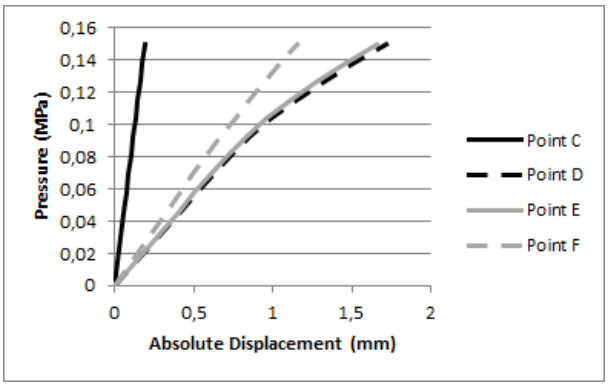

(b) Displacement obtained using RPIM

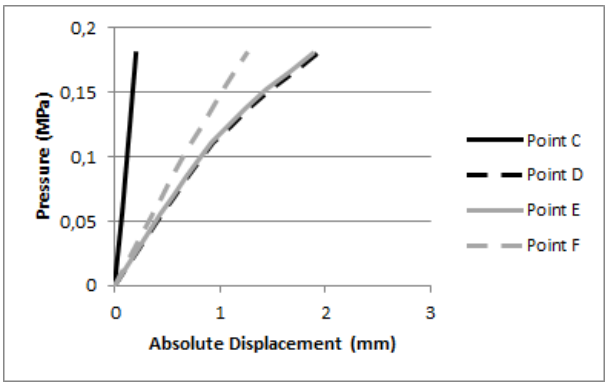

(c) Displacement obtained using NNRPIM

Figure 6.61: 2D Model IV - Moderately Calcified - Displacement in Oy vs. Luminal Pressure

The following von Mises Stress Fields and Effective Plastic Strain Fields were also obtained. It can be seen 3 different stages of the plastic deformation progression starting when the Yield Pressure was met.

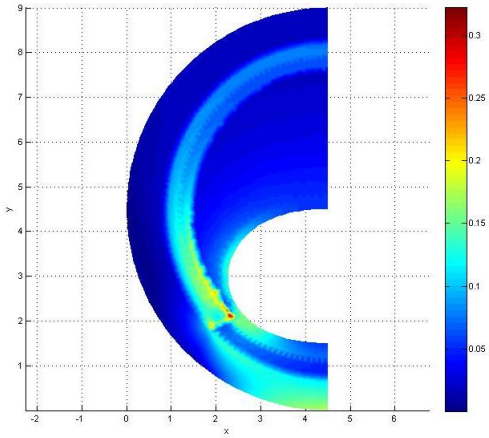

(a) von Mises Tension - Luminal Pressure = 0.06 MPa (color bar up to 0.3 MPa)

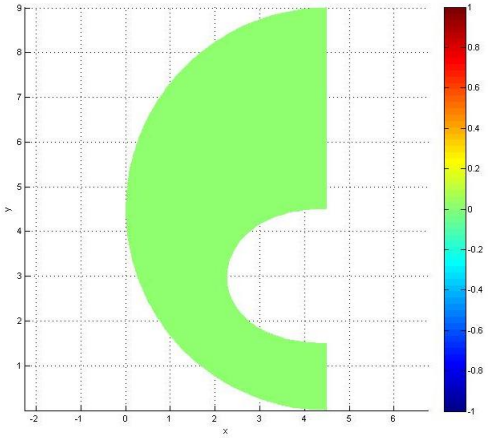

(b) Effective Plastic Strain - Luminal Pressure = 0.06 MPa (no significant values)

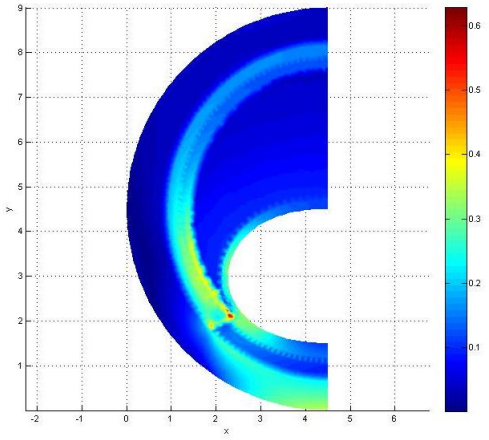

(c) von Mises Tension - Luminal Pressure = 0.105 MPa (color bar up to 0.6 MPa)

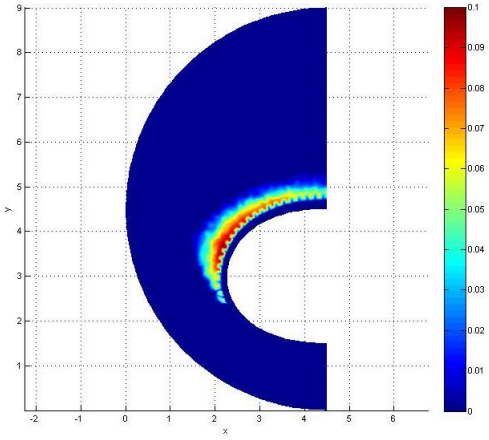

(d) Effective Plastic Strain - Luminal Pressure = 0.105 MPa (color bar up to 0.1)

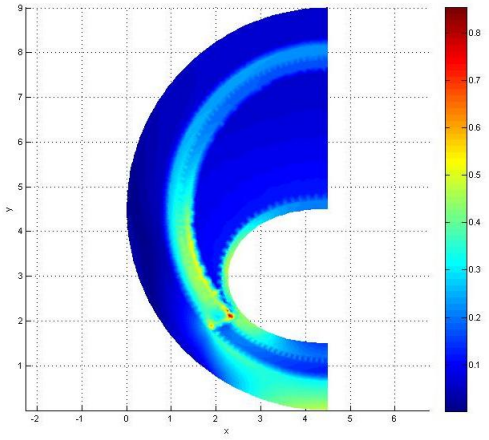

(e) vonvon Mises Tension - Luminal Pressure = 0.15 MPa (color bar up to 0.8 MPa)

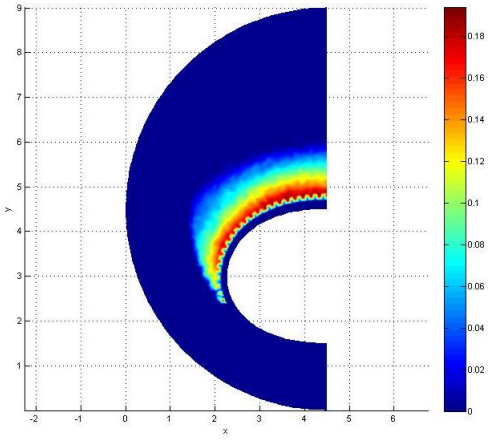

(f) Effective Plastic Strain - Luminal Pressure = 0.15 MPa (color bar up to 0.18)

Figure 6.62: 2D Artery Model IV - Medially Calcified Atherosclerotic Plaque - FEM (Axis Units: 1 mm)

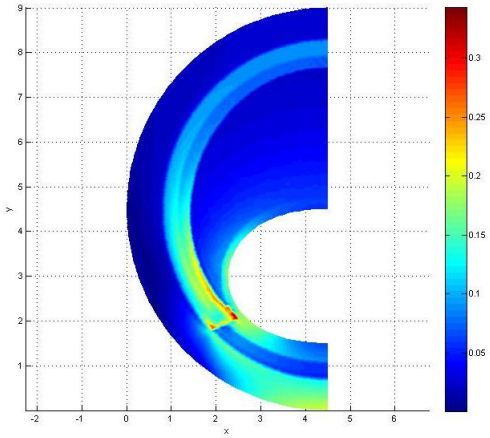

(a) Von Mises Tension - Luminal Pressure = 0.06 MPa (color bar up to 0.3 MPa)

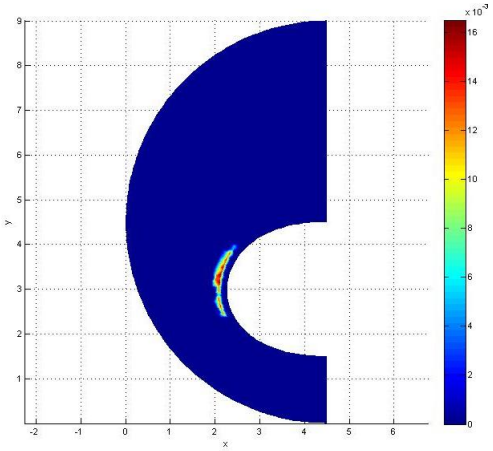

(b) Effective Plastic Strain - Luminal Pressure = 0.06 MPa (color bar up to 0.016)

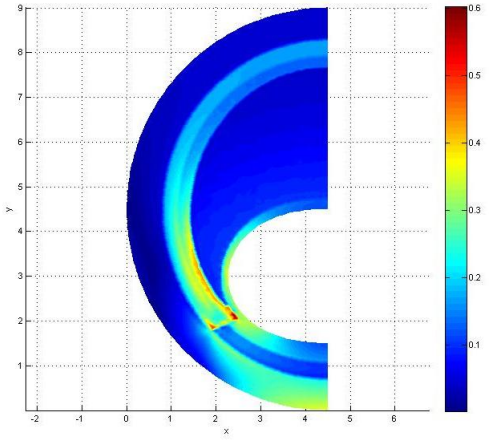

(c) von Mises Tension - Luminal Pressure = 0.105 MPa (color bar up to 0.6 MPa)

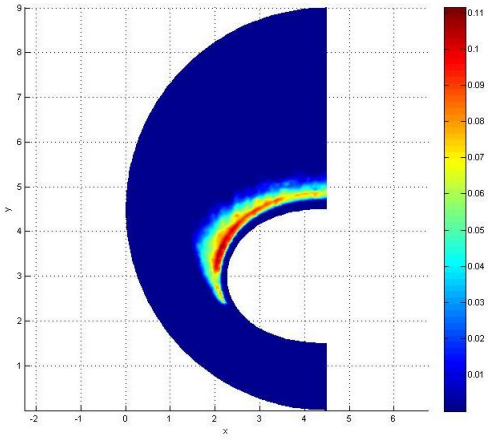

(d) Effective Plastic Strain - Luminal Pressure = 0.105 MPa (color bar up to 0.11)

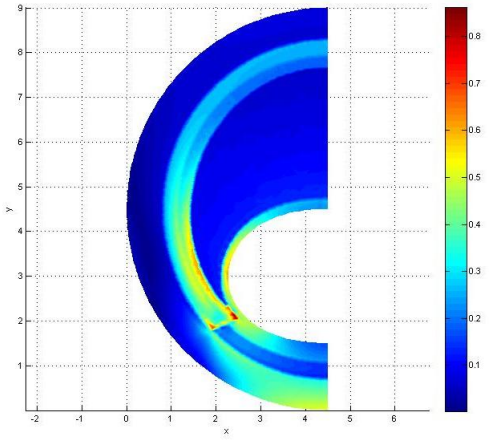

(e) von Mises Tension - Luminal Pressure = 0.15 MPa (color bar up to 0.8 MPa)

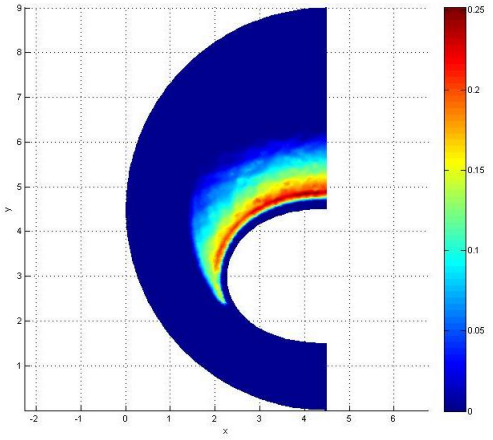

(f) Effective Plastic Strain - Luminal Pressure = 0.15 MPa (color bar up to 0.25)

Figure 6.63: 2D Artery Model IV - Medially Calcified Atherosclerotic Plaque - RPIM (Axis Units: 1 mm)

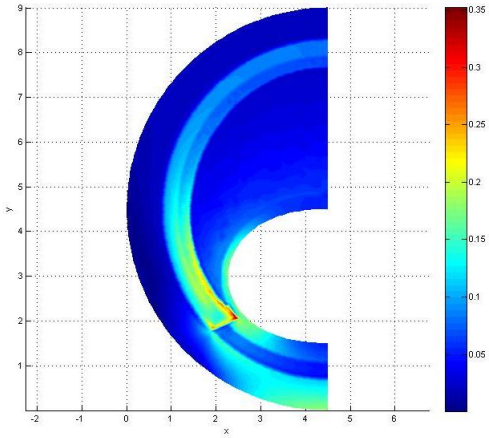

(a) von Mises Tension - Luminal Pressure = 0.06 MPa (color bar up to 0.35 MPa)

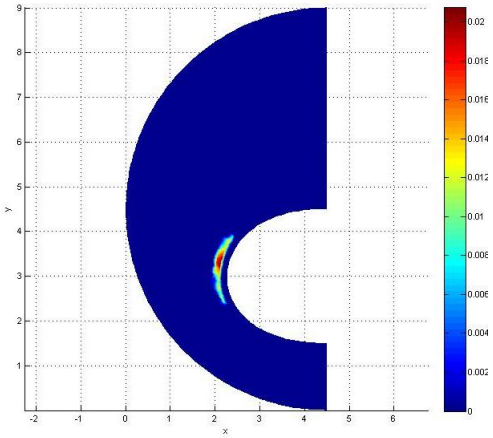

(b) Effective Plastic Strain - Luminal Pressure = 0.06 MPa (color bar up to 0.02)

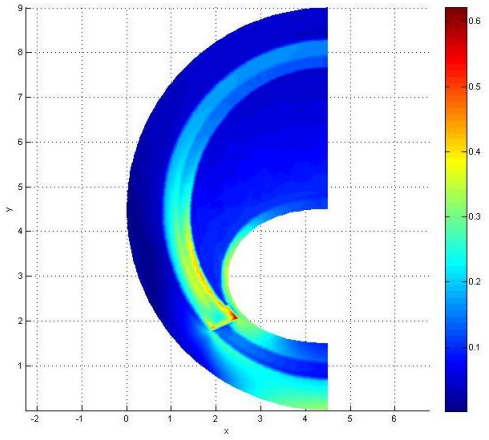

(c) von Mises Tension - Luminal Pressure = 0.105 MPa (color bar up to 0.6 MPa)

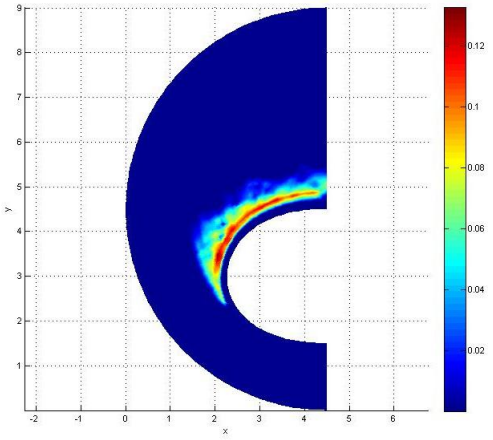

(d) Effective Plastic Strain - Luminal Pressure = 0.105 MPa (color bar up to 0.12)

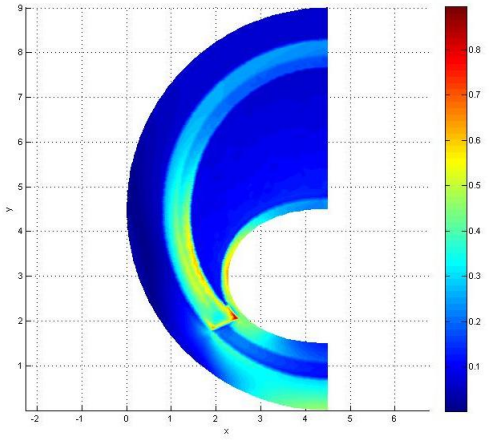

(e) von Mises Tension - Luminal Pressure = 0.15 MPa (color bar up to 0.8 MPa)

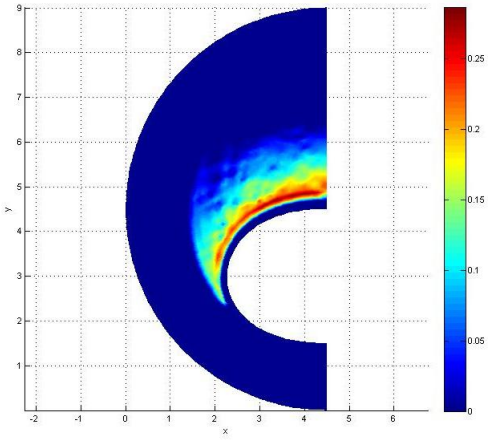

(f) Effective Plastic Strain - Luminal Pressure = 0.15 MPa (color bar up to 0.25)

Figure 6.64: 2D Artery Model IV - Medially Calcified Atherosclerotic Plaque - NNRPIM (Axis Units: 1 mm)

6.2.4.3 Heavily Calcified

The following plots represent the relation between the internal luminal pressure and the displacement seen in points C, D, E and F.

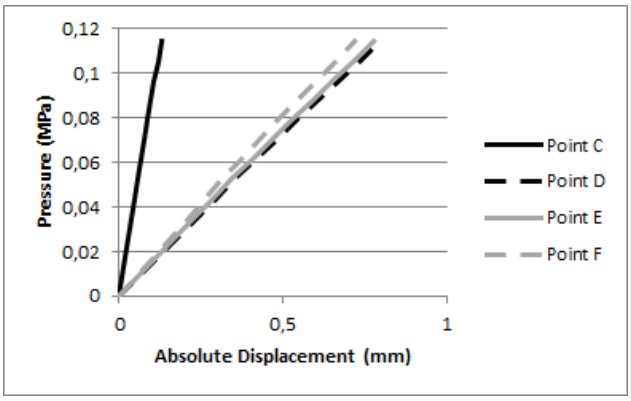

(a) Displacement obtained using FEM

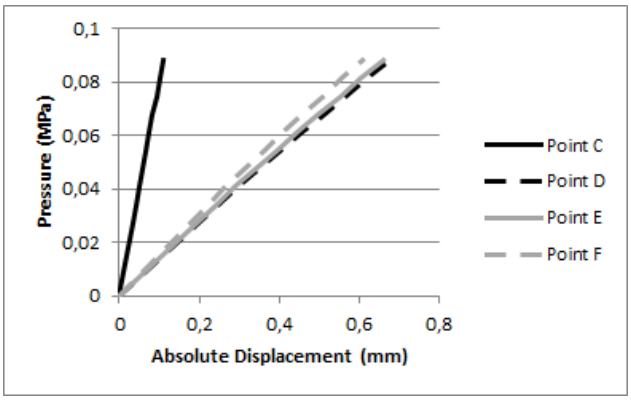

(b) Displacement obtained using RPIM

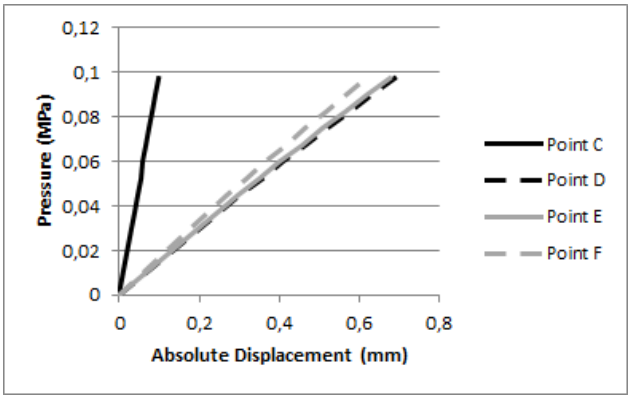

(c) Displacement obtained using NNRPIM

Figure 6.65: 2D Model IV - Heavily Calcified - Displacement in Oy vs. Luminal Pressure

The following von Mises Stress Fields and Effective Plastic Strain Fields were also obtained. It can be seen 3 different stages of the plastic deformation progression starting when the Yield Pressure was met.

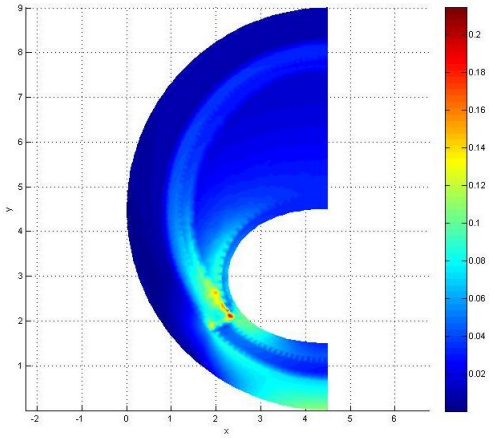

(a) von Mises Tension - Luminal Pressure = 0.035 MPa (color bar up to 0.2 MPa)

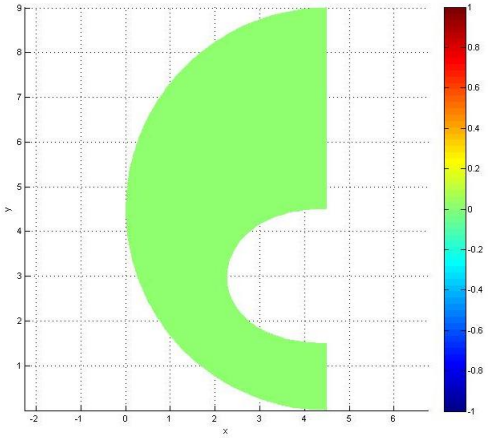

(b) Effective Plastic Strain - Luminal Pressure = 0.035 MPa (no significant values)

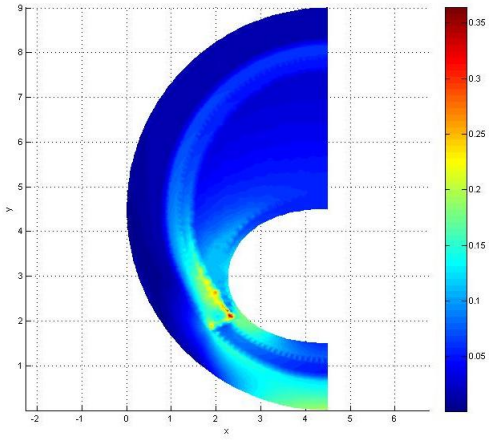

(c) von Mises Tension - Luminal Pressure = 0.06 MPa (color bar up to 0.35 MPa)

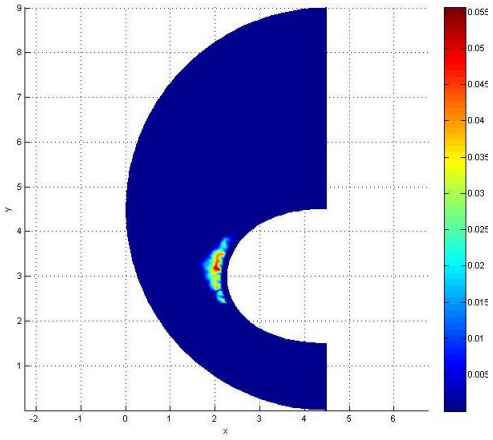

(d) Effective Plastic Strain - Luminal Pressure = 0.06 MPa (color bar up to 0.05)

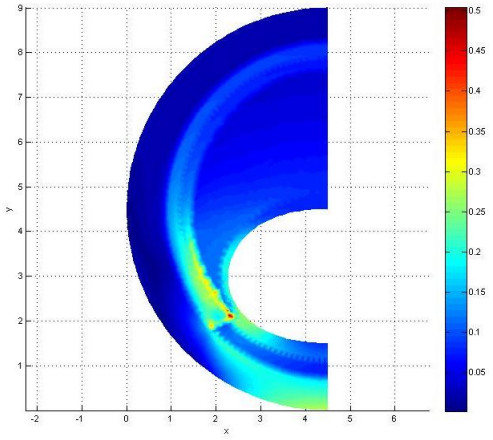

(e) von Mises Tension - Luminal Pressure = 0.09 MPa (color bar up to 0.5 MPa)

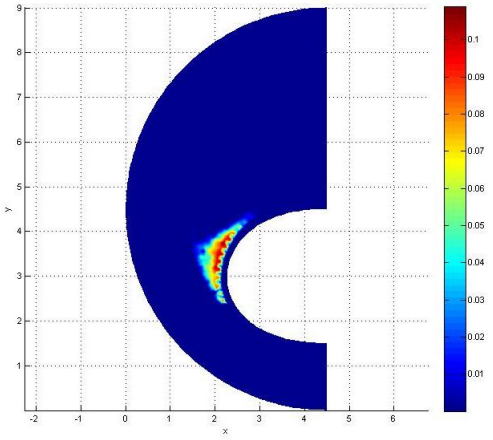

(f) Effective Plastic Strain - Luminal Pressure = 0.09 MPa (color bar up to 0.15)

Figure 6.66: 2D Artery Model IV - Highly Calcified Atherosclerotic Plaque - FEM (Axis Units: 1 mm)

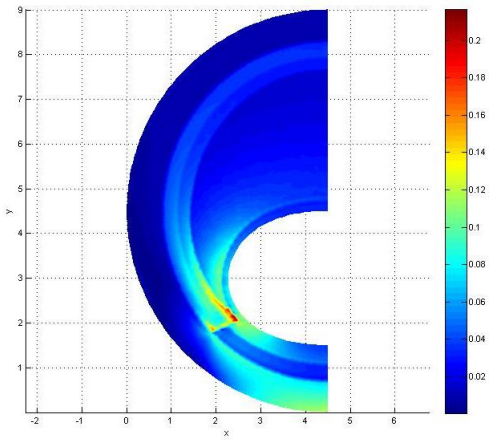

(a) von Mises Tension - Luminal Pressure = 0.035 MPa (color bar up to 0.2 MPa)

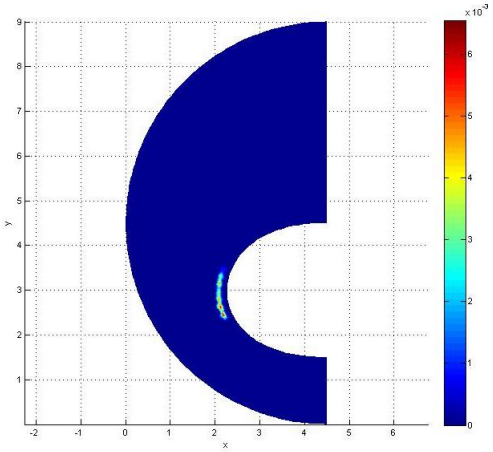

(b) Effective Plastic Strain - Luminal Pressure = 0.035 MPa (color bar up to 0.006)

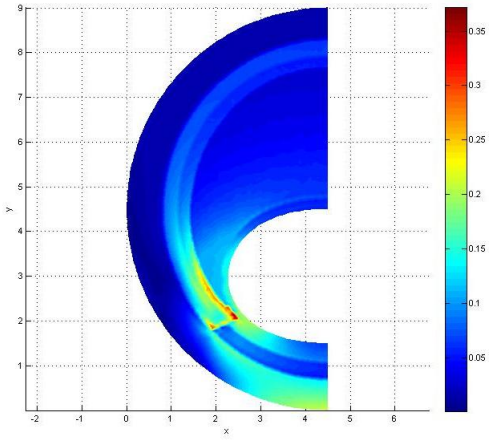

(c) von Mises Tension - Luminal Pressure = 0.06 MPa (color bar up to 0.35 MPa)

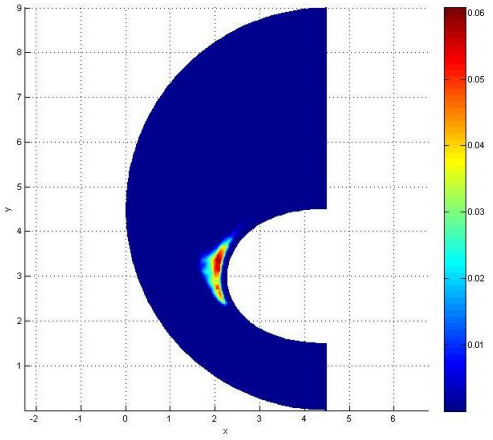

(d) Effective Plastic Strain - Luminal Pressure = 0.06 MPa (color bar up to 0.06)

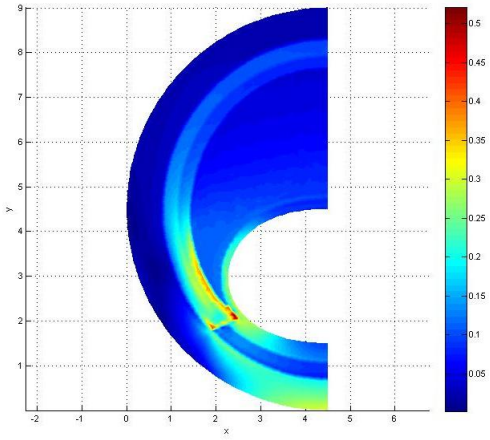

(e) von Mises Tension - Luminal Pressure = 0.09 MPa (color bar up to 0.5 MPa)

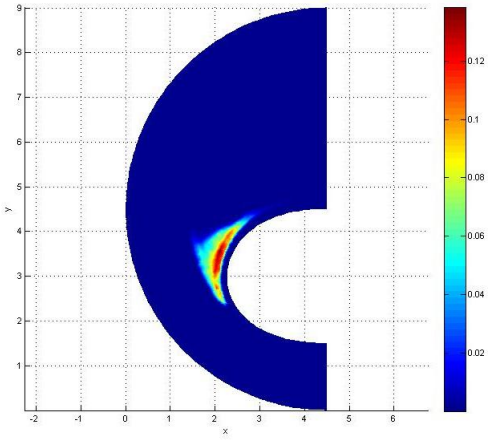

(f) Effective Plastic Strain - Luminal Pressure = 0.09 MPa (color bar up to 0.12)

Figure 6.67: 2D Artery Model IV - Highly Calcified Atherosclerotic Plaque - RPIM (Axis Units: 1 mm)

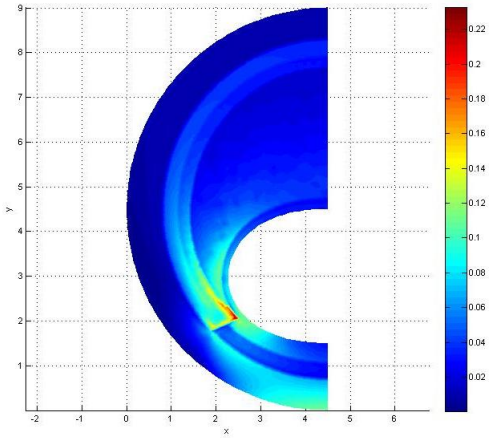

(a) von Mises Tension - Luminal Pressure = 0.035 MPa (color bar up to 0.22 MPa)

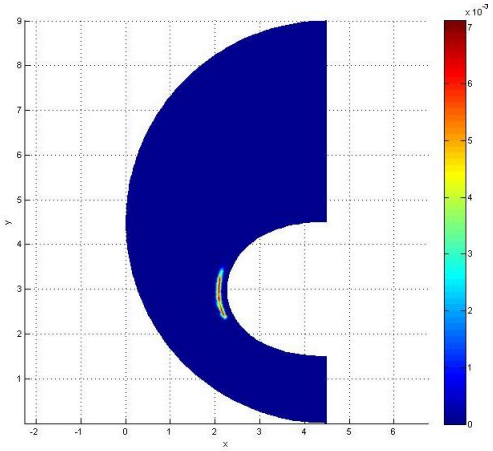

(b) Effective Plastic Strain - Luminal Pressure = 0.035 MPa (color bar up to 0.007)

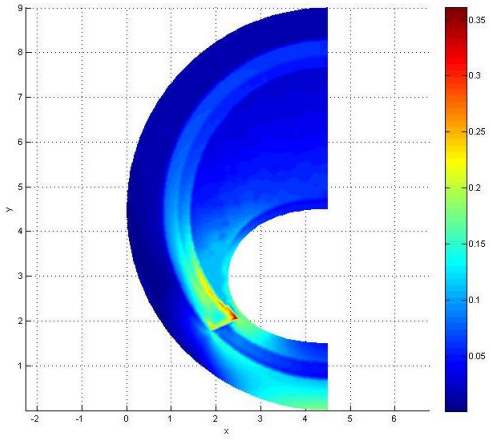

(c) von Mises Tension - Luminal Pressure = 0.06 MPa (color bar up to 0.35 MPa)

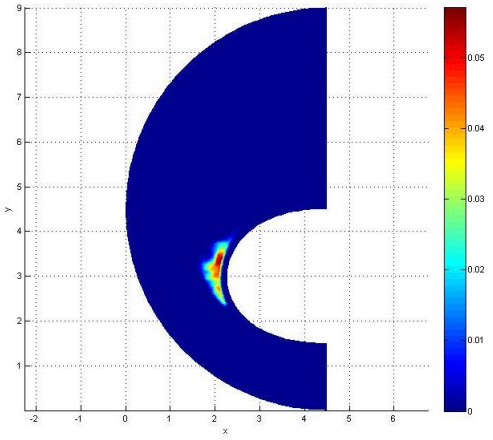

(d) Effective Plastic Strain - Luminal Pressure = 0.06 MPa (color bar up to 0.05)

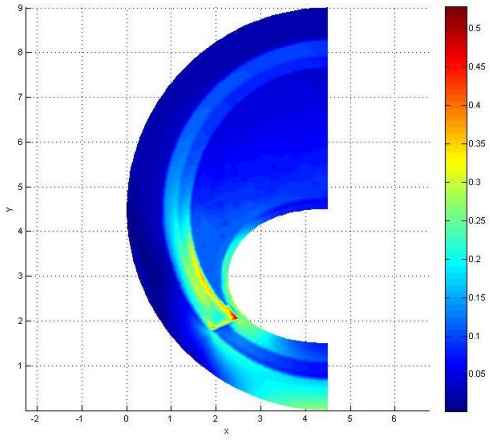

(e) von Mises Tension - Luminal Pressure = 0.09 MPa (color bar up to 0.5 MPa)

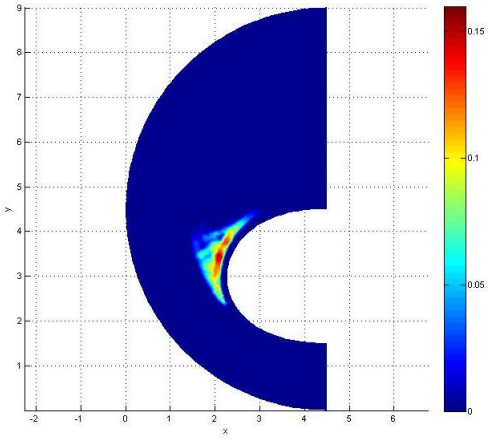

(f) Effective Plastic Strain - Luminal Pressure = 0.09 MPa (color bar up to 0.15)

Figure 6.68: 2D Artery Model IV - Highly Calcified Atherosclerotic Plaque - NNRPIM (Axis Units: 1 mm)

6.2.4.4 Discussion

In Figures 6.57, 6.61, as it was seen with all other 2D arterial models, the points C and F have their displacement only affected by elastic materials and therefore show a linear displacement relation with the luminal pressure. In comparison, points D and E whose displacement is affected by the atherosclerotic plaque start to show more clearly a non-linear progression as the pressure increases. This non-linear behaviour is not seen in Figure 6.65 obtained from a heavily calcified atherosclerotic plaque. This stands from the fact that, as seen in the Effective Plastic Strain fields and von Mises Stress Fields (Figures 6.58, 6.59, 6.60, 6.62, 6.63, 6.64, 6.66, 6.67 and 6.68), given the large thickness of the central part of the plaque compared to its lateral areas, it still hasn't started experiencing plastic deformation and it seen a concentration of stresses in that lateral areas.

When looking at the comparison between the deformation of point E in each plaque (Figure 6.69) and the variation in distance between point E and F for each plaque (Figure 6.70) it is seen, as in the previous examples, the non-linear behaviour of the atherosclerotic plaque with plastic deformation starting around the expected yield point, with the exception of the highly calcified atherosclerotic plaque on which that pressure wasn't reached. In this model is also possible to see that at normal systolic blood pressure (0.01867 MPa) [91] none of the atherosclerotic plaques had experienced plastic deformations.

Once again the von Mises Tension fields show a accumulation of tension in the interface between the damaged *media* and the healthy *media* due to the sudden change of material properties between the tissues. It can also be seen here an accumulation of tensions in the *intima*'s luminal wall that is an effect of the high pressures the arteries was been subjected in order for the atherosclerotic plaque to suffer plastic deformation.

As it can be seen by comparison of the three numerical methods, the results are coherent and similar between them. In Figure 6.71 it can be seen a comparison of the displacement of point E obtained from three numerical methods with each set of material properties.

When comparing now between the results obtained for each model in terms of displacement of point E (Figures 6.72, 6.73, 6.74) it can be seen that, as the thickness of the plaque rises the displacement achieve for the same luminal pressure in each material becomes smaller. This effect is most seen more significantly when when analysing the results for a heavily calcified atherosclerotic plaque. From these results it would be possible to infer that has the atherosclerotic plaque becomes thicker, even though the material properties might not change, the plaque becomes more stiff.

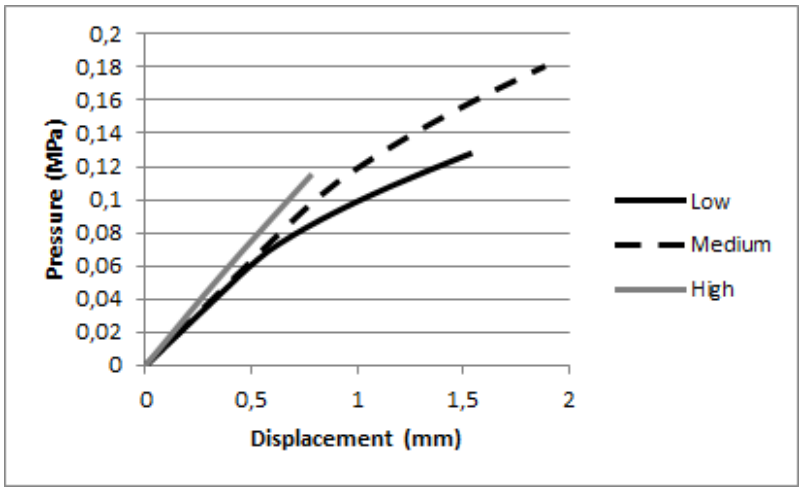

(a) Displacement obtained using FEM

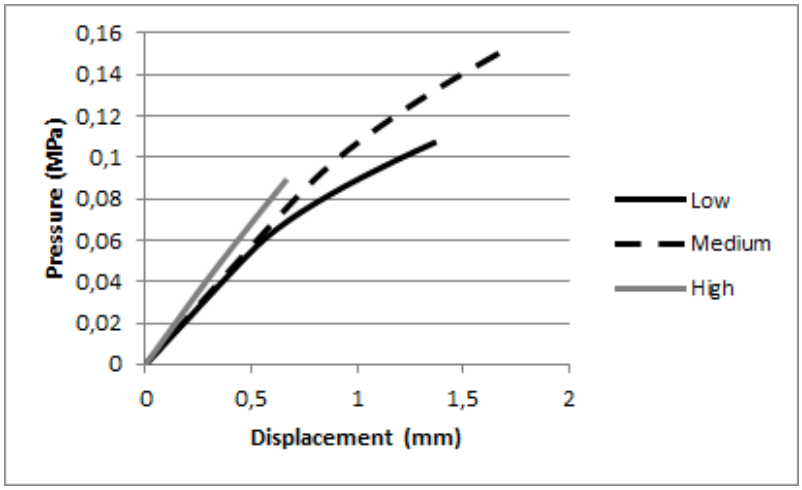

(b) Displacement obtained using RPIM

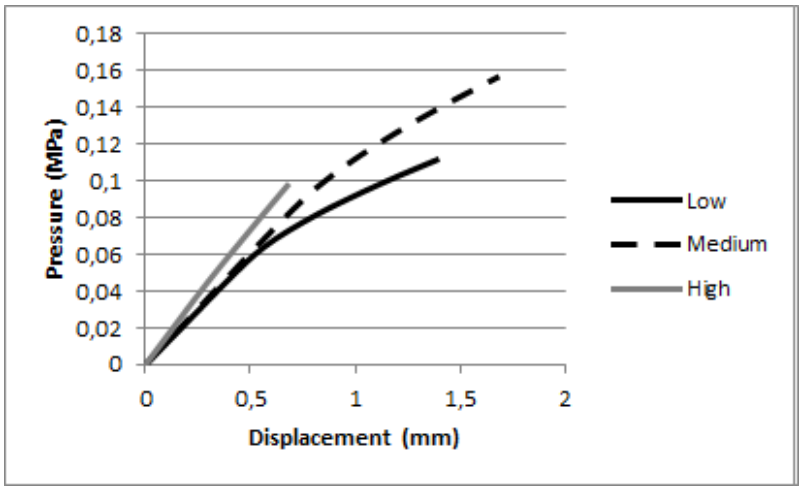

(c) Displacement obtained using NNRPIM

Figure 6.69: 2D Model IV - Comparison of Displacements of Point E in different levels of calcification

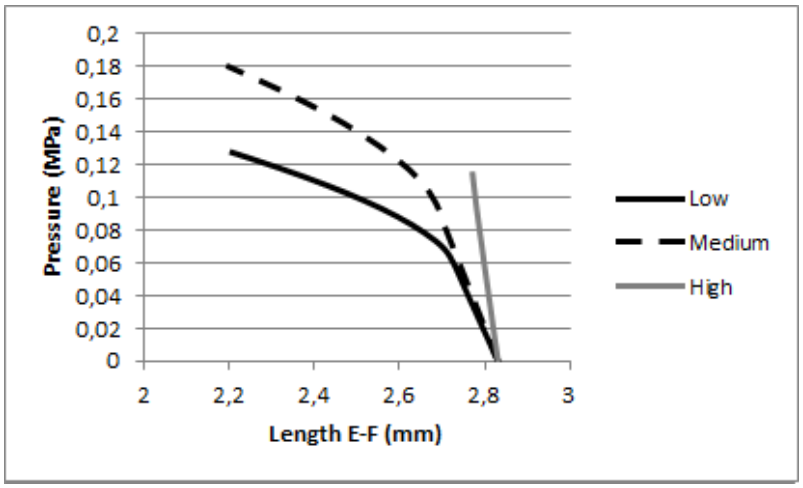

(a) Displacement obtained using FEM

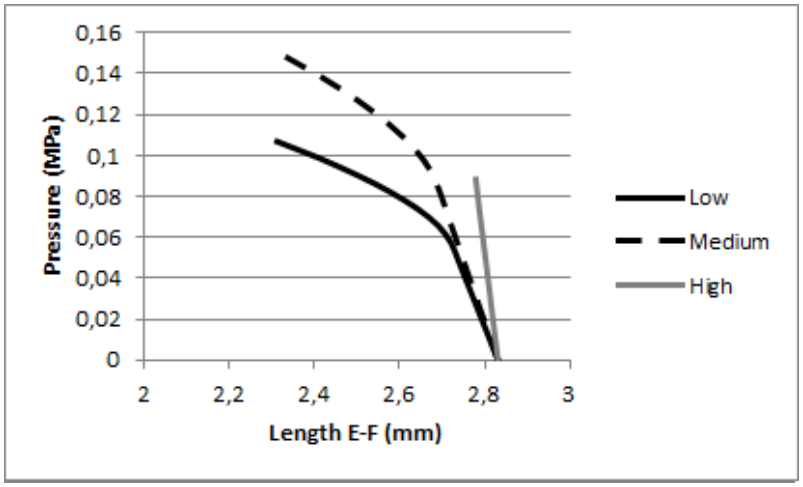

(b) Displacement obtained using RPIM

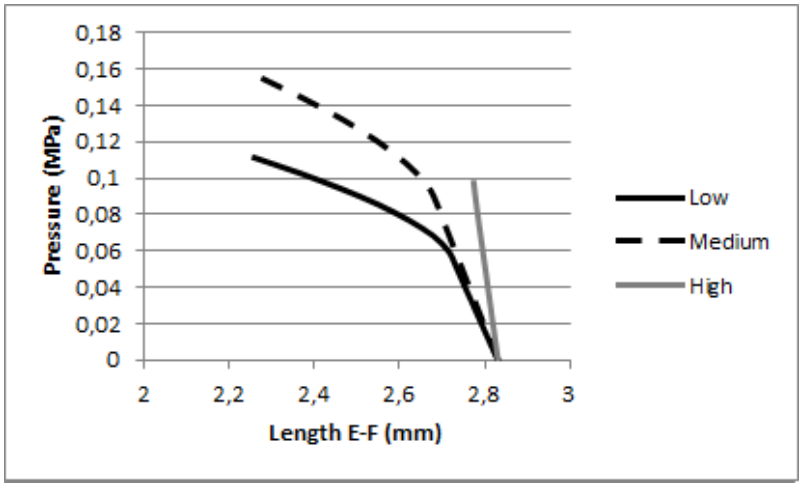

(c) Displacement obtained using NNRPIM

Figure 6.70: 2D Model IV - Comparison of length of segment FE

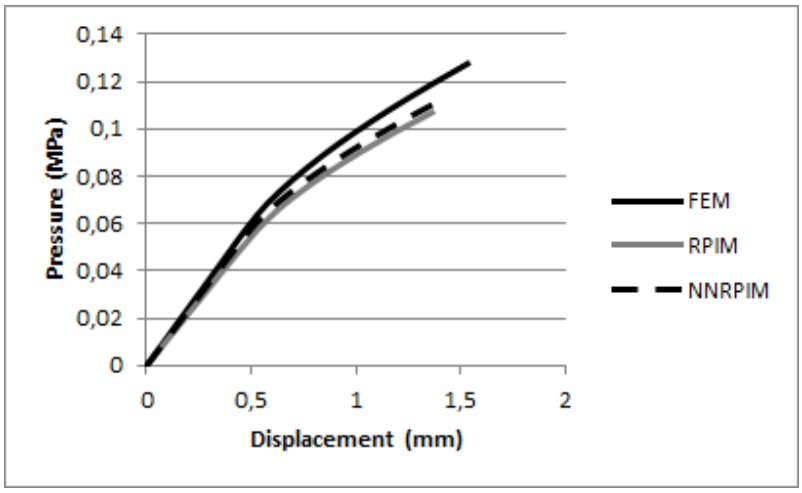

(a) Displacement obtained with the Lightly Calcified material properties

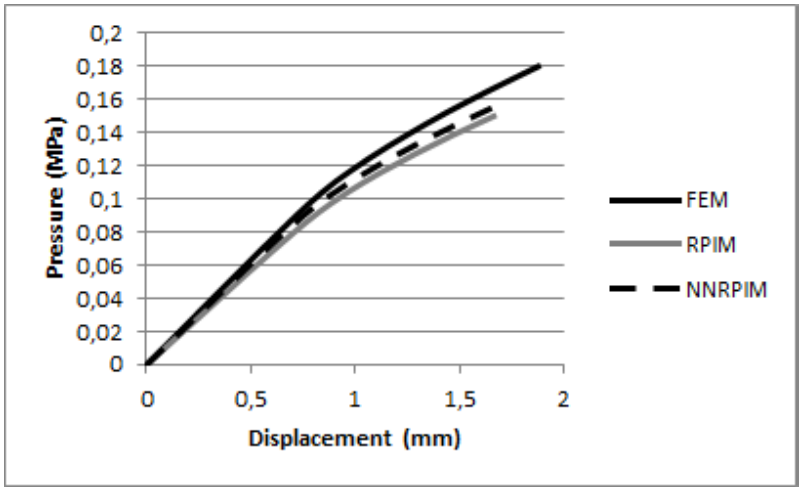

(b) Displacement obtained with the Moderately Calcified material properties

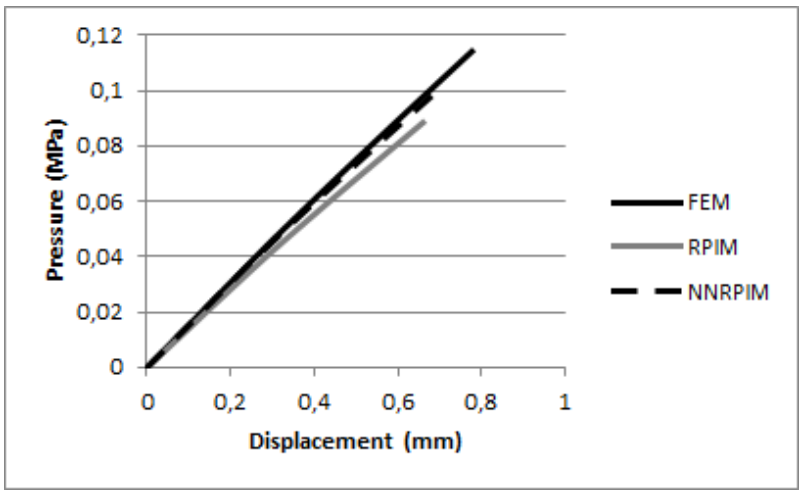

(c) Displacement obtained with the Heavily Calcified material properties

Figure 6.71: 2D Model IV - Comparison of displacement of point E with different numerical methods

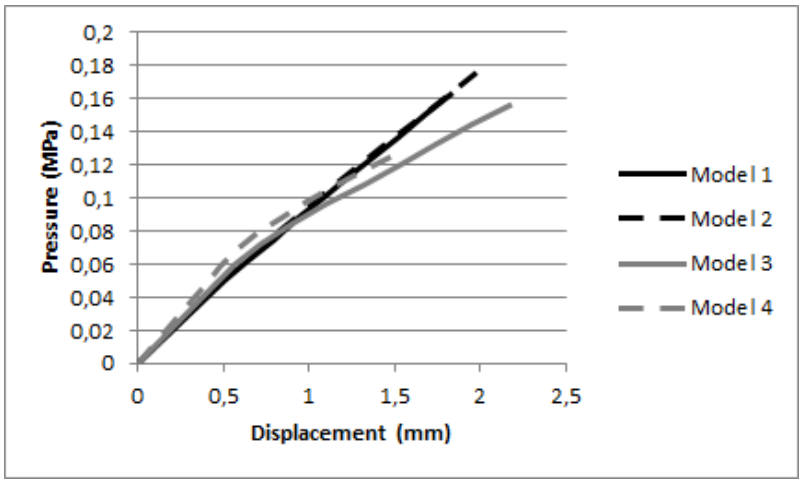

(a) Displacement obtained with FEM

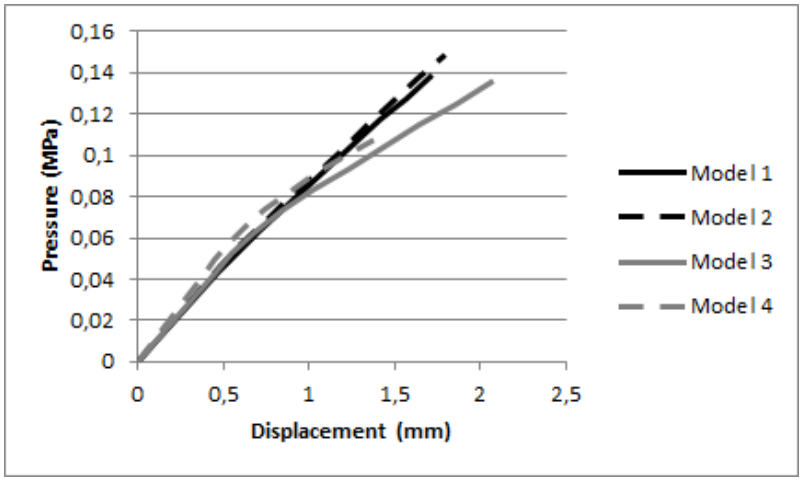

(b) Displacement obtained with RPIM

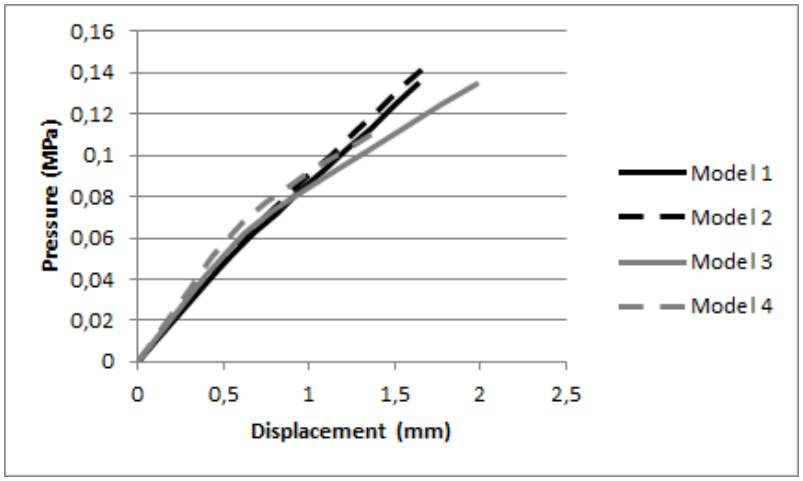

(c) Displacement obtained with NNRPIM

Figure 6.72: Comparison between 2D Models - Displacement of Point E - Lightly Calcified Plaque

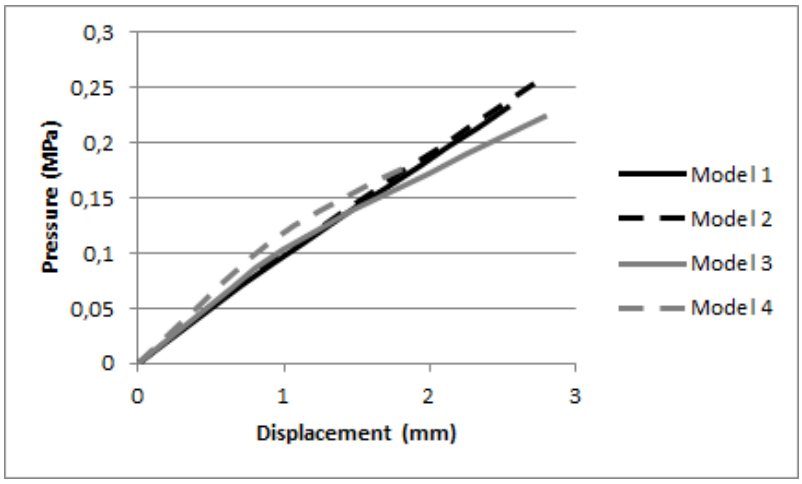

(a) Displacement obtained with FEM

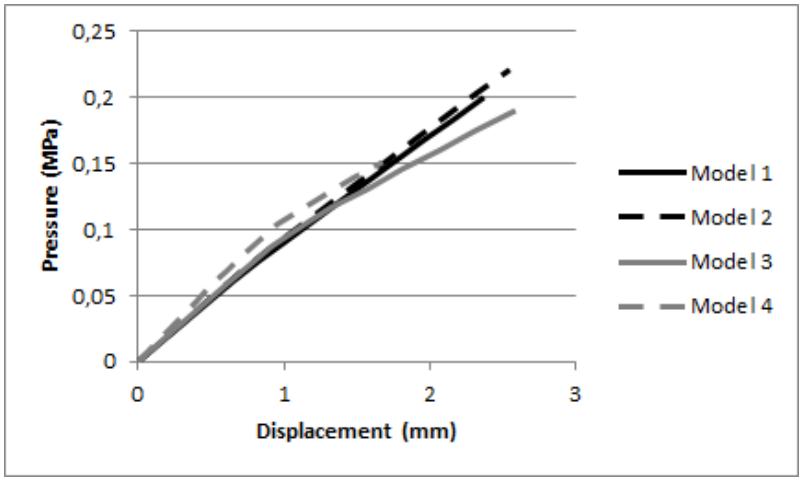

(b) Displacement obtained with RPIM

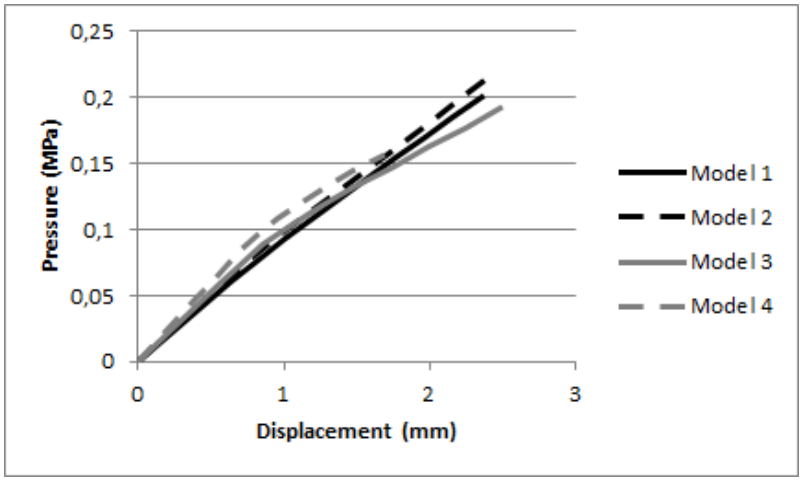

(c) Displacement obtained with NNRPIM

Figure 6.73: Comparison between 2D Models - Displacement of Point E - Moderately Calcified Plaque

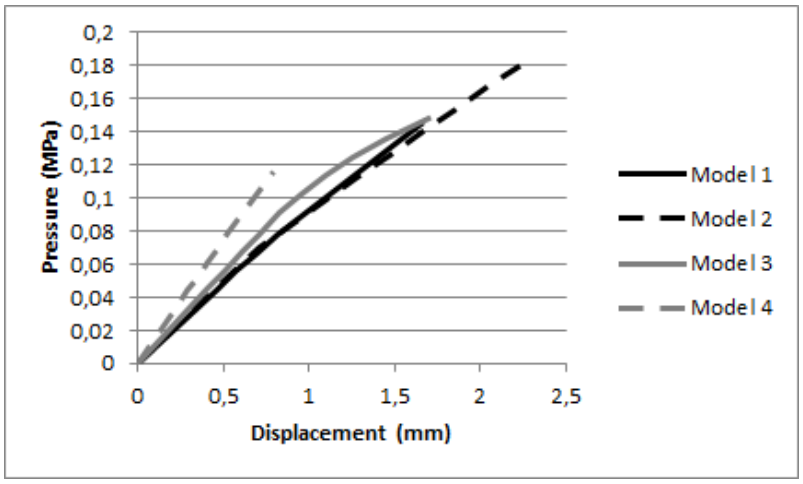

(a) Displacement obtained with FEM

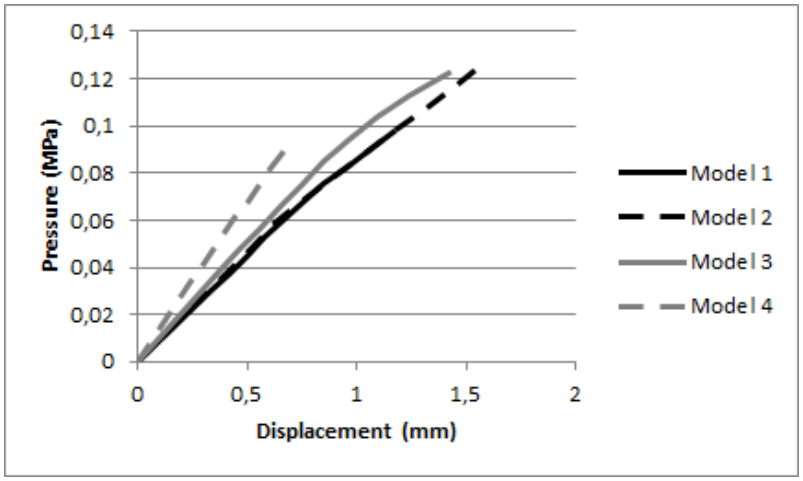

(b) Displacement obtained with RPIM

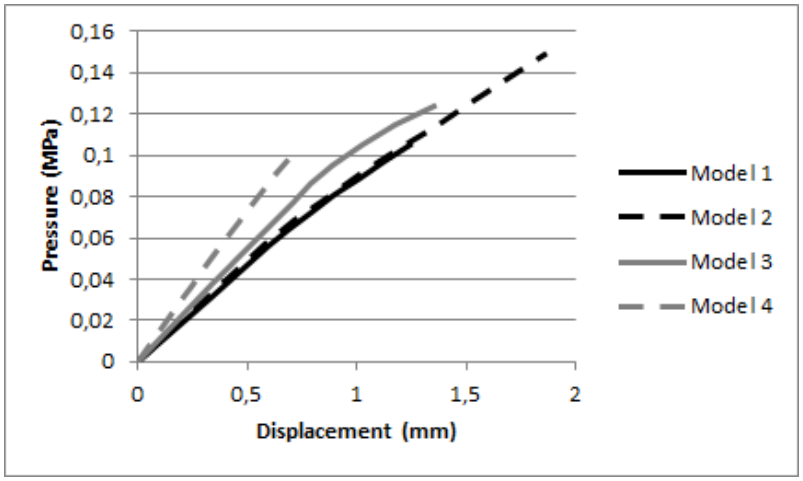

(c) Displacement obtained with NNRPIM

Figure 6.74: Comparison between 2D Models - Displacement of Point E - Heavily Calcified Plaque

6.3 3D Analysis

6.3.1 3D Model I

For this example it was taken into consideration a solid domain $\omega \in \Re^3$ representing a atherosclerotic artery containing a plaque inducing an stenosis of a third of the lumen diameter. The plaque simulated is a continuous plaque extending through the complete radius of the artery. Due to the natural symmetry of the simplified model, only 1/8 of the artery was analysed. It was applied to the domain symmetry constrains. The numerical model was designed using 3951 nodes and was analysed using three different numerical methods (FEM, RPIM and NNRPIM). An image of the nodal distribution used can be seen in Figure 6.75

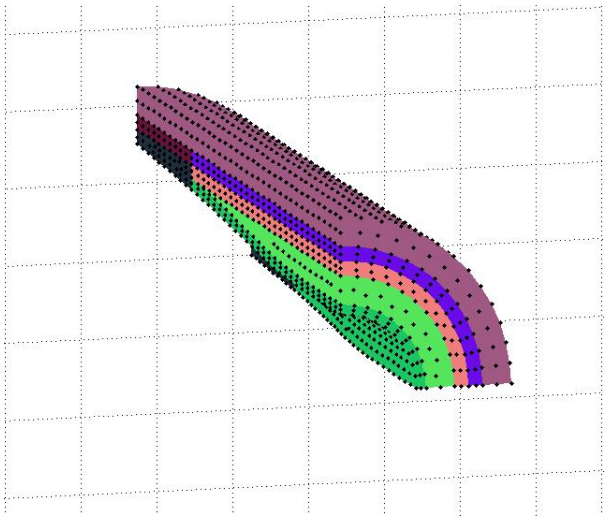

Figure 6.75: 3D Model of Artery with Atherosclerotic Plaque - Model I

The von Mises Stress field were analysed for each of the atherosclerotic plaque set of material properties on the thicker end of the atherosclerotic plaque. The longitudinal view of the model under each of the conditions was also analysed in order to study the effect of the transition to the diseased area. Besides this, it was also analysed the displacement in Oz in specific interface nodes between tissues at two different positions of the model. The location of these nodes can be seen in the diagram of Figure 6.76, where S1 is the first position analysed and S2 the second. The displacement seen was analysed against to the pressure applied in the artery's lumen.

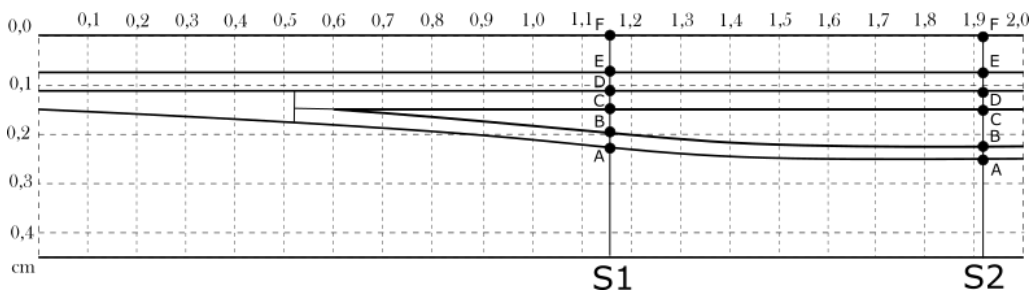

Figure 6.76: 3D Model Stage I - Points location - View Oxz

6.3.1.1 Lightly Calcified

For a Lightly Calcified atherosclerotic plaque, the following von Mises stress fields and Effective Plastic Strain Fields were obtained. This fields were obtained at the highest luminal pressure of each numerical analysis.

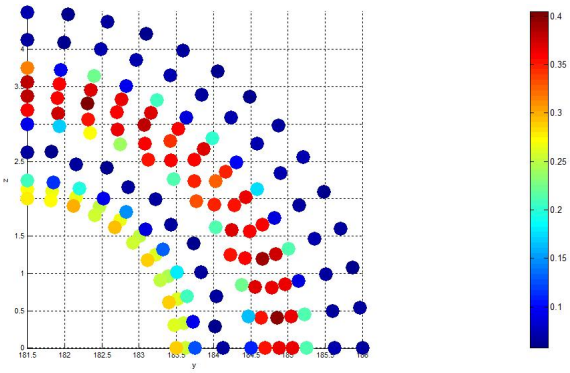

(a) von Mises Tension - FEM - Luminal Pressure = 0.096 MPa (color bar up to 0.4 MPa)

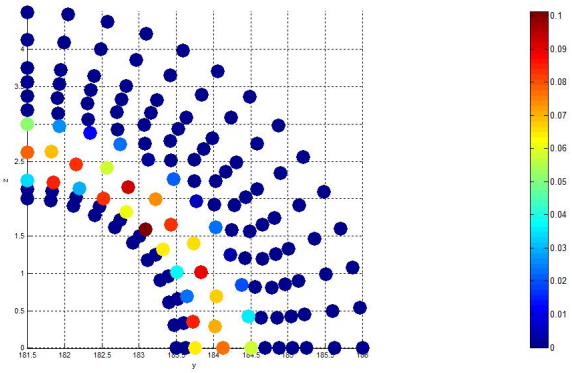

(b) Effective Plastic Strain - FEM - Luminal Pressure = 0.096 MPa (color bar up to 0.1)

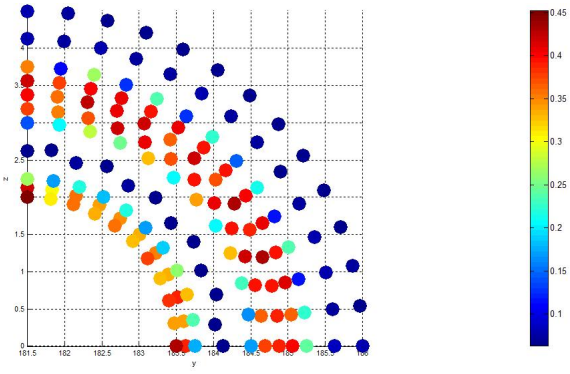

(c) von Mises Tension - RPIM - Luminal Pressure = 0.10 MPa (color bar up to 0.45 MPa)

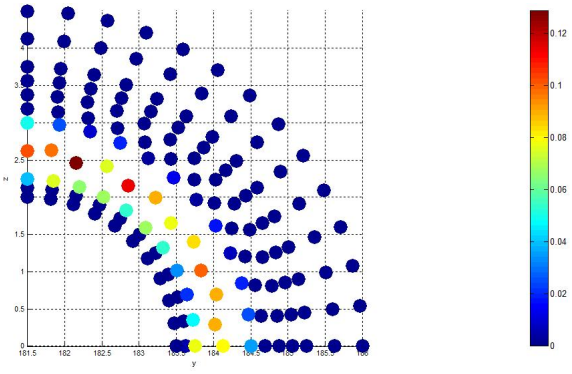

(d) Effective Plastic Strain - RPIM - Luminal Pressure = 0.10 MPa (color bar up to 0.12)

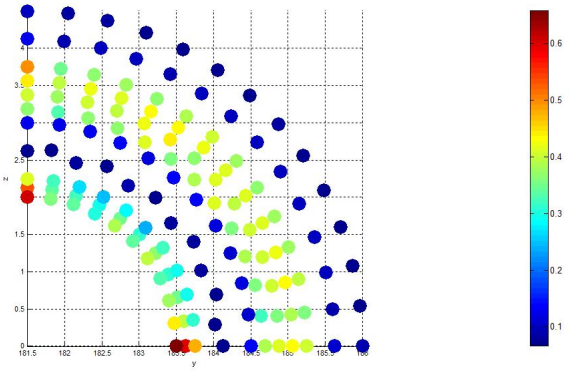

(e) von Mises Tension - NNRPIM - Luminal Pressure = 0.11 MPa (color bar up to 0.6 MPa)

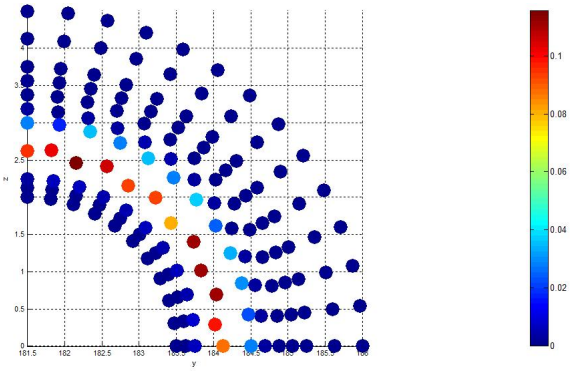

(f) Effective Plastic Strain - NNRPIM - Luminal Pressure = 0.11 MPa (color bar up to 0.1)

Figure 6.77: 3D Artery Model I - Lightly Calcified Atherosclerotic Plaque - Cross-section at the Highest Stenosis point

In the following figure we can see a deformed longitudinal view of the von Mises Tension Field.

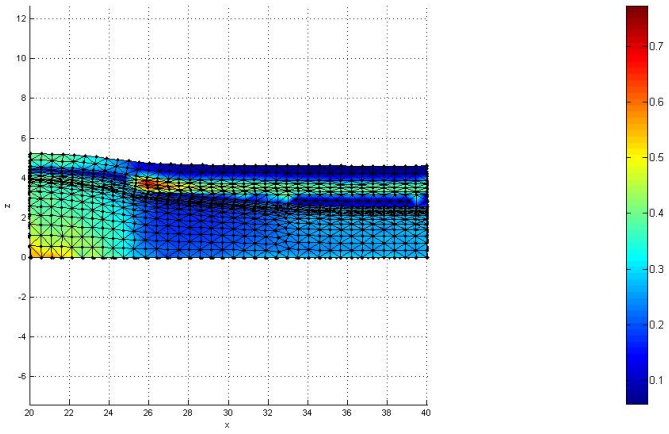

(a) Result obtained from FEM (color bar up to 0.7 MPa)

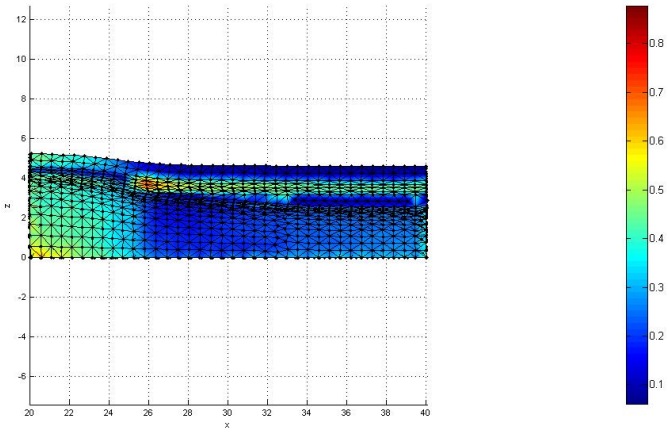

(b) Result obtained with RPIM (color bar up to 0.8 MPa)

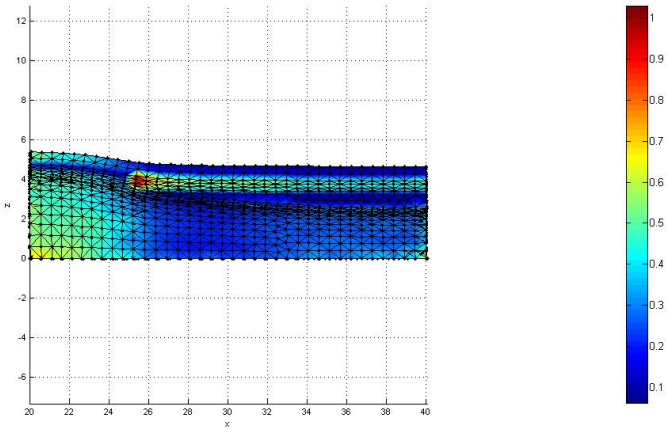

(c) Result obtained with NNRPIM (color bar up to 1.0 MPa)

Figure 6.78: 3D Model I - Deformed Longitudinal view with von Mises Tension Field - Lightly Calcified Plaque

6.3.1.2 Moderately Calcified

For a Moderately Calcified atherosclerotic plaque, the following von Mises stress fields and Effective Plastic Strain Fields were obtained. This fields were obtained at the highest luminal pressure of each numerical analysis.

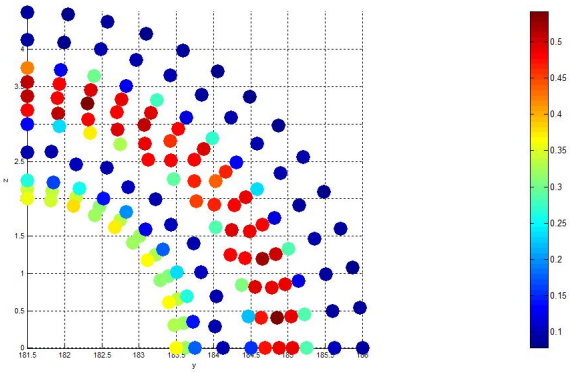

(a) von Mises Tension - FEM - Luminal Pressure = 0.12 MPa (color bar up to 0.5 MPa)

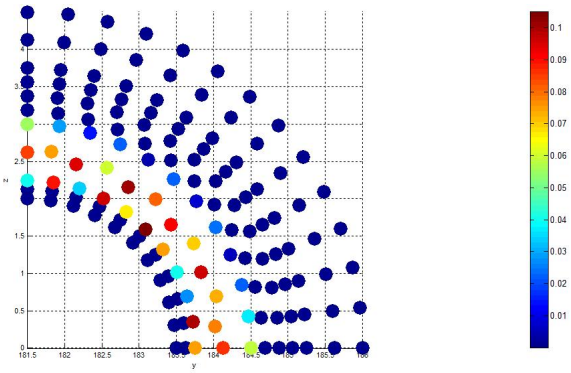

(b) Effective Plastic Strain - FEM - Luminal Pressure = 0.12 MPa (color bar up to 0.1)

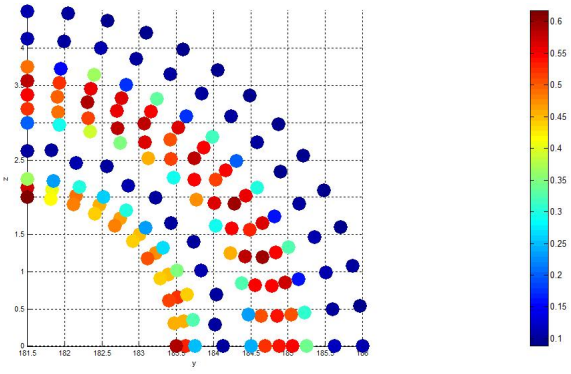

(c) von Mises Tension - RPIM - Luminal Pressure = 0.13 MPa (color bar up to 0.6 MPa)

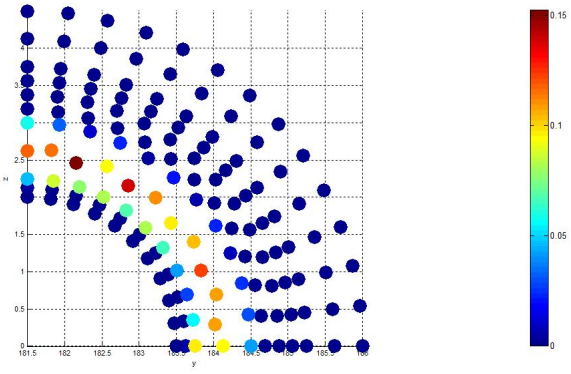

(d) Effective Plastic Strain - RPIM - Luminal Pressure = 0.13 MPa (color bar up to 0.15)

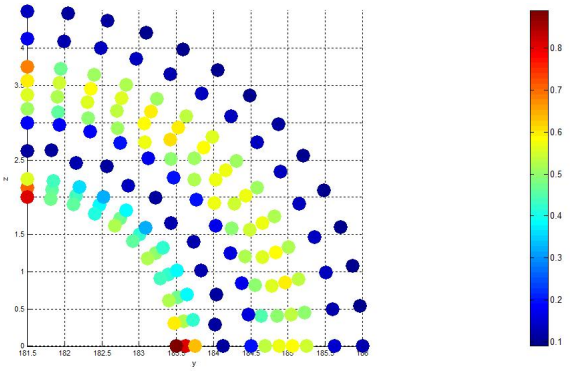

(e) von Mises Tension - NNRPIM - Luminal Pressure = 0.14 MPa (color bar up to 0.8 MPa)

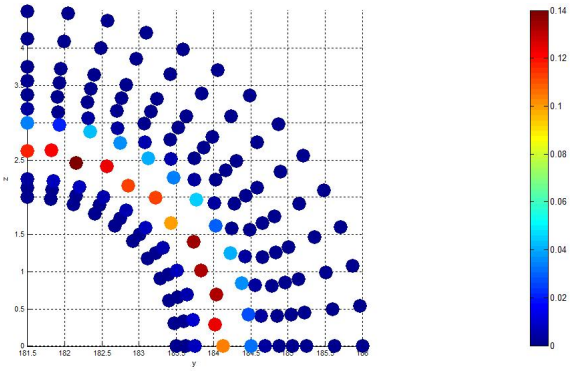

(f) Effective Plastic Strain - NNRPIM - Luminal Pressure = 0.14 MPa (color bar up to 0.14)

Figure 6.79: 3D Artery Model I - Moderately Calcified Atherosclerotic Plaque - Cross-section at the Highest Stenosis point

In the following figure we can see a deformed longitudinal view of the von Mises Tension Field.

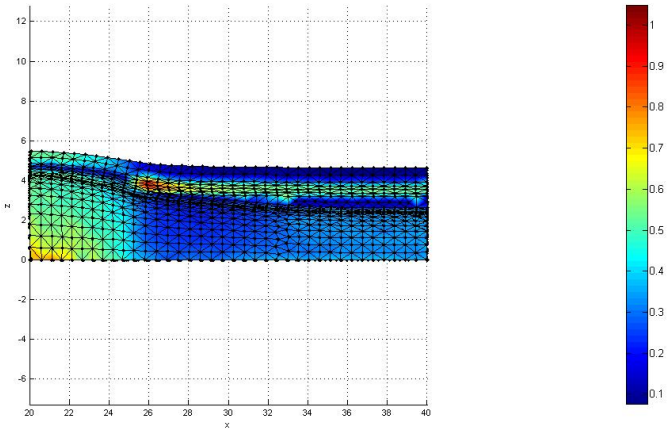

(a) Result obtained from FEM (color bar up to 1.0 MPa)

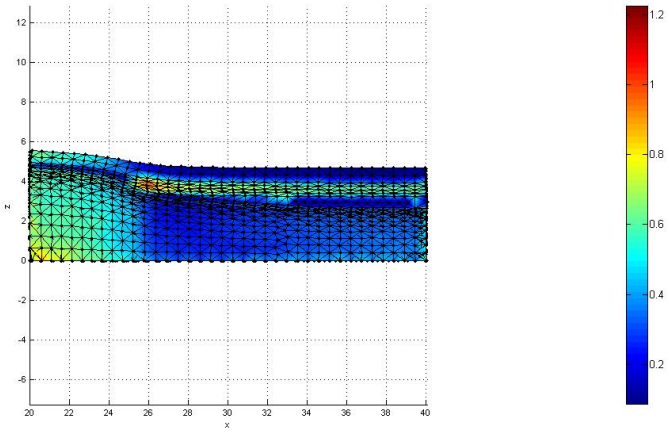

(b) Result obtained with RPIM (color bar up to 1.2 MPa)

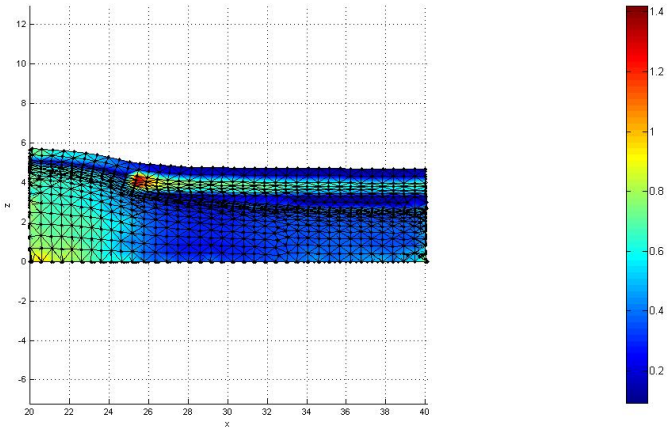

(c) Result obtained with NNRPIM (color bar up to 1.4 MPa)

Figure 6.80: 3D Model I - Deformed Longitudinal view with von Mises Tension Field - Moderately Calcified Plaque

6.3.1.3 Heavily Calcified

For a Heavily Calcified atherosclerotic plaque, the following von Mises stress fields and Effective Plastic Strain Fields were obtained. This fields were obtained at the highest luminal pressure of each numerical analysis.

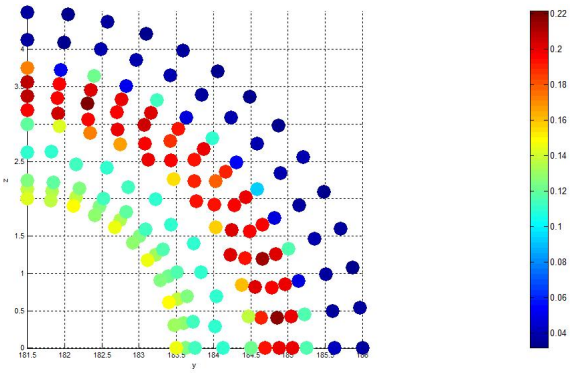

(a) von Mises Tension - FEM - Luminal Pressure = 0.07 MPa (color bar up to 0.22 MPa)

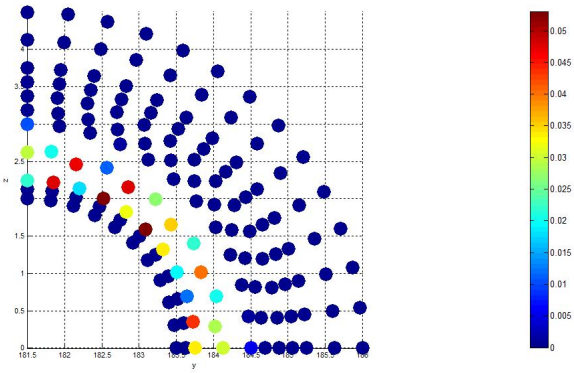

(b) Effective Plastic Strain - FEM - Luminal Pressure = 0.07 MPa (color bar up to 0.05)

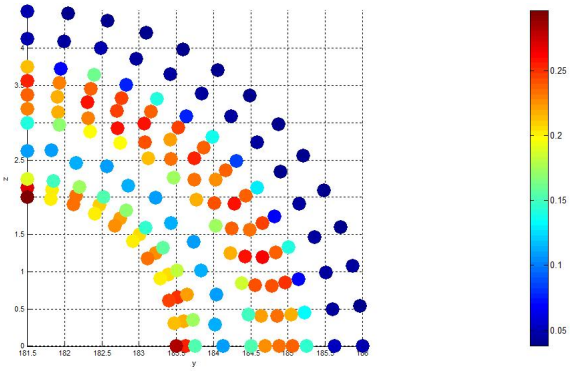

(c) von Mises Tension - RPIM - Luminal Pressure = 0.08 MPa (color bar up to 0.25 MPa)

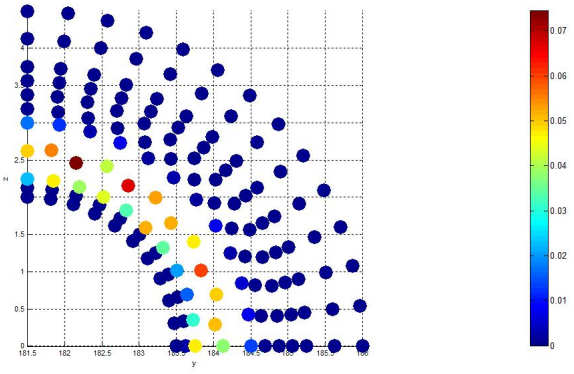

(d) Effective Plastic Strain - RPIM - Luminal Pressure = 0.08 MPa (color bar up to 0.07)

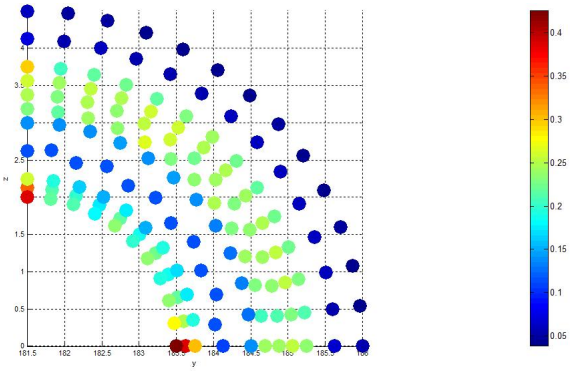

(e) von Mises Tension - NNRPIM - Luminal Pressure = 0.08 MPa (color bar up to 0.4 MPa)

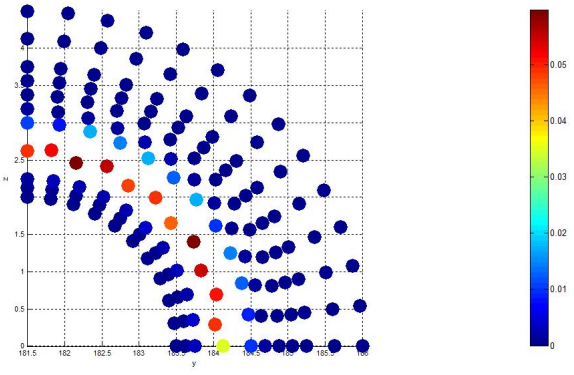

(f) Effective Plastic Strain - NNRPIM - Luminal Pressure = 0.08 MPa (color bar up to 0.05)

Figure 6.81: 3D Artery Model I - Highly Calcified Atherosclerotic Plaque - Cross-section at the Highest Stenosis point

In the following figure we can see a deformed longitudinal view of the von Mises Tension Field.

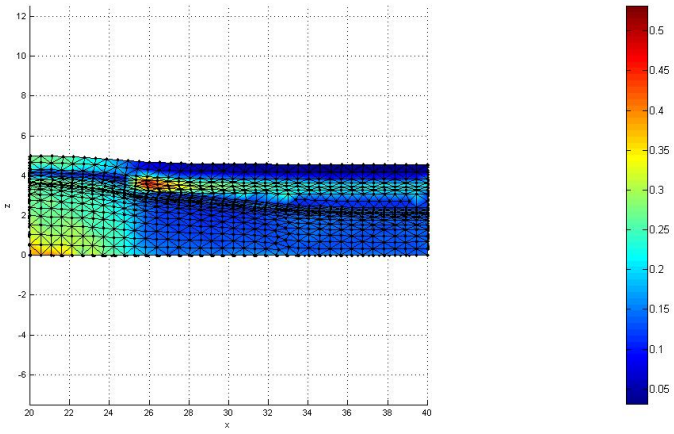

(a) Result obtained from FEM (color bar up to 0.5 MPa)

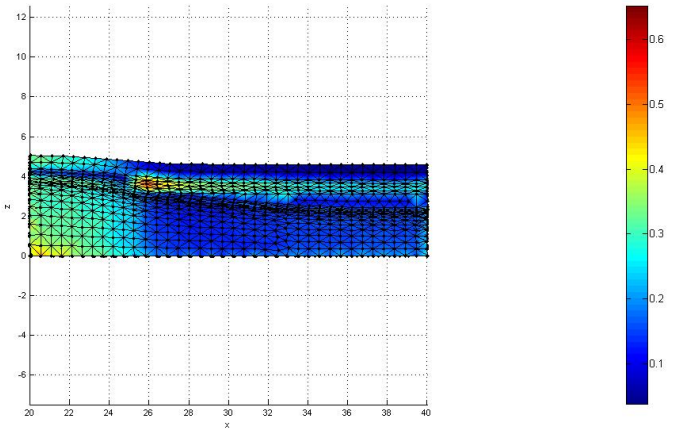

(b) Result obtained with RPIM (color bar up to 0.6 MPa)

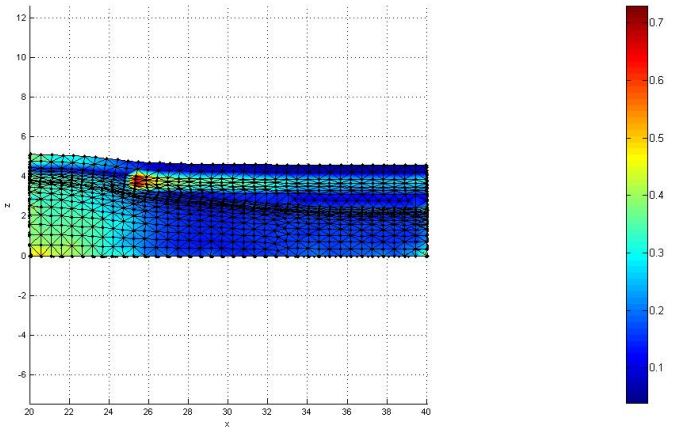

(c) Result obtained with NNRPIM (color bar up to 0.7 MPa)

Figure 6.82: 3D Model I - Deformed Longitudinal view with von Mises Tension Field - Heavily Calcified Plaque

6.3.1.4 Section I Results

By analysing the relation between the luminal pressure and the displacement of Point B of Section 1 with each level of calcification, the following plots were made.

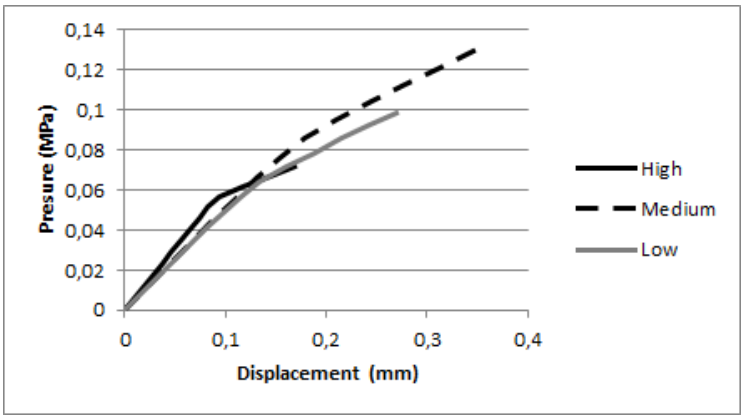

(a) Result obtained with FEM

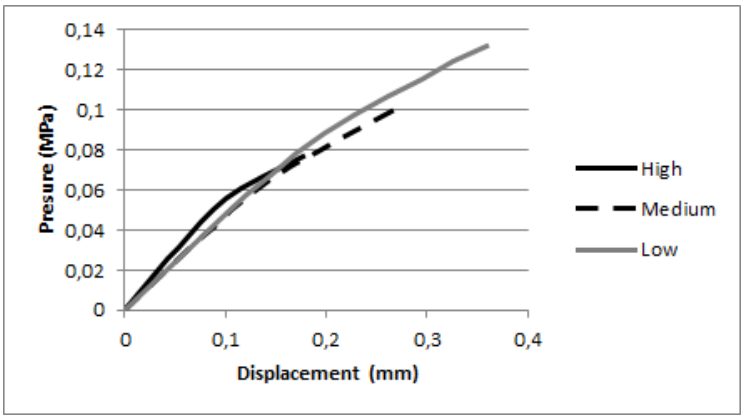

(b) Result obtained with RPIM

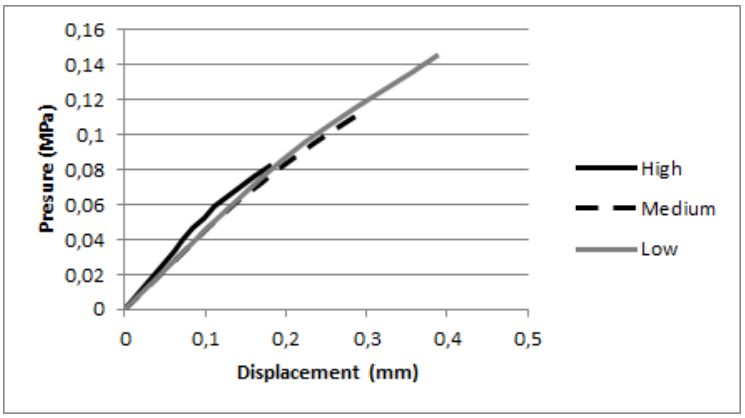

(c) Result obtained with NNRPIM

Figure 6.83: 3D Model I - Displacement in Oz of Point B in Section 1 vs. Luminal Pressure

In Figure 6.84 it is shown the variation of the length of segment B-C which each plaque.

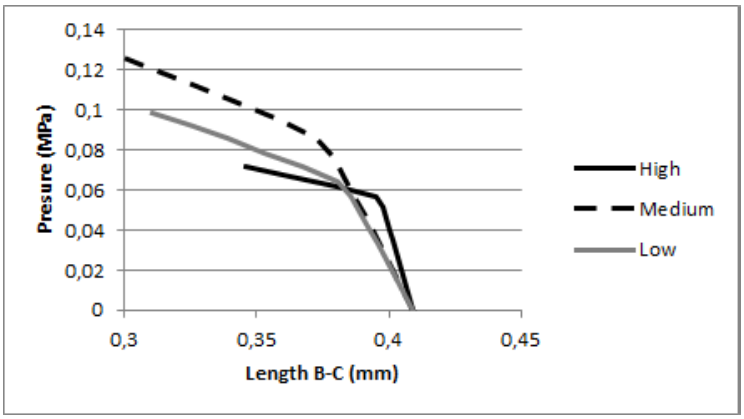

(a) Result obtained from FEM

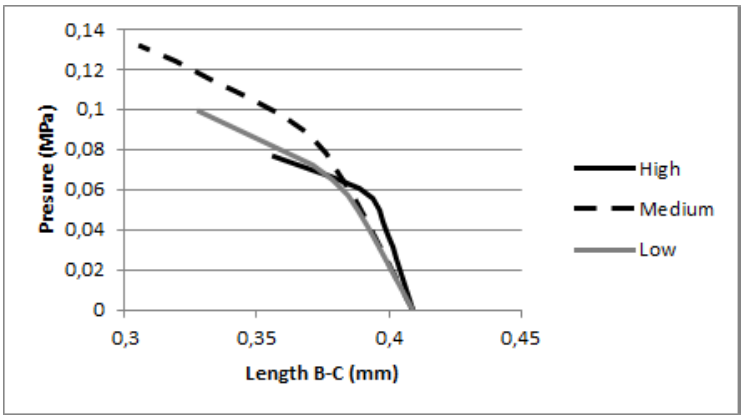

(b) Result obtained with RPIM

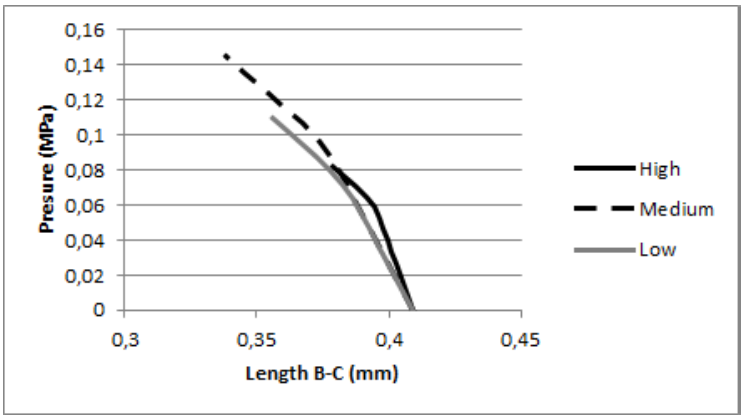

(c) Result obtained with NNRPIM

Figure 6.84: 3D Model I - Length of Segment of Point B-C in Section 1 vs. Luminal Pressure

6.3.1.5 Section II Results

By analysing the relation between the luminal pressure and the displacement of Point B of Section 2 with each level of calcification, the following plots were made.

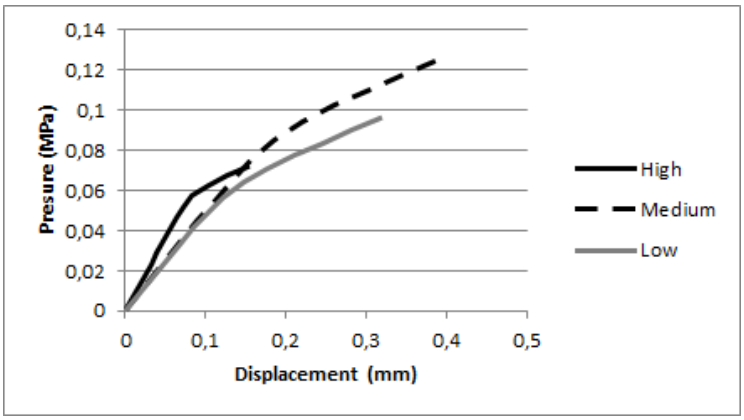

(a) Result obtained with FEM

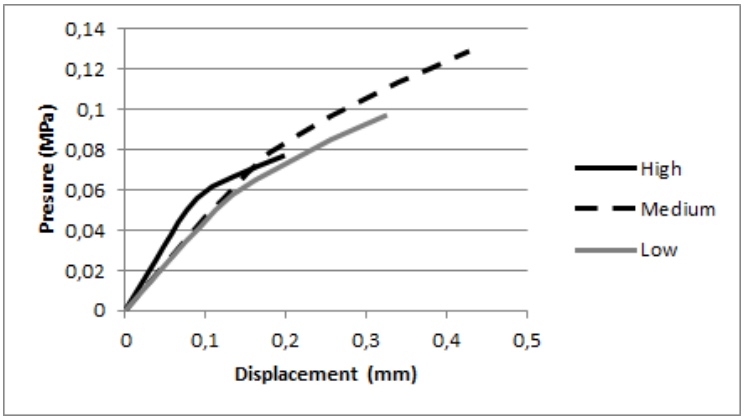

(b) Result obtained with RPIM

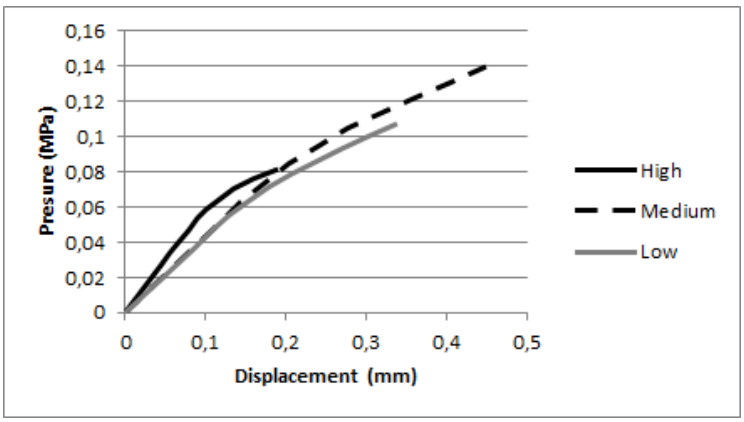

(c) Result obtained with NNRPIM

Figure 6.85: 3D Model I - Displacement in Oz of Point B in Section 2 vs. Luminal Pressure

In Figure 6.86 it is shown the variation of the length of segment B-C which each plaque.

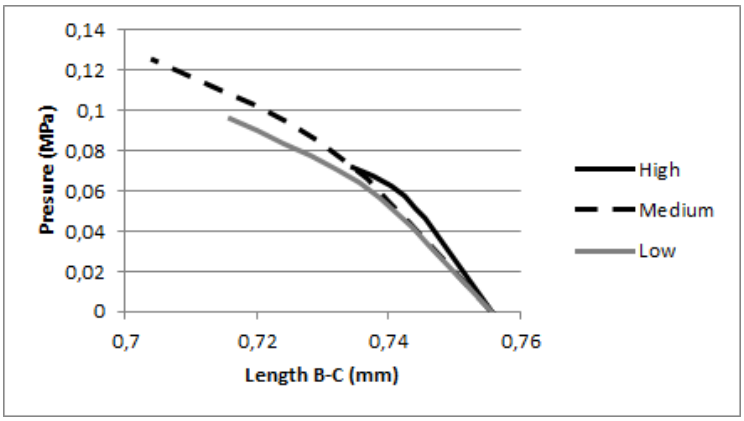

(a) Result obtained from FEM

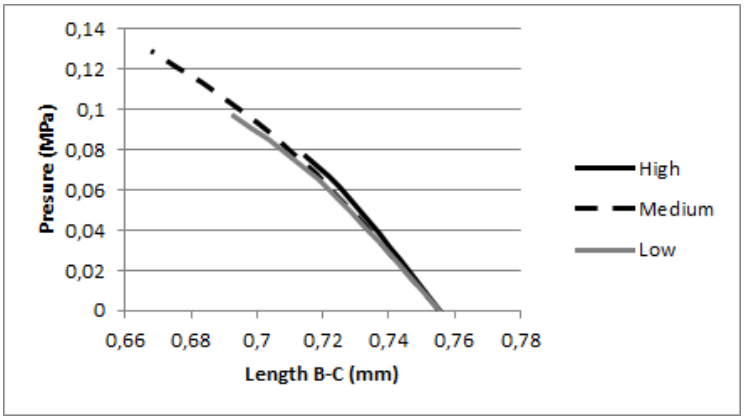

(b) Result obtained with RPIM

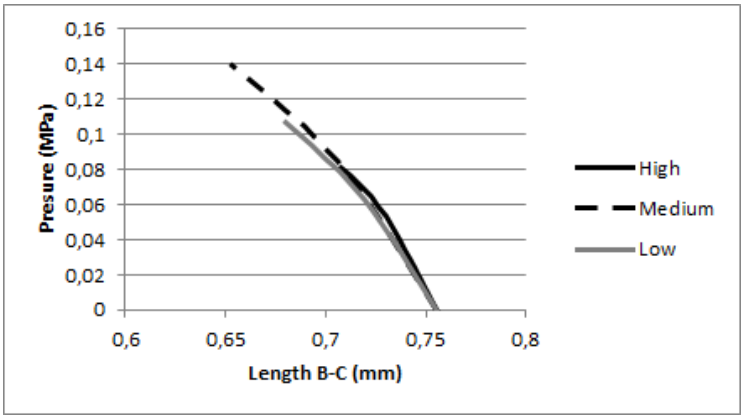

(c) Result obtained with NNRPIM

Figure 6.86: 3D Model I - Length of Segment B-C in Section 2 vs. Luminal Pressure

6.3.1.6 Discussion

One of the first differences seen between the 2D and 3D numerical examples is the diference in magnitude of the displacements seen. While on the 2D analysis the displacements seen could reach more than 2mm, in Figure 6.83 and 6.85 the displacement never surpass 0.5mm. This can be explained by the different configuration of the two models. While on the 2D models the plaque and the damaged tissues only represented part of the arteries surface, in the 3D model, due to the symmetry conditions applied, it is being analysed an artery with a continuous plaque through all its surface. As the plaque and the damaged tissues present a higher Young's Modulus then the healthy tissues the artery in 3D model is stiffer and, as a consequence, will present lower displacements.

In section I, as it was possible to visualize with thinner atherosclerotic plaques in the 2D analysis, the displacement curve, while showing some non-linear behaviour there is not much difference between the various types of plaque. This difference can be more clearly visible in section 2 where it is seen a change of stiffness between the levels of calcification. In this section while it is possible to see the yielding of the lightly and moderately calcified plaques on the expected pressures, the heavily calcified plaque appears to start to yield at lower pressures. The same effect is seen on the variation of length of B-C in section 1, as for on section 2 this analysis does not show a very significant plastification. The plots relating to this variation are presented in Figures 6.84 and 6.86 The low level of plastification near the thicker end of the model can also be seen in low level of plastification shown in the Effective Plastic Strain fields (Figures 6.77, 6.79 and 6.81).

As for the longitudinal von Mises Tension fields (Figures 6.78, 6.80 and 6.82), as seen in the 2D examples, there is a accumulation of tension in the interface between the damaged *media* and the healthy *media* due to the previously mentioned limitations of the model. But it can also be seen in those fields the effects of the artery's stiffening in the healthy tissues with the large expansion and higher tensions that exist in the healthier part of the artery.

The 3D model, as with the 2D examples, shows that at normal systolic blood pressure (0.01867 MPa) [91] none of all of the atherosclerotic plaques experience plastic deformations, as seen in the displacement variations with the increase of pressure.

When comparing the three numerical methods in both sections, Figure 6.87 and 6.88, the results show a good overlay between them for the lightly and moderately. In the case of the heavily calcified plaque the results seem to show some variance that could be a result of the lower nodal density used for the 3D analysis.

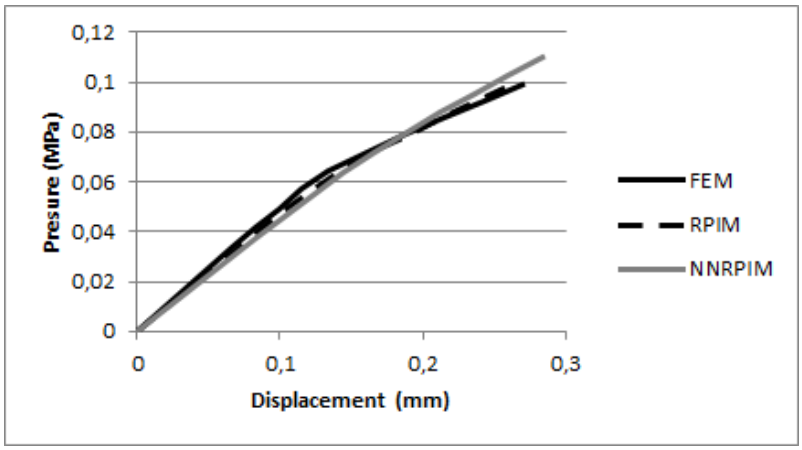

(a) Result obtained from Lightly Calcified plaque

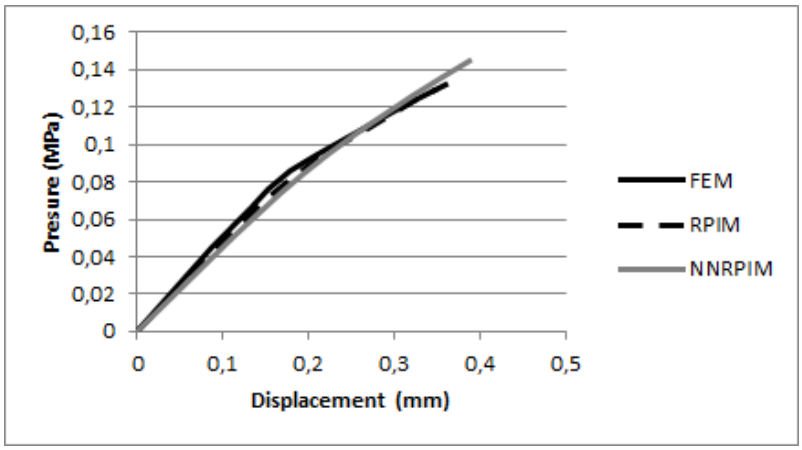

(b) Result obtained with Moderately Calcified plaque

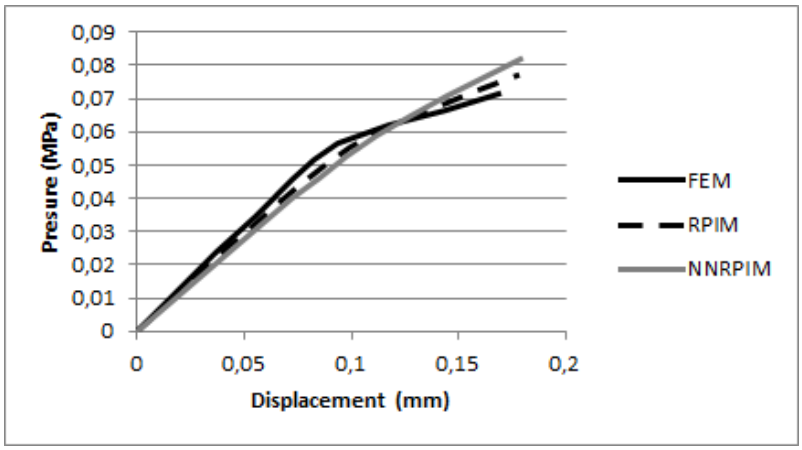

(c) Result obtained with Heavily Calcified plaque

Figure 6.87: 3D Model I - Comparison of displacement of point B with different numerical methods - Section 2

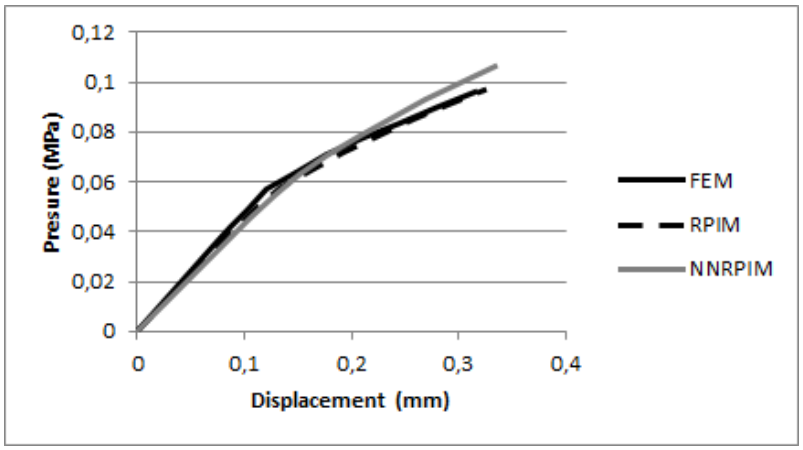

(a) Result obtained from Lightly Calcified plaque

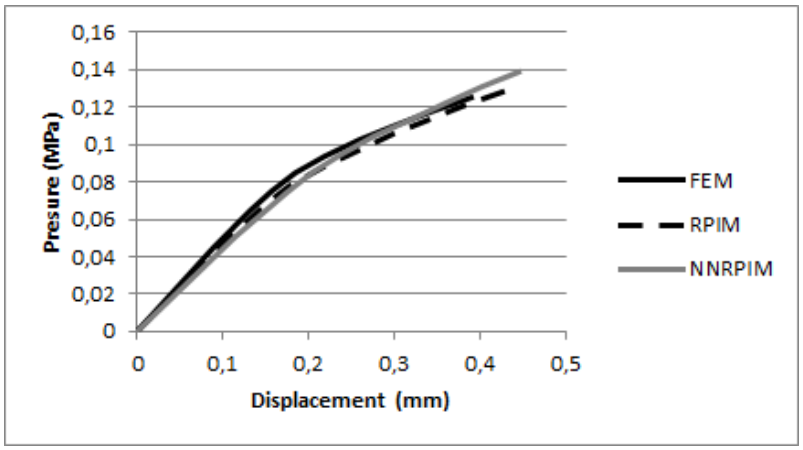

(b) Result obtained with Moderately Calcified plaque

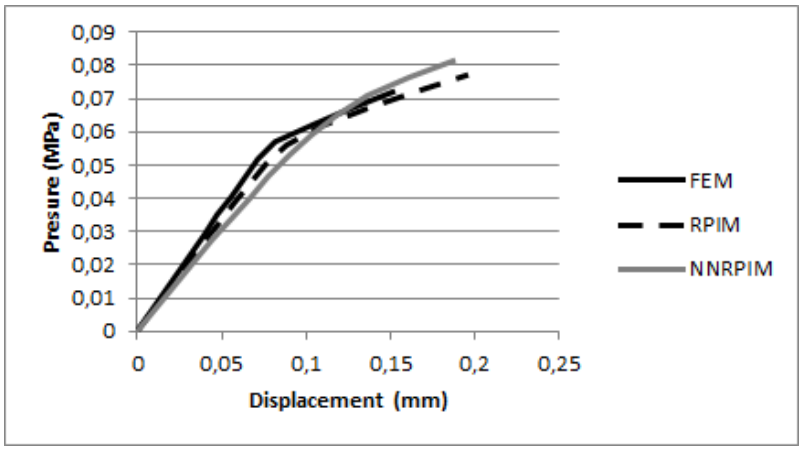

(c) Result obtained with Heavily Calcified plaque

Figure 6.88: 3D Model I - Comparison of displacement of point B with different numerical methods - Section 2

6.3.2 3D Model II

For this example it was taken into consideration a solid domain $\omega \in \Re^3$ representing a atherosclerotic artery containing a plaque provoking an stenosis of two thirds of the lumen diameter. The plaque simulated is a continuous plaque extending through the complete radius of the artery. Due to the natural symmetry of the simplified model, only 1/8 of the artery was analysed. It was applied to the domain symmetry constrains. The numerical model was designed using 3985 nodes and was analysed using three different numerical methods (FEM, RPIM and NNRPIM). An image of the nodal distribution used can be seen in Figure 6.89

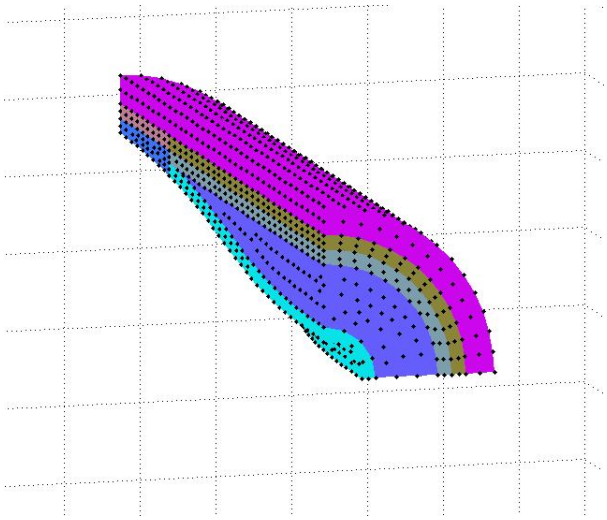

Figure 6.89: 3D Model of Artery with Atherosclerotic Plaque - Model 2

The von Mises Stress field were analysed for each of the atherosclerotic plaque set of material properties on the thicker end of the atherosclerotic plaque. The longitudinal view of the model under each of the conditions was also analysed in order to study the effect of the transition to the diseased area. Besides this, it was also analysed the displacement in Oz in specific interface nodes between tissues at two different positions of the model. The location of these nodes can be seen in the diagram of Figure 6.90, where S1 is the first position analysed and S2 the second. The displacement seen was analysed against to the pressure applied in the artery's lumen.

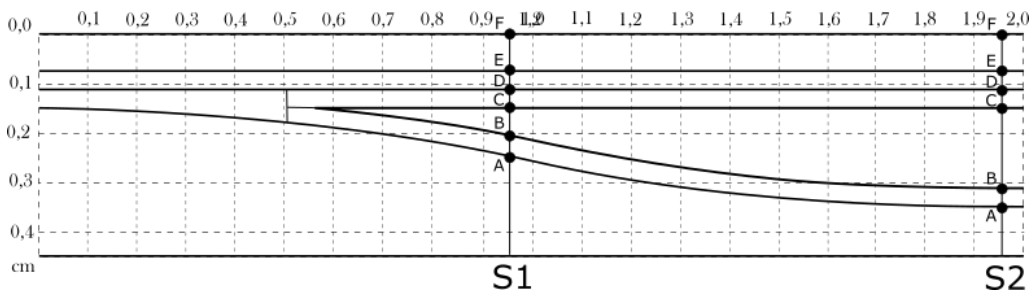

Figure 6.90: 3D Model Stage II - Points location

6.3.2.1 Lightly Calcified

For a Lightly Calcified atherosclerotic plaque, the following von Mises stress fields and Effective Plastic Strain Fields were obtained. This fields were obtained at the highest luminal pressure of each numerical analysis.

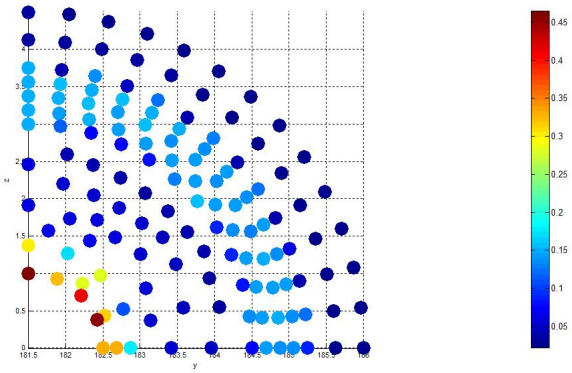

(a) von Mises Tension - FEM - Luminal Pressure = 0.10 MPa (color bar up to 0.45 MPa)

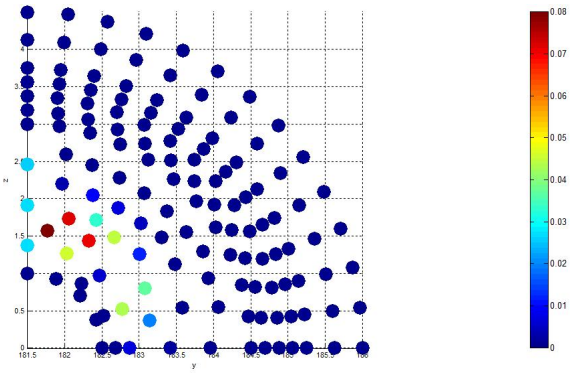

(b) Effective Plastic Strain - FEM - Luminal Pressure = 0.10 MPa (color bar up to 0.08)

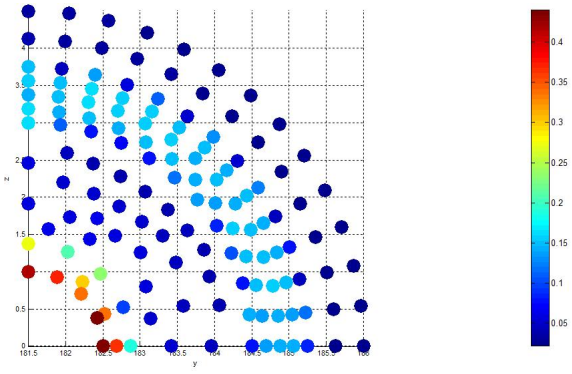

(c) von Mises Tension - RPIM - Luminal Pressure = 0.10 MPa (color bar up to 0.4 MPa)

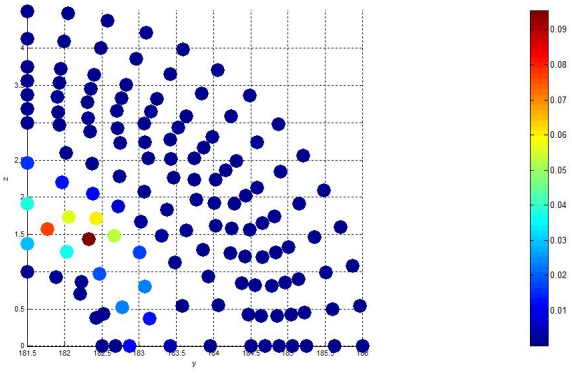

(d) Effective Plastic Strain - RPIM - Luminal Pressure = 0.10 MPa (color bar up to 0.09)

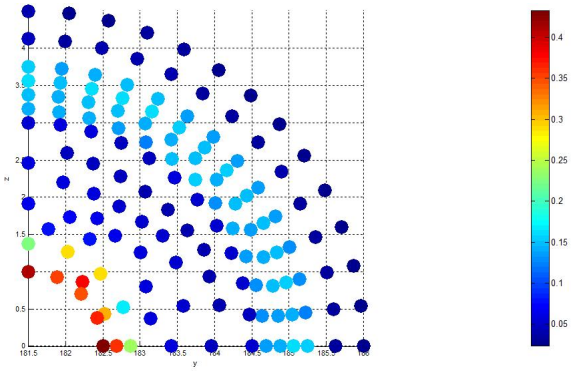

(e) von Mises Tension - NNRPIM - Luminal Pressure = 0.11 MPa (color bar up to 0.4 MPa)

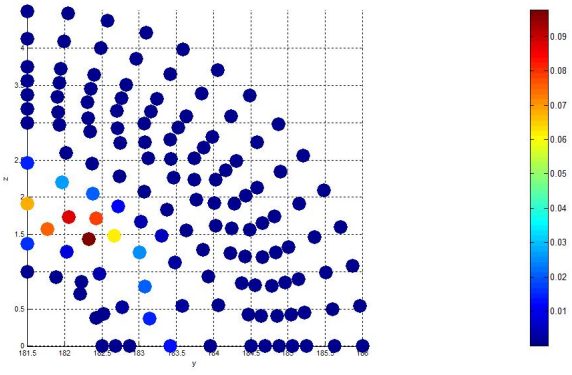

(f) Effective Plastic Strain - NNRPIM - Luminal Pressure = 0.11 MPa (color bar up to 0.09)

Figure 6.91: 3D Artery Model II - Lightly Calcified Atherosclerotic Plaque - Cross-section at the Highest Stenosis point

In the following figure we can see a deformed longitudinal view of the von Mises Tension Field.

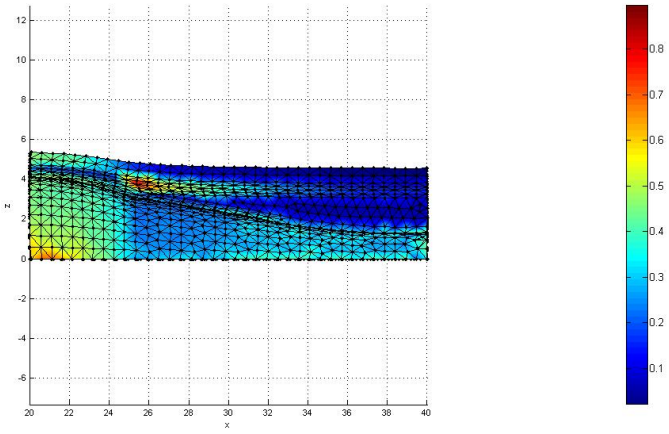

(a) Result obtained from FEM (color bar up to 0.8 MPa)

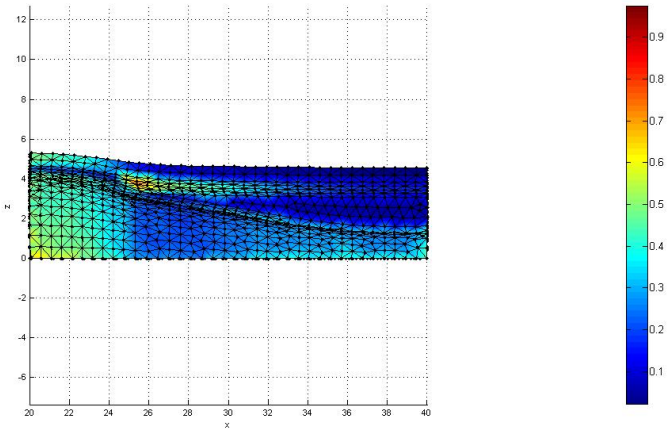

(b) Result obtained with RPIM (color bar up to 0.9 MPa)

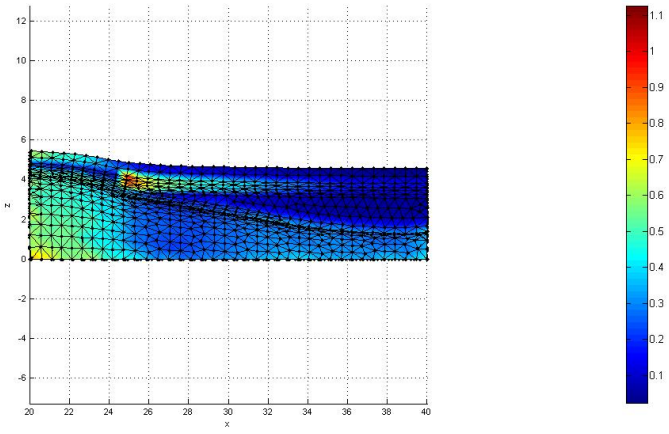

(c) Result obtained with NNRPIM (color bar up to 1.1 MPa)

Figure 6.92: 3D Model II - Deformed Longitudinal view with von Mises Tension Field - Lightly Calcified Plaque

6.3.2.2 Moderately Calcified

For a Moderately Calcified atherosclerotic plaque, the following von Mises stress fields and Effective Plastic Strain Fields were obtained. This fields were obtained at the highest luminal pressure of each numerical analysis.

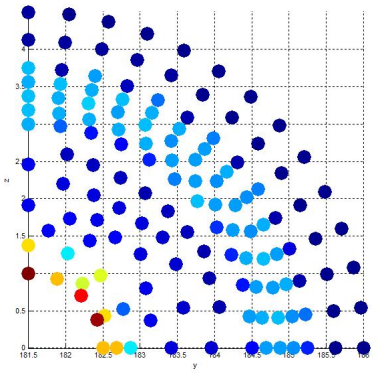

(a) von Mises Tension - FEM - Luminal Pressure = 0.13 MPa (color bar up to 0.6 MPa)

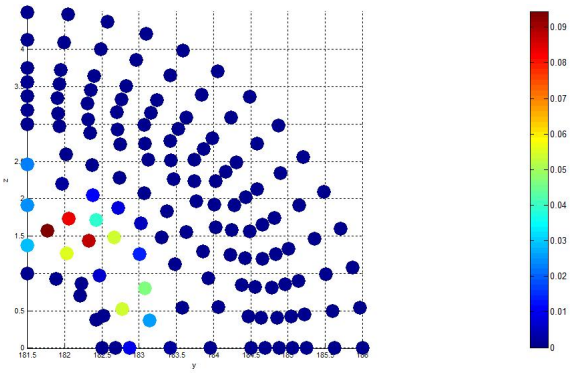

(b) Effective Plastic Strain - FEM - Luminal Pressure = 0.13 MPa (color bar up to 0.09)

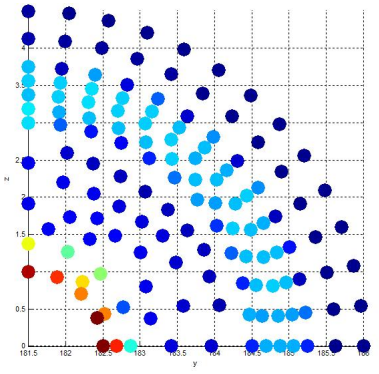

(c) von Mises Tension - RPIM - Luminal Pressure = 0.13 MPa (color bar up to 0.55 MPa)

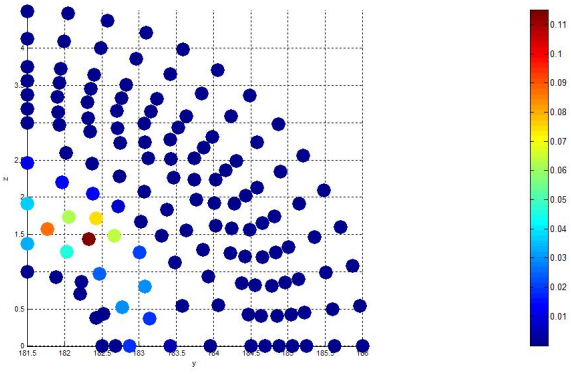

(d) Effective Plastic Strain - RPIM - Luminal Pressure = 0.13 MPa (color bar up to 0.11)

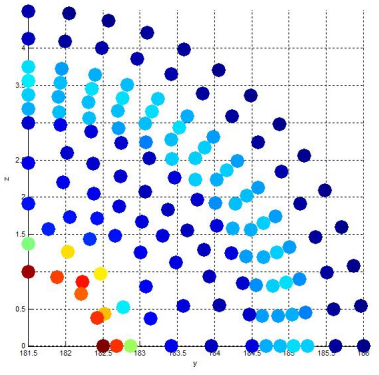

(e) von Mises Tension - NNRPIM - Luminal Pressure = 0.14 MPa (color bar up to 0.55 MPa)

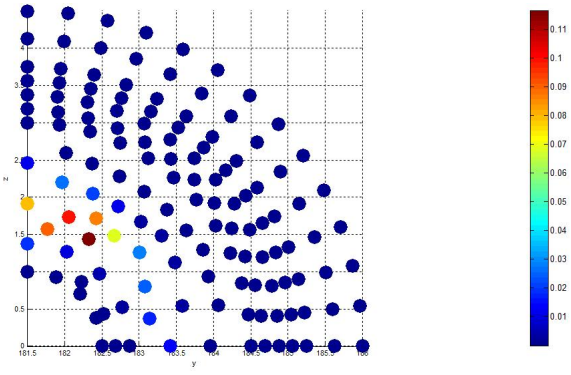

(f) Effective Plastic Strain - NNRPIM - Luminal Pressure = 0.14 MPa (color bar up to 0.11)

Figure 6.93: 3D Artery Model II - Moderately Calcified Atherosclerotic Plaque - Cross-section at the Highest Stenosis point

In the following figure we can see a deformed longitudinal view of the von Mises Tension Field.

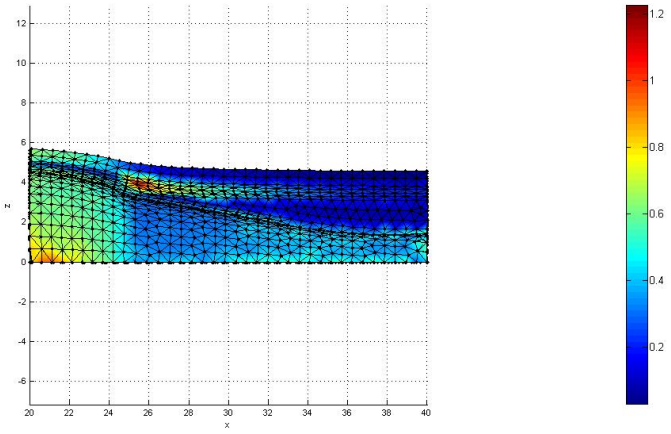

(a) Result obtained from FEM (color bar up to 1.2 MPa)

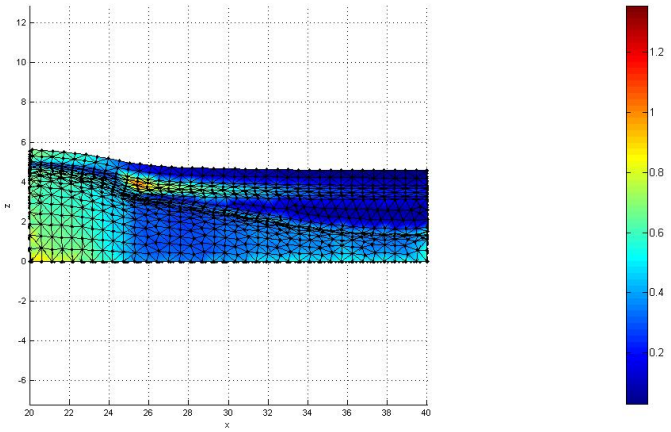

(b) Result obtained with RPIM (color bar up to 1.2 MPa)

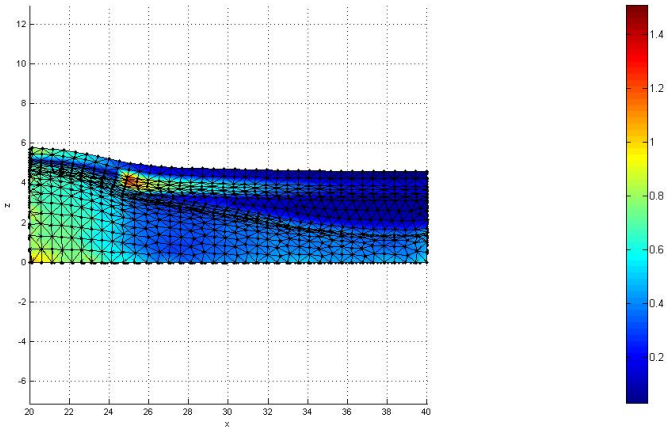

(c) Result obtained with NNRPIM (color bar up to 1.4 MPa)

Figure 6.94: 3D Model II - Deformed Longitudinal view with von Mises Tension Field - Moderately Calcified Plaque

6.3.2.3 Heavily Calcified

For a Heavily Calcified atherosclerotic plaque, the following von Mises stress fields and Effective Plastic Strain Fields were obtained. This fields were obtained at the highest luminal pressure of each numerical analysis.

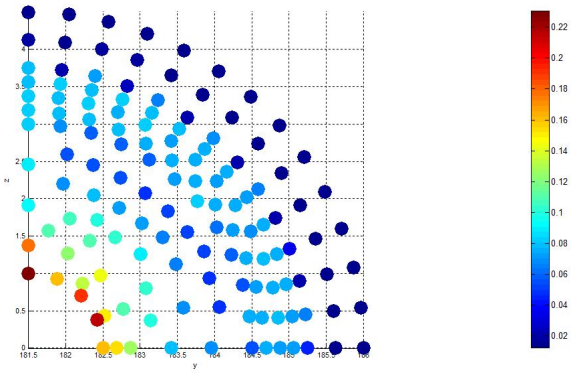

(a) von Mises Tension - FEM - Luminal Pressure = 0.09 MPa (color bar up to 0.22 MPa)

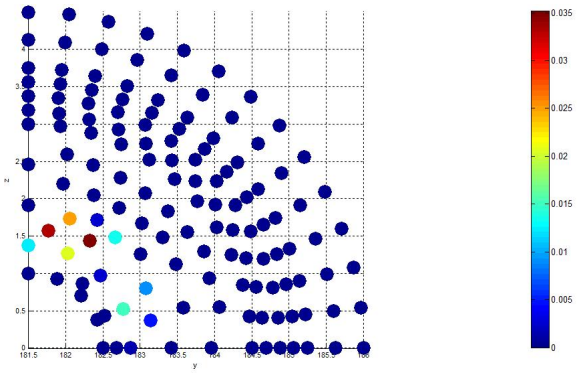

(b) Effective Plastic Strain - FEM - Luminal Pressure = 0.09 MPa (color bar up to 0.035)

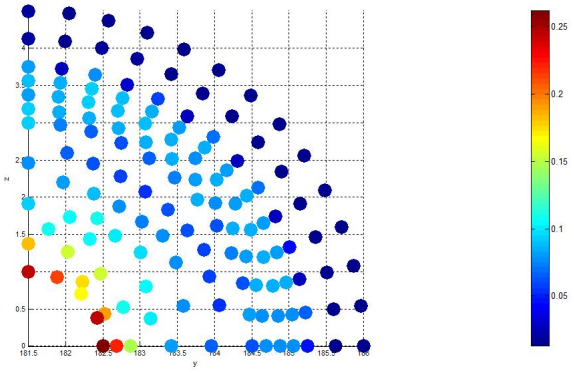

(c) von Mises Tension - RPIM - Luminal Pressure = 0.09 MPa (color bar up to 0.25 MPa)

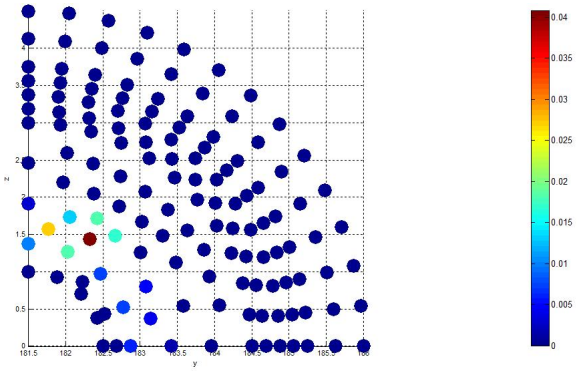

(d) Effective Plastic Strain - RPIM - Luminal Pressure = 0.09 MPa (color bar up to 0.04)

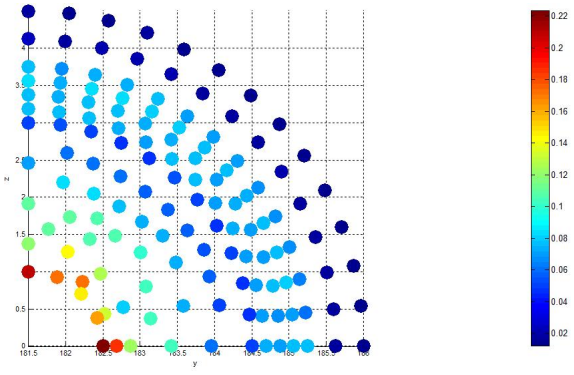

(e) von Mises Tension - NNRPIM - Luminal Pressure = 0.08 MPa (color bar up to 0.22 MPa)

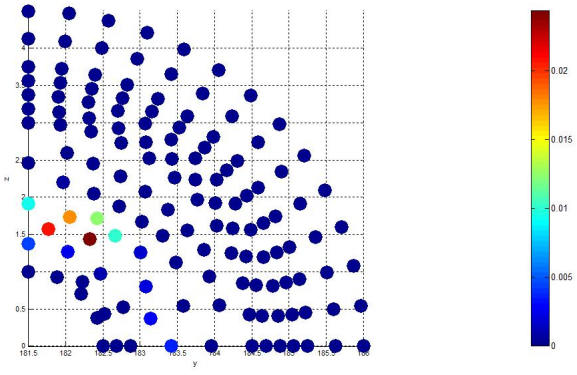

(f) Effective Plastic Strain - NNRPIM - Luminal Pressure = 0.08 MPa (color bar up to 0.02)

Figure 6.95: 3D Artery Model II - Highly Calcified Atherosclerotic Plaque - Cross-section at the Highest Stenosis point

In the following figure we can see a deformed longitudinal view of the von Mises Tension Field.

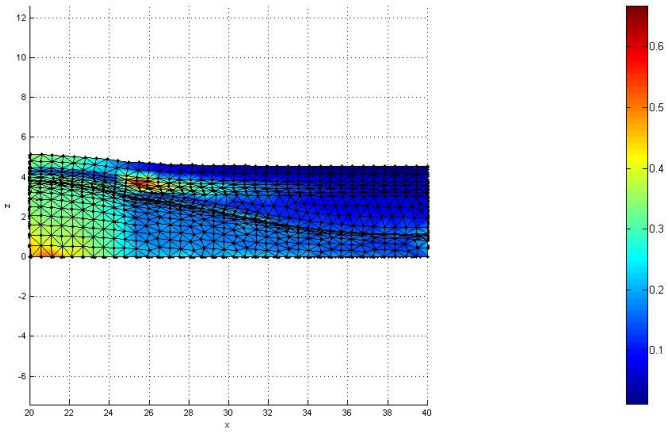

(a) Result obtained from FEM (color bar up to 0.6 MPa)

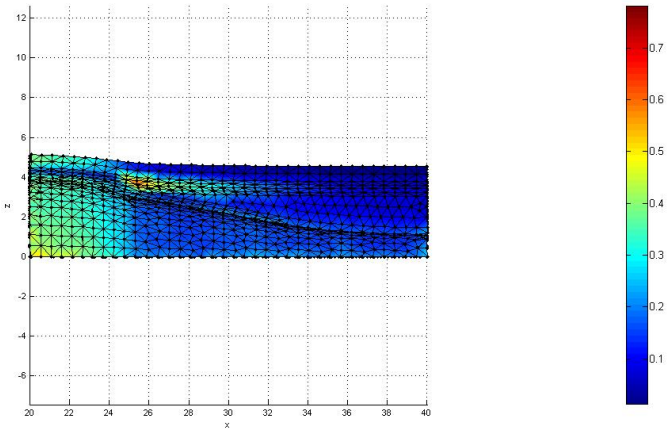

(b) Result obtained with RPIM (color bar up to 0.7 MPa)

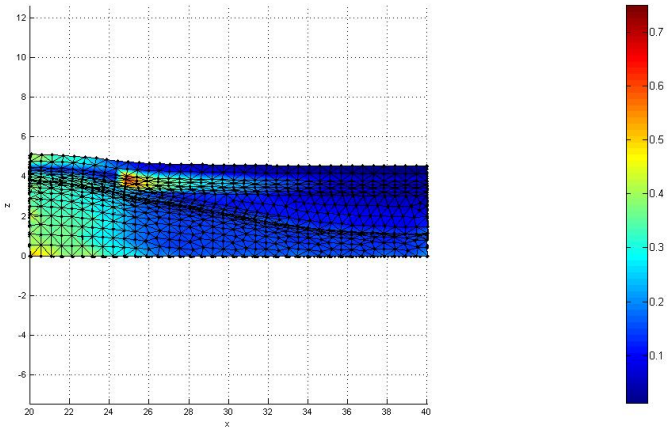

(c) Result obtained with NNRPIM (color bar up to 0.7 MPa)

Figure 6.96: 3D Model II - Deformed Longitudinal view with von Mises Tension Field - Heavily Calcified Plaque

6.3.2.4 Section I Results

By analysing the relation between the luminal pressure and the displacement of Point B of Section 1 with each level of calcification, the following plots were made.

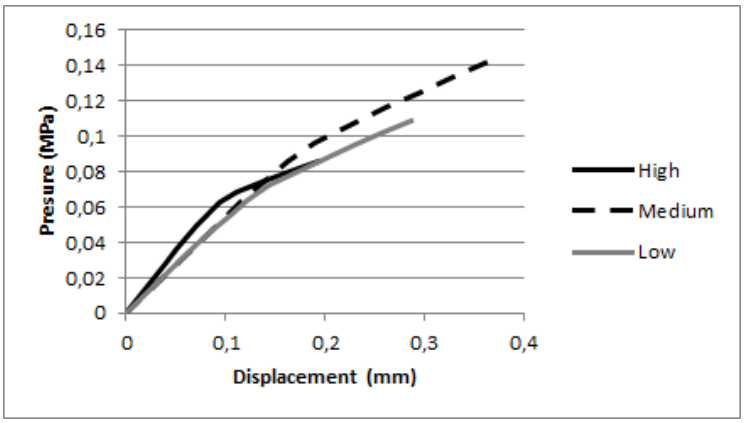

(a) Result obtained with FEM

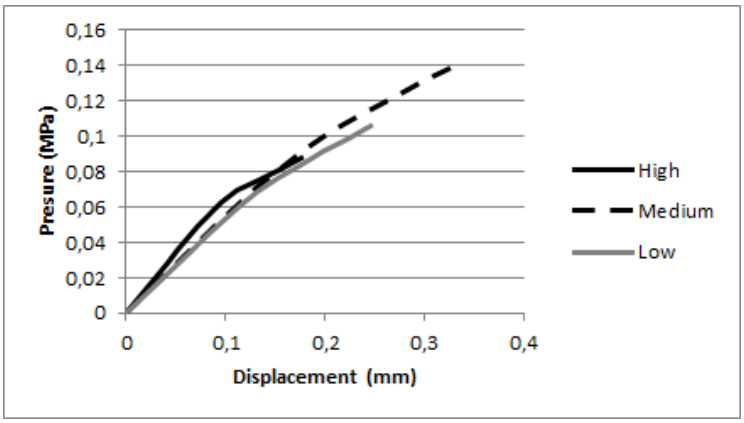

(b) Result obtained with RPIM

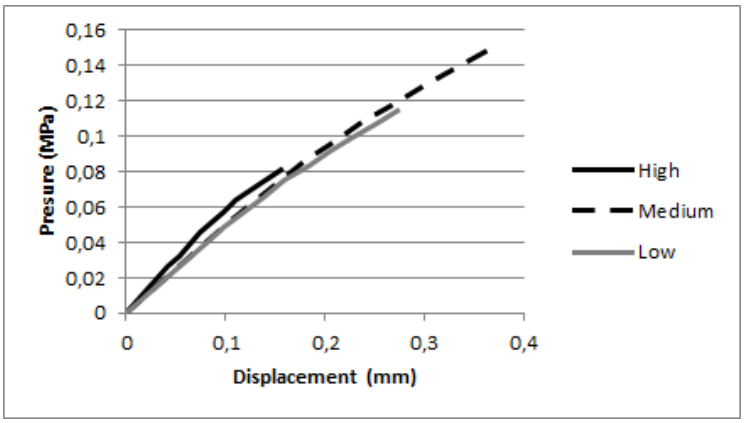

(c) Result obtained with NNRPIM

Figure 6.97: 3D Model II - Displacement in Oz of Point B in Section 1 vs. Luminal Pressure

In Figure 6.98 it is shown the variation of the length of segment B-C which each plaque.

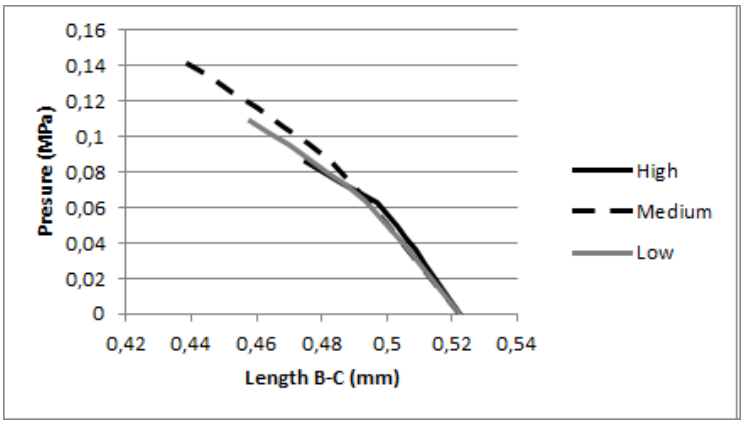

(a) Result obtained with FEM

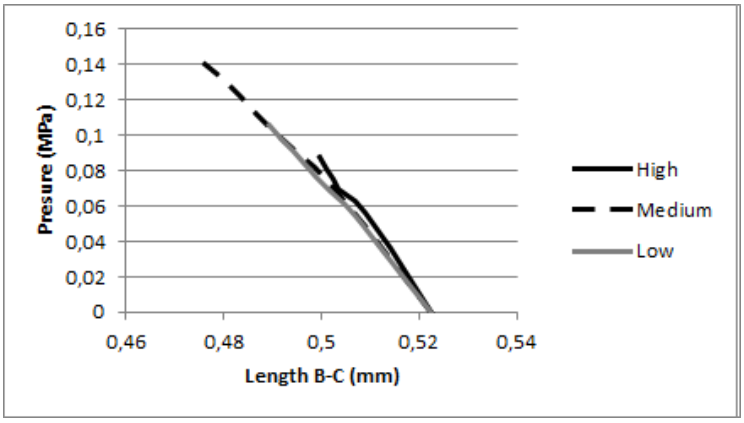

(b) Result obtained with RPIM

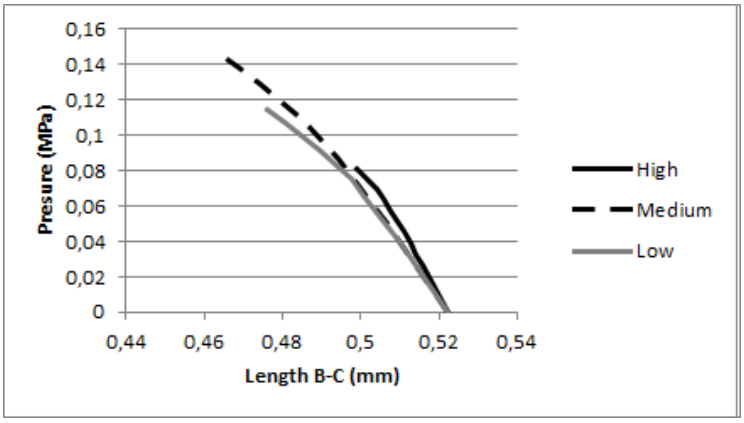

(c) Result obtained with NNRPIM

Figure 6.98: 3D Model II - Length of Segment of Point B-C in Section 1 vs. Luminal Pressure

6.3.2.5 Section II Results

By analysing the relation between the luminal pressure and the displacement of Point B of Section 2 with each level of calcification, the following plots were made.

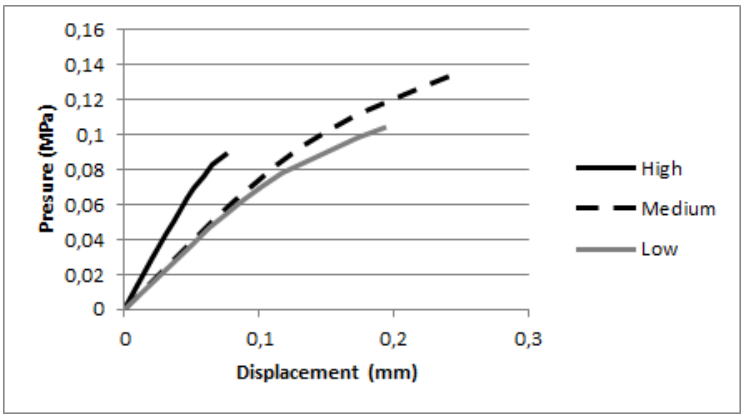

(a) Result obtained with FEM

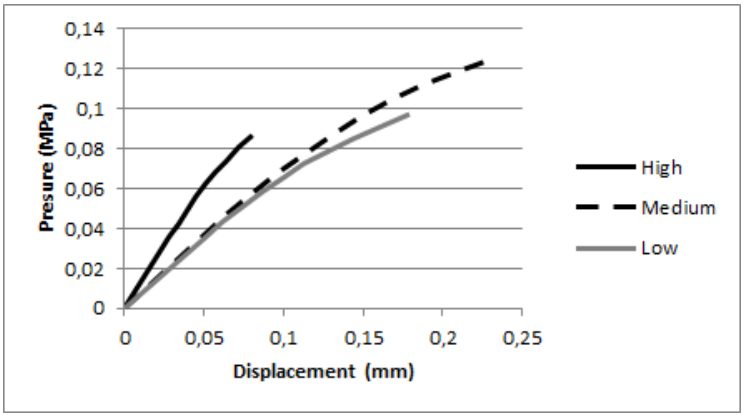

(b) Result obtained with RPIM

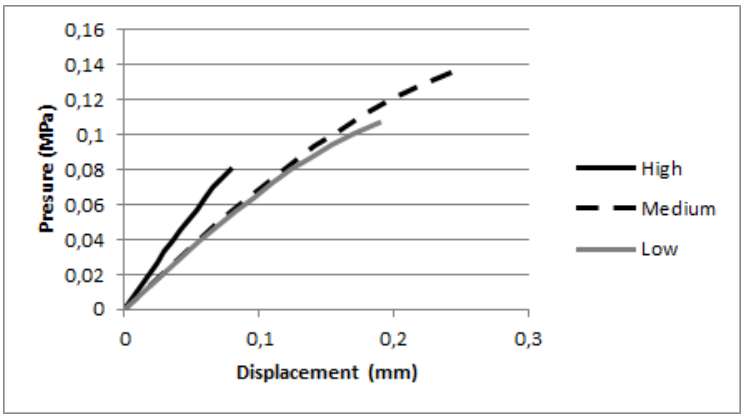

(c) Result obtained with NNRPIM

Figure 6.99: 3D Model II - Displacement in Oz of Point B in Section 2 vs. Luminal Pressure

In Figure 6.100 it is shown the variation of the length of segment B-C which each plaque.

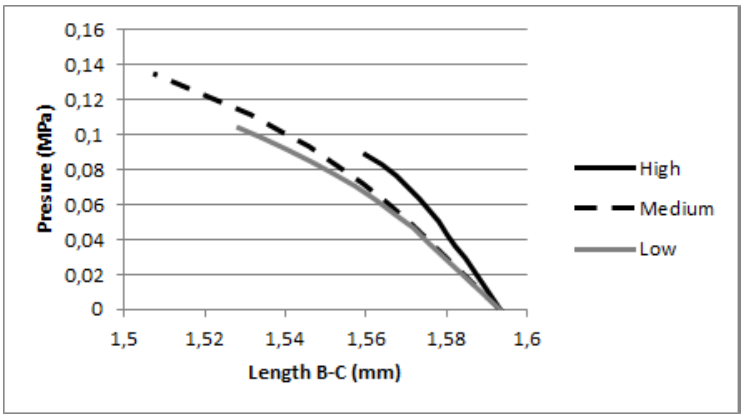

(a) Result obtained with FEM

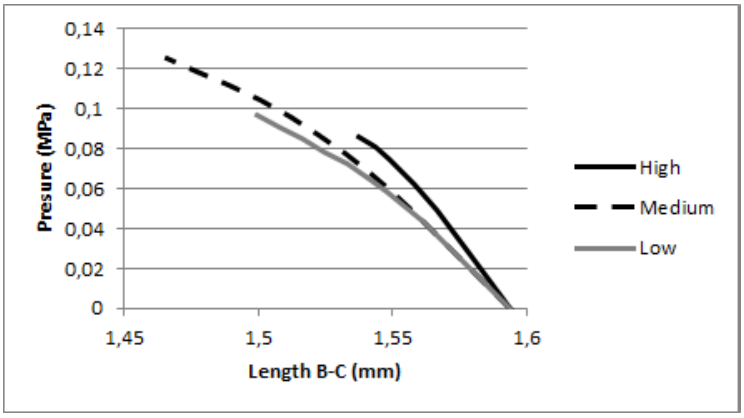

(b) Result obtained with RPIM

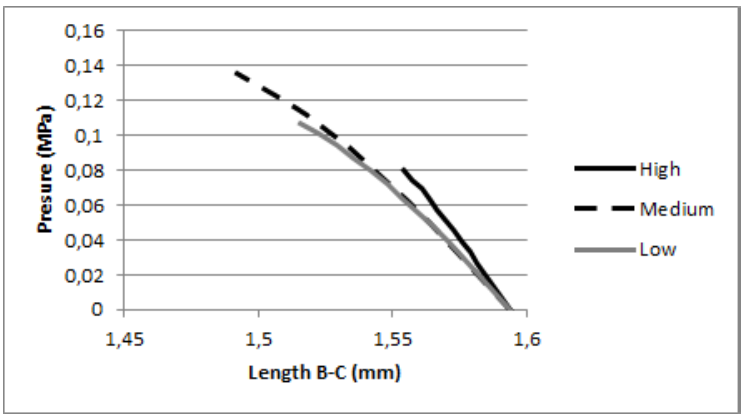

(c) Result obtained with NNRPIM

Figure 6.100: 3D Model II - Length of Segment B-C in Section 2 vs. Luminal Pressure

6.3.2.6 Discussion

In resemblance to the first 3D example, it is seen the same difference in the value of displacement between the 2D and 3D numerical examples. While this difference was already explained in the previous discussion, it can also be noted a difference between the displacement values of section 2 on each of the models. This should be expected since as model II presents a higher level of stenosis, and given the Young's Modulus values for the plaque and damaged tissues, it should also present a higher stiffness. The displacement of each of the analysed sections of model II can be seen in Figure 6.97 and 6.99.

In the displacement curves of section I, the RPIM and the NNRPIM results while showing a small increase in the plaques stiffness has the level of calcification rises, the results appear to be very similar between plaques. As for the FEM results, besides a visible difference in stiffness between the heavily calcified plaque and the others, it shows a yielding of the ligthly and moderately calcified plaques around the expected pressure. Similarly to the previous model the heavily calcified model appears to enter on yielding on a lower pressure then expected. When looking to Section 2, the result of all methods present the same behaviour. While the moderately and lightly calcified plaques appear to show similar stiffness, it can be seen the material to start to yield at their expected pressure, at 0.055 MPa and 0.085 MPa respectively. As for the heavily calcified, the results show a significant difference in its stiffness when compared with the others.

By analysing the variations in length in segment B-C, seen in Figures 6.98 and 6.100, it is observed that this variation is small and with a very smooth behaviour, being difficult to see a clear yield point. Even so, the heavily calcified plaque stills shows a clear higher stiffness than the others on section 2. This difficult in detect the plaques yield point could be explained by the low level of plastification seen in them, as shown in Figures 6.91, 6.93 and 6.95

In the longitudinal von Mises Tension fields (Figures 6.92, 6.94 and 6.96) as seen in the all previous examples, there is a accumulation of stress in the interface between the damaged *media* and the healthy *media* due to the previously mentioned limitations of the model. Another observation to make, as seen in the first 3D model, there is a large expansion and higher streses in the healthier part of the artery. As with the previous examples, this model also shows, as seen in the displacement plots, that at normal systolic blood pressure (0.01867 MPa) [91] none of all of the atherosclerotic plaques experience plastic deformations.

Finally, by comparing the numerical methods in both sections, Figure 6.101 and 6.102, the results show a good overlay between them for the lightly and moderately, while the heavily calcified plaque the results seem to show some variance. This phenomena, as mentioned before, could be a result of the lower nodal density used for the 3D analysis.

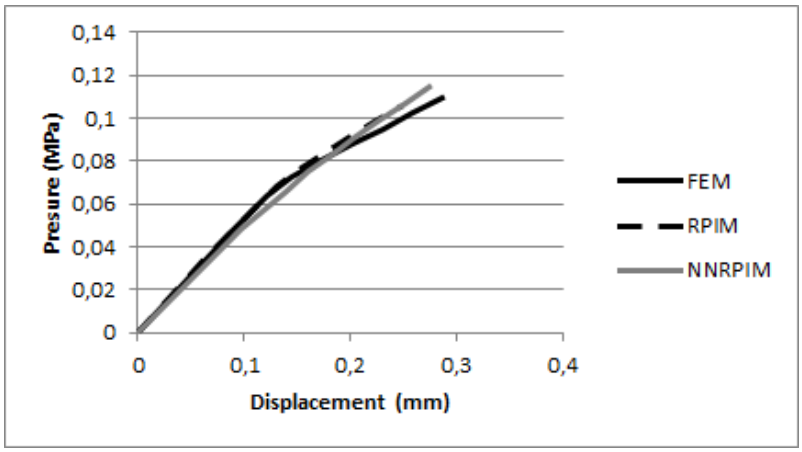

(a) Result obtained with Lightly Calcified plaque

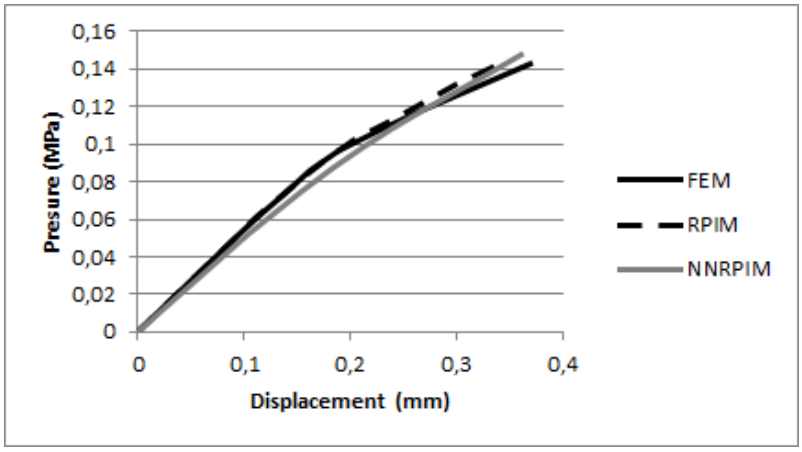

(b) Result obtained with Moderately Calcified plaque

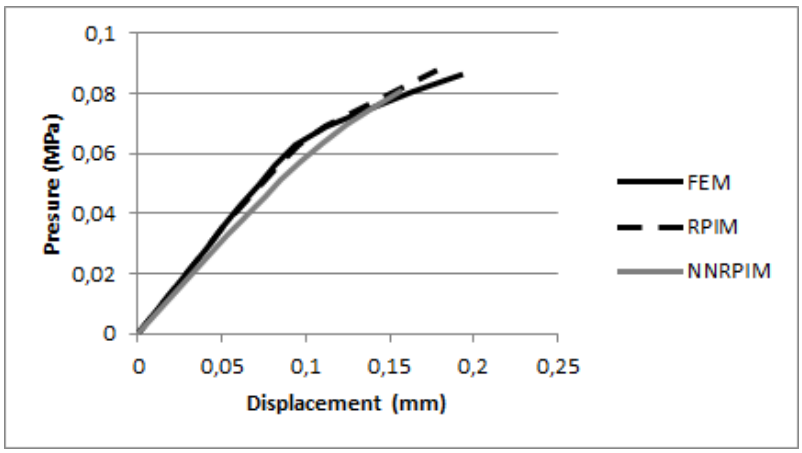

(c) Result obtained with Heavily Calcified plaque

Figure 6.101: 3D Model II - Comparison of displacement of point B with different numerical methods - Section 2

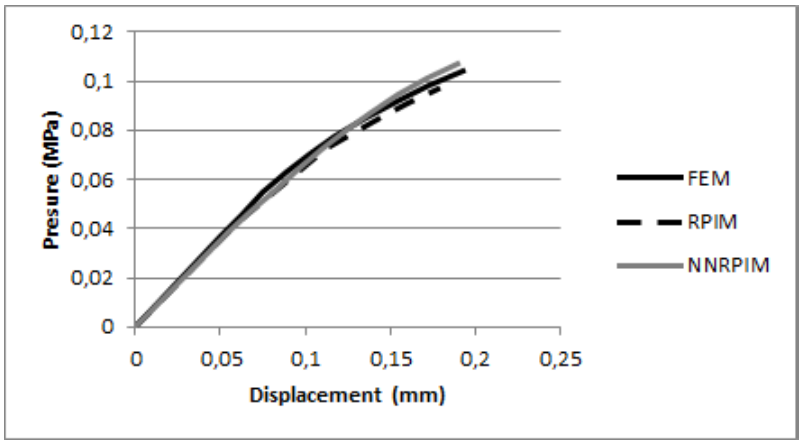

(a) Result obtained with Lightly Calcified plaque

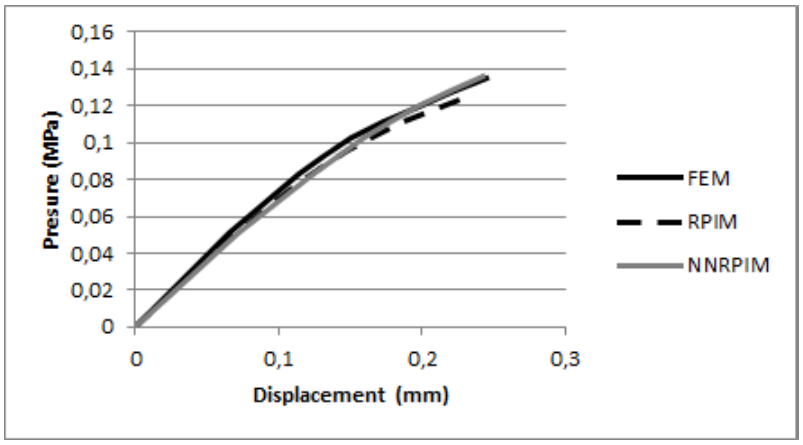

(b) Result obtained with Moderately Calcified plaque

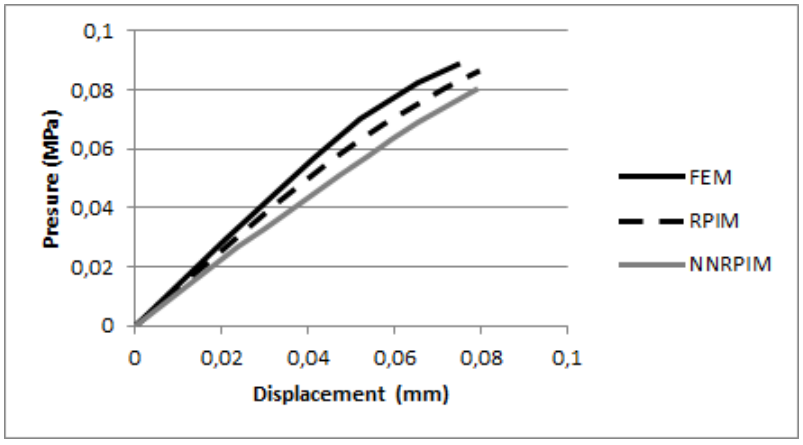

(c) Result obtained with Heavily Calcified plaque

Figure 6.102: 3D Model II - Comparison of displacement of point B with different numerical methods - Section 2

Chapter 7

Conclusions and Future Work

CVD's and atherosclerosis are an important health concern in today's society, as it has already been mentioned, and the biomechanics of the atherosclerotic plaque is still an area in need of further study. In this work the use of the Radial Point Interpolation Method (RPIM) and the Natural Neighbour Radial Point Interpolation Method (NNRPIM) was extended for the analysis of Atherosclerotic Plaque in two-dimensional and three-dimensional models, being the first time the RPIM has been used with this purpose.

The main objectives of this thesis were to perform a elasto-plastic analysis of atherosclerotic arteries using meshless methods and with this, study the effects that plaque thickening and change of plaque's material properties due to tissue calcification could have in the mechanical behaviour of the artery. Besides these two main objectives, it was also aimed to draw from this work further comparisons from FEM and the meshless methods used.

As it was reported in the previous chapter, this analysis was performed as intended, allowing to see that as the level of calcification rises, so thus the artery's stiffness. The same can be said for the thickness of the artery's plaque, as it could be seen from the 2D study. At a physiological level it was also proven, by both the 2D and 3D analysis, that the atherosclerotic plaque does not suffer any plastic deformations, only reaching its yield point at a supraphysiological state.

The use of meshless methods also proved to be adequate, as it could be seen by significant and recurring overlay of results between this methods and the more widely use FEM. As problems in biomechanics often present a high degree of complexity, either by their geometry or phenomena involved, the reliability of the RPIM and NNRPIM concluded from the present work, added to the facility that meshless methods show in modelling complex geometries or large deformations, should make them a primary tool for the study of mechanobiologic problems in biomechanics.

While this work reached all of the proposed objectives, it also had some limitations. Firstly, while the elasto-plastic model used to predict the mechanical behaviour of the plaque revealed to be adequate, as seen by the good overlay between it and the experimental values, it was also a simplification of the plaque's actual behaviour that is much more complex. This behaviour could also not be better assessed since there is a lack of mechanical experimental data on atherosclerotic plaque, being only found two research studies in the literature, in which the mechanical data is

correlated with the plaques composition.

Secondly, the hardware available limited the level of discretization that could be achieved, as the numerical analysis had to be limited to around 4000 nodes. While this did not hinder the results in the 2D analysis, it clearly had an effect on the 3D models, recall that in the 2D analysis it was used around 4000 nodes to discretize an infinitesimal slice of the problem, in the 3D analysis each slice of the model could only have around 70 or 80 nodes.

Another point to raise is, that the 2D analysis could not be compared with the 3D analysis. This was not only because of the different levels of discretization, but also by the two different configurations used for each of the models, being one of the a continuous plaque around the artery and the other only a partial plaque.

Finally it could be raised that the lack of any damage model, of the anysotropic and hyper-elastic characteristics of arterial tissues or of the pulsatile forces characteristic of the circulatory system are also limitations of this study.

For the future further work could be made to develop the methodology presented here. It would be advised to consider the anisotropic and hiperelastic characteristics of the tissues and to gather further experimental data in order to develop a constitutive model of the atherosclerotic plaque. A multi-scale analysis, the combination of an inflammatory model with a mechanobiologic models or a dynamic analysis simulating the pulsatile stress that the artery is subjected would also be advised routes for further research.

Bibliography

[1] "Cardiovascular Diseases (CVDs)," 2015. [Online]. Available: http://www.who.int/mediacentre/factsheets/fs317/en/

[2] J. Perk, G. De Backer, H. Gohlke, I. Graham, Z. Reiner, W. M. M. Verschuren, C. Albus, P. Benlian, G. Boysen, R. Cifkova, C. Deaton, S. Ebrahim, M. Fisher, G. Germano, R. Hobbs, A. Hoes, S. Karadeniz, A. Mezzani, E. Prescott, L. Ryden, M. Scherer, M. Syvänne, W. J. M. Scholte Op Reimer, C. Vrints, D. Wood, J. L. Zamorano, and F. Zannad, "European Guidelines on cardiovascular disease prevention in clinical practice (version 2012): The Fifth Joint Task Force of the European Society of Cardiology and Other Societies on Cardiovascular Disease Prevention in Clinical Practice (constituted by re," *Atherosclerosis*, vol. 223, no. 1, pp. 1–68, jul 2012. [Online]. Available: http://www.sciencedirect.com/science/article/pii/S0021915012002882

[3] S. Ylä-Herttuala, J. Luoma, H. Kallionpää, M. Laukkanen, P. Lehtolainen, and H. Viita, "Pathogenesis of atherosclerosis," *Maturitas*, vol. 23, pp. S47–S49, may 1996. [Online]. Available: http://www.sciencedirect.com/science/article/pii/0378512296010110

[4] W. Wang, Y. Lee, and C. H. Lee, "Review: the physiological and computational approaches for atherosclerosis treatment." *International journal of cardiology*, vol. 167, no. 5, pp. 1664–76, sep 2013. [Online]. Available: http://www.sciencedirect.com/science/article/pii/S0167527312013162

[5] K. B. Seung, D.-W. Park, Y.-H. Kim, S.-W. Lee, C. W. Lee, M.-K. Hong, S.-W. Park, S.-C. Yun, H.-C. Gwon, M.-H. Jeong, Y. Jang, H.-S. Kim, P. J. Kim, I.-W. Seong, H. S. Park, T. Ahn, I.-H. Chae, S.-J. Tahk, W.-S. Chung, and S.-J. Park, "Stents versus Coronary-Artery Bypass Grafting for Left Main Coronary Artery Disease," *New England Journal of Medicine*, vol. 358, no. 17, pp. 1781–1792, 2008.

[6] R. Hoffmann, G. S. Mintz, G. R. Dussaillant, J. J. Popma, A. D. Pichard, L. F. Satler, K. M. Kent, J. Griffin, and M. B. Leon, "Patterns and Mechanisms of In-Stent Restenosis: A Serial Intravascular Ultrasound Study ," *Circulation*, vol. 94, no. 6, pp. 1247–1254, sep 1996. [Online]. Available: http://circ.ahajournals.org/content/94/6/1247.abstract

[7] A. P. Antoniadis, P. Mortier, G. Kassab, G. Dubini, N. Foin, Y. Murasato, A. A. Giannopoulos, S. Tu, K. Iwasaki, Y. Hikichi, F. Migliavacca, C. Chiastra, J. J. Wentzel, F. Gijsen, J. H. C. Reiber, P. Barlis, P. W. Serruys, D. L. Bhatt, G. Stankovic, E. R. Edelman, G. D. Giannoglou, Y. Louvard, and Y. S. Chatzizisis, "Biomechanical Modeling to Improve Coronary Artery Bifurcation Stenting: Expert Review Document on Techniques and Clinical Implementation." *JACC. Cardiovascular interventions*, vol. 8, no. 10, pp. 1281–96, aug 2015. [Online]. Available: http://www.sciencedirect.com/science/article/pii/S1936879815009759

[8] N. Eshghi, M. Hojjati, M. Imani, and A. Goudarzi, "Finite Element Analysis of Mechanical Behaviors of Coronary Stent," *Procedia Engineering*, vol. 10, pp. 3056–3061, 2011. [Online]. Available: http://www.sciencedirect.com/science/article/pii/S1877705811006941

[9] A. Fortier, V. Gullapalli, and R. A. Mirshams, "Review of biomechanical studies of arteries and their effect on stent performance," *IJC Heart & Vessels*, vol. 4, pp. 12–18, sep 2014. [Online]. Available: http://www.sciencedirect.com/science/article/pii/S2214763214000261

[10] E. M. Cunnane, J. J. E. Mulvihill, H. E. Barrett, and M. T. Walsh, "Simulation of human atherosclerotic femoral plaque tissue: the influence of plaque material model on numerical results," *BioMedical Engineering OnLine*, vol. 14, no. Suppl 1, pp. S7–S7, jan 2015. [Online]. Available: http://www.ncbi.nlm.nih.gov/pmc/articles/PMC4306121/

[11] J. Belinha, L. Dinis, and R. N. Jorge, "The natural neighbour radial point interpolation method: dynamic applications," *Engineering Computations*, vol. 26, no. 8, pp. 911–949, 2009.

[12] E. Süli, "Finite Element Methods for Partial Differential Equations," 2012.

[13] M. Turner, R. Clough, H. Martin, and L. Topp, "Stiffness and Deflection Analysis of Complex Structures," *Journal of the Aeronautical Sciences (Institute of the Aeronautical Sciences)*, vol. 23, no. 9, pp. 805–823, sep 1956. [Online]. Available: http://arc.aiaa.org/doi/abs/10.2514/8.3664

[14] J. Argyris, "Energy Theorems and Structural Analysis: A Generalized Discourse with Applications on Energy Principles of Structural Analysis Including the Effects of Temperature and Non-Linear Stress-

Strain Relations," pp. 347–356, 1954. [Online]. Available: http://www.emeraldinsight.com/journals.htm?issn=0002-2667{&}volume=26{&}issue=10{&}articleid=1679779{&}show=html

[15] G. Battista, L. Evangelisti, C. Guattari, and R. D. L. Vollaro, "On the Influence of Geometrical Features and Wind Direction over an Urban Canyon Applying a FEM Analysis," *Energy Procedia*, vol. 81, pp. 11–21, dec 2015. [Online]. Available: http://www.sciencedirect.com/science/article/pii/S1876610215027034

[16] S. Matsunaga, N. Takano, Y. Tamatsu, S. Abe, and Y. Ide, "Biomechanics of Jaw Bone Considering Structural Properties of Trabecular Bone," *Journal of Oral Biosciences*, vol. 53, no. 2, pp. 143–147, jan 2011. [Online]. Available: http://www.sciencedirect.com/science/article/pii/S1349007911800174

[17] J. Reddy, *An Introduction to the Finite Element Method*. McGraw-Hill Education, 2005. [Online]. Available: https://books.google.pt/books?id=8gqnRwAACAAJ

[18] S. S. Bhavikatti, *Finite Element Analysis*. New Age International, 2005. [Online]. Available: https://books.google.pt/books?id=YzecxxuNJPwC

[19] T. Belytschko, Y. Krongauz, D. Organ, M. Fleming, and P. Krysl, "Meshless methods: An overview and recent developments," *Computer Methods in Applied Mechanics and Engineering*, vol. 139, no. 1-4, pp. 3–47, dec 1996. [Online]. Available: http://www.sciencedirect.com/science/article/pii/S004578259601078X

[20] K. Liew, X. Zhao, and A. J. Ferreira, "A review of meshless methods for laminated and functionally graded plates and shells," *Composite Structures*, vol. 93, no. 8, pp. 2031–2041, jul 2011. [Online]. Available: http://www.sciencedirect.com/science/article/pii/S0263822311000663

[21] J. Belinha, *Meshless Methods in Biomechanics: Bone Tissue Remodelling Analysis*, ser. Lecture Notes in Computational Vision and Biomechanics. Springer International Publishing, 2014. [Online]. Available: https://books.google.pt/books?id=0c4lBAAAQBAJ

[22] T. Liszka and J. Orkisz, "The finite difference method at arbitrary irregular grids and its application in applied mechanics," *Computers & Structures*, vol. 11, no. 1-2, pp. 83–95, feb 1980. [Online]. Available: http://www.sciencedirect.com/science/article/pii/0045794980901492

[23] J. Monaghan, "An introduction to SPH," *Computer Physics Communications*, vol. 48, no. 1, pp. 89–96, jan 1988. [Online]. Available: http://www.scopus.com/inward/record.url?eid=2-s2.0-0023165466{&}partnerID=tZOtx3y1

[24] D. W. Holmes, J. R. Williams, and P. Tilke, "Smooth particle hydrodynamics simulations of low reynolds number flows through porous media," *International Journal for Numerical and Analytical Methods in Geomechanics*, vol. 35, no. 4, pp. 419–437, 2011. [Online]. Available: http://dx.doi.org/10.1002/nag.898

[25] Wing Kam Liu, Sukky Jun, and Yi Fei Zhang, "Reproducing kernel particle methods," pp. 1081–1106, 1995. [Online]. Available: http://www.scopus.com/inward/record.url?eid=2-s2.0-0029102512{&}partnerID=tZOtx3y1

[26] B. Nayroles, G. Touzot, and P. Villon, "Generalizing the finite element method: Diffuse approximation and diffuse elements," *Computational Mechanics*, vol. 10, no. 5, pp. 307–318, 1992. [Online]. Available: http://www.scopus.com/inward/record.url?eid=2-s2.0-0027035536{&}partnerID=tZOtx3y1

[27] T. Belytschko, Y. Y. Lu, and L. Gu, "Element-free Galerkin methods," *International Journal for Numerical Methods in Engineering*, vol. 37, no. 2, pp. 229–256, 1994. [Online]. Available: http://www.scopus.com/inward/record.url?eid=2-s2.0-0028259955{&}partnerID=tZOtx3y1

[28] N. S. Atluri and T. Zhu, "A new Meshless Local Petrov-Galerkin (MLPG) approach in computational mechanics," *Computational Mechanics*, vol. 22, no. 2, pp. 117–127. [Online]. Available: http://dx.doi.org/10.1007/s004660050346

[29] S. De and K. J. Bathe, "The method of finite spheres," *Computational Mechanics*, vol. 25, no. 4, pp. 329–345, 2000.

[30] E. Oñate and S. Idelsohn, "A mesh-free finite point method for advective-diffusive transport and fluid flow problems," *Computational Mechanics*, vol. 21, no. 4-5, pp. 283–292, 1998. [Online]. Available: http://www.scopus.com/inward/record.url?eid=2-s2.0-0032071696{&}partnerID=tZOtx3y1

[31] E. Kansa, "Multiquadrics—A scattered data approximation scheme with applications to computational fluid-dynamics—I surface approximations and partial derivative estimates," *Computers & Mathematics with Applications*, vol. 19, no. 8-9, pp. 127–145, 1990. [Online]. Available: http://www.sciencedirect.com/science/article/pii/089812219090270T

[32] ——, "Multiquadrics—A scattered data approximation scheme with applications to computational fluid-dynamics—II solutions to parabolic, hyperbolic and elliptic partial differential equations," *Computers & Mathematics with Applications*, vol. 19, no. 8-9, pp. 147–161, 1990. [Online]. Available: http://www.sciencedirect.com/science/article/pii/089812219090271K

[33] L. Dinis, R. Natal Jorge, and J. Belinha, "Analysis of 3D solids using the natural neighbour radial point interpolation method," *Computer Methods in Applied Mechanics and Engineering*, vol. 196, no. 13-16, pp. 2009–2028, mar 2007. [Online]. Available: http://www.sciencedirect.com/science/article/pii/S0045782506003446

[34] G. R. Liu and Y. T. Gu, "A point interpolation method for two dimensional solids," vol. 50, no. FEBRUARY 2001, pp. 937–951, 2001.

[35] G. Liu, "A point assembly method for stress analysis for two-dimensional solids," *International Journal of Solids and Structures*, vol. 39, no. 1, pp. 261–276, jan 2002. [Online]. Available: http://www.sciencedirect.com/science/article/pii/S002076830100172X

[36] S. R. Idelsohn, E. Oñate, N. Calvo, and F. Del Pin, "The meshless finite element method," *International Journal for Numerical Methods in Engineering*, vol. 58, no. 6, pp. 893–912, 2003. [Online]. Available: http://dx.doi.org/10.1002/nme.798

[37] L. Traversoni, "Natural neighbour finite elements," *Transactions on Ecology and the Environment*, vol. 8, 1994.

[38] N. Sukumar, B. Moran, A. Y. Semenov, and V. V. Belikov, "Natural neighbour Galerkin methods," *International Journal for Numerical Methods in Engineering*, vol. 50, no. 1, pp. 1–27, 2001.

[39] J. Braun and M. Sambridge, "A numerical method for solving partial differential equations on highly irregular evolving grids," *Nature*, vol. 376, no. 6542, pp. 655–660, aug 1995. [Online]. Available: http://dx.doi.org/10.1038/376655a0

[40] N. Sukumar, B. Moran, and T. Belytschko, "The natural element method in solid mechanics," *International Journal for Numerical Methods in Engineering*, vol. 43, no. 5, pp. 839–887, 1998. [Online]. Available: http://dx.doi.org/10.1002/(SICI)1097-0207(19981115)43:5<839::AID-NME423>3.0.CO;2-R

[41] E. Cueto, M. Doblaré, and L. Gracia, "Imposing essential boundary conditions in the natural element method by means of density-scaled alpha-shapes," *International Journal for Numerical Methods in Engineering*, vol. 49, no. 4, pp. 519–546, 2000. [Online]. Available: http://dx.doi.org/10.1002/1097-0207(20001010)49:4<519::AID-NME958>3.0.CO;2-0

[42] J. G. Wang and G. R. Liu, "A point interpolation meshless method based on radial basis functions," *International Journal for Numerical Methods in Engineering*, vol. 54, no. 11, pp. 1623–1648, 2002.

[43] J. Wang and G. Liu, "On the optimal shape parameters of radial basis functions used for 2-D meshless methods," *Computer Methods in Applied Mechanics and Engineering*, vol. 191, no. 23-24, pp. 2611–2630, mar 2002. [Online]. Available: http://www.sciencedirect.com/science/article/pii/S0045782501004194

[44] R. G. Liu, Y. G. Zhang, T. Y. Gu, and Y. Y. Wang, "A meshfree radial point interpolation method (RPIM) for three-dimensional solids," *Computational Mechanics*, vol. 36, no. 6, pp. 421–430, 2005. [Online]. Available: http://dx.doi.org/10.1007/s00466-005-0657-6

[45] K. M. Liew and X. L. Chen, "Mesh-free radial point interpolation method for the buckling analysis of mindlin plates subjected to in-plane point loads," *International Journal for Numerical Methods in Engineering*, vol. 60, no. 11, pp. 1861–1877, 2004. [Online]. Available: http://dx.doi.org/10.1002/nme.1027

[46] G. R. Liu, K. Y. Dai, K. M. Lim, and Y. T. Gu, "A radial point interpolation method for simulation of two-dimensional piezoelectric structures," *Smart Materials and Structures*, vol. 12, no. 2, p. 171, 2003. [Online]. Available: http://stacks.iop.org/0964-1726/12/i=2/a=303

[47] R. Sibson *et al.*, "A brief description of natural neighbour interpolation," *Interpreting multivariate data*, vol. 21, pp. 21–36, 1981.

[48] G. Voronoi, "Nouvelles applications des paramètres continus à la théorie des formes quadratiques. deuxième mémoire. recherches sur les parallélloèdres primitifs." *Journal für die reine und angewandte Mathematik*, vol. 134, pp. 198–287, 1908. [Online]. Available: http://eudml.org/doc/149291

[49] B. Delaunay, "Sur la sphére vide. A la memoire de Georges Voronoï. Izv. Akad. Nauk SSSR," *Otdelenie Matematicheskih i Estestvennyh Nauk*, vol. 7, pp. 793–800, 1934.

[50] Q. Liu and H.-C. Han, "Mechanical buckling of artery under pulsatile pressure." *Journal of biomechanics*, vol. 45, no. 7, pp. 1192–8, apr 2012. [Online]. Available: http://www.scopus.com/inward/record.url?eid=2-s2.0-84862815936{&}partnerID=tZOtx3y1

[51] ——, "Mechanical buckling of arterioles in collateral development." *Journal of theoretical biology*, vol. 316, pp. 42–8, jan 2013. [Online]. Available: http://www.scopus.com/inward/record.url?eid=2-s2.0-84867423373{&}partnerID=tZOtx3y1

[52] H.-C. Han, "A biomechanical model of artery buckling," *Journal of Biomechanics*, vol. 40, no. 16, pp. 3672–3678, feb 2007. [Online]. Available: http://dx.doi.org/10.1016/j.jbiomech.2007.06.018

[53] ——, "The theoretical foundation for artery buckling under internal pressure." *Journal of biomechanical engineering*, vol. 131, no. 12, p. 124501, dec 2009. [Online]. Available: http://www.scopus.com/inward/record.url?eid=2-s2.0-71549123777{&}partnerID=tZOtx3y1

[54] ——, "Blood vessel buckling within soft surrounding tissue generates tortuosity." *Journal of biomechanics*, vol. 42, no. 16, pp. 2797–801, dec 2009. [Online]. Available: http://www.scopus.com/inward/record.url?eid=2-s2.0-71549122262{&}partnerID=tZOtx3y1

[55] A. Y. Lee, A. Sanyal, Y. Xiao, R. Shadfan, and H.-C. Han, "Mechanical instability of normal and aneurysmal arteries." *Journal of biomechanics*, vol. 47, no. 16, pp. 3868–75, dec 2014. [Online]. Available: http://www.sciencedirect.com/science/article/pii/S0021929014005296

[56] Y. Fung, *Biomechanics: mechanical properties of living tissues*, ser. Biomechanics / Y. C. Fung. Springer-Verlag, 1981. [Online]. Available: https://books.google.pt/books?id=OKU0AAAAMAAJ

[57] D. M. Pierce, T. E. Fastl, B. Rodriguez-Vila, P. Verbrugghe, I. Fourneau, G. Maleux, P. Herijgers, E. J. Gomez, and G. A. Holzapfel, "A method for incorporating three-dimensional residual stretches/stresses into patient-specific finite element simulations of arteries." *Journal of the mechanical behavior of biomedical materials*, vol. 47, pp. 147–64, jul 2015. [Online]. Available: http://www.sciencedirect.com/science/article/pii/S1751616115001058

[58] D. Nikolić, M. Radović, S. Aleksandrić, M. Tomašević, and N. Filipović, "Prediction of coronary plaque location on arteries having myocardial bridge, using finite element models." *Computer methods and programs in biomedicine*, vol. 117, no. 2, pp. 137–44, nov 2014. [Online]. Available: http://www.sciencedirect.com/science/article/pii/S0169260714003009

[59] C. K. Chai, A. C. Akyildiz, L. Speelman, F. J. H. Gijsen, C. W. J. Oomens, M. R. H. M. van Sambeek, A. van der Lugt, and F. P. T. Baaijens, "Local axial compressive mechanical properties of human carotid atherosclerotic plaques-characterisation by indentation test and inverse finite element analysis," *Journal of Biomechanics*, vol. 46, no. 10, pp. 1759–1766, 2013. [Online]. Available: http://dx.doi.org/10.1016/j.jbiomech.2013.03.017

[60] C.-K. Chai, A. C. Akyildiz, L. Speelman, F. J. H. Gijsen, C. W. J. Oomens, M. R. H. M. van Sambeek, A. van der Lugt, and F. P. T. Baaijens, "Local anisotropic mechanical properties of human carotid atherosclerotic plaques - characterisation by micro-indentation and inverse finite element analysis." *Journal of the mechanical behavior of biomedical materials*, vol. 43, pp. 59–68, mar 2015. [Online]. Available: http://www.sciencedirect.com/science/article/pii/S175161611400383X

[61] J. J. Mulvihill, E. M. Cunnane, S. M. McHugh, E. G. Kavanagh, S. R. Walsh, and M. T. Walsh, "Mechanical, biological and structural characterization of in vitro ruptured human carotid plaque tissue." *Acta biomaterialia*, vol. 9, no. 11, pp. 9027–35, nov 2013. [Online]. Available: http://www.sciencedirect.com/science/article/pii/S1742706113003516

[62] A. C. Akyildiz, L. Speelman, and F. J. H. Gijsen, "Mechanical properties of human atherosclerotic intima tissue." *Journal of biomechanics*, vol. 47, no. 4, pp. 773–83, mar 2014. [Online]. Available: http://www.sciencedirect.com/science/article/pii/S0021929014000487

[63] C.-K. Chai, L. Speelman, C. W. J. Oomens, and F. P. T. Baaijens, "Compressive mechanical properties of atherosclerotic plaques–indentation test to characterise the local anisotropic behaviour." *Journal of biomechanics*, vol. 47, no. 4, pp. 784–92, mar 2014. [Online]. Available: http://www.sciencedirect.com/science/article/pii/S0021929014000475

[64] J. Belinha, L. Dinis, and R. N. Jorge, "An elasto-plastic model to analyse the biomechanical behaviour of the atherosclerotic plaque tissue," *2015 IEEE 4th Portuguese Meeting on Bioengineering (ENBENG)*, no. February, pp. 279–284, 2015.

[65] G. Sommer, *Mechanical Properties of Healthy and Diseased Human Arteries*, 2008.

[66] T. C. Gasser, R. W. Ogden, and G. A. Holzapfel, "Hyperelastic modelling of arterial layers with distributed collagen fibre orientations," *Journal of The Royal Society Interface*, vol. 3, no. 6, pp. 15–35, 2006. [Online]. Available: http://rsif.royalsocietypublishing.org/content/3/6/15

[67] M. Bulelzai, J. Dubbeldam, and H. Meijer, "Bifurcation analysis of a model for atherosclerotic plaque evolution," *Physica D: Nonlinear Phenomena*, vol. 278-279, pp. 31–43, jun 2014. [Online]. Available: http://www.sciencedirect.com/science/article/pii/S0167278914000827

[68] H. C. Stary, A. B. Chandler, R. E. Dinsmore, V. Fuster, S. Glagov, W. Insull, M. E. Rosenfeld, C. J. Schwartz, W. D. Wagner, and R. W. Wissler, "A Definition of Advanced Types of Atherosclerotic Lesions and a Histological Classification of Atherosclerosis : A Report From the Committee on Vascular Lesions of the Council on Arteriosclerosis, American Heart Association," *Circulation*, vol. 92, no. 5, pp. 1355–1374, sep 1995. [Online]. Available: http://circ.ahajournals.org/cgi/content/long/92/5/1355

[69] H. C. Stary, "Natural History and Histological Classification of Atherosclerotic Lesions : An Update," *Arteriosclerosis, Thrombosis, and Vascular Biology*, vol. 20, no. 5, pp. 1177–1178, may 2000. [Online]. Available: http://atvb.ahajournals.org/cgi/content/long/20/5/1177

[70] E. M. Cunnane, J. J. E. Mulvihill, H. E. Barrett, D. A. Healy, E. G. Kavanagh, S. R. Walsh, and M. T. Walsh, "Mechanical, biological and structural characterization of human atherosclerotic femoral plaque tissue," *Acta Biomaterialia*, vol. 11, pp. 295–303, 2015. [Online]. Available: http://www.sciencedirect.com/science/article/pii/S1742706114004073

[71] F. L. Matthews and R. D. Rawlings, *Composite Materials: Engineering and Science*, ser. Woodhead Publishing Series in Composites Science and Engineering. Elsevier Science, 1999. [Online]. Available: https://books.google.pt/books?id=dVGkAgAAQBAJ

[72] J. Park and R. S. Lakes, *Biomaterials: An Introduction*. Springer New York, 2007. [Online]. Available: https://books.google.pt/books?id=bb68wb0R{_}EAC

[73] J.-S. Chen, C.-T. Wu, S. Yoon, and Y. You, "A stabilized conforming nodal integration for galerkin mesh-free methods," *International Journal for Numerical Methods in Engineering*, vol. 50, no. 2, pp. 435–466, 2001. [Online]. Available: http://dx.doi.org/10.1002/1097-0207(20010120)50:2<435::AID-NME32>3.0.CO;2-A

[74] W. Elmer, J. S. Chen, M. Puso, and E. Taciroglu, "A stable, meshfree, nodal integration method for nearly incompressible solids," *Finite Elements in Analysis and Design*, vol. 51, pp. 81–85, 2012. [Online]. Available: http://www.sciencedirect.com/science/article/pii/S0168874X11002150

[75] K. Y. Sze, J. S. Chen, N. Sheng, and X. H. Liu, "Stabilized conforming nodal integration: exactness and variational justification," *Finite Elements in Analysis and Design*, vol. 41, no. 2, pp. 147–171, 2004. [Online]. Available: http://www.sciencedirect.com/science/article/pii/S0168874X04000848

[76] P. Wriggers, *Computational Contact Mechanics*. Springer Berlin Heidelberg, 2006. [Online]. Available: https://books.google.pt/books?id=oBMBy4eMYsQC

[77] C. Lawson, "Software for C1 Surface Interpolation," *J.R. Rice (Ed.), Mathematical Software III, vol. 3 Academic Press, New York, NY*, 1977.

[78] P. Lancaster and K. Salkauskas, "Surfaces generated by moving least squares methods," *Mathematics of Computation*, vol. 37, no. 155, pp. 141–141, 1981.

[79] R. Hardy, "Theory and applications of the multiquadric-biharmonic method 20 years of discovery 1968–1988," *Computers & Mathematics with Applications*, vol. 19, no. 8-9, pp. 163–208, 1990. [Online]. Available: http://www.sciencedirect.com/science/article/pii/089812219090272L

[80] J. Belinha, "The natural neighbour radial point interpolation method : solid mechanics and mechanobiology applications," Ph.D. dissertation, Faculty of Engineering of the University of Porto, 2010.

[81] ——, "Elasto-Plastic Analysis Considering the Element Free Galerkin Method," Ph.D. dissertation, Faculty of Engineering of the University of Porto, 2004.

[82] D. R. J. Owen and E. Hinton, *Finite elements in plasticity: theory and practice*. Pineridge Press, 1980. [Online]. Available: https://books.google.pt/books?id=IzcIAQAAIAAJ

[83] L. D. Landau, E. M. Lifshitz, A. M. Kosevich, and Pitaevski\u\i, *Theory of Elasticity*. Elsevier, 1986.

[84] R. Hill, *The Mathematical Theory of Plasticity*, ser. Oxford classic texts in the physical sciences. Clarendon Press, 1998. [Online]. Available: https://books.google.pt/books?id=Wy{_}kuQZzfdIC

[85] M. A. Crisfield, *Non-linear Finite Element Analysis of Solids and Structures: Essentials*, ser. Non-Linear Finite Element Analysis of Solids and Structures. Wiley, 1991. [Online]. Available: https://books.google.pt/books?id=Vr5RAAAAMAAJ

[86] L. M. J. S. de Dinis, R. M. N. Jorge, and J. Belinha, *The Radial Natural Neighbours Interpolators Extended to Elastoplasticity*. Dordrecht: Springer Netherlands, 2009, pp. 175–198. [Online]. Available: http://dx.doi.org/10.1007/978-1-4020-8821-6{_}11

[87] T. Sandgren, B. Sonesson, Å. R. Ahlgren, and T. Länne, "The diameter of the common femoral artery in healthy human: Influence of sex, age, and body size," *Journal of Vascular Surgery*, vol. 29, no. 3, pp. 503–510, 1999. [Online]. Available: http://www.sciencedirect.com/science/article/pii/S074152149970279X

[88] J. T. Ottesen, M. S. Olufsen, and J. K. Larsen, *Applied Mathematical Models in Human Physiology*, ser. Monographs on Mathematical Modeling and Computation. Society for Industrial and Applied Mathematics, 2004. [Online]. Available: https://books.google.pt/books?id=iq4faX4Mn-AC

[89] R. R. Kasliwal, M. Bansal, D. Desai, and M. Sharma, "Carotid intima–media thickness: Current evidence, practices, and Indian experience," *Indian Journal of Endocrinology and Metabolism*, vol. 18, no. 1, pp. 13–22, 2014. [Online]. Available: http://www.ncbi.nlm.nih.gov/pmc/articles/PMC3968727/

[90] H. E. Barrett, E. M. Cunnane, E. G. Kavanagh, and M. T. Walsh, "On the effect of calcification volume and configuration on the mechanical behaviour of carotid plaque tissue," *Journal of the Mechanical Behavior of Biomedical Materials*, vol. 56, pp. 45–56, 2016. [Online]. Available: http://www.sciencedirect.com/science/article/pii/S1751616115004191

[91] H. K. Walker, W. D. Hall, and J. W. Hurst, *Clinical Methods: The History, Physical, and Laboratory Examinations*. Butterworths, 1990. [Online]. Available: https://books.google.pt/books?id=qtz3JRBuwRIC